# USING SPECTRAL ANALYSIS AND FLUID DYNAMICS TO UNDERSTAND SUPRAGLACIAL STREAM NETWORKS ON THE GREENLAND ICE SHEET AND SEISMICITY AT KILAUEA VOLCANO

by

JOSHUA CROZIER

A DISSERTATION

Presented to the Department of Earth Sciences
and the Division of Graduate Studies of the University of Oregon
in partial fulfillment of the requirements
for the degree of
Doctor of Philosophy

June 2021

DISSERTATION APPROVAL PAGE

Student: Joshua Crozier

Title: Using Spectral Analysis and Fluid Dynamics to Understand Supraglacial Stream Networks on the Greenland Ice Sheet and Seismicity at Kīlauea Volcano

This dissertation has been accepted and approved in partial fulfillment of the requirements for the Doctor of Philosophy degree in the Department of Earth Sciences by:

| | |
|---|---|
| Leif Karlstrom | Chair |
| Alan Rempel | Core Member |
| Emilie Hooft | Core Member |
| Thomas Giachetti | Core Member |
| Boyana Norris | Institutional Representative |

and

| | |
|---|---|
| Andy Karduna | Interim Vice Provost for Graduate Studies |

Original approval signatures are on file with the University of Oregon Division of Graduate Studies.

Degree awarded June 2021

DISSERTATION ABSTRACT

Joshua Crozier

Doctor of Philosophy

Department of Earth Sciences

June 2021

Title: Using Spectral Analysis and Fluid Dynamics to Understand Supraglacial Stream Networks on the Greenland Ice Sheet and Seismicity at Kīlauea Volcano

Fluid dynamics are an integral component of many natural systems considered in earth sciences, including both ice sheets and volcanoes. I combine fluid dynamics modeling with multiple spectral analysis techniques and a variety of datasets to address questions in glaciology and volcanology.

I first examine what controls supraglacial meltwater routing on the Greenland Ice Sheet, and how this meltwater routing respond to changing ice sheet conditions. I approach this with fluid dynamical models of ice flow and multiple geomorphologial methods based on spectral analysis. I demonstrate that bedrock topography underlying the ice sheet is the dominant control on supraglacial drainage basin scale ice surface topography and meltwater routing. I then show that a thinning ice sheet or increasing basal sliding will result in smaller supraglacial drainage basins. This could cause more disperse subglacial

meltwater input and potentially further impact ice sheet flow, so may be important to incorporate into ice sheet evolution models.

I next examine what very long period seismicity from magma resonance can reveal about evolution of the shallow magma system at Kīlauea Volcano. To do this I develop a new automated workflow for detecting and classifying resonant signals based on wavelet transforms. I then create a catalog of very long period seismicity over the 2008-2018 summit eruption of Kīlauea Volcano. To analyze this catalog, I develop a coupled fluid-elastic model for the magma resonance. This model includes empirically constrained models for magma properties, joint H2O-CO2 solubility relationships, and accounts for stratified magma columns that could arise under disequilibrium outgassing regimes. I then conduct inversions for the seismic catalog, with constraints from other geophysical data and inversions. These inversions yield an unprecedented in-situ resolution of changes over time in both magma temperature and volatile contents. They show evolution of the magma system over a variety of timescales, and provide insights with implications for both hazard monitoring and understanding volcanic processes.

This dissertation includes previously published and unpublished co-authored material.

CURRICULUM VITAE

NAME OF AUTHOR: Joshua Crozier

GRADUATE AND UNDERGRADUATE SCHOOLS ATTENDED:

University of Oregon, Eugene, OR
Rice University, Houston, TX

DEGREES AWARDED:

Doctor of Philosophy, Earth Science, 2021, University of Oregon
Bachelor of Science, Earth Science, 2016, Rice University

AREAS OF SPECIAL INTEREST:

Geophysics, Volcanology, Seismology, Glaciology

PROFESSIONAL EXPERIENCE:

Graduate Employee, University of Oregon, 2016-2021

PUBLICATIONS:

Crozier, J. and Karlstrom, L. (2021). Wavelet-based characterization of very-long-period seismicity reveals temporal evolution of shallow magma system over the 2008-2018 eruption of Kīlauea Volcano. Journal of Geophysical Research: Solid Earth

C., Liang, Crozier, J. A., Karlstrom, L., and Dunham, E. M. (2020). Magma oscillations in a conduit-reservoir system, application to very long period (VLP) seismicity at basaltic volcanoes: 2. Data inversion and interpretation at Kīlauea Volcano. Journal of Geophysical Research: Solid Earth

Crozier, J., Karlstrom, L., and Yang, K. (2018). Basal control of supraglacial meltwater catchments on the Greenland Ice Sheet. The Cryosphere

Gonnermann, H. M., Giachetti, T., Fliedner, C., Nguyen, C. T., Houghton, B. F., Crozier, J. A., and Carey, R. J. (2017). Permeability during magma expansion and compaction. Journal of Geophysical Research: Solid Earth

# ACKNOWLEDGEMENTS

I thank Professor Leif Karlstrom for being an excellent advisor and collaborator. I thank my committee members Alan Rempel, Emilie Hooft, Thomas Giachetti, and Boyana Norris. I thank my other great collaborators Kang Yang, Josef Dufek, Chao Liang, Eric Dunham, Kyle Anderson, Weston Thelen, Mary Benage, Samantha Tramontano, Pablo Forte, Sara Olivia, and Helge Gonnermann. I thank many others who have been sources of scientific advice including Colin Meyer, Dan Ohara, Gene Humphreys, Amanda Thomas, and Phil Dawson. This research was supported in part by NASA award #NNX16AQ56G and by NSF EAR-1624557.

TABLE OF CONTENTS

LIST OF FIGURES

Figure Page

Figure Page

Figure Page

LIST OF TABLES

Table Page

# CHAPTER I

# INTRODUCTION

The topic of this work is using spectral analysis and fluid dynamics modeling to understand questions about ice sheets and volcanoes. Spectral analysis involves analyzing data or equations in the frequency or wavenumber domains. This can be useful for both processing and interpreting data or for solving equations. While ice sheets and volcanoes may seem disconnected, both are fluid dynamical systems involving processes acting over a range of spatial and temporal scales. In this work I apply multiple spectral analysis techniques to a variety of datasets to address important questions in glaciology and volcanology. In particular, I will examine what processes control ice sheet surface topography and meltwater routing on the Greenland Ice Sheet, and how these might respond to changing ice sheet conditions. I will also examine what information about magma systems can be obtained from very-long-period volcano seismicity caused by magma resonance over the 2008-2018 summit eruption of Kīlauea Volcano.

Modeling the fluid dynamics involved in both ice sheets and volcanoes is important for addressing these questions. To examine ice sheet surface topography and meltwater routing, the viscous flow of ice over underlying bedrock topography needs to be considered. The wavelength of bedrock topographic features controls how strongly they will be expressed on the ice sheet surface, where they could influence meltwater routing. To examine magma resonance, the corresponding signals first need to be accurately cataloged from a decade of continuous seismic data. The dynamics of a multi-phase fluid flowing through different magma

plumbing system structures then needs to be considered to infer properties of the magma system and how it evolves over time.

The rest of this introduction will provide a more detailed overview of each chapter in this dissertation, including information about author contributions and data availability.

## Ice Sheet Supraglacial Meltwater Catchments

Chapter II represents material written with co-authors Leif Karlstrom and Kang Yang that was published in The Cryosphere in 2018 under the title: "Basal control of supraglacial meltwater catchments on the Greenland Ice Sheet" [Crozier et al., 2018b]. Leif Karlstrom acknowledges funding from NASA award NNX16AQ56G. Kang Yang acknowledges support from the National Natural Science Foundation of China (41501452) and the Fundamental Research Funds for the Central Universities. We thank Colin Meyer, Dan O'Hara, and Alan Rempel for their input and discussions. We thank two anonymous reviewers for their constructive comments.

Ice surface topography controls the routing of surface meltwater generated in the ablation zones of glaciers and ice sheets. Meltwater routing is a direct source of ice mass loss, as well as a primary influence on subglacial hydrology and basal sliding of the ice sheet. Although the processes that determine ice sheet topography at the largest scales are known, controls on the topographic features that influence meltwater routing at supraglacial internally-drained-catchment (IDC) scales ($<$ 10s of km) are less well constrained. Here we examine the effects of two processes on ice sheet surface topography: transfer of bed topography to the surface of flowing ice and thermal-fluvial erosion by supraglacial meltwater

streams. We implement 2D basal transfer functions in seven study regions of the western Greenland Ice Sheet ablation zone using recent data sets for bed elevation, ice surface elevation, and ice surface velocities. We find that ∼1-10 km scale ice surface features can be well-explained by bed topography transfer in regions with different multi-year averaged ice flow conditions. We use flow-routing algorithms to extract supraglacial stream networks from 2-5 m resolution digital elevation models, and compare these with synthetic flow networks calculated on ice surfaces predicted by bed topography transfer. Multiple geomorphological metrics calculated for these networks suggest that bed topography can explain general ∼1-10 km scale supraglacial meltwater routing, and that thermal-fluvial erosion thus has a lesser role in shaping ice surface topography on these scales. We then use bed topography transfer functions and flow-routing to conduct a parameter study predicting how supraglacial internally drained catchment (IDC) configurations and subglacial hydraulic potential would change under varying multi-year averaged ice flow and basal sliding regimes. Predicted changes to subglacial hydraulic flow pathways directly caused by changing ice surface topography are subtle, but temporal changes in basal sliding or ice thickness have potentially significant influences on IDC spatial distribution. We suggest that changes to IDC size and number density could affect subglacial hydrology primarily by dispersing the englacial/subglacial input of surface meltwater.

All codes and data produced by the authors available upon request. Ice surface DEMs are from SETSM ArcticDEM 2-10 m resolution mosaics [ArcticDEM, 2017]. Bed DEMs are from Icebridge BedMachine [Morlighem et al., 2014, 2015]. Ice surface velocity data is from MEaSUREs [Joughin et al., 2010b,a]. 2015 Melt data is from RACMO 2.3p2 [Noel et al., 2015].

## Very-Long-Period Seismicity at Kīlauea

Chapter III represents material written with co-author Leif Karlstrom that has been published in Journal of Geophysical Research: Solid Earth in 2021 under the title: "Wavelet-based characterization of very-long-period seismicity reveals temporal evolution of shallow magma system over the 2008-2018 eruption of Kīlauea Volcano" [Crozier and Karlstrom, 2021]. Leif Karlstrom acknowledges support from NSF EAR-1624557. We thank Phil Dawson for providing an extended version of the Kīlauea VLP catalog published in 2014, seismic data from before 2012, and discussions of VLP seismicity categorization. USGS staff including Matt Patrick, Kyle Anderson, and Ingrid Johanson provided lava lake elevation, tilt-meter, and GPS data, as well as discussions about Kīlauea. Chao Liang and Eric Dunham provided codes and discussions of modeling magma resonance.

Very-long-period (VLP) volcano seismicity often encodes subsurface magma movement, and thus provides insight into subsurface magma transport processes. We develop a fully automated signal processing workflow using wavelet transforms to detect and assess period, decay rate, and ground motions of resonant VLP signals. We then generate a VLP catalog over the 2008-2018 open-vent summit eruption of Kīlauea Volcano containing thousands of events. Two types of magma resonance dominate our catalog: vertical sloshing of the open magma column in and out of the shallow magma reservoir, and lateral sloshing of magma in the lava lake. These events were triggered mainly from the surface and less commonly from depth. The VLP catalog is then combined with other geophysical datasets to characterize evolution of the shallow magma system. VLP ground motion patterns show both abrupt and gradual changes in shallow magma reservoir geometry.

Variation in resonant periods and decay rates of both resonance types occurred on timescales from hours to years, indicating variation in magma density and viscosity that likely reflect unsteady shallow outgassing and convection. A lack of correlation between decay rates of the two dominant resonant modes suggests a decoupling between magma in the conduit and lava lake. Known intrusions and rift zone eruptions often represented change points for resonance characteristics and their relations with other datasets. This data synthesis over a ten-year eruptive episode at Kīlauea Volcano demonstrates how VLP seismicity can sharpen insights into magma system evolution for use in monitoring and understanding eruptive processes.

Additional figures S1-S27 are included in the supplement.
The Kīlauea VLP seismicity catalog and codes used to make and analyze it are available at https://doi.org/10.7910/DVN/2UGFKE and https://bitbucket.org/crozierjosh1/vlp-seismicity-catalog-codes/src/master/, and the authors will provide updated versions and/or assistance upon request. Seismic data from 2008-2011 was obtained from the USGS, subsequent seismic data is publicly available from IRIS. GPS data is publicly available from UNAVCO. Tiltmeter data is available at [Johanson, 2020]. Lava lake elevation data was obtained from the USGS, and is published up to 2018 in [Patrick et al., 2019b]. $SO_2$ data from 2007-2010 is available at [Elias and Sutton, 2012]. $SO_2$ emission from 2014-2017 is available at [Elias et al., 2018]. The VLP seismicity catalog extended from the methods of [Dawson and Chouet, 2014] was obtained from the USGS.

## Kīlauea Very-Long-Period Seismicity Inversion

Chapter IV represents material written with co-author Leif Karlstrom that is in preparation for submission to Journal of Geophysical Research: Solid Earth. Leif Karlstrom acknowledges support from NSF EAR-1624557. We thank Emily Montgomery-Brown for providing codes implementing a model for the south flank slip. Matt Patrick provided lava lake elevation data. Other USGS staff including Kyle Anderson and Ingrid Johanson provided additional data and discussions about Kīlauea. Chao Liang provided discussions of modeling magma resonance.

Magma rheology and volatile contents play an important role in controlling eruptive potential and eruption dynamics, and can change over a wide range of timescales due to a variety of processes. Inferring in-situ information about these magma properties is thus vital for both understanding volcanic processes and for hazard monitoring. Very-long-period (VLP) seismic signals that represent magma movement are prevalent at many volcanoes, and can provide important information about magma system geometry and magma properties. The 2008-2018 open-vent eruption of Kīlauea Volcano provides an ideal test of what physics-based inversions of VLP seismicity can reveal about the evolution of a magmatic system. This is facilitated by the availability of a detailed catalog of thousands of impulsive VLP seismic events over ten years, an understanding of the VLP source mechanisms gained from modeling and inversions of select events, and a wealth of additional data and observations. We develop models for the dominant resonance type which represents vertical sloshing of magma in the conduit and shallow reservoir that incorporate viscous boundary layer flow and stratified magma density profiles arising from disequilibrium outgassing of magmatic water and $CO_2$. Using this model to conduct joint inversions for VLP seismicity and geodetic

data yields an unprecedented resolution of evolving magma volatile contents and temperature over timescales from days to years. Variation of magma properties at different depths, including consistent precursors to known intrusions and East Rift Zone eruptions, suggests changes in the convective/outgassing regime due to both magma recharge and lava lake overturn.

Codes used for inversions and analysis are available from the authors. GPS data is publicly available from UNAVCO or NGL. Lava lake elevation and surface area data was obtained from the USGS, and is published up to 2018 in [Patrick et al., 2019b].

# CHAPTER II

# ICE SHEET SUPRAGLACIAL MELTWATER CATCHMENTS

This chapter represents material published in The Cryosphere in 2018 with co-authors Leif Karlstrom and Kang Yang under the title: "Basal control of supraglacial meltwater catchments on the Greenland Ice Sheet" [Crozier et al., 2018b]. Joshua Crozier implemented most modeling and data analysis with input from Leif Karlstrom and Kang Yang; the extraction of observed supraglacial stream networks was done by Kang Yang. Joshua Crozier wrote the manuscript with input from Leif Karlstrom and Kang Yang. Leif Karlstrom, Kang Yang, and Joshua Crozier conceived of the study. Leif Karlstrom and Kang Yang obtained funding.

## Introduction

During warmer months on the Greenland ice sheet, surface melting in the ablation zone generates a large volume of water. Some meltwater is stored in or flows through porous firn or weathered ice, but most flows across the ice surface forming networks of supraglacial streams and lakes (such as the stream network shown in Fig. 2.1.B) [Fountain and Walder, 1998, van˜den˜Broeke et al., 2009, Andersen et al., 2015]. The majority of these streams feed into the englacial and subglacial hydrological systems either by flowing directly into open moulins [e.g., Chu, 2014, Smith et al., 2015], or by flowing into supraglacial lakes which can drain when enough water pressure builds up to hydraulically fracture the ice [Das et al., 2008, Selmes et al., 2011, Stevens et al., 2015]. Much of the meltwater will ultimately end up in the ocean [Enderlin et al., 2014, Andersen et al., 2015]. Along

the way, subglacial water and temporal variations in subglacial water flux can significantly influence ice advection by modulating basal sliding resistance [e.g., Zwally et al., 2002, Schoof, 2010, Sole et al., 2011, Shannon et al., 2013, Tedstone et al., 2014]. The spatial and temporal flux of surface meltwater to the subglacial hydrological system, how this flux evolves with changing climate and/or ice flow, and how subglacial hydraulic pathways evolve in response to meltwater input, are all poorly constrained and largely not incorporated into current ice sheet mass balance models [Larour et al., 2012, Gillet-Chaulet et al., 2012, Gagliardini et al., 2013, Lipscomb et al., 2013, Khan et al., 2015, Smith et al., 2017].

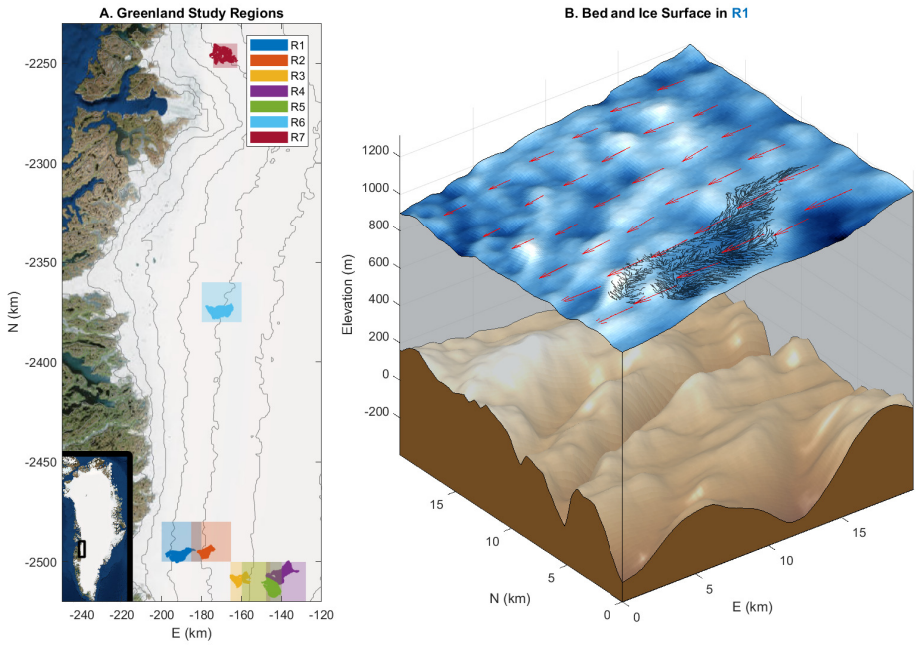


FIGURE 2.1. (A) Study IDCs (solid colored patches) of western Greenland with bounding boxes (semi-transparent squares) indicating corresponding domain used for bed transfer and admittance calculations. Black 200 m elevation contours are from BedMachine/GIMP [Howat et al., 2014, Morlighem et al., 2017b]. Imagery is from ArcGIS ERSI world imagery basemap. Information on all regions is shown in Table 1. (B) Ice surface and bed elevations (from BedMachine/GIMP) in study region R1, with stream channels from study drainage network shown in black and velocity field shown by red arrows.

Ice sheet surface meltwater flows downhill as dictated by surface topography. The largest scale of Greenland Ice Sheet topography is a continental-scale ($\sim$ 1000 km) gravity current profile, where average surface slopes are very gradual in the interior of the ice sheet (on the order of $10^{-2.5}$ radians or less) and steepen approaching the margins (on the order of $10^{-2}$ radians in our ablation zone study regions) [Cuffey and Paterson, 2010]. Deviations from this geometry at smaller wavelengths, however, reflect a combination of other physical processes. Some are products of the surface energy balance, such as solar radiation-driven ice melting/sublimation, melting of ice by flowing surface water (we will refer to this process as thermal-fluvial incision), and snow accumulation [Cuffey and Paterson, 2010, Karlstrom and Dunham, 2016, Boisvert et al., 2017, Meyer and Hewitt, 2017]. Others are products of ice flow processes such as crevassing [Echelmeyer et al., 1991, Cuffey and Paterson, 2010], propagating ice flux waves [Weertman, 1958, Nye, 1960, van˜de˜Wal and Oerlemans, 1995, Hewitt and Fowler, 2008], and the transfer of spatially variable bed topography, basal sliding, and ice rheology (due to temperature, grain alignment, or impurities) to the surface [Gudmundsson, 2003, Raymond and Gudmundsson, 2009, Sergienko, 2013, Graham et al., 2017].

The advection of ice over rough bed topography (such as that shown in Fig. 2.1.A) [Budd, 1970, Hutter et al., 1981, Gudmundsson, 2003, De Rydt et al., 2013, Joughin et al., 2013] is thought to be a significant source of IDC scale ($\sim$1-10 km) ice surface topography, and is a primary focus of our study. Supraglacial IDC and lake locations generally remain fixed year to year despite ice advection, which suggests a basal controlling process [Lampkin, 2011, Lampkin and van˜der˜Berg, 2011, Selmes et al., 2011, Sergienko, 2013, Igneczi et al., 2016, Karlstrom and Dunham, 2016]. We use the term "bed" loosely to refer to whatever

material composes the substrate under an ice sheet. In many locations the bed contains a deformable till layer which may not influence ice flow in the same way as rigid bedrock [Tulaczyk et al., 2000, Cuffey and Paterson, 2010], and bedrock erodes under the action of ice motion [Sugden, 1978, Hart, 1995].

Thermal-fluvial incision is also important for the evolution of surface topography and meltwater channel networks [e.g., Parker, 1975]. Surface melt rates in many areas of the Greenland Ice Sheet ablation zone are greater than 1 m/yr [Noel et al., 2015]; stream channels can be meters deep, and are in places observed to flow in directions not parallel to the surrounding ice surface slope or to slice through topographic ridges [Smith et al., 2015, Yang et al., 2015]. [Karlstrom and Dunham, 2016] suggested that longitudinal elevation profiles of supraglacial streams might even be inverted for primary production rate of meltwater, the analog to inferring climate variations and tectonic uplift rates from river profiles in terrestrial settings. However, although thermal-fluvial incision is required to make channels in the first place (e.g., lowering rate in channels must be greater than surroundings), it is unclear whether dynamic stream incision is efficient enough compared to other topographic influences to significantly affect IDC-scale topography and meltwater routing [Karlstrom and Dunham, 2016]. In this way supraglacial streams may be more analogous to ephemeral gullies on earth flows [Mackey and Roering, 2011] than to terrestrial river networks. The ice surface in ablation zones advects stream channels horizontally at velocities greater than 100 m/yr [Joughin et al., 2010b,a, Nagler et al., 2015], deforming or offsetting stream networks as they incise. This has been observed where Greenland supraglacial stream channels form along offset but parallel pathways as channels from previous years are advected out of topographic lows during winter months, though there are

also stream channels that are reused for multiple years [Karlstrom and Dunham, 2016].

Understanding the relative contributions of processes that govern ablation zone surface topography should yield better predictions of meltwater routing through time. Here, we use multiple data sets to examine the effects and significance of bed topography transfer and thermal-fluvial incision on ice sheet surface topography and meltwater routing. Ice surface velocity measurements, high resolution ice surface imagery and digital elevation models (DEMs), and bed elevation DEMs are now concurrently available over large expanses of the Greenland ice sheet ablation zone [Joughin et al., 2010b,a, Helm et al., 2014, Morlighem et al., 2017b,a, Nagler et al., 2015, Noel et al., 2015, ArcticDEM, 2017]. Many of these data sets are rapidly increasing in quality and temporal coverage, and developing methods to efficiently integrate such large data sets is thus important.

We implement approximate analytical solutions for bed topography transfer through flowing ice [Gudmundsson, 2003] over 2D regions of the Greenland ablation zone, evaluating the extent to which this transfer can explain observed ice surface topography as a function of wavelength. To examine what influences supraglacial meltwater routing, we apply flow-routing algorithms both to ice surface DEMs and to synthetic ice surfaces predicted from modeling bed topography transfer. In the resulting flow networks we examine channel slope versus accumulated drainage area trends to assess the fluvial erosion signature, and we examine steam network conformity with surrounding ice surface topography to quantify the importance of different wavelengths for explaining stream network spatial structure. We identify bed topography transfer as the primary control

on IDC-scale (∼1-10 km) surface topography and meltwater routing, and then use bed topography transfer functions to predict how Greenland surface IDC configuration and subglacial hydraulic flow pathways would change in response to varying ice flow conditions.

## Methods

### *Data*

We use stereo imagery derived ArcticDEM 2-5 m resolution mosaics for 2011 Greenland Ice Sheet surface elevation [ArcticDEM, 2017, Noh and Howat, 2015]. These DEMs were created by piecing together smaller DEM strips that in some cases come from data taken over multiple months. This is a potential source of error in our analysis since ice sheet surface topography can vary temporally due to a variety of processes including horizontal ice advection (on the order of 100 m/yr in our study areas [Joughin et al., 2010b,a, Nagler et al., 2015]), ablation (on the order of 1 m/yr [Bartholomew et al., 2011]), accumulation (on the order of 1 m/yr [Koenig et al., 2016]), and advection-related thickening/thinning such as that caused by changes in basal properties (on the order of 1 m/yr [Das et al., 2008, Helm et al., 2014]). In our study regions we observe $< \sim 1$ m vertical and $< \sim 10$ m horizontal offsets from surface DEM stitching (where different raw source data sets are combined).

We use the Icebridge BedMachine v3 150 m resolution Greenland bed elevation DEM [Morlighem et al., 2017b,a]. This product is derived from radar data, and in some regions also from ice mass conservation modeling. This product has large error (as much as 500 m) in areas with low radar pass density; we selected study regions with a range of bed DEM quality (shown in Fig. 2.2).

Many regions of the ablation zone, including our study regions, are where mass conservation modeling was used to extrapolate raw radar transects into contiguous bedrock DEMs. This approach and its advantages are explained in detail by [Morlighem et al., 2011] and [Morlighem et al., 2014]. Surface elevations, surface velocities, and mass balances estimates are used to produce more accurate bed DEMs that are consistent with multiple radar-derived data sets which have limited spatial coverage (as shown in Fig. 2.2). The mass conservation modeling does not preclude us from using these DEMs to evaluate the effectiveness of bed topography transfer functions at predicting surface topography, since the approach used in creating the bed DEMs only solves mass conservation equations and does not take into account the momentum balance accounted for by the transfer functions (described in Section 2.2). However, as an additional precaution, we focus our analysis primarily on regions with more dense radar transect coverage. DEMs in these regions should most closely reflect the raw radar data, and also generally have higher effective resolution.

We use 2009 InSAR derived MEaSUREs [Joughin et al., 2010b,a] for 500 m resolution Greenland winter ice surface velocities. We use Landsat imagery to identify moulins, lakes, and stream channels [Yang and Smith, 2016]. We use RACMO 2.3p2 at 1 km resolution for melt data from the full year 2015 [Noel et al., 2015] to indicate relative melting between different regions of Greenland. All data sets do not necessarily correspond temporally, which is a potential source of error in our analysis since ice velocity, ice surface topography, and bed topography can vary temporally [Sugden, 1978, Hart, 1995, Bartholomew et al., 2011, Sole et al., 2011, Helm et al., 2014]. We focus our analysis and discussions on multi-year averaged ice flow properties, and do not attempt to model seasonal dynamics.

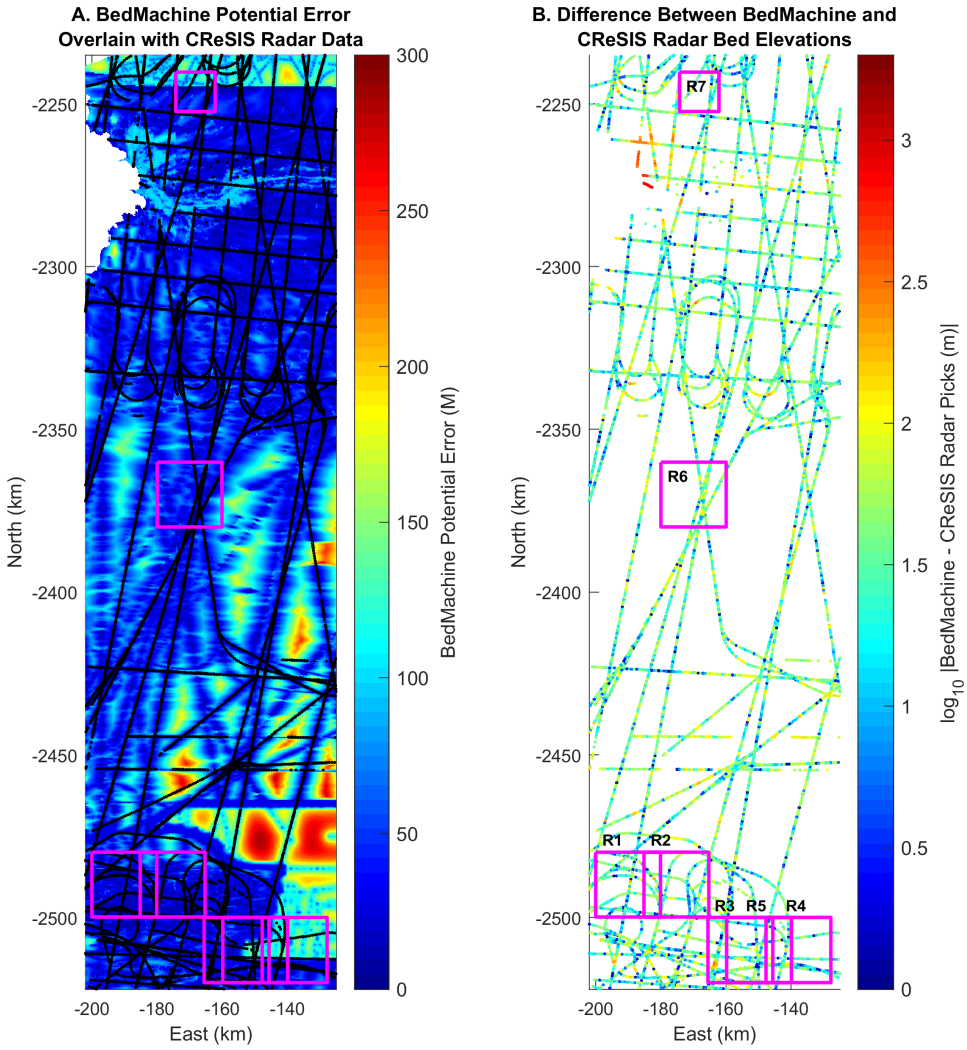


FIGURE 2.2. (A) BedMachine v3 potential bed elevation error overlain by CReSIS radar bed elevation picks [Morlighem et al., 2017b,a, CReSIS, 2016]. BedMachine includes radar data from other sources not shown here, and is also constrained with mass conservation modeling over most of the region shown. BedMachine error generally decreases where elevations are better constrained by radar data. Our study regions (magenta) encompass a broad range of bed DEM quality (Fig. 2.1.A, Table 1). (B) Difference between bed elevations from BedMachine and CReSIS radar picks (only including radar picks marked as good quality). In many regions there is appreciable scatter in radar elevation picks and significant error in the derived bed DEM; we examine the impact this uncertainty has on ice surface predictions.

*Study regions*

We focus on areas of the Greenland Ice Sheet ablation zone that exhibit significant supraglacial drainage networks, are not heavily crevassed, and do not contain ice streams (pathways where ice is advecting very rapidly relative to the surrounding regions of an ice sheet). We additionally require areas with high resolution (2-5 m) surface DEMs and near-uniform ice surface velocities. Using these criteria we select seven internally drained catchments (IDCs) from the western Greenland Ice Sheet as primary study regions (shown in Fig. 2.1.A, with additional information in Table 1). These regions cover a significant range of the elevations, ice thicknesses, ice surface slopes, and ice surface velocities over which extensive supraglacial stream networks form on western Greenland.

TABLE 1. Study region information (locations in Fig 2.1.A) and bed topography transfer function surface prediction results. We note that the mean misfit metric used here is not a comprehensive indicator of fit quality, and that in regions R3, R4 and R5, and R6 surface topographic relief is significantly under-predicted. In all regions the transfer function surface predictions appear to be optimized with higher values of basal sliding than have been determined with other methods [MacGregor et al., 2016, Ryser et al., 2014b], we expect this is due to a combination of non-Newtonian rheology and poor bed DEM resolution.

| Study region | $H$ (m) | $U$ (m/yr) | $\alpha$ (rad) | RACMO melt rate (mm/yr water) | Bed DEM mean error (m) | Surface prediction mean misfit with $C^{0*} = 10$ (% topographic relief) | Best fitting $C^{0*}$ |
|---|---|---|---|---|---|---|---|
| R1 | 824 | 86 | 0.013 | 2107 | 28.9 | 13.3 | 10 |
| R2 | 1075 | 87 | 0.009 | 1145 | 30.0 | 9.35 | 6 |
| R3 | 1233 | 88 | 0.009 | 793 | 41.1 | 10.4 | 13 |
| R4 | 1335 | 81 | 0.006 | 556 | 80.0 | 12.4 | 29 |
| R5 | 840 | 214 | 0.017 | 1321 | 55.8 | 13.9 | 23 |
| R6 | 1266 | 87 | 0.007 | 711 | 53.2 | 11.2 | 11 |
| R7 | 1187 | 92 | 0.011 | 1552 | 49.1 | 13.7 | 11 |

*Bed topography and basal sliding transfer*

Linear transfer functions

The governing equations of flowing ice are the Stokes equations for conservation of momentum and mass balance for an incompressible fluid. Ice is often described with a nonlinear constitutive relation know as Glen's law [Cuffey and Paterson, 2010], but here a linear Newtonian ice rheology is assumed. Ice rheology is also assumed to be spatially and temporally constant, though the rheology of ice generally varies with temperature, grain geometry, and impurities. The momentum equations we solve are

$$\vec{\nabla} p = \eta \vec{\nabla}^2 \vec{u} + \rho_i \vec{g}, \tag{2.2.1}$$

where $p$ is pressure, $\eta$ is effective dynamic ice viscosity, $\vec{u}$ is ice velocity, and $\rho_i$ is ice density. Cartesian coordinates are used, where the $z$-axis is aligned normal to the mean ice surface and the $x$-axis points in the direction of maximum bed gradient. $\vec{g}$ is the gravitational acceleration (in the $-z$ direction). Conservation of mass is given by

$$\vec{\nabla} \cdot \vec{u} = 0. \tag{2.2.2}$$

Linear stability analysis of Eqs. (2.2.1) and (2.2.2) by Gudmundsson [2003] provides analytical transfer functions that predict approximate ice surface topography over underlying rough bed topography or basal sliding variations. In the spectral domain, transfer functions are generally of the form $\hat{X}_o(\vec{k}) = \hat{X}_i(\vec{k})\hat{T}(\vec{k})$ where $\vec{k} = (k_x, k_y)$ is a wavenumber (inverse wavelength) vector, $X_o$ is output data (ice surface elevation in our case), $X_i$ is input data (bed elevation

in our case), and $T$ is the transfer function relating outputs to inputs. Transfer functions are possible to obtain for linear time-invariant systems; the basic underlying principals are that the output for such systems may be calculated for any single wavenumber input, that any input may be represented as a sum of individual wavenumber components via Fourier transform, and that the output will be a sum of the independent outputs from each input component [Stein and Wysession, 2005]. In the rest of this section we will summarize the derivation of the transfer functions (described fully in [Gudmundsson, 2003]) and the important approximations made in this derivation.

Bed elevation is assumed to not change temporally beyond an initial perturbation. Basal melting/freezing are also ignored, assumptions that are likely reasonable from a mass conservation perspective due to the generally slow rates of basal melting/freezing [Huybrechts, 1996]. Basal sliding velocity $\vec{u}_b$ is assumed to be governed by a sliding law of the form

$$\vec{u}_b(x,y) = C(x,y)\vec{\tau}_b(x,y) \tag{2.2.3}$$

where $\vec{\tau}_b$ is basal shear stress and $C(x,y)$ is a sliding parameter. We will often refer to non-dimensionalized basal sliding coefficient $C^*(x,y) = C(x,y)\frac{2\eta}{H}$ (approximately equivalent to slip ratio, the ratio of basal sliding velocity to ice deformational velocity). Other forms of sliding law have been proposed [Fowler, 1986, Tulaczyk et al., 2000, Cuffey and Paterson, 2010]. The basal boundary condition (at the bed-ice interface) combines this sliding law with a no-flow condition dictating zero ice velocity normal to the boundary. Surface accumulation/ablation are ignored, which is reasonable as both rates are generally small compared to ice advection rates [van˜den˜Broeke et al., 2011]. The ice

surface boundary conditions are zero traction plus the kinematic boundary condition

$$\frac{\partial Z}{\partial t} = u_z - u_x \frac{\partial Z}{\partial x} - u_y \frac{\partial Z}{\partial y}. \tag{2.2.4}$$

Thus the ice surface boundary is the only source of time variation in the system.

Parameters including ice thickness, surface velocity, and surface slope are assumed to be similar over the domain of interest, which allows for solutions to be obtained as perturbations to a zeroth-order infinite plane slab solution. In order for these assumptions to be valid, it is assumed that bed topography amplitude is much smaller than ice thickness, and that the domain of interest is small compared to the horizontal dimensions of the ice sheet. The zeroth-order ice surface $Z^0$ is a plane with slope $\alpha$ in the direction of ice flow. Zeroth-order ice thickness $H$ is the mean ice thickness in the domain. Zeroth-order basal shear stress is given by $\tau_b = \rho g H \sin(\alpha)$, and zeroth-order deformational velocity is given by $U_d = \frac{1}{2\eta}\tau_b H$, where $\rho$ is (spatially constant) ice density.

Bed elevation $B$ is expressed as $B = B^0 + \epsilon F_B^\epsilon$, where $B^0$ is zeroth-order (horizontal plane) bed elevation, $F_B^\epsilon$ represents perturbations to $B^0$, and $\epsilon =$ bed topography amplitude$/H \ll 1$. Basal sliding coefficient $C$ is similarly expressed as $C = C^0 + \beta F_C^\beta$ where $0 \leq \beta \ll 1$. Equations 2.2.1 and 2.2.2 are linearized around $\epsilon, \beta = 0$ and solved in the Fourier domain. Ice surface elevation is then given by

$$Z = Z^0 + \epsilon F_Z^\epsilon + \beta F_Z^\beta + \mathcal{O}(\epsilon^2, \beta^2, \epsilon\beta), \tag{2.2.5}$$

where $\epsilon F_Z^\epsilon$ and $\beta F_Z^\beta$ represent the first order (linear) ice surface response to $B$ and $C$ perturbations. Higher order terms $\mathcal{O}(\epsilon^2, \beta^2, \epsilon\beta)$ are discarded.

The full time-dependent transfer functions can be found in [Gudmundsson, 2003]. A steady state surface configuration to bed topography and basal sliding perturbations is approached as $t \rightarrow \infty$. We note that ice flow parameters in the transfer functions are not strictly independent, such that there are restricted parameter combinations that correspond to real ice flow configurations.

Although the linear transfer functions derived by [Gudmundsson, 2003] do not capture all the complexities of ice motion, they have some significant advantages over other methods for solving our desired ice flow problem. They do not make a shallow ice approximation (which ignores longitudinal stresses and thus breaks down at length scales on the order of ice thickness $H$ [e.g., Cuffey and Paterson, 2010]), and are thus valid at spatial scales $< H$. Additionally, they can be efficiently implemented over 2D IDC-scale regions without requiring initial conditions, flow line geometry, and domain-edge boundary conditions that many numerical flow simulators need. We will show that the functions reproduce general topographic features and amplitude spectra of our Greenland Ice Sheet study regions well, and thus provide a useful predictive tool.

Transfer function implementation

When implementing the transfer functions in all following analysis we will assume the ice surface has reached a steady state in response to the underlying bed topography and basal sliding conditions. To examine the validity this assumption, we calculate the transfer function perturbation adjustment timescales for parameters representative of the western Greenland ablation zone (from study region R1 (Fig. 2.1.A, Table 1) with $C^{0*} = 10$ and $\eta = 10^{14}$ Pa s) using the time-dependent transfer functions defined in [Gudmundsson, 2003]. For the range

of ice flow parameters we are interested in, there is no appreciable downstream advection of surface perturbations, and so the surface response soon after a basal perturbation is essentially a lower amplitude scaling of the steady state (maximum amplitude) surface response. We find that the time scale for bed topography or basal sliding transfer amplitudes to reach 95% of their steady state values is as much as 60 years for the longest wavelengths of topography in our typical study areas (∼20 km), and is ∼3-20 years for wavelengths that typically exhibit the highest transfer (∼1-10 km). It is unlikely that bed topography, ice sheet thickness, or ice sheet surface slope change significantly over these timescales, but ice velocity and basal sliding can vary on day to year timescales, meaning that the steady state assumption is a potential source of error in our analysis [Das et al., 2008, Bartholomew et al., 2011, Sole et al., 2011, Helm et al., 2014, Chandler et al., 2013, Tedstone et al., 2014].

Methods have recently been developed and applied for implementing the linear basal transfer functions along flowlines with spatially varying parameters [Igneczi et al., 2018, Ng et al., 2018], which allows for implementation of the transfer functions over large regions. However, implementing the transfer functions just along flowlines can result in significant inaccuracy. With ice flow parameters representative of the western Greenland Ice Sheet ablation zone, the transfer amplitude of IDC-scale (∼1-10 km) bed features predicted by the linear transfer functions could vary by up to a factor of 10 depending upon the 2D alignment of those features (see supplement). Our approach retains the simpler constant-parameter model but accounts for 2D effects. We implement the basal transfer functions over rectangular domains of small enough size ( 20 km across) that ice flow parameters are relatively uniform within each domain.

To implement the transfer functions in (east, north, vertical) Cartesian coordinates, we calculate absolute wavenumbers as $k = \|\vec{k}\|$ and wavenumbers in the ice flow direction as $k_U = \frac{\vec{k} \bullet \vec{U}}{\|\vec{U}\|}$. We can then calculate transfer function matrices $\hat{T}_B(k_x, k_y)$ and $\hat{T}_C(k_x, k_y)$ corresponding to the discrete wavenumber components of a given bed DEM. The amplitude matrices $\left(|\hat{T}_{B,C}|\right)$ are symmetric about the line perpendicular to the ice flow direction, and the phase matrices $\left(\arg(\hat{T}_{B,C})\right)$ are anti-symmetric about this line. The transfer amplitude for bed topographic features aligned with the direction of ice flow approaches one as wavelength approaches infinity, but non-zero values of the basal sliding parameter $C^{0*}$ result in an additional peak in transfer amplitudes at intermediate wavelengths (as illustrated in Fig. 2.3, [Gudmundsson, 2003]). Transfer amplitudes approach zero at small wavelengths or as topographic features approach a flow-perpendicular alignment. Transfer function phase shift is also important, and results in a wavelength-dependent offset between bed features and their surface expression (as illustrated in Fig. 2.4.B).

Prior to taking 2D discrete Fourier transforms (DFTs, see for example [Press et al., 2007]) of bed DEMs, we first shift each bed DEM to have zero mean elevation. We do not detrend bed DEMs, as that is not consistent with the zeroth-order bed conditions. We then mirror each bed DEM in all directions by connecting east-west reversed copies of each DEM to the east and west sides of itself, connecting north-south reversed copies of each DEM to the north and south sides of itself, and connecting north-south and east-west reversed copies of each DEM to all corners of itself. Next we apply a cosine taper such that all elevations along the edges of each mirrored bed DEM are zero, and the original domain in the center is unaffected. These processing steps are taken to minimize edge effects

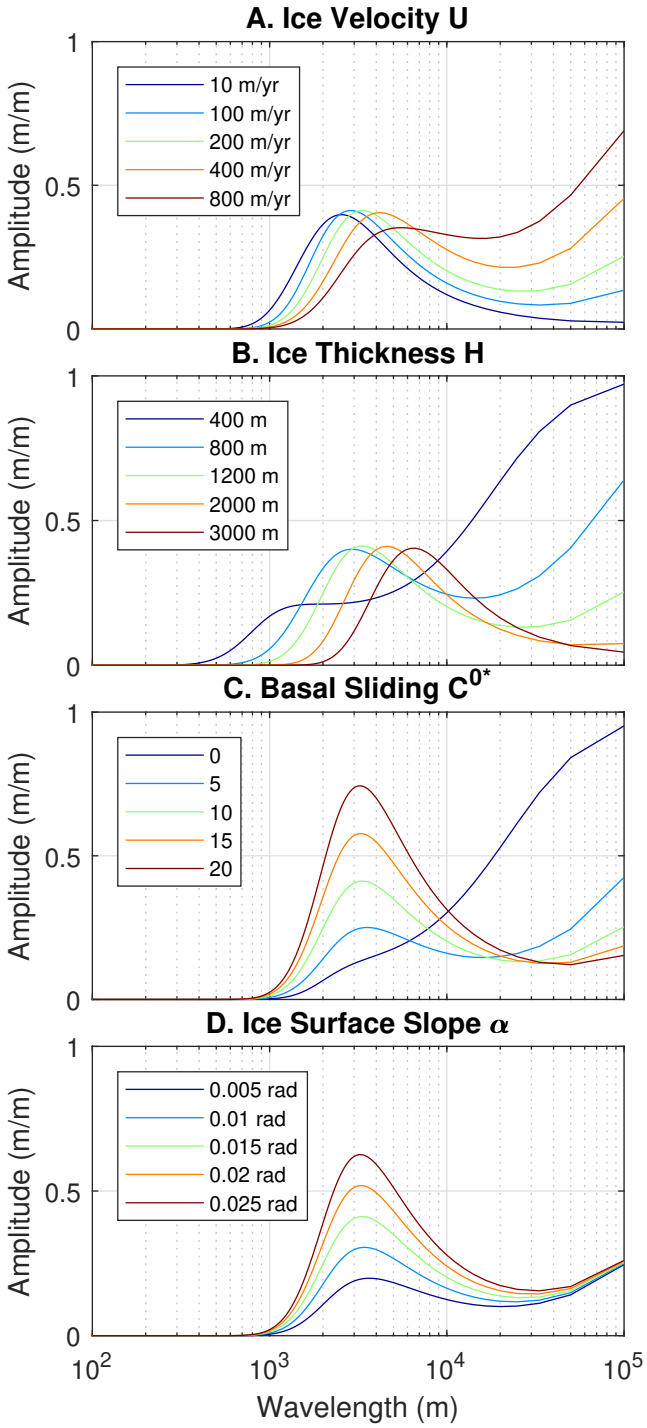


Figure 2.3 (A-D) Bed topography transfer function amplitudes in the ice flow direction (along an ice flowline). In all plots the parameters not otherwise indicated are: $U = 200$ m/yr, $H = 1200$ m, $C^{0*} = 10$, $\alpha = 0.015$ radians, and $\eta = 10^{14}$ Pa s. The spread of plotted parameters broadly encompasses the range of parameters found in our study regions (Fig. 2.1.A, Table 1). Transfer amplitude peaks between around 1-10 km for a wide range of parameters.

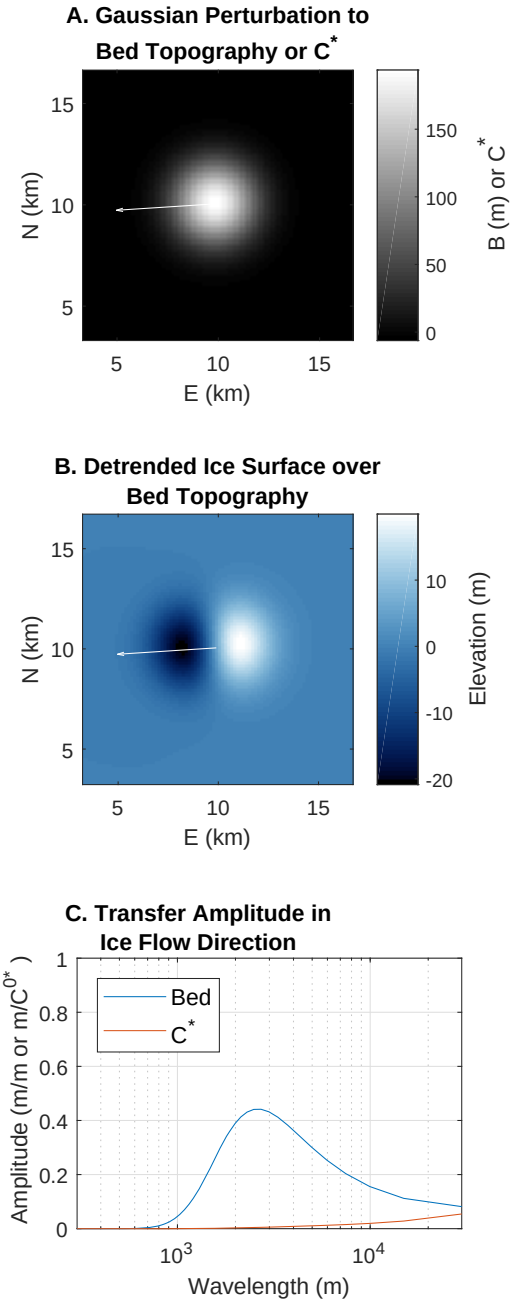


Figure 2.4 Illustration of steady state basal transfer for ice flow parameters representative of the western Greenland ablation zone. Ice flow parameters are from region R1 (Fig. 2.1.A, Table 1) with $\eta = 10^{14}$ Pa s. (A) Gaussian bed topography or basal sliding perturbation. (B) Detrended predicted ice surface over the Gaussian bed topography perturbation (with $C^{0*} = 10$). White arrows in plots A and B indicate the ice flow direction. (C) Transfer amplitudes in the ice flow direction (along a flowline) for bed topography and basal sliding $C^*$ perturbations. The transfer functions also have important phase components not shown here (see [Gudmundsson, 2003]). With these flow parameters, surface topography created from basal sliding perturbations should generally be of much lower amplitude than surface topography created from bed topography.

[Perron et al., 2008]. We then take 2D DFTs of the mirrored bed DEMs, and use the transfer functions to obtain predicted ice surface elevation $Z'$ as:

$$Z'(x,y) = Z^0(x,y) + \mathcal{F}_D^{-1}\Big(\hat{T}_B(k_x,k_y)\hat{B}(k_x,k_y) + \hat{T}_C(k_x,k_y)\hat{C}(k_x,k_y)\Big) \qquad (2.2.6)$$

where $B$ is the zero-mean bed elevation, $Z^0$ is the zeroth-order ice surface (with average elevation $H$ and slope $\alpha$, obtained by a plane fit to the ice surface DEM $Z$), and $\mathcal{F}_D^{-1}$ represents the inverse 2D DFT. We then trim enough space from the edges of each predicted surface so that we are only considering a region that will not contain any edge effects.

Ice viscosity and basal sliding estimation

Two important and poorly constrained parameters in our bed topography transfer method are ice viscosity $\eta$ and basal sliding parameter $C^*(x,y)$. One possible application of the transfer functions is to invert for these parameters as a function of space from observed surface and bed DEMs [Raymond and Gudmundsson, 2009]. We do not take this approach here as our primary focus is an assessment of how well ice surface topography can be explained by transfer of basal conditions. However, we do need to choose values for $\eta$ and $C^*(x,y)$ (or at least a uniform value of $C^*(x,y) = C^{0*}$).

We examine the importance of spatial variations in $C^*(x,y)$ by comparing the predicted ice surface over Gaussian $B(x,y)$ and $C^*(x,y)$ perturbations with 2 km standard deviations and 200 m height or 200 $C^*$ amplitude, using ice flow parameters from region R1 (Fig. 2.1.A, Table 1) with $\eta = 10^{14}$ Pa s (and with $C^*(x,y) = C^{0*} = 10$ for the Gaussian bed topography test case); the results are shown in Fig. 2.4. Bed topography perturbations on the order of 200 m occur

commonly [Morlighem et al., 2017b], but inferred slip ratios away from ice steams in the western Greenland ablation zone are typically less than $\sim$ 10 [Morlighem et al., 2013, MacGregor et al., 2016]. Thus Fig. 2.4.C indicates that in these flow conditions, unless there are exceptionally large $C^*(x, y)$ spatial perturbations (on the order of 1000), the ice surface expression from $C^*(x, y)$ perturbations will be of much smaller amplitude and more disperse than the surface expressions that can arise from reasonable amplitude bed topography. Accordingly, we assume spatially constant $C^*$ (so $C^*(x, y) = C^{0*}$ at all locations) for all of our analysis, so that we only need to choose a single value of $C^{0*}$ in each region.

We next assess the uniqueness with which $C^{0*}$ and $\eta$ can be inverted for using the transfer functions, by minimizing misfit $\big($defining misfit for DEMs of size $m \times n$ as: $\frac{1}{nm} \sum_{x=x_1}^{x_n} \sum_{y=y_1}^{y_m} |Z(x, y) - Z'(x, y)|\big)$ between observed and bed topography transfer predicted ice surfaces. Example inversion results are shown in Fig. 2.5. Over our seven study regions of the Greenland Ice Sheet ablation zone (Fig. 2.1.A, Table 1), the values of viscosity that produce best fits between predicted and observed ice surfaces are within half an order of magnitude of $10^{14}$ Pa s. For all further analysis we fix the value of $\eta$ to $10^{14}$ Pa s, which is within the range of ice viscosity estimates [Cuffey and Paterson, 2010].

The best fitting values of $C^{0*}$ in our study regions range between 6 and 35, and are often not very tightly constrained. Some of these values are significantly higher than other ice sheet ablation zone estimates [Morlighem et al., 2013, MacGregor et al., 2016]. Such anomalously high $C^{0*}$ values are not unexpected, for at least two reasons. The first is poor effective bed DEM resolution in some regions, which could result in transfer amplitudes (and thus basal sliding) needing to be artificially high to produce observed surface topographic relief. In regions

with lower mean bed DEM error, our inversions result in lower values of sliding (Table 1). The second reason is that the Newtonian rheology used to derive the analytical transfer functions produces generally lower transfer amplitudes than are found with a more realistic (power law) ice rheology [Raymond and Gudmundsson, 2011], so artificially high basal sliding values are needed to produce observed transfer amplitudes. Except where otherwise noted we therefore set $C^{0*} = 10$, which is consistent with the linear transfer functions and likely over-predicts true average slip ratios. Much of our analysis will focus on the wavelengths at which bed topography transfer peaks, which are relatively insensitive to the value of $C^{0*}$. This is because $C^{0*}$ affects transfer peak amplitude but not wavelengths (as can be seen in Fig. 2.3.C); for parameters representative of our study regions a significant peak is still predicted as long as $C^{0*} >\sim 2$.

Bed DEM error analysis

A significant source of error in our bed topography transfer function method is bed DEM accuracy. The BedMachine v3 bed DEM has a corresponding potential error map which represents the uncertainty in bed elevations (shown

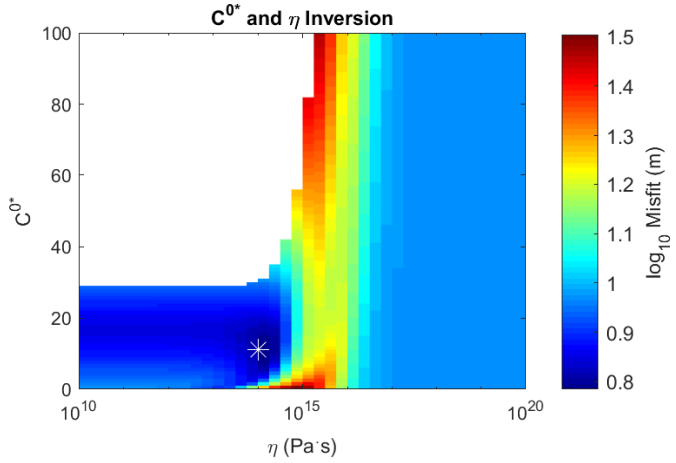


Figure 2.5 Misfit minimization for $\eta$ and $C^{0*}$ between the ice surface DEM and bed topography transfer predicted ice surfaces in study region R1 (Fig. 2.1.A, Table 1). White star indicates the location of minimum misfit, at $C^{0*} = 10$ and $\eta = 10^{14}$. Blank plot area is the region where parameters are nonphysical (resulting in transfer amplitudes $> 1$).

in Fig. 2.2.A). This uncertainty primarily reflects poor radar transect coverage and generally increases with distance from the nearest radar data, but also depends on uncertainty in other data used for mass conservation modeling [Morlighem et al., 2014, 2017b]. We use many randomly generated possible error configurations to quantitatively bound the variation in our ice surface topography predictions that is allowed by bed DEM uncertainty. This allows us to assess the robustness of our surface predictions, and to examine the bed DEM accuracy needed for reasonable predictions.

We pseudo-randomly generate 100 possible error configurations for each of 100 different bandpass filter wavelengths $\lambda_n$ (where $\lambda_n$ spans the range of wavelengths resolvable in each domain). Each error configuration is created from a different pseudo-random complex wavenumber matrix. The matrices have the same dimensions as the bed DEM, symmetric real components, and anti-symmetric imaginary components. Each wavenumber matrix is multiplied with a frequency domain Gaussian bandpass filter centered at frequency $\frac{1}{\lambda_n}$. An inverse DFT is taken of each wavenumber matrix to create an error surface containing primarily topographic wavelengths near $\lambda_n$. Each error surface is then scaled so that all values vary between -1 and 1, and multiplied by the bed DEM potential error map to generate a possible error configuration. We add each error configuration to the bed DEM and use bed topography transfer functions to predict the ice surface over each resulting error-injected bed DEM.

Observed admittance of ice surface/bed topography

We wish to evaluate how well the observed frequency domain empirical admittance of bed topographic features to the ice surface corresponds to predicted

transfer amplitudes, to determine the wavelengths at which observed ice surface topographic amplitudes are consistent with predicted bed topography transfer (over given bed DEMs). We can calculate the frequency domain empirical admittance of bed topography to ice surface topography as $\hat{Y}(k_x, k_y) = \hat{Z}(k_x, k_y)/\hat{B}(k_x, k_y)$. If ice surface topography was only caused by bed topography transfer, then empirical admittance $\hat{Y}$ should closely correspond to predicted bed topography transfer amplitudes. However, due to the noise present in 2D empirical admittance computations, interpreting $\hat{Y}(k_x, k_y)$ directly is challenging. We thus employ two methods to estimate average empirical 1D admittance $\hat{Y}(k)$, which we can then compare to predicted transfer amplitudes.

One method to estimate 1D empirical admittance involves binning and averaging absolute wavenumber components from 2D DFTs. We first take 2D discrete Fourier transforms (DFTs) of mirrored and tapered ice surface and bed DEMs (as described in Section 2.2), then calculate the complex magnitudes of all values in these DFTs to yield 2D surface and bed amplitude spectra. We then bin and average all points in each amplitude spectra by absolute wavenumber to obtain 1D surface and bed amplitude spectra. We lastly divide binned 1D surface amplitude spectra by binned 1D bed spectra. This method considers both ice-flow-parallel and non-ice-flow-parallel topographic wavelengths, which could decrease the resulting admittance relative to admittance expected purely in the ice flow direction (since transfer should be highest for topographic wavelengths aligned in this direction).

The second method to estimate 1D empirical admittance involves binning and averaging 1D amplitude spectra from multiple ice flowlines. We first interpolate bed and surface elevations along a series of offset near-parallel ice

flowlines. We mirror and taper each flowline elevation profile, then take DFTs of each profile to obtain a series of 1D surface and bed amplitude spectra. We next bin and average each 1D amplitude spectrum by wavenumber, and average these spectra between all profiles of the same type (surface or bed). We lastly divide binned and averaged 1D ice surface amplitude spectra by binned and averaged 1D bed amplitude spectra. This method thus avoids the non-ice-flow-parallel muting effect from the first method, but does not account for the effects of surrounding 2D topography on each flowline (as discussed in Section 2.2).

*Supraglacial meltwater routing and thermal-fluvial incision*

Mechanics of fluvial incision

In terrestrial settings, bedrock fluvial incision is often modeled by the "stream power" law [Howard and Kerby, 1983, Seidl and Dietrich, 1992]. This model can be combined with another semi-empirical relation Hack's law [Hack, 1957], relating downstream distance to accumulated flow area. This permits prediction of surface lowering by fluvial erosion $E$ of the substrate at point $s$ along a stream channel downstream of a drainage divide at time $t$

$$E(s,t) = K(s,t)A(s,t)^m \left| \frac{\partial Z(s,t)}{\partial s} \right|^n , \tag{2.2.7}$$

where $A(s,t)$ is accumulated drainage area, $K(s,t)$ is an experimentally determined erodibility coefficient that may vary in space and time, $m$ and $n$ are empirically determined exponents, and $Z(s,t)$ is channel elevation. This model, combined with models for tectonic uplift or hillslope creep, well-predicts large-scale features of many fluvially-dominated terrestrial landscapes. Commonly observed

concave-up longitudinal stream elevation profiles and negative slope-drainage area trends are generally interpreted in the context of equation 2.2.7, which then may inverted for tectonics and climate, or used to constrain substrate properties such as erodibility $K$ [Gilbert, 1877, Whipple and Tucker, 1999, Montgomery, 2001]. Convexities such as those induced by base level changes, non-uniform uplift, and variable climate or substrate properties propagate upstream as kinematic waves [Whipple and Tucker, 1999, Royden and Perron, 2013, O'Hara et al., 2019].

In supraglacial environments fluvial incision occurs by melting, and an analog of the stream power law may be derived with $n = 1$ [Karlstrom and Dunham, 2016]. Exponent $m$ is dependent upon the relation between water flux and accumulated drainage area and the relation between channel width and water flux, and has been estimated at between 0.7-0.9 for supraglacial streams [Karlstrom and Dunham, 2016]. If surface motions introduced by ice advection (analogous to unsteady and non-uniform uplift) are accounted for, fluvially-dominated supraglacial stream profiles with fixed terminal elevations (such as supraglacial lakes) should still approach a concave-up configuration if thermal-fluvial erosion outpaces ice advection [Karlstrom and Dunham, 2016]. Equation 2.2.7 also implies that for fluvially-dominated stream profiles without fixed terminal elevations (such as those flowing into moulins), convexities can progressively propagate upstream from the moulin causing persistent transient topography. Indeed, convexities at various scales are readily visible in supraglacial stream elevation profiles (see supplement), but these deviations from idealized longitudinal profiles could arise from other processes as well. Spatially varying background ice flow, kinematic waves transmitting uplift or erosion transients (such as from unsteady surface melting or supraglacial lake drainage [Hoffman et al., 2011]), transient surface

waves caused by ice flux variations [van˜de˜Wal and Oerlemans, 1995], and/or deviations of the local ice velocity vector from the direction of stream flow (such as from stream meanders, e.g., [Karlstrom et al., 2013]) could all generate convexities in fluvially-dominated supraglacial stream profiles. Alternately, if thermal-fluvial incision is slow enough relative to ice advection and/or other surface processes, stream profiles might not be primarily controlled by fluvial incision, and instead would conform to the shape of the surrounding topography that is controlled by other processes.

Modeling the dynamic interaction between thermal-fluvial incision and ice advection is beyond the scope of this work, and such modeling would still be limited by the resolution of current bed DEMs that affects our transfer function implementation (e.g., Sections 2.2, 2.2, and 2.3). We thus instead employ two empirical approaches to search for signatures of IDC-scale landscape modification by thermal-fluvial incision, and to quantify the observed pattern of supraglacial stream networks in relation to bed topography transfer. The first approach is to compare slope versus accumulated drainage/flow area relations, a traditional terrestrial landscape metric [Gilbert, 1877, Whipple and Tucker, 1999, Montgomery, 2001], between real supraglacial stream networks and synthetic flow networks calculated on bed topography transfer predicted surfaces (described in Section 2.2). The second approach is to use two stream conformity metrics to quantify how well supraglacial stream network geometry is explained by the surrounding ice surface topography filtered at various wavelength thresholds (described in Section 2.2).

Supraglacial stream network and synthetic flow network extraction

We use satellite imagery, DEMs, and flow-routing algorithms to extract supraglacial stream networks from seven regions of the western Greenland Ice Sheet ablation zone [Karlstrom and Dunham, 2016, Yang and Smith, 2016]. Satellite imagery is used to identify moulins by hand, which are treated as water sinks. We then use flow-routing to calculate accumulated flow/drainage area patterns on the surface (as shown in the example stream network in Fig. 2.6.A). We use the D8 (steepest descent) flow-routing algorithm with channel area threshold set to maximize agreement with visible stream channels, between 8000 and 30000 $m^2$ depending upon region. In general, flow-routing is an imperfect means of finding real stream channels, especially on a relatively flat landscape such as the Greenland Ice Sheet. DEM resolution is not high enough to resolve narrow ($< \sim$2 m wide) supraglacial stream channels, so such streams may be missed by flow-routing, particularly those that are not aligned with the steepest descent direction [Smith et al., 2015, Yang et al., 2015]. However, most streams found via our flow-routing method agree with visually identified stream channels [Yang and Smith, 2016].

Bed topography transfer provides a way of constructing synthetic flow networks to examine how meltwater would route in the absence of supraglacial thermal-fluvial incision, since incision is not accounted for by the transfer functions. We use transfer functions to predict the ice surface over bed DEMs, then place artificial moulins as water sinks at the base of large surface depressions and calculate synthetic flow networks numerically. These are not perfectly comparable with real supraglacial stream networks, since moulins also occur outside of depressions [Catania et al., 2008, Yang et al., 2015, Yang and Smith,

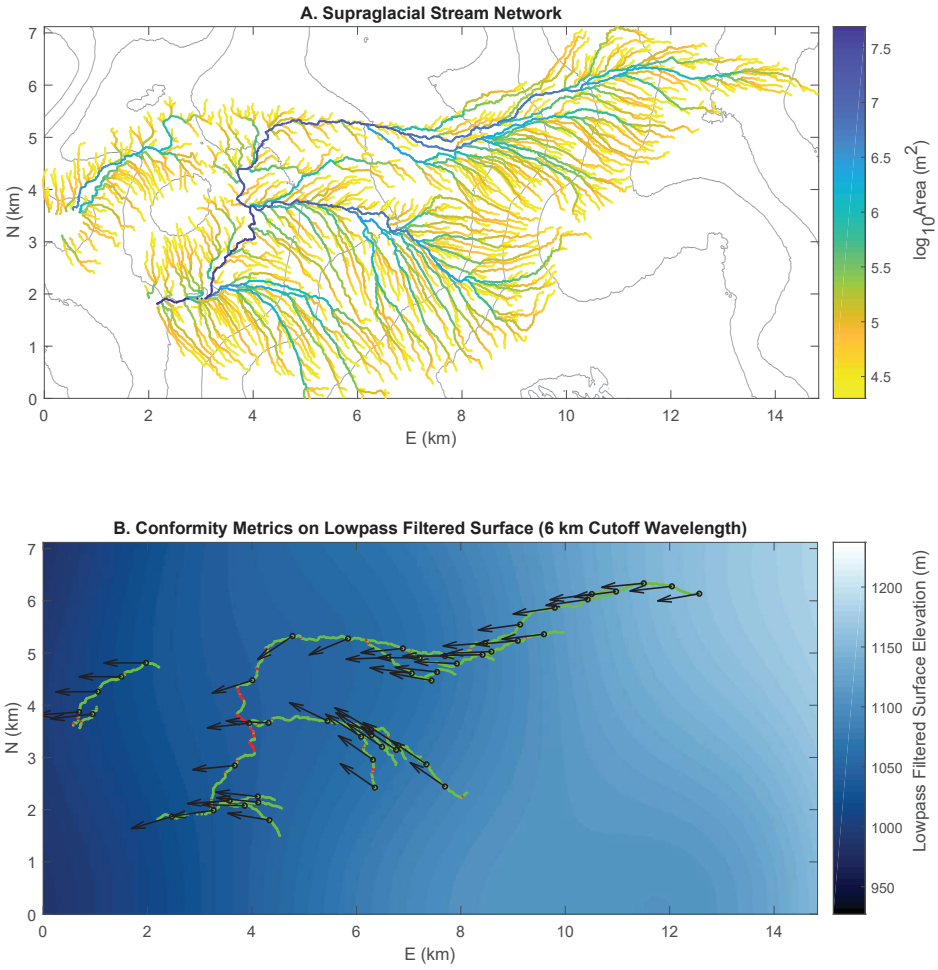


FIGURE 2.6. (A) Supraglacial stream network obtained by flow-routing on 2 m DEMs from study region R1 (Fig. 2.1.A, Table 1), colored by accumulated upstream drainage area. Surface elevation is shown with 20 m black contours. Fluvial incision rate should increase with increasing slope and drainage area (Eq. 2.2.7). (B) Illustration of stream conformity metrics for select streams from the same network, projected onto topography lowpass filtered at a 6 km cutoff wavelength. Sections of streams that would be flowing uphill on this filtered surface are colored red and other sections are green; this data is used to calculate percent downhill $\%d$. Black arrows indicate steepest descent directions on this filtered surface; the angle between these directions and the corresponding stream channel orientations is used to calculate conformity factor $\Lambda$.

2016]. We calculate these synthetic flow networks with the TopoToolbox [Schwanghart W, 2014] D8 method, with channel area threshold set to 20000 $m^2$.

Supraglacial stream network slope and accumulated drainage area relations

Our first approach for quantifying controls on meltwater routing comes from the hypothesis that bed topography transfer can explain supraglacial stream longitudinal elevation profiles, without appealing to significant landscape shaping by thermal-fluvial incision. Although modeling the transient competition between ice flow over bed topography and thermal-fluvial incision is outside the scope of the present work, if bed topography transfer is the dominant process then slope-drainage relations on synthetic flow networks will match those from observed supraglacial stream networks. If instead supraglacial stream incision is a primary control on ice surface topography at km scales, the interplay between thermal-fluvial erosion and ice flow will set the longitudinal profiles of streams and the relationship between slope and accumulated drainage area of observed stream networks may consistently differ from synthetic flow networks.

We compare local channel slope to local accumulated upstream flow/drainage area at all points in each stream network. Prior to doing this we smooth all stream longitudinal profiles to remove small-scale slope variations. Profile smoothing is done by first breaking each stream network into multiple separate stream profiles, discarding all profiles less than 800 m long, then twice applying a moving average filter with a span of 200 m (analogous to a lowpass filter) to each remaining profile, and finally trimming 100 m from both ends of each profile to remove smoothing-induced edge effects. We then calculate stream longitudinal slopes with a second order centered finite difference stencil. There is a large scatter in

the resulting slope versus drainage area relations, so for each stream network we divide data points into logarithmically spaced area bins and calculate the mean and standard deviation of slopes in each bin [Montgomery, 2001, Warren et al., 2004].

Supraglacial stream network topographic conformity

Our second approach for quantifying controls on meltwater routing is to implement two measures of stream network conformity to surrounding ice surface topography, as in Black et al. [2017]. This approach assesses the degree to which stream patterns are "explained by" the current configuration of surrounding ice surface topography at various wavelengths. For a given stream/flow network projected onto a given DEM, percent downhill ($\%d$) measures the percentage of channel length over which water forced along the channels would be flowing downhill, and conformity factor ($\Lambda$) measures the mean deviation of channel pathways from the local direction of steepest descent on the DEM surface (as illustrated in Fig. 2.6.B). We low-pass filter ice surface DEMs using a series of decreasing cutoff and taper wavelengths, then calculate $\%d$ and $\Lambda$ by projecting stream networks onto each filtered surface (as illustrated in Fig. 2.6.B). We note that applying these conformity metrics to stream networks calculated with flow-routing may result in a bias towards artificially high conformity, since as mentioned in Section 2.2 flow-routing on imperfect DEMs may miss some narrow stream channels that are are not aligned with the steepest descent direction on the ice surface. However, our flow-routing is done on sufficiently high-resolution DEMs to correctly capture the majority of observed stream network structures.

As filter cutoff wavelength decreases, both conformity metrics will increase if stream network geometry is controlled by the progressively shorter wavelengths of topography that are being included [Black et al., 2017]. Given a DEM with high enough resolution to resolve all stream channels, as filter cutoff wavelength approaches zero $\%d$ should generally increase and approach 100% since water does not flow uphill (except at vertical scales smaller than water flow depth). Similarly, $\Lambda$ should generally increase and approach 1, since water should generally flow in the direction of steepest descent. Stream network structure might depend on particular wavelengths of topography for a variety of reasons, for example if those wavelengths encompass topographic features that predate stream formation and thus contributed to the routing of the stream channels when they formed. Alternately, stream networks might not perfectly conform to the surrounding longer wavelength topography if fluvial meanders have shifted channels away from the background direction of steepest descent, or if the surrounding topography has been modified post stream-incision by processes such as ice advection [e.g., for tectonic processes, Black et al., 2017, Wegmann et al., 2007]. We do not focus on why stream network conformity might be imperfect at any given wavelength, but instead use the conformity metrics to indicate what topographic wavelengths are important for explaining current supraglacial meltwater routing.

To calculate the two conformity metrics, we apply pre-processing steps as described in Section 2.2 to minimize edge effects, then low-pass filter ice surface DEMs using one-sided Gaussian filters. We then project flow networks (as computed on the unfiltered DEMs) onto each filtered surface (as illustrated in Fig. 2.6). We calculate $\%d$ as the percent of discrete locations along stream channels that are higher in elevation than the next downstream location. To calculate $\Lambda$, at

each discrete location along a stream we calculate the angle between the horizontal direction vector of the stream channel (the direction water is flowing) and the horizontal direction vector of steepest descent down the ice surface. $\Lambda$ is then given by the mean absolute value of the cosine of this angle at all discrete stream channel locations. Exact expressions for $\%d$ and $\Lambda$ are given in the supplement.

*Predicting supraglacial topographic drainage basins and subglacial hydraulic flow pathways*

Bed topography transfer functions provide a tool for examining the effects various multiple-year averaged ice flow parameters have on ice surface topography. To do this we first predict ice surface topography (as described in Section 2.2) in a given region with different ice flow parameters. We can then explore the effects these changes in surface topography might have on both supraglacial and subglacial hydrology.

To examine potential changes in supraglacial hydrology, we delineate surface topographic drainage basins on the predicted ice surfaces. We do this using flow-routing (with all topographic local minima treated as water sinks, as described in Section 2.2) to identify topographic drainage basin divides, counting all edge terminating basins separately. Topographic basins will not exactly correspond to IDCs, since moulins fragment topographic basins and/or there could be places where streams have incised through topographic divides [Yang et al., 2015]. In practice there is reasonable correspondence between topographic basins and IDCs if appropriate DEM processing is used [Yang and Smith, 2016], so this approach provides a reasonable indication of how IDC configuration and number density would vary with changing multiple-year averaged ice flow parameters.

To explore potential changes in subglacial hydrology that might arise from changing ice flow conditions, we model quasi-static water flow patterns under the predicted ice surfaces. We first calculate subglacial hydraulic potential $\phi_h$ as a function of relative bed elevation and ice thickness following [Hewitt, 2011]

$$\phi_h(x,y) = \rho_w g B(x,y) + \rho_i g H(x,y) \left(\frac{P_w}{P_i}\right) \tag{2.2.8}$$

where $\frac{P_w}{P_i}$ is the ratio of basal water pressure to ice overburden pressure. Significant spatial and temporal variation in subglacial effective pressure ($P_i - P_w$) under the Greenland Ice sheet has been measured, with basal water pressure ranging from less than half of ice overburden pressure to greater than ice overburden pressure (generally by only on the order of tens of bars, though brief pulses of much higher pressure have been recorded in some settings [Kavanaugh and Clarke, 2000]); this effective pressure variation is related to time of year, time of day, basal sliding velocity, and location within subglacial drainage networks [Ryser et al., 2014a, Andrews et al., 2014, Hoffman et al., 2016]. Here we assume basal water pressure is equal to ice overburden pressure everywhere, which provides a reasonable upper-bound estimate of the direct impact ice surface topography could have on subglacial hydraulic potential. Subglacial water is often modeled as flowing down gradients in hydraulic potential [Hewitt, 2011, Wright et al., 2016]. We thus apply flow-routing to the hydraulic potential fields to determine water flow paths and create accumulated flow/drainage area maps. We first fill sinks (local minima) in the hydraulic potential field in order to force all water to flow out of the domain. We then apply a multi-direction flow-routing algorithm from TopoToolbox [Schwanghart W, 2014] since this produces more realistic flow pathways than D8 flow-routing in low-gradient areas [Quinn et al.,

1991]. We cannot account for water flow into the domain from up-gradient regions with this approach, so the drainage areas we calculate are lower bounds. These simple calculations also do not account for many important factors influencing subglacial hydrology such as basal melting/freezing, permeability, and subglacial channelization [Rempel, 2009, Schoof, 2010, Sole et al., 2011, Werder et al., 2013, Chandler et al., 2013], nor do they account for variation of flow pathways on timescales that differ from ice flow changes. However, they provide a useful tool for exploring the sensitivity of subglacial hydrology to the perturbations in surface topography caused by changing multiple-year averaged ice flow parameters.

## Results

### *Bed topography transfer*

We use two methods (as described in Section 2.2) to calculate the empirical admittance of bed topography from BedMachine DEMs [Morlighem et al., 2017b,a]) to observed ice surface topography in our seven study regions on the western Greenland Ice Sheet ablation zone. Results are shown in Fig. 2.7. In all regions, both calculations of empirical admittance (Fig. 2.7.B and Fig. 2.7.C) correspond well to predicted bed topography transfer amplitudes (Fig. 2.7.A, the transfer functions are described in Section 2.2) at wavelengths $>\sim$1 km. Notably, both calculations of empirical admittance generally exhibit peaks at wavelengths from $\sim$1-10 km, consistent with what would be predicted from bed topography transfer. However, in both calculations empirical admittance at wavelengths $<$ 1 km is higher than would be predicted from bed topography transfer. We expect this is in part due to limited effective bed DEM resolution at these shorter wavelengths, and in part due to other processes creating short-wavelength surface

topography (such as fluvial incision and crevassing). That there is good agreement between the transfer functions and both calculations of empirical admittance at wavelengths >∼1 km provides one piece of evidence that bed topography transfer is a dominant control on surface topography at these scales.

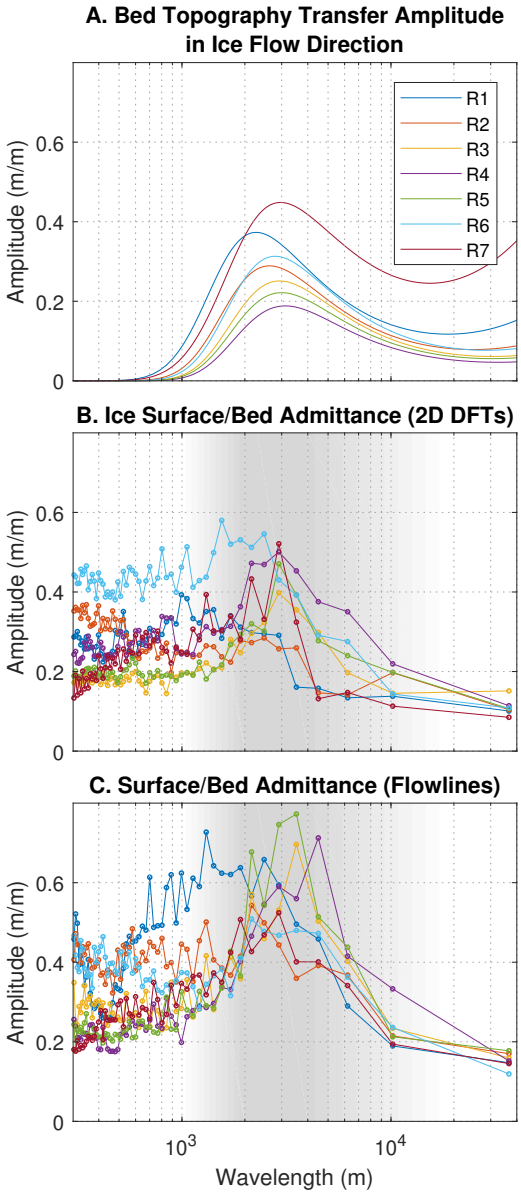


Figure 2.7 (A) Predicted bed topography transfer amplitudes from our seven study regions (Fig. 2.1.A, Table 1), with $\eta = 10^{14}$ Pa s and $C^{0*} = 10$ in all regions. (B) Results from one method for calculating empirical admittance of measured bed topography to observed ice surface topography by binning and averaging absolute wavenumber components of 2D DFTs (see Section 2.2). (C) Results from a second method for calculating empirical bed-to-surface admittance by of binning and averaging 1D DFTs from multiple ice flowline transects. For all regions both calculations of empirical admittance (B and C) generally match predicted transfer amplitudes (A) at wavelengths greater than ∼ 1 km and exhibit similar peaks between ∼1-10 km (shaded regions in B and C). At wavelengths less than ∼1 km both empirical admittance calculations are higher than predicted transfer amplitudes.

We then use the steady-state bed topography transfer functions to predict ice surface topography (as described in Section 2.2) in our seven study regions (Fig. 2.1.A, Table 1). Example results from region R1 are shown in (Fig. 2.8). In regions R1, R2, and R7 the transfer functions qualitatively well predict general IDC-scale (∼1-10 km, consistent with our admittance calculations) features of the ice surface, such as large ridges and depressions (see Fig. 2.8.A,B and supplement). In regions R3, R4, R5, and R6 the transfer functions significantly "under-predict" surface topography by creating noticeably smoother surfaces than observed. We expect that this is primarily due to the limited effective bed DEM resolution in these regions, as discussed below.

To quantitatively evaluate the effectiveness of our ice surface topography predictions, we calculate mean misfit as a percentage of surface topographic relief in each study region. For a DEM of size $m \times n$ this misfit metric is expressed as: $\frac{1}{nm} \frac{100}{\text{Range}(Z)} \sum_{x=x_1}^{x_n} \sum_{y=y_1}^{y_m} |Z(x,y) - Z'(x,y)|$; we note this metric is not necessarily a comprehensive indicator of fit quality. Mean misfits for all study regions are shown in Table 1, and an example misfit map is shown in Fig. 2.8.C. Even in regions where bed topography transfer predictions qualitatively well produce km-scale surface topographic features misfit is still significant; mean misfit values are 9-14% of regional topographic relief. As discussed in Sections 2.2 and 2.2, there are many potential causes of such misfit: bed DEM error, the various assumptions made in deriving and implementing the transfer functions (such as assuming Newtonian ice rheology, linearity, and a steady-state limit), and/or unaccounted for processes such as fluvial incision and kinematic ice waves. We use the approach described in Section 2.2 to examine the potential effects of bed DEM error on ice surface predictions in our study regions. This can

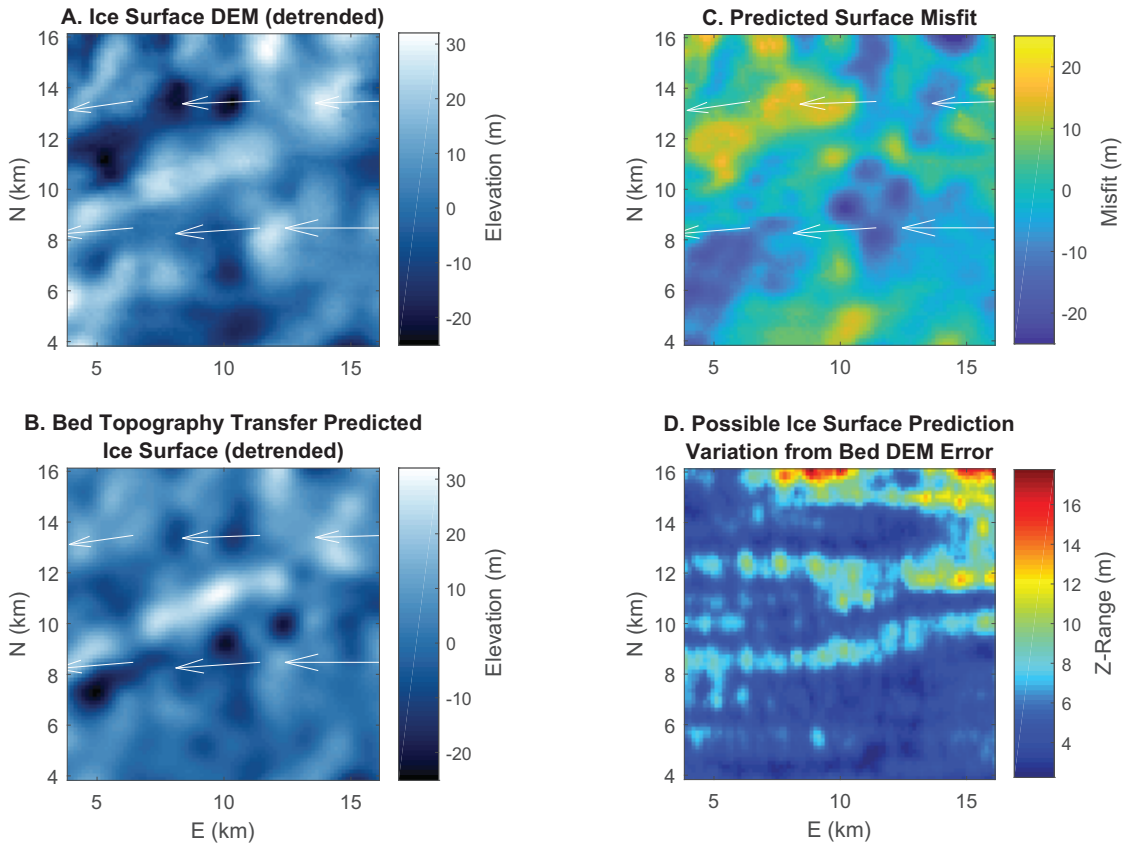


FIGURE 2.8. Example ice surface prediction and error analysis from study region R1 (Fig. 2.1.A, Table 1). (A) Detrended ice surface DEM. (B) Detrended bed topography transfer predicted ice surface, with $\eta = 10^{14}$ Pa s and $C^{0*} = 10$. We note that km-scale depressions and ridges/peaks are generally configured similarly to the real ice surface DEM in plot A, and that topographic relief also corresponds well. (C) Prediction misfit (subtraction between the actual and predicted ice surfaces in plots A and B). Prediction misfit is often significant (mean misfit in this region is 13.3% of the regional topographic relief), which might be expected for a number of reasons discussed in Sections 2.2, 2.2, and 2.2. (D) Potential effects of bed DEM error on ice surface predictions (see error map in Fig. 2.2.A). Where bed DEM error is less than ∼60 m the potential surface prediction variation is much less than the amplitude of surface topography. White arrows in all plots indicate ice surface velocity field, and the bed DEM underlying this region is shown in Fig. 2.1.B.

be significant, ranging from ∼40% to larger than 100% of regional ice surface relief depending upon the configuration and magnitude of DEM error. However, where bed DEMs are relatively accurate (generally less than ∼60-100 m potential error) these error effects are smaller than the regional ice surface relief (as shown in Fig. 2.8.D), indicating that large-scale features of surface predictions in these areas should be meaningful. Unfortunately potential bed DEM error is currently worse than 100 m over much of the Greenland Ice Sheet ([Morlighem et al., 2017b,a], Fig. 2.2), limiting the possible precision of surface predictions or inversions for parameters like basal sliding ($C^*$) in many regions.

Thus we have shown that, where bed DEMs are sufficiently accurate, bed topography transfer can explain IDC-scale (∼1-10 km) ice surface amplitude spectra and IDC-scale ice surface topographic features. This provides verification that bed topography is a dominant control on IDC scale surface topography, though with insufficient resolution to directly quantify the significance of other processes like thermal-fluvial incision that are superimposed on the effects of bed topography.

*Supraglacial stream network slope and accumulated drainage area relations*

Supraglacial stream networks from our seven study areas (Fig. 2.1.A, Table 1) all exhibit negative slope versus drainage area relationships (thus positive concavity), as shown in Fig. 2.9. This is expected in a fluvially controlled landscape (as discussed in Section 2.2, or see [Montgomery, 2001]). However, negative slope-area relations can arise without fluvial incision in randomly generated DEMs [Schorghofer and Rothman, 2002], so in isolation this geomorphic metric is challenging to invert uniquely for process. We thus use control cases with

no fluvial influence for comparison; these controls are synthetic flow networks created by artificially placing moulins on bed topography transfer predicted ice surfaces (as described in Section 2.2). The map-view structure of synthetic flow networks is not realistic, since the bed topography transfer predicted surfaces are very smooth and D-8 flow-routing then produces straight and parallel channels. However, in slope-drainage area space, synthetic flow networks in regions with qualitatively reasonable surface predictions (R1, R2, and R7) exhibit similar negative slope-area trends to the corresponding observed stream networks, as shown in Fig. 2.9. The slope area trends of regions R3, R4, and R5 are noticeably flatter than the corresponding observed stream networks. We expect this is mainly because limited effective bed DEM resolution results in under-predicted surface topography, on which all surface slopes deviate minimally from the regional background slope ($\alpha$).

In regions with more reliable surface predictions (R1, R2, and R7), synthetic and observed slope-area trends have similar slopes, as shown by the power-law fits in Fig. 2.9. There are deviations between observed stream networks and synthetic flow networks in regions R1, R2, and R7, but there is not a clear consistency in such deviations between these regions. Given the very large scatter inherent to slope-area relations (shown in Fig. 2.9 and discussed by [Warren et al., 2004]) and the limitations of our surface predictions, it is difficult to say from this data if there are consistent differences between observed slope-area relationships and those calculated on bed topography transfer predicted surfaces that could indicate fluvial modification of stream longitudinal elevation profiles. Further study with better bed DEMs and more detailed ice flow modeling might tease out such fluvial signatures. However, our results are sufficient to show that given accurate enough

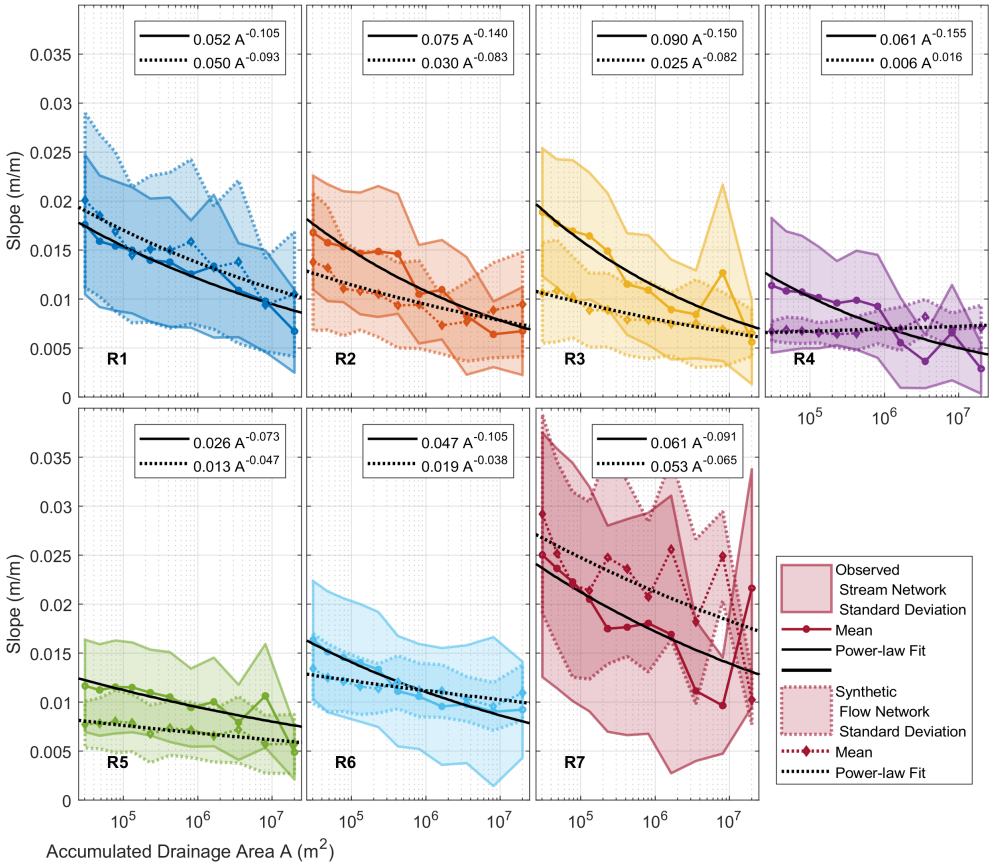


FIGURE 2.9. Mean stream channel slopes binned by accumulated upstream drainage/flow area from our seven study regions (Fig. 2.1.A, Table 1). Results are shown from both observed supraglacial stream networks and synthetic flow networks calculated on bed topography transfer predicted surfaces (see Sections 2.2 and 2.2). The standard deviation of slope within each area bin is indicated by shaded patches, where patches with solid outlines correspond to observed stream networks and patches with dotted outlines to synthetic flow networks. Mean slopes are shown by solid and dotted colored lines and power law fits by solid and dotted black lines. Under the (likely inaccurate) assumptions that supraglacial stream longitudinal elevation profiles are incisionally controlled and in a steady-state configuration under ice flow conditions analogous to uniform uplift, the power-law fit coefficients and exponents should correspond to $K^{-1}$ and $-m$ from equation 2.2.7. Synthetic flow networks from regions R3, R4, R5, and R6 may not be meaningful due to surface under-prediction (see Section 2.3).

bed DEMs, bed topography transfer alone can produce synthetic stream networks with longitudinal slope-area structure approximately similar to observed stream networks.

*Supraglacial stream network topographic conformity*

We calculate both stream network topographic conformity metrics (as described in Section 2.2) for supraglacial stream networks from our seven study regions (Fig. 2.1.A, Table 1); results are shown in Fig. 2.10. In all regions there are consistent trends in both $\%d$ (percent downhill) and $\Lambda$ (conformity factor). At the longest wavelength cutoffs $\%d$ and $\Lambda$ are at their lowest regional values, and including shorter topographic wavelengths generally results in increases in both metrics. $\%d$ and $\Lambda$ plateau at values between $\sim\ 88 - 97\%$ and $\sim\ 0.75 - 0.81$ respectively. That these values plateau at less than the maximum respective values of 100 and 1 in real stream networks could be due to varying channel depths and/or DEM inaccuracy; we normalized the values of both metrics in Fig. 2.10 to better highlight how the metrics change from their plateau values as progressively longer topographic wavelengths are removed.

In all stream networks the most significant decreases in both $\%d$ and $\Lambda$ occur in bands of cutoff wavelengths roughly between 1 and 10 km. This indicates that these wavelengths of topography are the wavelengths that are most important for explaining the overall structure of supraglacial stream networks. These wavelength bands match the wavelengths at which predicted bed topography transfer is highest, and also where we find peak admittance between surface and bed DEMs (see Fig. 2.7). In particular, we note that the region where stream conformity is more affected by smaller wavelengths (solid red curves) would be expected to

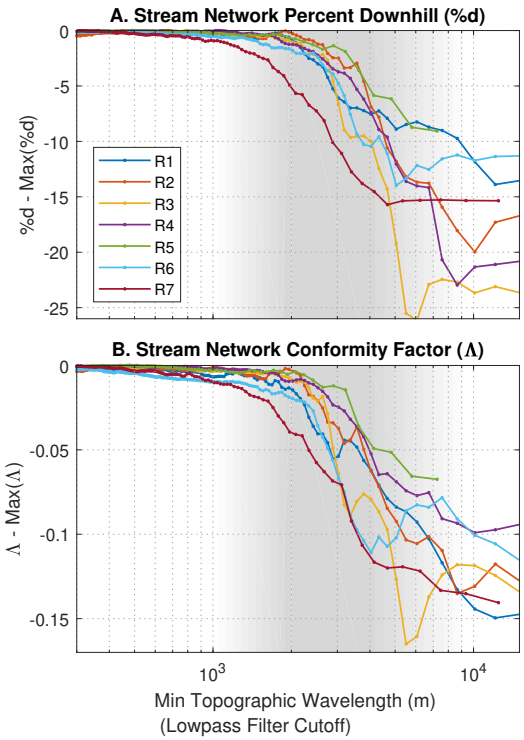


Figure 2.10 (A) Percent downhill $\%d$. (B) Conformity factor $\Lambda$. Values for both stream metric topographic conformity metrics are calculated in our seven study regions(Fig. 2.1.A, Table 1). All values are normalized to the maximum values in each network due to the variability in plateau values of $\%d$ and $\Lambda$ between networks. For all supraglacial stream networks the cutoff filter wavelengths over which $\%d$ and $\Lambda$ decrease most significantly are between ∼1-10 km (shaded regions), similar to the bed topography wavelengths predicted to transfer most strongly (2.7).

exhibit comparatively high bed topography transfer at these smaller wavelengths. The regions where stream conformity is less affected by smaller wavelengths (solid yellow, green, and purple curves) would be expected to exhibit comparatively low bed topography transfer at these wavelengths. Thus in all of our study regions the general routing of surface meltwater according to these conformity metrics is consistent with control by bed topography.

Our combined results thus demonstrate that given sufficiently accurate bed DEMs, bed topography transfer alone can reasonably well explain ablation zone IDC-scale ($\sim$1-10 km) ice surface topography and meltwater routing. This conclusion is supported by surface topographic admittance calculations, bed transfer predictions of surface topography, and three different geomorphological metrics of supraglacial stream network structure. This suggests that the effects of thermal-fluvial incision on IDC-scale supraglacial meltwater routing are secondary, superimposed on the dominant basal control of surface topography.

## Discussion

### *Predicting supraglacial IDC evolution*

Given moulin locations and ice flow conditions, our results imply that bed topography transfer should generally explain IDC configurations, such as the trend observed by [Yang and Smith, 2016] where average IDC area increases with increasing ice surface elevation/thickness. The bed topography transfer functions also provide a tool to perform a parameter study and predict IDC-scale surface topography under different multi-year averaged ice flow conditions. Even without predicting moulin locations, we can still use our methodology to examine the general response of surface topographic basins to changing ice flow conditions

as described in Section 2.2. This is important since surface topography and IDC configuration could impact subglacial hydrology, as we discuss in the next section (Section. 2.4). Additionally, it is expected that the ablation zone of the Greenland Ice Sheet will move to higher elevations in coming years as global climate warms [Rae et al., 2012, Fettweis et al., 2013, Leeson et al., 2015]. Given moulin locations, an approach similar to what we implement here could be used to obtain precise predictions of the of the spatial and temporal input of surface meltwater into moulins if combined with tools such as hydrographs [e.g., Smith et al., 2017].

The topographic basins associated with a predicted ice surface in different multiple-year averaged ice flow conditions are shown in Fig. 2.11. Variations from current ice flow parameters by factors of 1/2 and 2 illustrate parameter sensitivity, and are not based off of any predictions for how much each multi-year averaged parameter might change in a particular timescale. We also note that topographic basins will not exactly correspond to IDCs [Smith et al., 2015, Yang et al., 2015, Yang and Smith, 2016]; for comparison we show IDC configurations obtained solely from satellite imagery by [Yang and Smith, 2016] in Fig. 2.11.A. Despite the visible differences between our bed topography transfer predicted topographic basin configuration and the observed IDC configuration, the overall basin and IDC number densities are similar. This is consistent with results from [Yang and Smith, 2016] showing that surface topography roughly predicts IDC configurations. We thus expect that changes in topographic basin density predicted with changing ice flow conditions should generally correspond to changes in IDC density. Topographic basin density is not significantly affected by factor-of-four increases in ice surface slope $\alpha$ (Fig. 2.11.B7-B8, from 0.12-0.10 basins/km$^3$) or ice surface velocity $U$ (Fig. 2.11.B3-B4, from 0.10-0.11 basins/km$^3$). However,

topographic basin density decreases appreciably with factor-of-four increases in ice thickness $H$ (Fig. 2.11.B1-B2, from 0.16-0.08 basins/km$^3$), and increases appreciably with factor-of-four increases in basal sliding $C^{0*}$ (Fig. 2.11.B5-B6, from 0.08-0.18 basins/km$^3$). Our analysis thus indicates that ice surface topographic basin density in the Greenland Ice Sheet ablation zone could be significantly affected by changes in multi-year averaged ice thickness or basal sliding.

As discussed in Section 2.2, the timescale over which the ice sheet surface approaches 95% of its steady state configuration in response to a basal perturbation is on the order of 3-60 years depending upon perturbation wavelength, so the results here (and in the following Section 2.4) should be interpreted as predicting multiple-year averaged ice surface configurations. Minimal adjustment to changing ice flow or basal sliding conditions is predicted on shorter seasonal timescales, although increasingly high temporal resolution observations could motivate such shorter timescale modeling in the future.

*Potential coupling between ice surface topography and subglacial hydrology*

We have shown in Section 2.4 that changing ice flow conditions should result in changing ice surface topography and supraglacial IDC configuration (see Fig. 2.11); we can now explore and speculate upon how such changes might affect subglacial hydrology and/or basal sliding.

Perturbations to surface topography could have direct impacts on subglacial hydraulic potential, and thus on subglacial water flow pathways. We calculate such pathways as described in Section 2.2; the results are shown in Fig. 2.12. The predicted variations in subglacial meltwater flow patterns are subtle, but there is some change in all cases. This is most visible where the configuration of high-flow-

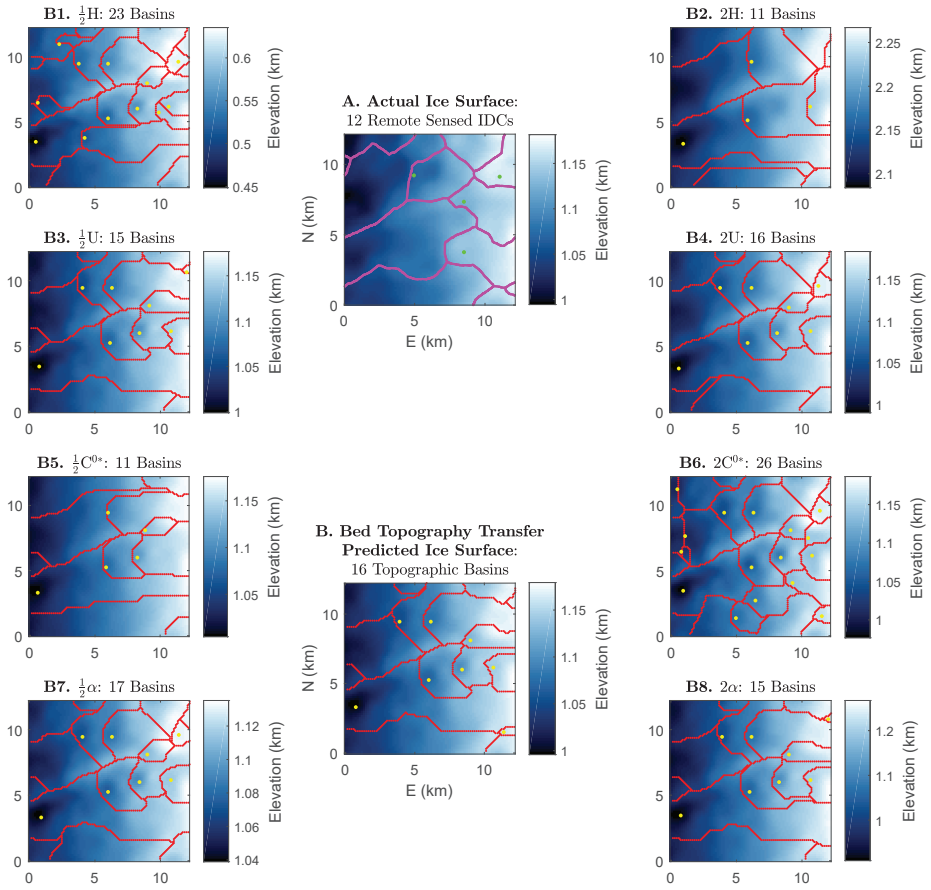


FIGURE 2.11. (A) IDCs (magenta outlines) and moulins (green dots) obtained from satellite images by [Yang and Smith, 2016]. (B, B1-B8) Ice Surface topographic basins (red outlines) and local minima (yellow dots) on bed topography transfer predicted ice surfaces with various ice flow parameters. From study region R1 (Fig. 2.1.A, Table 1) with $\eta = 10^{14}$ Pa s and baseline $C^{0*} = 10$. While the bed transfer predicted topographic basin configuration in plot B is different from the IDC configuration in plot A, the basin densities are similar. Changing ice thickness $H$ or basal sliding parameter $C^{0*}$ by factors of two produces significant changes in predicted topographic basin configurations (B1-B2 and B5-B6).

area paths changes, as can be seen near the center of the study region between Fig. 2.12.B5 and Fig. 2.12.B6. The threshold flow-area we use to calculate areal percentages in Fig. 2.12 ($5 \times 10^6$ m$^2$) was chosen to highlight pathways of high relative flow area. Subglacial channelization (discussed more later in this section) should occur preferentially around such pathways, since water flux should generally increase with increasing flow area [Hewitt, 2011, Wright et al., 2016]. Doubling $C^{0*}$ or $\alpha$ slightly increases the percent of the study region covered by such higher-flow pathways, while doubling $U$ or $H$ has the opposite effect. The magnitude of these changes is generally less than around 20% of the baseline areal coverage for any chosen flow-area threshold. Dynamic subglacial hydrology models (such as [Schoof, 2010] or [Werder et al., 2013]) are needed to more completely assess the potential impacts of these changes. However, our results indicate that unless any of the multiple-year averaged ice flow parameters changes by more than a factor of two, the effects (that are directly caused by perturbations in surface topography) such changes will have on subglacial hydraulic pathways are likely to be subtle.

Our calculations suggest that the more important influence of ice surface topography on subglacial hydrology may be from the dispersion of surface meltwater input caused by changing surface topographic basin (or IDC) number density (as shown in Fig. 2.11). For a given melt production rate, if topographic basin density increases then meltwater input to the subglacial environment will be dispersed among more moulins, up to the point at which some basins become small enough that they fill and overtop without building up enough water pressure to generate moulins through hydrofracturing [Banwell et al., 2012, 2016]. This dispersion of moulin water input could impact subglacial hydrology in several ways. If such dispersion results in average subglacial water pressure increases

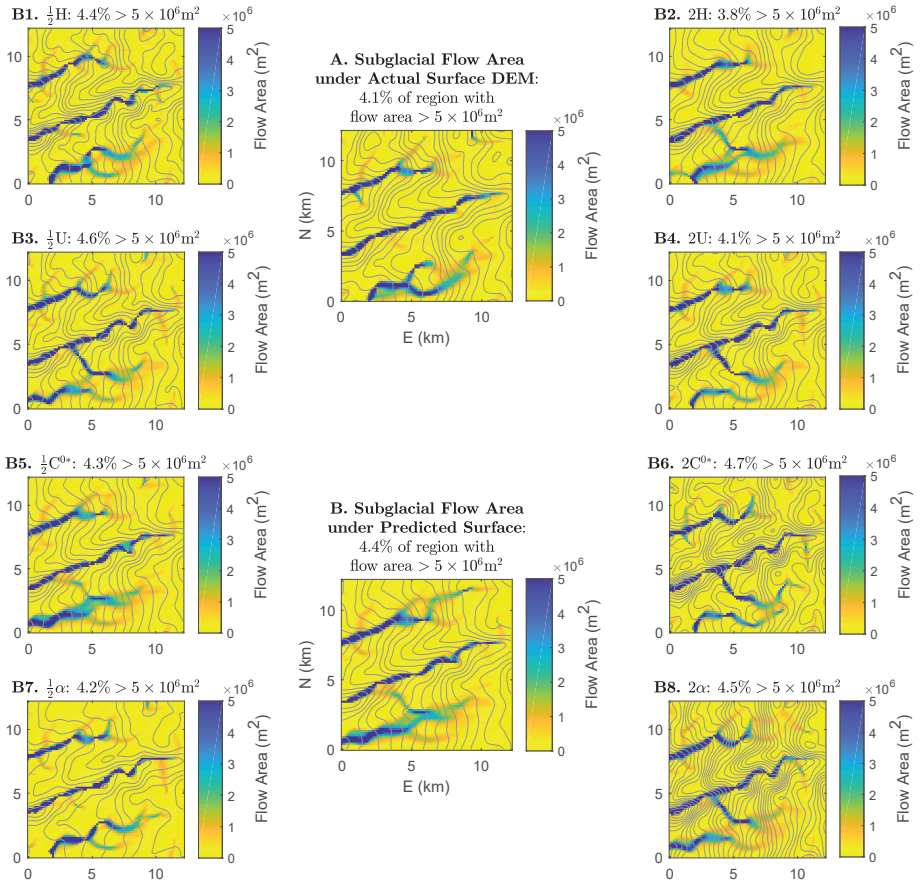


FIGURE 2.12. (A) Subglacial accumulated flow (drainage) area obtained via flow-routing on hydraulic potential fields calculated under the actual ice surface DEM from BedMachine/GIMP, [Howat et al., 2014, Morlighem et al., 2017b]. Grey contours in all plots are 0.1 MPa hydraulic potential contours. (B, B1-B8) Subglacial accumulated flow area calculated under the bed topography transfer predicted ice surface with various ice flow parameters. From study region R1 (Fig. 2.1.A, Table 1) with $\eta = 10^{14}$ Pa s and baseline $C^{0*} = 10$. The flow-area threshold displayed ($5 \times 10^6$ m$^2$) was chosen to highlight pathways of high relative water flux.

due to less effective or slower development of subglacial channels, this could lead to lower average basal effective stresses and increased basal sliding [Werder et al., 2013, Banwell et al., 2016, Hoffman et al., 2018]. Alternately, if subglacial channelization happens rapidly regardless of meltwater input rate, then the dispersion of meltwater input may not be particularly significant or may result in more effective subglacial channel networks [Banwell et al., 2016]. The extent to which subglacial channelization occurs is debated [Meierbachtol et al., 2013], but some subglacial channelization may occur on timescales of hours to days with continuing evolution over the length of melt seasons, and in the Greenland Ice Sheet ablation zone moulin meltwater input is a significant source of basal water affecting this subglacial drainage development [Schoof, 2010, Sole et al., 2011, Werder et al., 2013, Chandler et al., 2013]. Of course, the total amount and timing of surface meltwater flux will also change if the annual surface energy budget varies [Cuffey and Paterson, 2010, Ahlstrøm et al., 2017], if the average albedo of IDCs varies [Leeson et al., 2015], or if partitioning between slow (porous snow/weathering crust flow, firn aquifer) and fast (stream channel) pathways varies [e.g., Karlstrom et al., 2014, Cooper et al., 2018, Liao et al., 2018]. We see including such effects in glacial surface models as a promising avenue for future research.

Basal sliding is the parameter that generally has the most significant effect on surface topographic basin density (as shown in Fig. 2.11). Basal sliding can change significantly over timescales from hours to years, and often has strong seasonal cycles [Selmes et al., 2011, Sole et al., 2011, Chandler et al., 2013, Shannon et al., 2013]. As discussed in Sections 2.2 and 2.2, the long term averaged basal sliding parameter we assume in implementing basal transfer functions may

not directly relate to the real seasonally varying values of basal slip ratio [Tedstone et al., 2014]. However, the effects from relative changes in basal sliding that our methods predict should be more robust, and it is reasonable to expect that persistent changes in basal sliding during melt seasons and/or in the length of melt seasons could have effects on surface topography that are analogous to this multi-year averaged basal sliding parameter. Our results thus indicate that there are potential feedbacks wherein changes in multi-year averaged basal sliding affect surface IDC configurations, which could in turn affect subglacial hydrology and basal sliding.

*Thermal-fluvial incision on sub-IDC scales*

Our analysis suggests that the influence thermal-fluvial incision has on large ($> 1$ km) scale surface topography and stream network structures must be secondary and superimposed on the dominant influence of bed topography. However, empirical admittance calculations show that other influences on ice surface topography could become more significant at scales $< \sim$1 km (see Fig. 2.7). We expect fluvial incision to be a primary influence on surface topography and meltwater routing pathways at these scales. Models that couple transient ice flow over rough bed topography to a surface energy balance, along with accurate bed DEMs, will be necessary to quantitatively constrain the influence of thermal-fluvial incision on ice surface topography and meltwater routing. Such models are also required to address observed supraglacial channel network coarsening (time evolution of channel density, [e.g., Yang and Smith, 2016]), and to establish how diurnally and seasonally varying melt rates are imprinted on stream networks.

From the standpoint of predicting Greenland Ice Sheet-wide hydrology, our work may simplify future modeling efforts. If thermal-fluvial incision does not significantly modify the ice surface at IDC-scales, as our results suggest, supraglacial stream incision would not need to be fully coupled with ice sheet models in order to predict meltwater routing and the larger-scale evolution of ice surface topography over long timescales. Future work towards this goal should focus on better determining bed elevations and predicting moulin formation [Joughin et al., 2013, Young et al., 2018].

## Conclusions

Understanding the processes that govern surface meltwater routing on the Greenland Ice Sheet, and how this meltwater routing might change with changing climate or ice flow conditions, is important for understanding and predicting subglacial hydrology and ice sheet evolution. We implement linear transfer functions that predict the ice surface over rough bed topography in multiple 2D regions of the western Greenland Ice Sheet ablation zone. We verify that bed topography transfer alone, in the steady state limit, can largely explain $\sim$1-10 km wavelength ice surface topography under a range of ice flow conditions, given sufficient quality bed DEMs.

We then apply flow-routing to extract supraglacial flow networks from observed ice surface DEMs and from bed topography transfer predicted ice surfaces. We quantify stream network conformity to surrounding topography and estimate the relation between supraglacial channel slope and accumulated drainage area. These metrics are consistent with the inference that transfer of bed topography to the surface is the dominant process controlling general IDC-scale

(∼1-10 km) supraglacial meltwater routing on the Greenland Ice Sheet ablation zone.

Finally, we conduct a parameter sensitivity study to predict the adjustment of surface topography, supraglacial IDCs, and subglacial hydraulic potential that would occur in response to changing multi-year averaged ice flow conditions in a representative western Greenland site. We show that the surface topography perturbations caused by changing ice flow can have direct effects on subglacial hydraulic pathways. However, the more significant impact on subglacial hydrology may result from the increasing number density of surface IDCs, and the corresponding dispersion of englacial/subglacial surface meltwater input, that we show would be caused by decreasing ice thickness or increasing multi-year averaged basal sliding. This suggests a possible coupling between surface IDC configuration, subglacial hydrology, and basal sliding efficacy.

## Bridge

This chapter has demonstrated the use of spectral analysis combined with fluid dynamics modeling to address questions in glaciology. In particular, this chapter utilized one and two-dimensional Fourier transforms of spatial data and equations. The next two chapters will focus on a new setting, Kīlauea Volcano. They will still involve spectral analysis, but of temporal or time-series data instead of spatial data. The next chapter in particular will focus on wavelet transforms, an alternate form of spectral analysis to Fourier transforms.

# CHAPTER III

# VERY-LONG-PERIOD SEISMICITY AT KīLAUEA

This chapter represents material that was written with co-author Leif Karlstrom and that has been published in Journal of Geophysical Research: Solid Earth in 2021 under the title: "Wavelet-based characterization of very-long-period seismicity reveals temporal evolution of shallow magma system over the 2008-2018 eruption of Kīlauea Volcano" [Crozier and Karlstrom, 2021]. Joshua Crozier implemented modeling and data analysis with input from Leif Karlstrom. Joshua Crozier wrote the manuscript with input from Leif Karlstrom. Leif Karlstrom and Joshua Crozier conceived of the study. Leif Karlstrom obtained funding.

## Introduction

Volcano seismicity provides vital information for studying processes inside volcanoes and for monitoring changes in volcanic activity that inform hazards [e.g., Chouet and Matoza, 2013, Ripepe et al., 2015, McNutt and Roman, 2015]. Amongst the rich variety of seismic signals that are commonly observed at volcanoes, so-called very-long-period (VLP) seismic events are of particular interest for magmatism as they likely represent fluid movement and/or resonance in magmatic transport structures [e.g., Chouet and Matoza, 2013, Jolly et al., 2017, Cesca et al., 2020]. This type of seismicity can provide otherwise unobtainable in situ insight into magma properties and magma plumbing system geometry, and can be sensitive to different properties of the system than the longer timescale deformation observed with geodesy [e.g., Kumagai, 2006, Chouet et al., 2008, Dawson et al., 2011].

VLP seismicity is typically defined as having a disproportionate amount of energy at periods greater than ∼2 s [Chouet and Matoza, 2013]. VLP seismicity can occur as isolated impulses, oscillations persisting for multiple cycles (often exhibiting roughly exponential decay over time), or tremor that can persist for hours-days or longer. Waveforms can be either periodic (with energy focused into discrete spectral peaks including harmonics), exhibit 'gliding' frequencies that change smoothly over time, or irregular [e.g., Aster et al., 2008, Arciniega-Ceballos et al., 2008, Haney et al., 2013, Chouet and Matoza, 2013]. VLP seismicity at volcanoes has been proposed to represent various processes including magma transport through constrictions, bubble slug ascent, pressure changes in hydrothermal systems, or resonant oscillations of magma flowing within plumbing system components [e.g., Kumagai et al., 2003, Aster, 2003, Lokmer et al., 2008, Nakamichi et al., 2009, Chouet and Matoza, 2013, Dawson and Chouet, 2014, Cesca et al., 2020]. Signals in volcanic settings that have been proposed to represent resonance of either magma or hydrothermal fluids often also occur in the so-called long-period (LP) band (typically 0.2-2 s) [e.g., Chouet and Matoza, 2013, Chouet and Dawson, 2016], and some can also be detected in infrasound data [e.g., Garcés et al., 2009, Fee and Matoza, 2013, Matoza et al., 2018]. Isolated VLP events have been documented to be triggered by a variety of processes including eruptions, gas slug release, rapid depressurization of magmatic or hydrothermal features, rockfalls into a lava lake, or tectonic events [e.g., Lyons and Waite, 2011, Maeda and Takeo, 2011, Orr et al., 2013, Chouet and Matoza, 2013]. Persistent forcing could be caused by repeating discrete triggers or processes such as magma flow through irregular channels, bubble-cloud oscillations, or turbulence [e.g., Julian, 1994, Hellweg, 2000, Matoza et al., 2010, Unglert and Jellinek, 2015].

Here we develop an automated signal processing workflow for cataloging VLP seismic events from continuous seismic data, and then apply this workflow to generate and analyze a catalog of VLP seismicity at Kīlauea Volcano from 2008-2018. We focus on classifying signals that consist of periodic oscillations with impulsive onsets and monotonic decays in amplitude over time, as are produced by damped magma resonance. Our methods yield more robust and precise estimates of quality factors than previous approaches and are readily applicable to near-real-time monitoring and/or to other volcanic settings. Our catalog reveals a rich temporal evolution of Kīlauea VLP seismicity, which we contextualize by comparing to other geophysical data and observed volcanic activity such as intrusions and rift zone eruptions. This catalog augments multiparameter data that inform the evolution of the Kīlauea shallow magma system over 10 years, representing a unique window into the dynamics of a long-lived open-vent eruption.

### *Cataloging VLP seismicity*

Numerous studies have created catalogs of long-period and very-long period volcanic seismicity [e.g., Battaglia, 2003, Aster et al., 2008, Dawson et al., 2010, Zuccarello et al., 2013, Dawson and Chouet, 2014, Knox et al., 2018, Wech et al., 2020, Park et al., 2020]. These signals can require different detection approaches than tectonic earthquakes, and all previously used approaches have some limitations that motivate the development of a new workflow for cataloging the resonant signals of interest here.

Time-domain moving short-term-average/long-term-average (STA/LTA) detectors will miss many events with small signal/noise ratios [Schaff, 2008].

Correlation-based template matching can be much more sensitive [Schaff, 2008] and has been used to detect long-period seismicity [e.g., Aster et al., 2008, Wech et al., 2020, Park et al., 2020], but is better suited to detecting repeating events than signals that exhibit a continuum of variation (i.e., in periods, decay rates, and trigger mechanisms) and is computationally slow [Yoon et al., 2015]. Approaches using feature-extraction to create and cluster waveform 'fingerprints' thus far are also best suited to detecting repeating events [Yoon et al., 2015]. Supervised machine learning approaches can be effective for detecting earthquakes [e.g., Perol et al., 2018, Jennings et al., 2019, Bergen and Beroza, 2019] and very-long-period seismicity [Dawson et al., 2010], but can require lots of pre-selected training examples, may not detect new types of signals robustly, will generally need at least partial re-design and/or re-training to be applied to new networks/volcanoes, and their 'black box' nature can make predicting when or why they fail difficult [e.g., Bell, 2014, Goodfellow et al., 2016]. Unsupervised learning methods have been used to cluster seismic data [Kohler et al., 2010, Mousavi et al., 2019], but have not yet been demonstrated to generate accurate or comprehensive event catalogs.

Accurately categorizing resonant VLP signals is also important, since the dominant periods ($T$), decay rates (quantified by quality factor $Q$, a ratio of energy stored to energy lost per cycle), and source motions (from ground motion patterns) can encode the underlying mechanism [e.g., Kumagai and Chouet, 2000, Kumagai et al., 2010]. Several methods have previously been used to estimate $Q$. The simplest is to calculate the full width at half the maximum amplitude (FWHM) of peaks in the power spectrum. This technique is often inaccurate in the presence of noise, complicated signal shapes, or multiple signals with similar frequency components [e.g., Kumazawa et al., 1990, Zadler et al., 2004]. To

overcome this limitation, autoregressive (AR) methods that fit decaying sinusoids to the coda of signals were developed [Kumazawa et al., 1990, Nakano et al., 1998, Lesage et al., 2002]. When the coda of a signal can be appropriately isolated, these methods work well for classifying dominant resonant oscillations. However, they often do not accurately detect or estimate $Q$ of secondary oscillations or oscillations with coda interrupted by other signals (Fig. B.3). Bandpass filtering can help isolate signals, but often a narrow passband is required which artificially increases $Q$ [Kumazawa et al., 1990].

We use continuous wavelet transforms (CWTs) to detect and classify $T$, $Q$, and ground motion patterns of resonant VLP seismic signals. CWTs are a method for determining the frequency content of signals over time [e.g., Alsberg et al., 1997, Selesnick et al., 2005] that have been previously used to analyze volcano seismicity and suggested as a means for automated signal detection and classification [Lesage, 2009, Lapins et al., 2020]. Our methods robustly determine $T$ and $Q$ in the presence of high noise, multiple resonant frequencies, and overlapping signals. These methods are also readily extendable to characterizing resonant signals in the LP band and in infrasound data, as well as some periodic tremor and gliding-frequency signals, but are likely not the optimal approach for analyzing signals that are not periodic. Our approach does not depend upon training data or templates, and thus can be applied to any instrument network or volcano with minimal configuration.

### *The 2008-2018 eruption of Kīlauea Volcano*

We examine the 2008-2018 summit eruptive episode of Kīlauea Volcano, a basaltic shield volcano on the island of Hawaii. This was the most recent period

of continuous summit activity following decades of quiescence or sporadic events largely focused along the East Rift Zone (ERZ) [e.g., Wright and Klein, 2014]. Over this timespan a summit lava lake persisted at the surface, then drained as part of a caldera collapse eruption sequence in May-August 2018 [e.g., Neal et al., 2019, Patrick et al., 2019a,b]. Kīlauea is one of the best monitored volcanoes in the world, with abundant data on ground deformation (from tilt-meters, GPS/GNSS stations, and InSAR), gas flux, magma composition, and lava lake activity [e.g., Edmonds et al., 2015, Elias et al., 2018, Patrick et al., 2019b] that can contextualize VLP seismicity.

The U.S. Geological Survey Hawaii Volcano Observatory operates a dense broadband seismic network at Kīlauea Volcano. VLP seismicity at Kīlauea has previously been cataloged up to 2013 using a hidden Markov model to detect events and the Sompi AR method to determine $T$ and $Q$ of these events [Dawson et al., 2010, Dawson and Chouet, 2014]. This provides a benchmark for our extended catalog, which includes prevalent VLP seismicity over the 2008-2018 timespan. Combining the new catalog with insights from additional types of data and magma resonance models previously used in inversions of select events at Kīlauea [Liang et al., 2020a, Liang and Dunham, 2020] probes changes within the shallow magma system on a variety of timescales.

## Methods

### *Seismic data*

The first step in our workflow is selecting and processing seismic data (Fig. 3.1). We use waveforms from 3-component broadband seismometers in the Hawaii Volcano Observatory (HVO) network that are within ∼3 km of the vent. We use

available data from the following stations: NPB, NPT, SRM, OBL, WRM, SDH, UWE, UWB, SBL, KKO, and RIMD (Fig. 3.2, 3.3). Some other stations in the area were not used due to low signal/noise ratios. Seismic data from 2008-2011 was obtained from the USGS, subsequent data is publicly available from IRIS (Incorporated Research Institutions for Seismology). We download and process data in 6 hr time windows and discard waveforms with data gaps longer than 2 s.

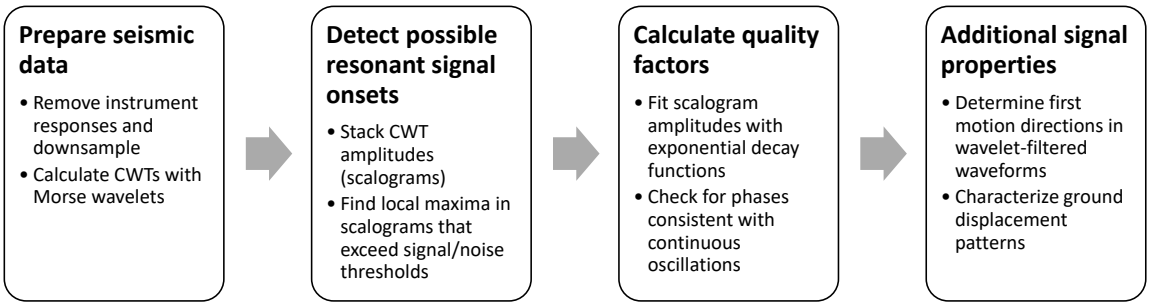


FIGURE 3.1. Signal processing workflow for VLP detection and characterization.

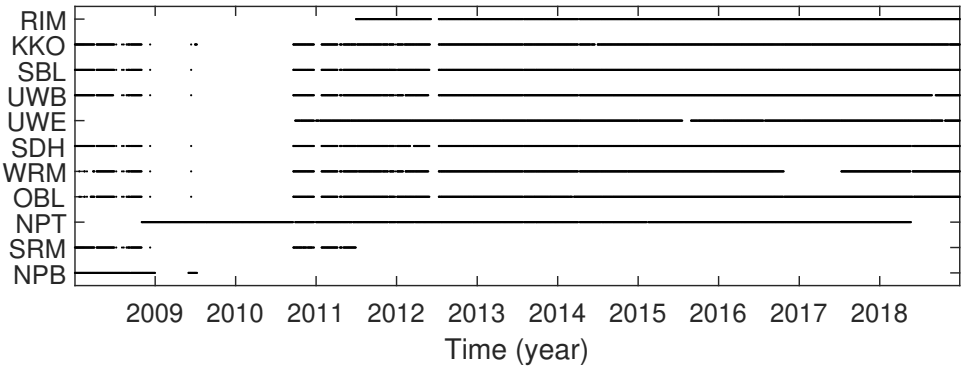


FIGURE 3.2. Timeline of data availability at the HVO broadband seismic stations used in this study.

We deconvolve the instrument responses to facilitate stacking of data from different instruments (Fig. B.4). A standard 'water level' is first applied to these

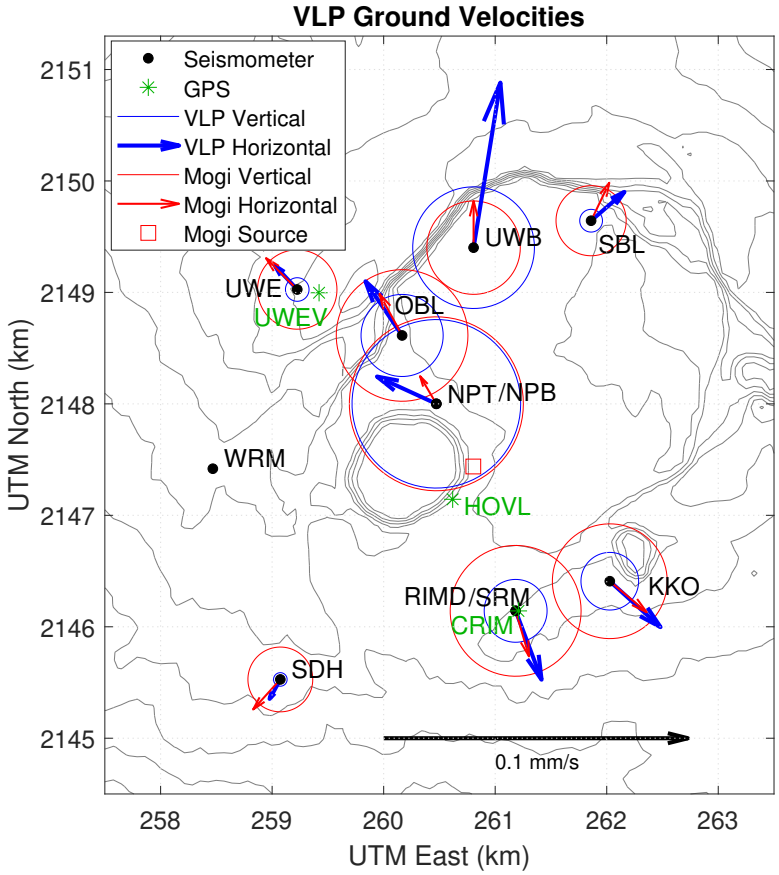


FIGURE 3.3. Map of seismometers and GPS stations also showing ground velocities and Mogi inflating spherical reservoir source inversions results for an example conduit-reservoir event on 2017-5-21 (plotted at the time of peak vertical velocity at station NPT). Horizontal velocities (arrows) and vertical velocities (circles, all positive/upward) are shown at the same scale. Horizontal components in the data and source inversion include both tilt and translation effects. UTM zone 5Q.

instrument responses so that the maximum amplification is 10 times the base amplification. This prevents over-magnification of noise at periods outside of the instrument sensitivity range. We note that this process is not causal and can introduce artificial tapers around discontinuities (e.g., step functions); an effect included in the synthetic seismograms we use to test our methods (B.1). All waveforms are then smoothed and resampled at 6 Hz (much higher than the signal frequencies of interest).

*Continuous wavelet transforms*

The second step (Fig. 3.1) in our method involves calculating time-frequency representations of the seismic data, which are well suited to identifying resonant signals [e.g., Köcher et al., 2014]. We use continuous wavelet transforms (CWTs), which offer several advantages over standard short-time Fourier-transforms (STFTs). CWTs involve specifying a base wavelet that can be stretched or 'scaled' to different frequencies and cross-correlated with data to determine the frequency content as a function of time [e.g., Alsberg et al., 1997, Selesnick et al., 2005]. Plots of CWT amplitudes are termed scalograms. For a given wavelet, CWTs provide increasing temporal resolution with increasing frequency. This is a primary advantage over STFTs which have the same temporal resolution for all frequencies [e.g., Lapins et al., 2020].

Useful wavelets for time-frequency analysis are often sinusoids scaled by some function with symmetric, compact support that decays in both directions from a central point (Fig. 3.4). We use Morse wavelets which are given in the spectral

domain (for angular frequency $\omega$) by

$$\Psi_{\beta,y}(\omega) = U(\omega) a_{\beta,y} \omega^{\beta} e^{-\omega^{\gamma}}, \tag{3.2.1}$$

where $U(w)$ is the Heaviside step function, $\beta$ governs wavelet duration (or decay rate), $\gamma$ governs wavelet symmetry, and $a_{\beta,y}$ is a normalizing constant [Lilly and Olhede, 2009]. We set $\gamma = 3$ which yields wavelets that are symmetric in the frequency domain [Lilly and Olhede, 2009].

Increasing wavelet duration (i.e., decreasing decay rate) will provide better frequency resolution but worse temporal resolution (Fig. 3.4), analogous to increasing the window length in a STFT. An arbitrary number of 'stretches' of a wavelet can be used to sample at any desired frequencies, although there is a limit to the effective frequency resolution possible with a given wavelet (Fig. 3.4). The gradual onset of wavelets introduces less artificial temporal 'jaggedness' than a standard STFT (where sinusoids truncate abruptly at the edges of each window), which allows for a more accurate determination of signal decay rates. The convolution between a wavelet and an impulsive signal (such as a single peak or step function) will have a duration and decay rate similar to the wavelet itself (Fig. B.5). This is analogous to temporal smearing of impulsive signals in STFTs over the window length used. Thus, wavelet duration determines the minimum signal duration that can be distinguished from an impulsive signal, so narrower wavelets can resolve lower $Q$ oscillations.

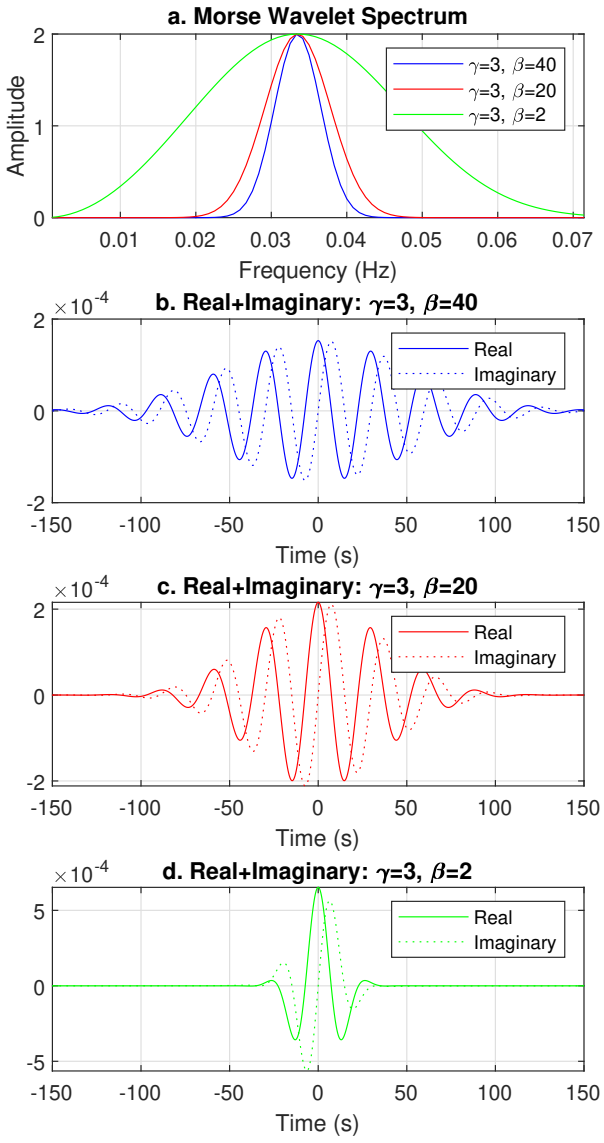


Figure 3.4 Morse wavelets used in this study (in this case scaled to a period of 30 s). (a) Amplitude spectra. (b) $\beta = 40$ wavelet used to make combined scalograms from which potential VLP signals are detected. (c) $\beta = 20$ wavelet used to make combined scalograms from which potential VLP signals are detected and for calculating $Q$ of signals. (d) $\beta = 2$ wavelet used for detecting first motions of signals.

*Detecting potential resonant signal onsets*

To mitigate the inherent trade-off between spectral and temporal resolution we make combined scalograms using wavelets with two different values of $\beta$, 40 and 20 (Fig. 3.4). The higher frequency resolution of the $\beta = 40$ wavelet helps more accurately determine resonant signal period. The $\beta = 20$ wavelet still provides enough frequency resolution to isolate typical Kīlauea VLP signals (Fig. B.6), but its increased temporal resolution helps reveal gaps that could indicate whether a signal is a continuous oscillation (Fig. B.7) and helps resolve signals with lower $Q$ (Fig. B.5). We exclude periods less than 10 s in this study because of the strong oceanic microseism at these periods over the Kīlauea seismic network [e.g., Berger et al., 2004, Dawson and Chouet, 2014]. We stack the scalograms from all available stations to increase the signal/noise ratio. Given the proximity of our stations, travel-time effects from seismic waves are negligible at periods of interest. For shear wave speeds of 1800 m/s [e.g., Dawson et al., 1999, Lin et al., 2014], the wavelength of a 10 s period wave will be 18 km, roughly four times the distance across our ∼5 km wide array. There is also no concern about destructive interference from stacking scalograms since they contain no phase information. For applying our workflow to shorter period resonant signals (e.g., some LP events), more expansive instrument arrays, or infrasound data travel time effects may need to be considered.

To detect potential resonant signal onsets in a stacked scalogram, we first calculate the moving long-term average (LTA) and moving standard deviation of each frequency component with 200 s windows (Fig. 3.5). We then introduce a frequency-dependent delay of four cycles to the LTA and standard deviation to account for non-causality in the scalogram. Next, in each frequency band of the

stacked scalogram we identify all points that are local maxima, have amplitudes that are above some chosen multiple of the LTA (which we term the STA/LTA threshold), and are also more than some threshold number of standard deviations above the LTA (Fig. 3.5). We select a value of 3 for both thresholds; chosen to minimize false detections while keeping most desired signals in both synthetic tests and real data (Fig. B.8, B.9, B.10). Finally, where local maxima are separated by less than a ratio of 1.07 in period (the minimum separation that can be robustly resolved with the wavelets we use) and less than 200 s in time, we keep the maxima corresponding to the highest energy integrated over the following two cycles. This is more robust than just keeping the highest maxima.

*Calculating quality factor (Q)*

The third step (Fig. 3.1) in our workflow is calculating $Q$ by fitting decaying exponentials to stacked scalogram amplitudes following each detected potential resonant signal onset (Fig. 3.6). We use only the narrower $\beta = 20$ CWTs that have better temporal resolution (Fig. 3.4); the minimum $Q$ that this wavelet can robustly resolve is around 6. Lower $\beta$ values could be used to resolve lower $Q$ events at the expense of worse frequency resolution. We extract scalogram amplitudes at the target frequency over one to eight cycles after the identified signal onset. The one cycle delay avoids the region near the onset of an impulsively initiated signal where amplitudes will be inherently underestimated since part of the wavelet will not be overlapping the signal (Fig. 3.6), and helps avoid artifacts that might be present from a trigger mechanism. Delays between 0.5 and 1.5 cycles yield negligibly different results. Eight cycles was found to be a sufficient duration

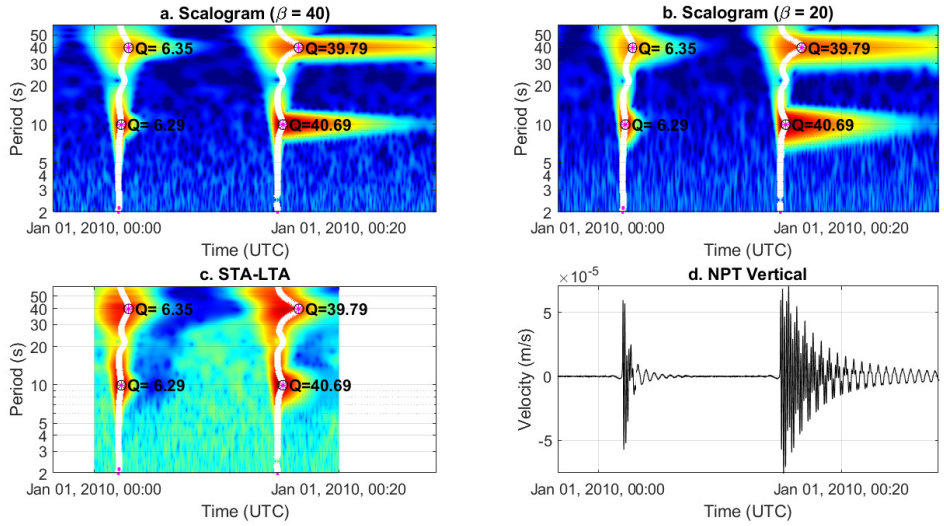


FIGURE 3.5. Example scalograms and cataloged events from a synthetic seismogram consisting of four VLP signals with [start time, $T$, $Q$] = [00:05, 40, 6], [00:05, 10, 6], [00:15, 40, 40], [00:15, 40, 40], plus white noise from a standard normal distribution scaled by 0.1% of the signal amplitude (B.1). Here $T$ and $Q$ of all resonant signals are recovered accurately. (a) $\beta = 40$ scalogram. White dots indicate temporal local maxima that meet the minimum STA/LTA criteria, and magenta dots indicate points that are spectral local maxima (integrated over two cycles). Black circles and text indicate the final selected event onsets and corresponding calculated $Q$. (b) $\beta = 20$ scalogram. (c) Frequency-dependent STA/LTA. (d) Synthetic seismogram. We note that the slight precursory oscillations arise from removing the instrument response.

for robustly capturing signal decay rates; increasing this duration further will not affect the accuracy of our fitting method.

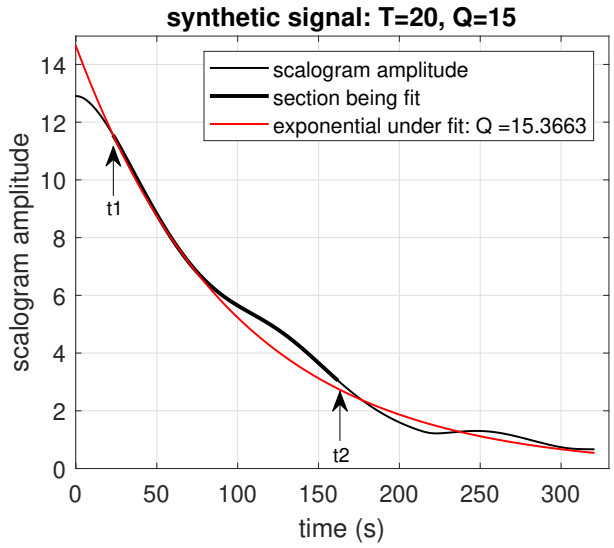


Figure 3.6 Example estimation of $Q$ by scalogram exponential fit from a synthetic seismogram. This seismogram consists of a VLP signal with $[T, Q] = [20$ s, 15], plus white noise from a standard normal distribution scaled by 1% of the signal amplitude. The bold part of the black line shows the part of the scalogram data that is being fit (from $t_1$ to $t_2$), and the red line shows the exponential 'under fit' (Eq. 3.2.2).

Standard least-squares exponential regressions can underestimate decay rate in the presence of noise or where another signal starts within the fitting window, thus overestimating $Q$ (Fig. B.11). We tested a variety of different exponential fitting approaches with varying fit timespans, maxima/minima, weighting schemes, outlier exclusion methods, and goodness-of-fit thresholds. An 'under-fit' is the most robust (Fig. 3.6, B.12). This involves an exponential fit with initial amplitude fixed to the initial scalogram amplitude $A(t_1)$ and with the slowest decay rate $\alpha$ that remains bounded from above by scalogram amplitudes in the timespan being fit ($t_1$ to $t_2$) (Fig. 3.6, B.11),

$$\alpha = -\min_{t=t_1}^{t_2} \left[ \frac{\ln\big(A(t)\big) - \ln\big(A(t_1)\big)}{t - t_1} \right]. \tag{3.2.2}$$

Quality factor is then given by $Q = \pi/(T\alpha)$. This fitting method is less sensitive to the choice of fitting timespan than least-squares regressions, since extending the timespan will have no effect unless the added amplitudes fall beneath the current fit. Additionally, other signals interrupting the coda of the target signal are less likely to affect this fitting method. The estimates from this method have a slight negative bias (<10% even for very high noise levels, Fig. B.12). However, this method has lower bias and higher overall accuracy than other regression methods (Fig. B.12) and outperforms the Sompi AR method which fails to detect the signals of interest in many of our tests.

Signals that are not a single continuous periodic oscillation could create a contiguous band of elevated energy in a scalogram that appears like a decaying resonant signal. To mitigate this, we also extract the phases of the $\beta = 20$ CWTs at each channel and check for consistent trends over the timespan being fit. For a continuous periodic oscillation, the phase $\theta(t)$ of a wavelet stretched to the oscillation frequency $f$ will increase steadily as it is convolved with the signal (Fig. 3.7, B.13) following

$$\theta(t) = 2\pi f t + \theta(0). \tag{3.2.3}$$

A signal that is not a continuous periodic oscillation can exhibit deviations from this expected phase (Fig. 3.7). To quantify how 'continuous' a signal is, we calculate the mean phase deviation ($E_\theta$) from the expected phase over the timespan being fit ($t_2 - t_1$) and over all $N$ channels as

$$E_\theta = \frac{1}{N}\frac{1}{t_2 - t_1}\sum_{n=1}^{N}\int_{t_1}^{t_2}\left|2\pi f t + \tilde{\theta}_n - \theta_n(t)\right|dt, \tag{3.2.4}$$

where $\tilde{\theta}_n$ is the constant phase offset that minimizes phase deviation at channel $n$. We use this phase offset instead of the actual initial phase $\theta_n(t_1)$ since there may be effects from the signal onset present at the start of the timespan. We then keep only signals with a mean phase deviation of less than a threshold value of 0.1 radians. This threshold minimizes inclusion of noise or non-continuous oscillations while keeping most continuous periodic oscillations in tests on both synthetic and real data (Fig. 3.7, B.13).

*Determining first motions*

First motions (polarities) are not well defined for signals without impulsive onsets. Even for impulsive onsets, picking first motions for a particular frequency component is difficult to do robustly because band-pass filtering a signal will distort the onset of that signal regardless of the filter used (i.e., causal or acausal, FIR or IIR) (Fig. 3.8). To partly mitigate this issue, we use a 'wavelet filter': we compute the CWT of a signal, then reconstruct the signal using an inverse CWT but keeping only the period of interest. This still produces artificial precursory oscillations in front of signals with impulsive onsets (Fig. 3.8), but the size of these oscillations is predictable for a given wavelet. We use a very narrow Morse wavelet ($\beta = 2$) which will produce only one appreciable precursory oscillation that will be less than half of the signal amplitude. However, such a narrow wavelet will be sensitive to a wider frequency range (Fig. 3.4), and so may not clearly delineate signals that are not dominant over that frequency range.

We then stack the amplitudes of the wavelet-filtered signals from all channels and identify local maxima around the signal onset time that exceed the thresholds for both STA/LTA and number of standard deviations above the LTA (Fig. 3.8).

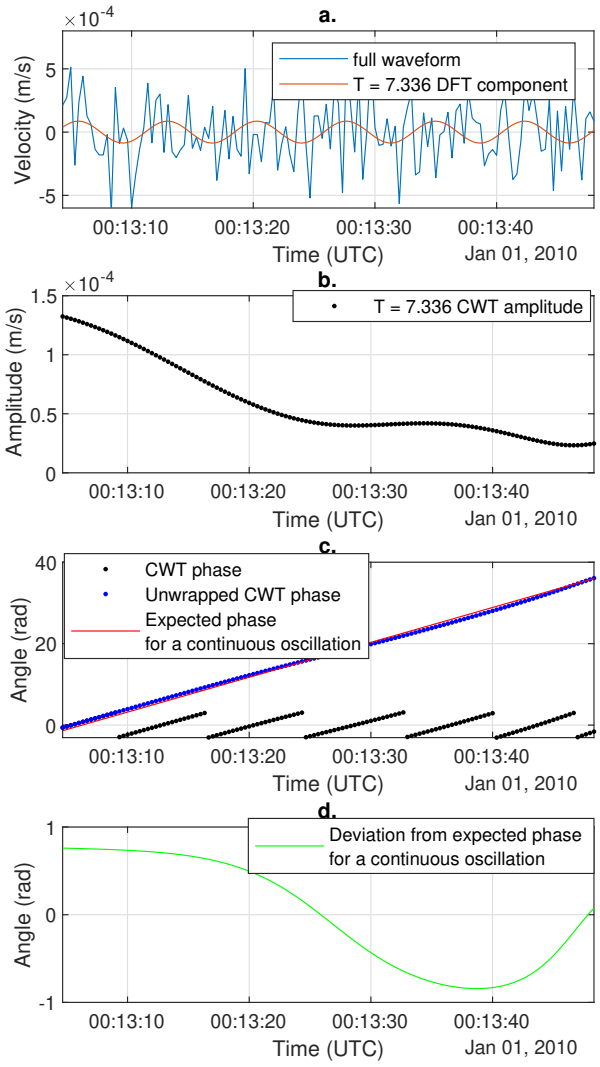


Figure 3.7 Example phase continuity from a spectral peak in synthetic random noise, where the high phase deviation correctly indicates that this is likely not a continuous oscillation. (a) Synthetic seismogram and 7.336 s DFT component. In a scalogram (or frequency spectrum) this signal exhibits a local maximum at this period. (b) CWT amplitude of the 7.336 s signal, which exhibits a roughly exponential decay. (c) CWT phase of the 7.336 s signal and expected phase for a continuous oscillation. (d) Difference between CWT phase and expected phase for a continuous oscillation.

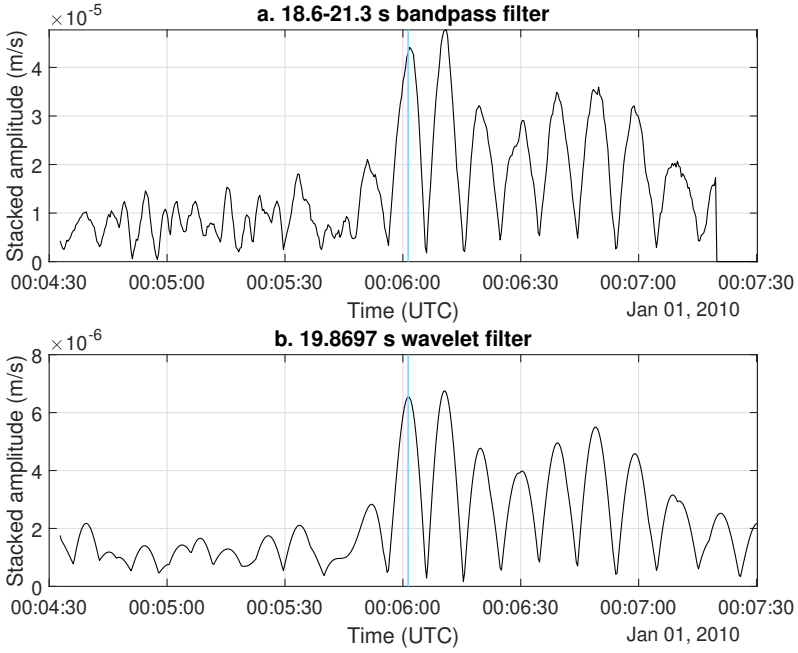


FIGURE 3.8. Example correct first motion pick from a synthetic seismogram for an impulsive onset oscillation with [start time, $T$, $Q$] = [00:06, 20, 20], plus a step displacement (velocity spike) at time 00:06, plus two other equal-amplitude oscillations with [start time, $T$, $Q$] = [00:05, 80, 20] and [00:05, 5, 20], and plus white noise from a standard normal distribution scaled by 0.1% of the signal amplitude. (a) Stacked amplitudes from waveforms filtered with an FIR bandpass filter. This is just shown for comparison and not used in picking first motions. The cyan line is the algorithm's first motion pick. (b) Stacked amplitudes from waveforms filtered with the wavelet filter we use for picking first motions.

We discard local maxima that are less than half of the global maximum, which for impulsive onset signals will exclude precursory oscillations caused by the wavelet filter. If no local maxima remain, which will occur either if the signal has a gradual onset or is too contaminated by other signals/noise, we consider the first motions undetermined. If one or more maxima remain, we select the first of these as the first motion time and then obtain the corresponding first motion directions at each channel from the wavelet filtered waveforms (Fig. 3.8). We store the STA/LTA ratio, standard deviations above the LTA, and fraction of the global maximum of this local maximum as indicators of pick confidence.

*Comparison with previous Kīlauea VLP catalog*

We compare our catalog to one produced using the methods from Dawson and Chouet [2014] extended through 2018: automated detection via a hidden Markov model trained on example events [Dawson et al., 2010] and estimation of $T$ and $Q$ via the Sompi AR model [Kumazawa et al., 1990]. For both catalogs adjustment of various threshold parameters is required to minimize false picks and poorly constrained events. In the catalog extended from Dawson and Chouet [2014] the most useful parameters to threshold are the event amplitude at station NPB or NPT and the standard deviation of $Q$ from Sompi cluster fits. We set these thresholds to 325 counts and 0.275, respectively, which results in a similar number of events in both catalogs ($\sim$3200). In both catalogs, changing these thresholds will greatly vary the number of events included, and less strict thresholds will include tens of thousands of additional events (Fig. B.9, B.10).

For the thresholds shown the two catalogs include around 1000 overlapping events, most of which are part of a dominant trend of events that spans most of

the timeline with periods varying from about 15-40 s (Fig. 3.9). There are more total events in this main event trend in the catalog extended from Dawson and Chouet [2014] than in ours, but there are also many events unique to our catalog both in this main event trend and forming additional event groups. Using less strict thresholds on both catalogs results in a larger number of overlapping events, primarily in the main event trend, but there are still many events unique to each catalog. Based on visual inspections of outlier events and a random subset of all events, at the thresholds shown both catalogs include on the order of 100 events that are likely bad detections. For this purpose we consider bad detections either signals with estimates of $T$ that appear inaccurate by more than $\sim$25%, or signals that do not appear to be continuous periodic oscillations (e.g., noise or tectonic earthquakes).

Accurate estimates of $T$ and $Q$ will be more valuable than total event counts for inferring properties of the magmatic system. Our catalog generally includes less scatter in both $T$ and $Q$ for the main event trend (most of the apparent $Q$ outliers in Fig. 3.9 plot b are not from the main event trend). The lower scatter in our catalog is also present when only comparing matching events (Fig. 3.9) and is present over a range of reasonable event thresholds for both catalogs. As discussed in section 3.2, our method cannot robustly detect events with $Q < 6$ given the wavelets we are using. The catalog extended from Dawson and Chouet [2014] extends to lower $Q$, though the accuracy with which low-$Q$ events can be characterized will be inherently limited as indicated by the large scatter in $T$ from late 2011-early 2012. Where the two methods estimate appreciably different values of $Q$ we find that there is often some complication (such as overlapping signals or strong noise) that causes the Sompi AR method to be inaccurate where our

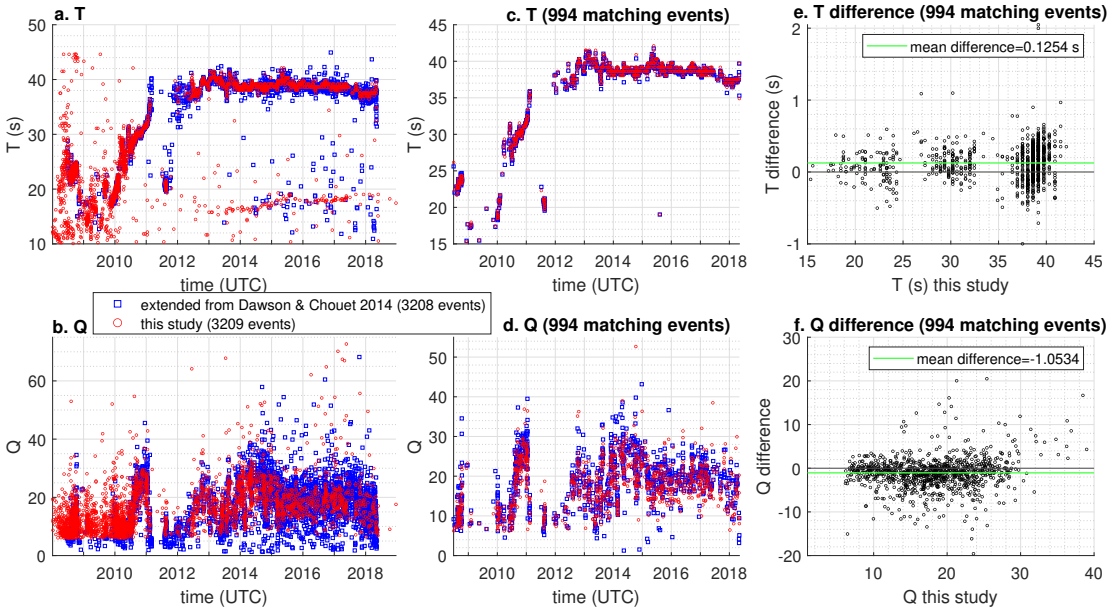


FIGURE 3.9. Comparison of detected VLP events from this study with a catalog extended from Dawson and Chouet [2014]. Event detection thresholds were chosen to produce a similar number of events in both catalogs (section 3.4). (a and b) $T$ and $Q$ over time in both catalogs. (c and d) $T$ and $Q$ over time from corresponding events that have start times within 3 minutes of each other and $T$ ratios within 4/5-5/4 of each other between the two catalogs. (e and f) Values of $T$ and $Q$ in our catalog minus values in the catalog extended from Dawson and Chouet [2014] for corresponding events.

method still produces reasonable estimates. $Q$ estimates in our catalog are very slightly lower on average (by $\sim$ 1) than those of matching events in the catalog extended from Dawson and Chouet [2014] (Fig. 3.9). This is consistent with the bias our exponential fitting method exhibits for noisy synthetic signals (section 3.2, Fig. B.12) which we expect is a beneficial trade-off for increased precision and robustness.

Most prominent among the groups of events unique to our catalog is a trend of events with $T$ ranging from 10-20 s between 2010 and 2018 (Fig. 3.9). The Sompi AR method can detect and provide accurate estimates of $T$ for many of these events [Dawson and Chouet, 2014], but often does not produce accurate estimates of $Q$ even with manual examination of the algorithm output. Our methods generally provide accurate estimates of $Q$ for these events, but still exclude many real events in this band when strict enough thresholds are used to minimize bad detections in the catalog as a whole. Our catalog also includes a clear event group with $T$ around 15 s in early 2009, and some other more isolated clusters between 2008 and 2010 (Fig. 3.9). Our catalog shows large scatter in $T$ prior to 2010, but many of these values do likely represent real VLP oscillations. Both catalogs show multiple isolated events after 2012 with $T$ from $\sim$10-15 and $\sim$20-35 s. Most of these detections in our catalog are gliding-frequency VLP events. Some in the catalog extended from Dawson and Chouet [2014] are also gliding-frequency VLP events, whereas others do not appear to be coherent VLP oscillations.

In summary, both detection methods produce incomplete catalogs, particularly for the secondary group of events with 10-20 s periods, and both involve trade-offs between missing real events and including too many bad

detections. The two catalogs contain many nonoverlapping events, so to obtain a maximally complete catalog there would be value in combining both detection methods. However, since our detection method does not require labeled training data and has demonstrated performance that is comparable overall and better in some respects than existing approaches for detecting resonant VLP seismicity, we expect it could be a useful tool in various volcanic settings.

*Characterizing ground motion patterns*

Our goal in this study is not to conduct detailed source inversions for every event, but rather to quantitatively characterize when changes in ground motion patterns occur. To do this we consider several metrics as well as inversions with a point source model. For all of these, we use the average phases and amplitudes at each channel calculated using the Goertzel DFT algorithm [Proakis and Monolakis, 1990] over a time window between one and five cycles after each event onset.

The first metric is average vertical/horizontal velocity ratio $R_{vh}$, defined for the target frequency component $f$ as

$$R_{vh} = \sum_{m=1}^{M} \frac{|\dot{\mathbf{u}}_{Z,m}(f)|}{|\dot{\mathbf{u}}_{E,m}(f) + \dot{\mathbf{u}}_{N,m}(f)|}, \tag{3.2.5}$$

for vertical ($Z$), east ($E$), and north ($N$) velocities ($\dot{\mathbf{u}}$) at all $M$ stations. This metric requires no assumptions of source location or mechanics, but it is sensitive to tilt which will increase the apparent amplitude of horizontal components at increasing $T$. The second metric, termed radial misfit, quantifies how radially oriented horizontal motion vectors are from the direction to an inferred source location. This is similar to 'semblance' [e.g., Legrand et al., 2000]. We set the

inferred source location based on previous geodetic (InSAR, GPS, and tilt) inversions for the shallow ground deflation source in early 2018 [Anderson et al., 2019] (Fig. 3.3). We note that this is similar to the centroid location inferred by other seismic and geodetic inversions over the past decade [Chouet et al., 2010, Chouet and Dawson, 2011, Anderson et al., 2015, Anderson and Poland, 2016, Liang et al., 2020a]. We then calculate radial misfit $E_{radial}$ as the mean angle between the target frequency component of observed $\dot{\mathbf{u}}$ and predicted $\dot{\mathbf{w}}$ (perfectly radial) velocity vectors,

$$E_{radial} = \frac{1}{MT} \sum_{m=1}^{M} \int_0^T \left| \arccos \left( \frac{\dot{\mathbf{u}}(t) \cdot \dot{\mathbf{w}}(t)}{|\dot{\mathbf{u}}(t)||\dot{\mathbf{w}}(t)|} \right) \right| dt. \tag{3.2.6}$$

For source inversions, we use the 'Mogi' point source approximation for an inflating/deflating spherical reservoir in an elastic half-space [Mogi, 1958]. The quasi-static elasticity used in the Mogi model should be approximately valid for the long period signals and short distances considered here (see section 3.2). Due to their simplicity, these inversions are most useful as an indicator of relative changes in source centroid depth and the radial symmetry of ground motions, rather than as a probe of detailed reservoir geometry. For example, changes in Mogi centroid depth could represent changes in the vertical extent of an ellipsoidal reservoir, and/or changes in the geometry or activation of any secondary dikes or sills that may also be contributing to the ground motions.

We fix the east and north source location based on previous geodetic inversions in Anderson et al. [2019] (Fig. 3.3). This both simplifies the interpretation of inversion results and reduces noise-induced scatter. We assume a shear modulus of 3 GPa and Poisson's ratio of 0.25. We include ground tilt

(detected as horizontal acceleration by broadband seismometers) in the Green's functions [Maeda et al., 2011] to predict displacements $\mathbf{w}$ as

$$\mathbf{w}(f) = \left( \mathbf{G}_t + \mathbf{G}_r \frac{g}{(2\pi i f)^2} \right) P(f), \tag{3.2.7}$$

where $\mathbf{G}_t$ and $\mathbf{G}_r$ are the translation and tilt Green's function matrices, $g$ is gravitational acceleration, and $P$ is forcing pressure. We solve for the $P$ that results in minimal misfit between $\mathbf{w}$ and observed displacements $\mathbf{u}$ for given Green's functions using a linear least-squares inversion. We then conduct a grid search to find the Mogi source depth that minimizes misfit $E$ between the target frequency component of $\mathbf{w}$ and $\mathbf{u}$ according to

$$E = \frac{\sum_{n=1}^{N} |\mathbf{u}_n(f) - \mathbf{w}_n(f)|}{\sum_{n=1}^{N} |\mathbf{u}_n(f)|}, \tag{3.2.8}$$

for all $N$ channels, with source depth bounded between 500 m and 2500 m beneath the caldera floor. We additionally conduct a set of moment tensor inversions with a fixed depth for comparison.

*Other geophysical data and observations*

To interpret the timeline of VLP seismicity cataloged in this work, we rely on a series of touchstone events that characterize the progression of the 2008-2018 Kīlauea eruptive episode. ERZ eruptions prior to 2018 have been compiled in Patrick et al. [2019b]: the March 2011 Kamoamoa fissure eruption [Orr et al., 2015], August 2011 Pu‘u ‘Ō‘ō vent opening, September 2011 Pu‘u ‘Ō‘ō vent opening, June 2014 Pu‘u ‘Ō‘ō vent opening [Poland et al., 2016], and May 2016 Episode 61g Pu‘u ‘Ō‘ō vent opening [Chevrel et al., 2018]. Timing of the 2018

eruption is given in Neal et al. [2019]. Documented summit intrusions have been compiled in Patrick et al. [2019b]: October 2012, May 2014, and May 2015 [Johanson et al., 2016]. Regional slow-slip events (SSEs) have been compiled in Montgomery-brown et al. [2015] and Wang et al. [2019]: February 2010, May 2012, and October 2015.

To indicate long-term ground deformation we use near-field (within ∼2 km of the vent) geodetic data: vertical displacements from GPS station HOVL, horizontal line-lengths between GPS stations UWEV and CRIM, and east and north tilt from tilt-meter UWE [Miklius, 2008, Johanson, 2020] (Fig. 3.3). We also use smoothed stacks of these four datasets to infer times of long-term inflation and deflation and provide additional visual reference points on figures. We smooth all four datasets with 30-day moving average filters and scale them to have a unit range. We then flip the sign of UWE east tilt-meter data so that increasing values indicate inflation, and then stack the four datasets. We consider any time when the stacked geodetic data is increasing to indicate long-term inflation. We note that the 30-day period was chosen purely to facilitate visualization, and that at many times there is significant inflation/deflation on shorter timescales including "DI" events [e.g., Anderson et al., 2015].

We use lava lake elevation and surface area data from Patrick et al. [2019b] (data extended through 2018 was obtained from the USGS HVO via Matt Patrick). This data is obtained from a combination of webcam images, thermal images, and laser rangefinders. $SO_2$ gas flux data from various monitoring stations for the whole timespan does exist [Whitty et al., 2020], but we only consider data from published studies using direct measurements of the summit plume. We use $SO_2$ emission data collected by a vehicle-based FLYSPEC UV spectrometer from

2007-2010 [Elias and Sutton, 2012]. We also use $SO_2$ emission data collected by an array of FLYSPEC UV spectrometers from 2014-2017 [Elias et al., 2018]. Both datasets have large uncertainties (Fig. 3.10, 3.11) due to spectral fitting limitations and uncertainty in plume speed and location [Elias and Sutton, 2012, Elias et al., 2018].

## Results

### *Types of VLP seismicity at Kīlauea from 2008-2018*

Conduit-reservoir resonance

The first category of signals we term 'conduit-reservoir oscillations'. These constitute the main trend of VLPs starting at $T$ ∼20 s in 2010, increasing to ∼40 s in early 2011, and fluctuating between 35-43 s from 2012 until the caldera collapse onset in May 2018 (Fig. 3.10, 3.11). Some other events prior to 2010 and during the series of lava lake draining events in 2011 may also fit into this category. The conduit-reservoir oscillation is the fundamental resonant eigenmode of the coupled conduit and shallow magma reservoir system, in which the magma column in the conduit and lava lake oscillates vertically and pushes magma in and out of the underlying reservoir [Chouet and Dawson, 2013, Liang et al., 2020a]. Other resonances such as from Krauklis (crack) waves or acoustic waves (organ pipe eigenmodes) are predicted to generally have higher frequencies and lower amplitudes [Karlstrom and Dunham, 2016, Liang et al., 2020b]. Restoring forces for the conduit-reservoir oscillation come from magma reservoir compressibility (combined wall rock elasticity and multiphase magma compressibility) and gravity/buoyancy, while damping primarily comes from viscous dissipation along

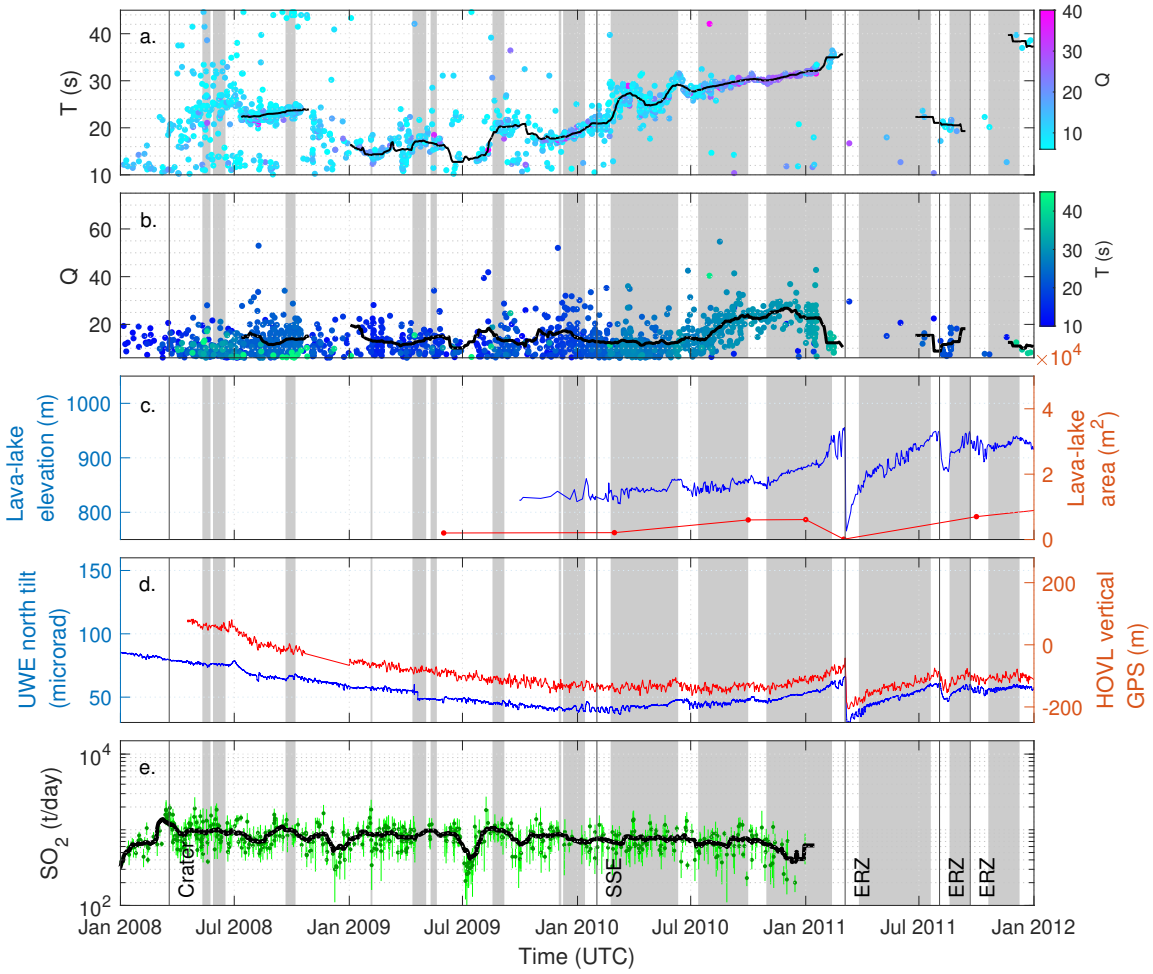


FIGURE 3.10. Section of the VLP catalog from 2008-2011. (a and b) Period and quality factor over time. Black lines show 30-day moving averages over the events we have labeled as potential conduit-reservoir oscillations, neglecting outliers or events from times with no consistent dominant period. (c) Lava lake surface elevation and surface area. (d) UWE north tilt and HOVL vertical GPS. (e) Average daily $SO_2$ (dark green dots) and standard deviations (light green lines). The black line is a 30-day moving average. 'Crater' indicates where the Halema'uma'u crater first formed, 'SSE' indicates slow slip events, 'Int' indicates documented summit intrusions, and 'ERZ' indicates eruptions along the East Rift Zone. Grey bars in all plots indicate times of long-term ground inflation (section 3.2).

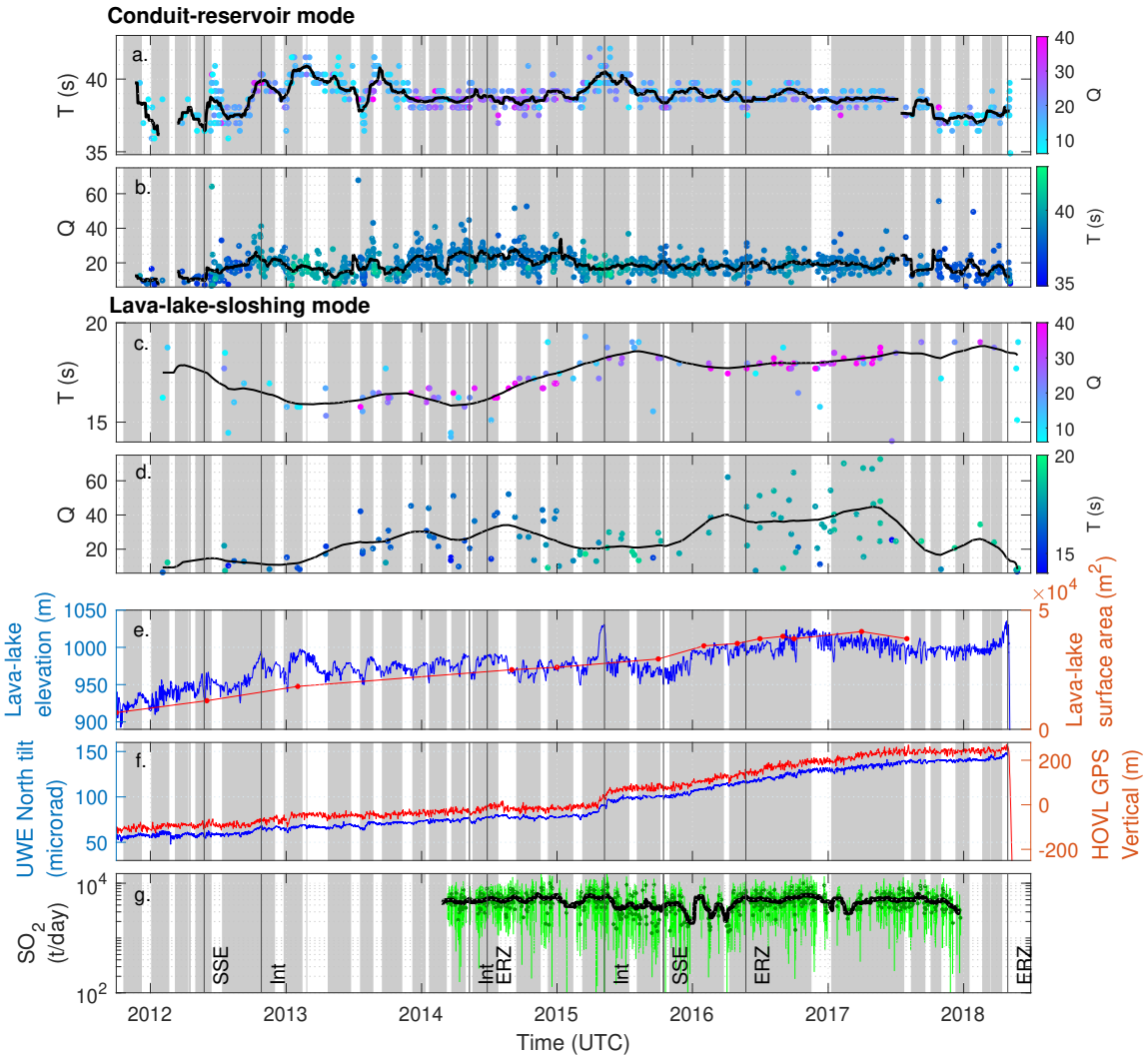


FIGURE 3.11. Section of the VLP catalog highlighting conduit-reservoir and lava lake sloshing resonance from 2012-2018. (a and b) Period and quality factor of conduit-reservoir events over time. Black lines show 30-day moving average. (c and d) Period and quality factor of lava lake sloshing over time. Black lines show 120 day moving average. (e) Lava lake surface elevation and surface area. (f) UWE north tilt and HOVL vertical GPS. (g) Average daily $SO_2$ (dark green dots) and standard deviations (light green lines). The black line is a 30-day moving average. 'SSE' indicates slow slip events, 'Int' indicates documented summit intrusions, and 'ERZ' indicates eruptions along the East Rift Zone. Grey bars in all plots indicate times of long-term ground inflation (section 3.2).

the conduit walls. Ground deformation during these events is primarily from uniform inflation/deflation of the magma reservoir; deformation from the conduit is orders of magnitude smaller by comparison.

Conduit-reservoir oscillations can be triggered/driven by a variety of different mechanisms, producing signals with different onset characteristics. We term conduit-reservoir oscillations with abrupt onsets and inflationary first motions 'Normal'; this category includes rockfall or lava lake surface explosion triggered events and is analogous to 'type 2' events in Dawson and Chouet [2014]. There is often high-frequency or broadband energy present at the onset of Normal events, as well as inflationary steps in tilt data [Chouet and Dawson, 2013, Orr et al., 2013, Dawson and Chouet, 2014] (Fig. 3.12, B.14, B.15). We term conduit reservoir oscillations with abrupt onsets and deflationary first motions 'Reverse'; analogous to 'type 3' events in Dawson and Chouet [2014] (Fig. 3.12). These events often do not have obvious high frequency triggers, and some exhibit deflationary tilt steps. The trigger for Reverse events is not known, but has been proposed to involve impulsive magma movement at depth due to flow transients or fracture/dike opening [Dawson and Chouet, 2014]. Some conduit-reservoir events do not fit very clearly into either category, for example those with gradual onsets or multiple step increases in oscillation amplitude (B.14, B.16).

Our first motion algorithm classifies 77% of conduit-reservoir events after 2012 as Normal, 17% as Reverse, and the remaining 6% as undetermined (Fig. 3.13). Prior to 2012 our classifications are less reliable due to the prevalence of VLP tremor and shorter resonant periods (which makes phase offsets between stations less negligible). The mean and median amplitudes of Normal events are both about twice as large as those of Reverse events, although both types of events

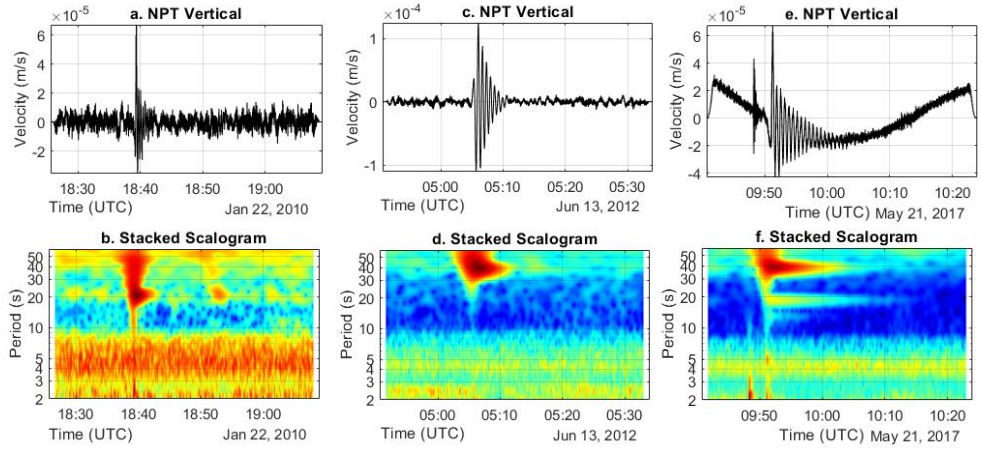


FIGURE 3.12. Example VLP events. (a and b) Normal conduit-reservoir oscillation event along with background VLP periodic tremor from January 2010, when the lava lake became persistent [Patrick et al., 2019b]. The event had an impulsive broadband onset and inflationary first motions, indicative of a rockfall trigger. The background VLP periodic tremor had the same dominant period as the impulsively triggered VLP event, but often unclear onsets and no higher frequency triggers. (c and d) Reverse VLP event from June 2012, shortly after the May 2012 SSE. This event had an impulsive onset but no high frequency trigger. There was a small initial inflationary motion but the first large oscillation was deflationary. (e and f) Normal conduit-reservoir event with two lava lake sloshing events from May 2017. A higher frequency impulsive signal occurred about 2 minutes before these events that may have been related to their triggering.

exhibit variation in amplitude over orders of magnitude (Fig. B.17). We do not find any appreciable differences in distributions of $T$ or $Q$ between Normal and Reverse events, though we do find that more of both events occur during times of deflation/lava lake draining (Fig. B.17). The percentages vary slightly depending upon whether raw or smoothed data from lava lake elevation or tilt is used, but about 60% of events occur during deflation/lava lake draining, despite deflation representing only about 35% of the total timespan.

Normal events might occur more frequently during deflation because rockfall is preferentially induced by the accompanying changes in the stress state along the crater walls, or because more of the crater walls are exposed as lava lake level drops, particularly if these portions of the crater walls have destabilized by recent contact with the lava lake. Any hypothesis about why Reverse events occur preferentially during deflation will be more speculative since the triggering mechanism is not known, although this observation could help inform potential trigger mechanisms. One possibility is that the patterns of magma flow occurring during deflation facilitate the buildup and/or impulsive release of bubble slugs at some depth in the magma system. Another is that the hydraulic pressure gradients and/or rock stress during inflation allow more steady flow through some constriction point in the shallow magma system, which becomes more constricted and causes intermittent flow during deflation.

Lava lake sloshing

The second category of signals we term 'lava lake sloshing'. These have $T$ of 10-20 s and are recognizable from 2010-2018 in our catalog (Fig. 3.10, 3.11). Inversions of select lava lake sloshing events by Liang and Dunham [2020] supports

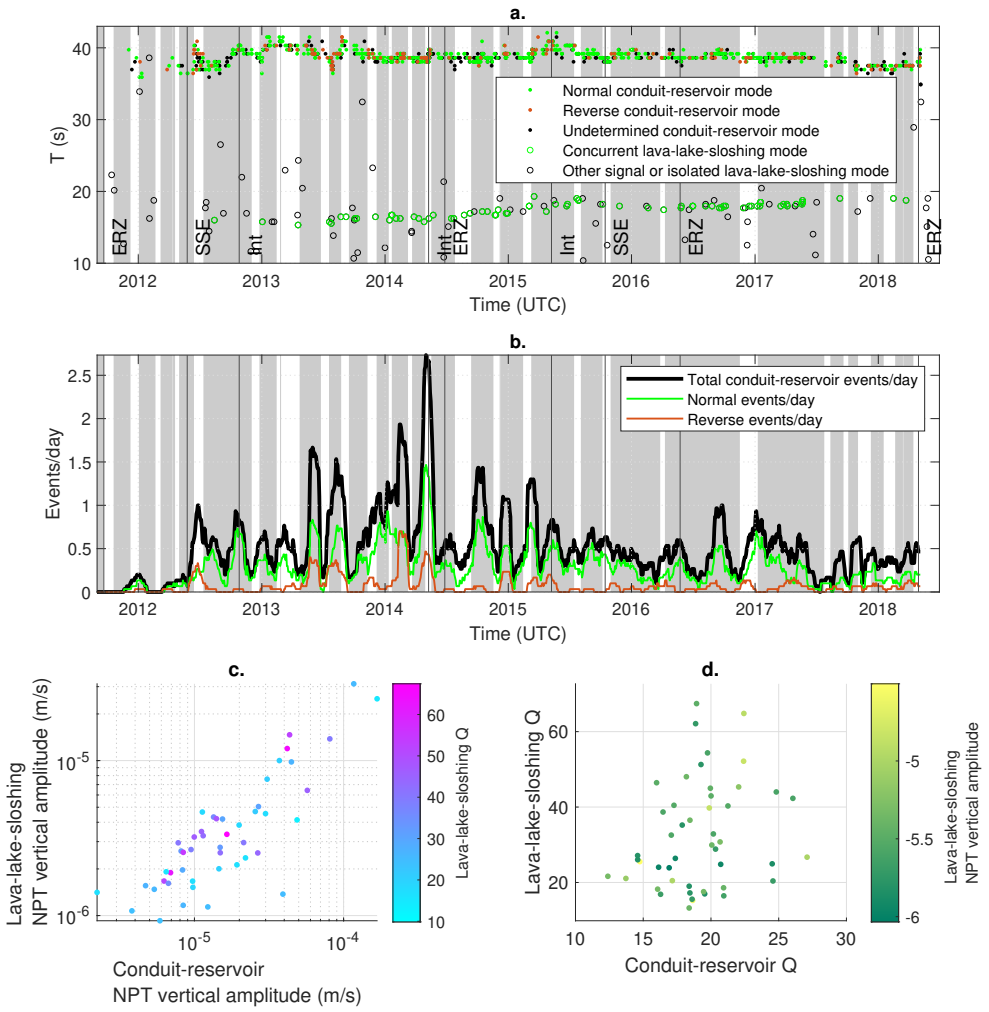


FIGURE 3.13. (a) Onset polarity (Normal or Reverse) of conduit-reservoir oscillations and lava lake sloshing that occurred alongside a detected conduit-reservoir event. (b) Conduit-reservoir event density calculated over 30-day windows. We note that event density will vary by orders-of-magnitude depending upon the event detection thresholds used (section 3.2), so is most useful for comparing relative event densities through time. 'Crater' indicates where the Halema'uma'u crater first formed, 'SSE' indicates slow slip events, 'Int' indicates documented summit intrusions, and 'ERZ' indicates eruptions along the East Rift Zone. Grey bars in plots a and b indicate times of long-term ground inflation (section 3.2). (c) amplitudes (from vertical velocity at station NPT) of conduit-reservoir oscillations vs corresponding lava lake sloshing. (d) Quality factor of conduit-reservoir oscillations vs corresponding lava lake sloshing.

suggestions by Dawson and Chouet [2014] that they are likely caused by lateral surface gravity wave resonance in the lava lake (i.e., 'sloshing'). The sloshing could also induce pressure perturbations at the top of the conduit, causing a forced oscillation of the conduit-reservoir system. Ground motions could thus be from a combination of pressure against the lava lake walls and reservoir inflation/deflation. There are some times where two distinct lava lake sloshing signals occur with slightly different periods (Fig. 3.12, B.14), likely representing sloshing along different axes of the lava lake [Dawson and Chouet, 2014, Liang and Dunham, 2020]. These are not very prevalent in our catalog at the thresholds shown, which may be partly because often one of the two signals will be too close in period to a larger lava lake sloshing signal or have too low of a signal/noise ratio to be included.

Around 75% of lava lake sloshing events in our catalog appear alongside Normal conduit-reservoir oscillations; the rest appear in isolation (Fig. 3.12, 3.13, B.14, B.18). That none appeared alongside Reverse oscillations is consistent with the idea that Reverse oscillations are triggered from depth [Dawson and Chouet, 2014] and so the lava lake is not directly perturbed. It also indicates that the magma flowing in/out of the top of the conduit during Reverse conduit-reservoir oscillations does not induce appreciable lava lake sloshing, which could be due to the small volumes of magma involved and/or to the top of the conduit not being laterally offset from the center of the lava lake.

Other VLP seismicity

We will use the term 'periodic tremor' to refer to signals with clearly elevated energy in one or more relatively focused periods, but that are not obviously

isolated in time and lack clear onsets and/or exponential decays. Our method will not return detections if the periodic tremor amplitude is constant, but where the amplitude is variable our method will consider any local amplitude maxima above the set detection thresholds. For such local maxima, the apparent decay rate could be controlled by the forcing time-function rather than the inherent damping of the resonator. Estimates of $Q$ returned by our method might thus not reflect the same physical properties as for impulsively triggered resonance. Periodic tremor occurs throughout the study timespan (Fig. 3.12, B.19, B.20, B.21, B.22, B.23, B.24), often with the same dominant periods as impulsively triggered conduit-reservoir or lava lake sloshing oscillations. We thus hypothesize that the periodic tremor often represents these same resonant mechanisms with continuous rather than discrete forcing.

Our catalog includes some VLP oscillations that exhibit gliding-frequencies over the duration of a single event (Fig. B.25, B.26). These constitute many of the events in our catalog with outlier values of $T$ (Fig. 3.9) and are more prevalent when a higher phase deviation threshold is used. The values of $T$ and $Q$ returned by our methods will not be representative of the whole signals, but visual inspection reveals that gliding-frequency VLP oscillations are present at various times throughout the studied timespan and with various starting and ending periods and durations. Gliding-frequencies have been previously identified in tremor at Kīlauea, but at much higher frequencies (0.6-6 Hz) and with gliding occurring over hours-days [Unglert and Jellinek, 2015]. In some cases, the gliding-frequency VLP oscillations appear to start or end at similar periods to non-gliding conduit-reservoir or lava lake sloshing oscillations, indicating that at least some of them may be related to these other oscillations. Some may represent rising

bubble slugs, which could create a varying oscillation period during ascent and then possibly trigger standard decaying conduit-reservoir resonance after bursting at the surface [e.g., James et al., 2008, Chouet et al., 2010]. Alternately, some may represent examples of either conduit-reservoir or lava lake sloshing resonances where magma properties change over the course of the resonance. This could occur if the perturbation that induces resonance destabilizes some aspect of the shallow magma system, such as by causing collapse of a foam layer in the lava lake or upward movement of a bubble slug or bubble cloud.

### *Correlations among datasets*

Here we analyze correlations between the various geophysical datasets, conduit-reservoir oscillation properties, and lava lake sloshing properties. Fig. 3.14 shows correlations over the 2008-2018 timespan (see Fig. B.27 for just the 2012-2018 timespan). When looking over such long timescales, only a few strong correlations are apparent. Fig. 3.15 shows moving 90-day correlations, which reveals more correlations between datasets but that these correlations change over time.

#### Ground deformation and lava lake elevation correlation

Ground surface deformation data from near field tilt-meters and GPS stations indicates the rate of ground inflation/deflation of the Kīlauea summit region. This primarily reflects pressure in the shallow summit reservoir, but may also be influenced by pressure in the proposed deeper south caldera reservoir or motion of the south flank [e.g., Owen et al., 2000, Baker and Amelung, 2012, Anderson et al., 2015]. Lava lake elevation has previously been shown to be

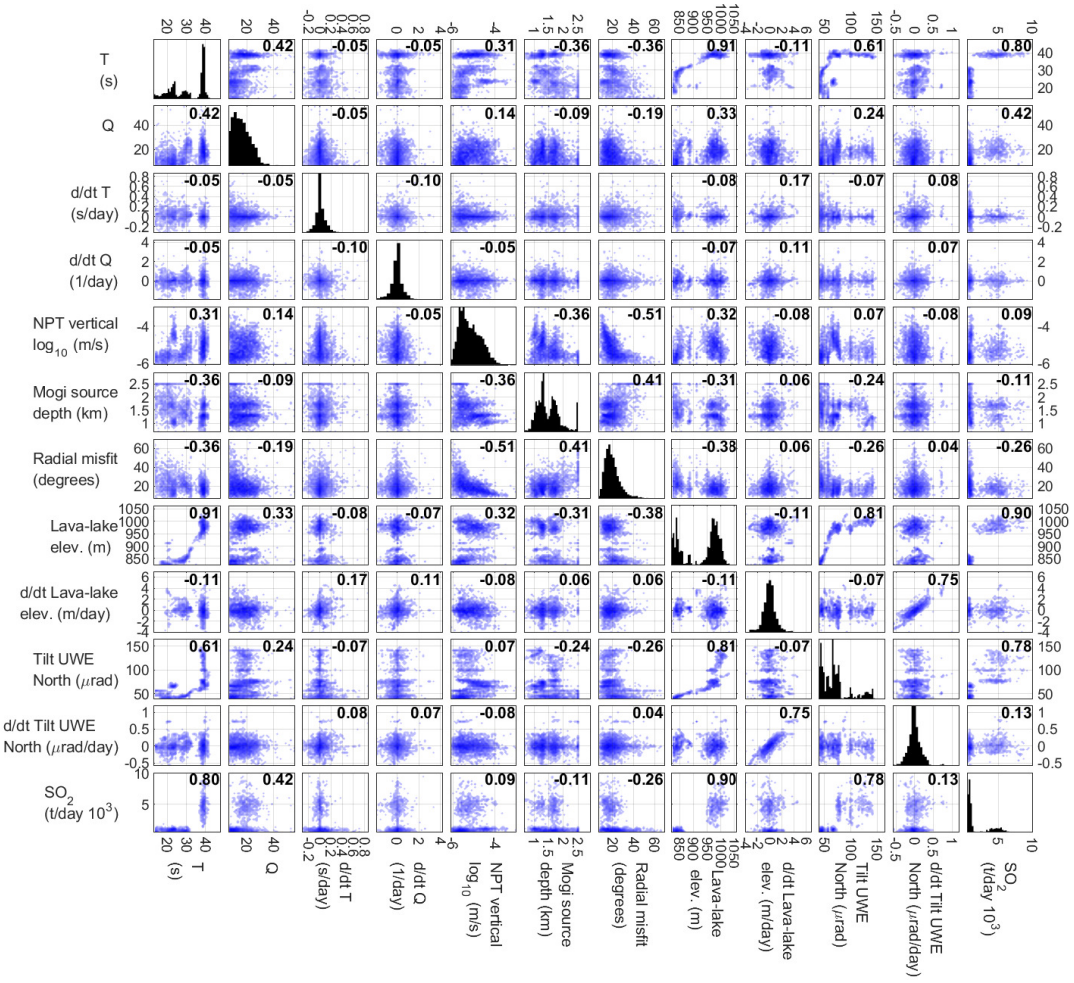


FIGURE 3.14. Conduit-reservoir oscillation correlation matrices from 2008-2018 (see Fig. B.27 for just the 2012-2018 timespan). Off-diagonal plots are shaded by the logarithm of the number of points in each parameter bin, and histograms on diagonal plots show the distribution of each parameter. Numbers are Pearson's correlation coefficients, only shown for correlations with P-values less than 0.05. All time derivatives, indicated by 'd/dt', were calculated with a 7-day cutoff-period differentiator filter.

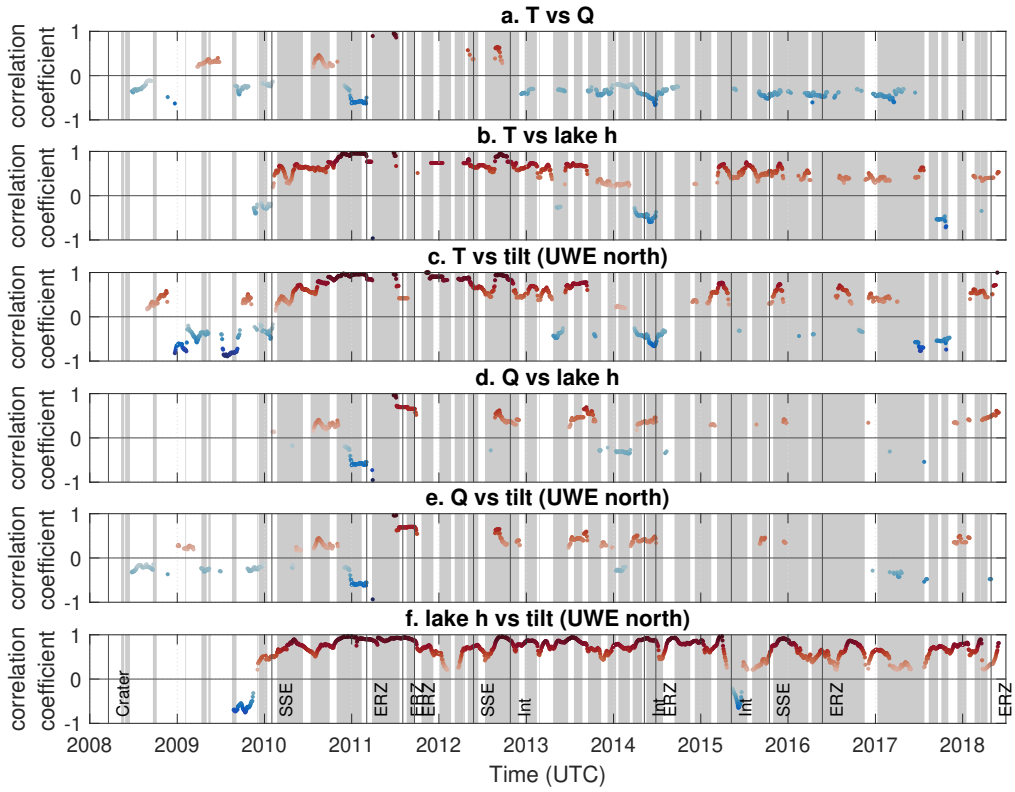


FIGURE 3.15. Conduit-reservoir oscillation Pearson's correlation coefficients calculated over moving 90-day windows. Windows with p-values greater than 0.05 were excluded. Red and blue highlight positive and negative correlations, respectively. 'SSE' indicates slow slip events, 'Int' indicates documented summit intrusions, and 'ERZ' indicates eruptions along the East Rift Zone. Grey bars in the all plots indicate times of long-term ground inflation (section 3.2).

correlated with ground inflation on timescales of hours or more, including during so-called deflation-inflation events, though not during some shorter-duration fluctuations in lava lake elevation related to gas-pistoning [e.g., Patrick et al., 2015, Anderson et al., 2015, Patrick et al., 2016b, 2019b]. This correlation is present over most of the 2008-2018 timespan, with a 0.8 overall correlation coefficient (Fig. 3.14, 3.15, B.27). The correlation implies that lava lake elevation is analogous to a pitot tube for the summit magma reservoir and responds proportionally to changes in reservoir pressure.

However, this relation is not constant as evidenced by both the nonlinear relationship between lava lake elevation and tilt (Fig. 3.14) and the variation in local correlation coefficients from almost 1 to negative values (Fig. 3.15). This indicates that the pitot tube relation between ground inflation and lava lake elevation changes over time. We believe that these deviations reflect a superposition of processes on different characteristic timescales. For example, in early 2017 ground inflation and lava lake elevation are positively correlated on timescales of days to months, but there is a long-term ground inflation trend despite average lava lake elevation remaining constant (Fig. 3.11). There are also abrupt events that change the relation between ground inflation and lava lake elevation, such as the May 2015 intrusion (Fig. 3.11).

Conduit-reservoir resonance correlations

During most of the timespan conduit-reservoir oscillation $T$ and $Q$ exhibit a weak negative correlation, with an overall correlation coefficient of -0.06 but local correlation coefficients often around -0.7 (Fig. 3.14, 3.15, B.27). There are isolated times where $T$ and $Q$ are positively correlated, such as in mid-2010 (correlation

coefficient near 1) and mid-2012 (correlation coefficient around 0.7) (Fig. 3.10, 3.11, 3.15).

Conduit-reservoir oscillation $T$ is positively correlated with lava lake elevation during most of the timespan, with correlation coefficients mostly between 0.3 and 1 (Fig. 3.15), and a weak overall correlation coefficient of 0.11 (Fig. 3.14, B.27). However, there are times with negative local correlations, such as around the 2014 Pu‘u ‘Ō‘ō eruption (correlation coefficient around -0.6), and in late 2017 (correlation coefficient around -0.7). The correlation between $T$ and ground inflation (i.e., tilt) exhibits a similar trend to the correlation between $T$ and lava lake elevation after the arrival of a persistent lava lake in late 2009, and exhibits a variable but mostly negative trend prior to this (Fig. 3.14, 3.15, B.27). Conduit-reservoir $T$ is positively correlated with event amplitude, even when considering only vertical velocity that should not be sensitive to instrument tilt (Fig. 3.14, B.27).

Conduit-reservoir oscillation $Q$ exhibits much less consistent correlations with ground inflation and/or lava lake elevation than $T$ does (Fig. 3.14, 3.15, B.27). Throughout much of the studied timeline, there is no significant correlation between $Q$ and either dataset. There are several isolated time-segments such as June-September 2011 where $Q$ is positively correlated with ground inflation and lava lake elevation, and one time-segment from December 2010 to March 2011 with a significant negative correlation (Fig. 3.15).

We find increases in both conduit-reservoir event density and $T$ around the inferred October 2012 and May 2015 intrusions. There is no obvious change in $Q$ corresponding to either intrusion, though the correlation between $T$ and $Q$ does change from positive to negative at the October 2012 intrusion (Fig. 3.9, 3.15).

Perhaps surprisingly, neither intrusion appears to correspond to changes in ground motion patterns (Fig. 3.16).

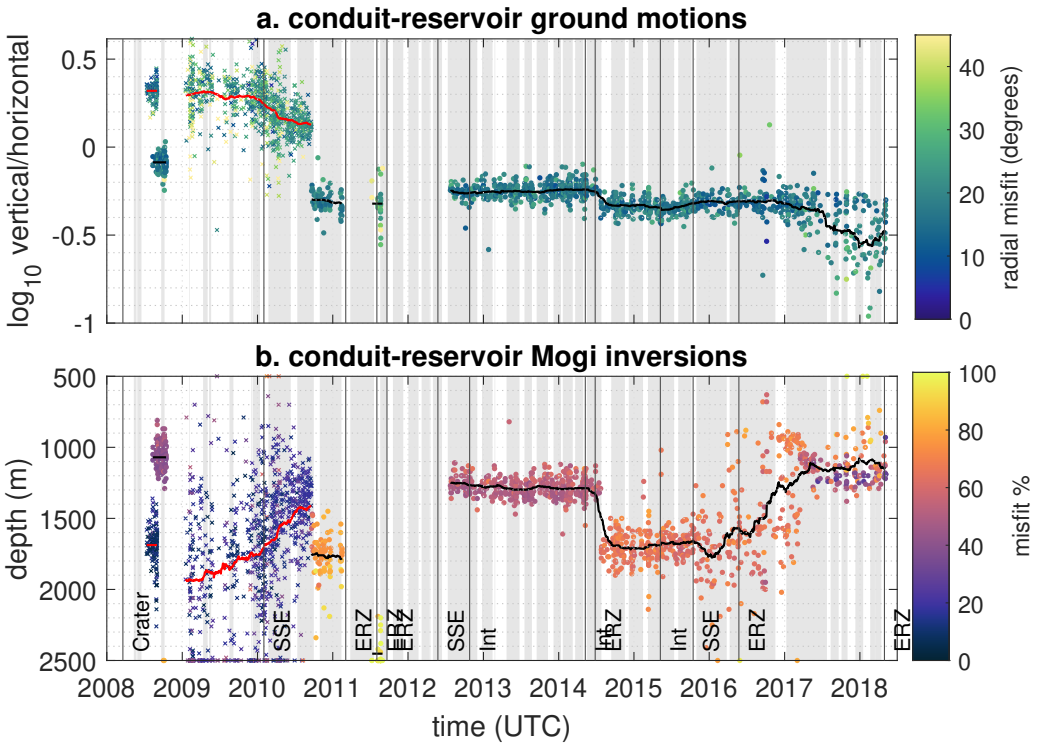


FIGURE 3.16. Characterization of conduit-reservoir oscillation ground motions. (a) Vertical/horizontal velocity ratio. Colored circles and black lines indicate events and 120-day moving averages for times with more than 6 stations available. Colored crosses and red lines indicate events and 120-day moving averages for times with only one station available (so poorly resolved ground motions). (b) Inverted Mogi spherical reservoir source depths relative to the caldera floor (∼1100 m ASL). Depths are relative to the caldera floor. 'Crater' indicates where the Halema'uma'u crater first formed, 'SSE' indicates slow slip events, 'Int' indicates documented summit intrusions, and 'ERZ' indicates eruptions along the East Rift Zone. Grey bars in all plots indicate times of long-term ground inflation (section 3.2).

ERZ eruptions for which we detect conduit-reservoir oscillations both before and after the events, i.e., the June 2014 and May 2016 Pu'u 'Ō'ō eruptions, do not clearly relate to changes in conduit-reservoir oscillation $T$ or $Q$. However,

sharp changes in the correlations between $T$ and $Q$, $T$ and lava lake elevation/tilt, and $Q$ and lava lake elevation/tilt occur alongside the June 2014 eruption, and more subtle changes in these correlations may also be present alongside the May 2016 eruption (Fig. 3.9, 3.15). Interestingly, there are changes in ground motion patterns following both eruptions that are apparent in the time series of Mogi source inversions and vertical/horizontal velocity ratios (Fig. 3.16).

Lava lake sloshing correlations

Due to the sparsity of well-characterized lava lake sloshing events, it is difficult to robustly examine correlations with other other datasets on timescales of months or less. Long-term average lava lake sloshing $T$ increased over most of the timespan, except for during 2012 (when lava lake sloshing events were sparse and exhibited large scatter in $T$) and a clear decrease during late 2015. The long-term increase in $T$ roughly corresponds to an observed long-term increase in lava lake surface area, and the decrease in lake 2015 roughly corresponds to a several month long decrease in average lava lake elevation. Lava lake sloshing $Q$ exhibits large scatter over most of the timespan, with the exception of during 2012 when $Q$ was generally less than 20, and during 2015 when $Q$ was generally between 10 and 30. There is a roughly linear relation between conduit-reservoir oscillation amplitude and lava lake sloshing amplitude, although with an appreciable amount of scatter (Fig. 3.13). Lava lake sloshing $Q$ does not appear to be correlated with conduit-reservoir oscillation $Q$ (Fig. 3.13), which suggests that damping mechanisms of the two resonant modes vary independently. This in turn implies that fluid motions on timescales of the lake sloshing VLP mode ($\sim$ 10s timescales) are somewhat mechanically decoupled.

## Discussion

Our new catalog of VLP seismic events provides an outstanding tool to document the progression of a long-lived (10 year) open vent eruptive episode at Kīlauea Volcano and probe shallow magma plumbing system geometry and magma properties through time. In the following discussion, we highlight how simple physical models for the resonant oscillations identified in Kīlauea seismic data may be used to understand some of the trends observed in the 2008-2018 eruptive sequence. We also identify observations that are not well explained by current models and that point to next steps for understanding VLP seismicity at Kīlauea. We focus on interpretion of the 2008-2018 timeline of VLP seismicity in the context of other available datasets and observations, leaving rigorous inversions of these events over the eruptive episode to future work.

### *Interpreting changes in conduit-reservoir resonance*

The conduit-reservoir oscillator model of Liang et al. [2020b], which extends earlier work by [Chouet and Dawson, 2013], provides estimates of $T$ and $Q$ in response to small amplitude perturbations such those that trigger VLP seismicity. This model assumes a cylindrical conduit and isothermal conditions, and neglects inertia and viscous drag in the overlying lava lake and compressibility of magma in the conduit. It parameterizes background variations in magma bulk density, such as might arise from slow convective exchange flow [e.g., Fowler and Robinson, 2018], and neglects non-Newtonian rheology associated with bubbles and crystals as well as possible conduit geometry variations. This model is thus of limited use in teasing apart the details of observed correlations between geophysical datasets assembled here. However, it is still a useful tool for understanding parameter trade

offs that lead to some of the first order variations in VLP characteristics observed over the 2008-2018 timeline.

The inviscid conduit-reservoir resonance period from Liang et al. [2020b] is

$$T_0 = 2\pi\sqrt{\frac{L_c\bar{\rho}_c}{\Delta\rho_c g\sin\alpha + A_c C_t^{-1}}}, \tag{3.4.9}$$

where $L_c$ is conduit length, $\bar{\rho}_c$ is average magma density in the conduit, $\Delta\rho_c$ is density difference between the bottom and top of the conduit, $\alpha$ is conduit dip angle, $A_c$ is conduit cross-sectional area, and $C_t$ is total reservoir storativity (from both magma compressibility and elastic reservoir stiffness). Viscous damping is governed by a momentum diffusion timescale

$$\tau_{visc} = \frac{R_c^2\bar{\rho}_c}{\mu_c}, \tag{3.4.10}$$

where $R_c$ is conduit radius and $\mu_c$ is average magma viscosity. Liang et al. [2020b] then use numerical methods used to solve for $T$ and $Q$. Decreasing $\tau_{visc}$ results in increased viscous damping, which decreases $Q$ and increases $T$. Figure 3.17 shows the effect of various parameters on this model.

Liang et al. [2020a] conducted stochastic inversions for 4 events from 2008-2013, and favor a geometry consisting of a spherical reservoir with a centroid $\sim$1.4 km beneath the vent and a radius of $\sim$1 km, resulting in a conduit length of a few hundred meters. In this regime, $T$ and $Q$ are controlled by conduit geometry and magma properties in the conduit and have minimal sensitivity to reservoir compressibility (Fig. 3.17). However, the inversions show that there are many trade-offs that make uniquely constraining model parameters for a given event difficult without additional constraints. Fig. 3.17 illustrates this problem:

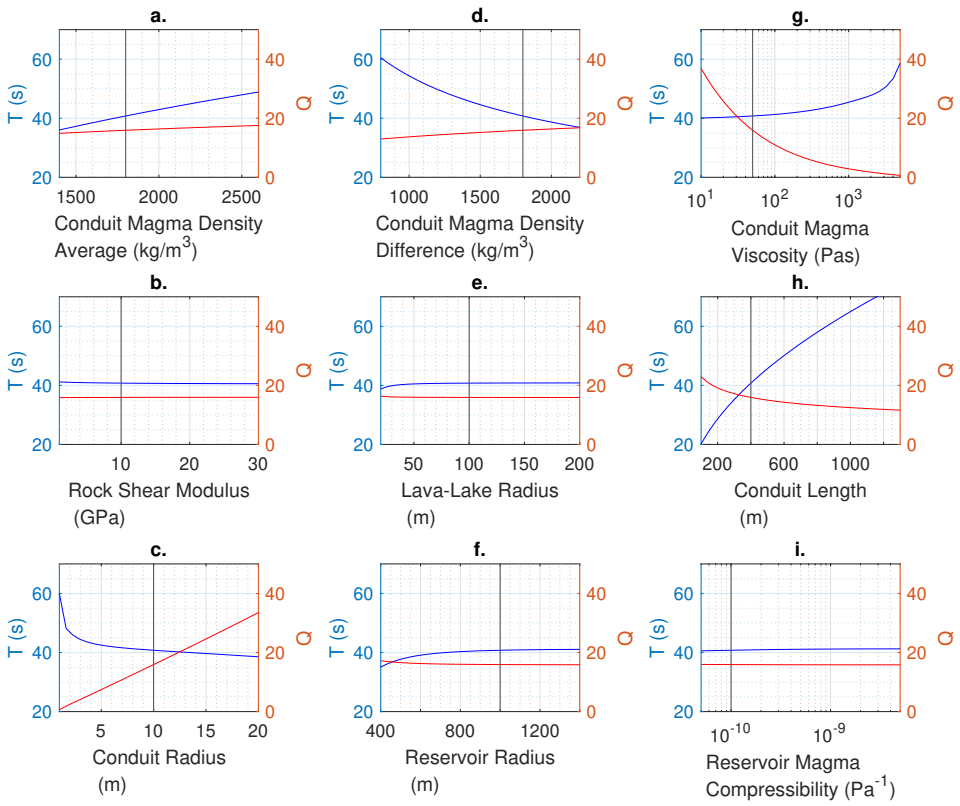


FIGURE 3.17. (a-i) Predicted variation in $T$ and $Q$ due to varying each model parameter in isolation in the conduit-reservoir resonance model of Liang et al. [2020b] (Eq. 3.4.9-3.4.10), assuming a spherical reservoir geometry. Black lines indicate the default value used for each parameter.

$T$ and $Q$ vary with multiple unknown parameters that likely covary in different ways and on differing timescales. The inversions do show probable differences in both magma properties (density, density contrast, and viscosity) and in magma system geometry (conduit length and radius) between the four events selected, although there is significant overlap of the probability density functions for these parameters.

Robustly constraining the Kīlauea shallow magma reservoir geometry at a given time is difficult, as indicated by the scatter in even the simple metrics shown in Fig. 3.16 and by the uncertainty and/or differing results obtained in previous seismic and geodetic inversions. Some previous seismic studies have inferred a source consisting of intersecting dikes [Chouet and Dawson, 2011, 2013], and multiple previous seismic and geodetic studies have supported a spherical or ellipsoidal reservoir geometry [Baker and Amelung, 2012, Anderson et al., 2015, Anderson and Poland, 2016, Liang et al., 2020a, Anderson et al., 2019]. We have not shown source models such as dikes or ellipsoids, since inversions with these more complex source models for single frequency components of these VLP events are often not well constrained [Crozier et al., 2018a].

Variation in magma properties over short timescales

If we focus on short timescales (hours-months), then it is probably reasonable to assume that the geometry of the system remains relatively constant, except at the few isolated times where abrupt changes in ground motion patterns occur (Fig. 3.16). Variation in $T$ and $Q$ on these short timescales is thus most likely related to changes in magma properties. Figure 3.17 shows that of these magma properties, $T$ is most sensitive to average magma density and magma density difference.

Assuming reasonable values for other model parameters based off the inversions of Liang et al. [2020a], variation in either density parameter of ∼500 kg/m$^3$ would be required to explain the observed month-scale variability in $T$ of up to ∼6 s (e.g., July-September 2013, Fig. 3.11). Similarly, the day-scale variability in $T$ of up to ∼3 s would require changes in either density parameter of ∼250 kg/m$^3$. $Q$ is most sensitive to magma viscosity (Fig. 3.17). Variation in magma viscosity of up to an order of magnitude would be required to explain the observed day-month timescale variability in $Q$ of up to a factor of four (e.g., Feb-April 2014, Fig. 3.11).

At many times there is a negative correlation between $T$ and $Q$ (Fig. 3.15). This could be produced by either isolated changes in magma density difference, magma viscosity, conduit radius, or conduit length, or by changes in various combinations of parameters (Fig. 3.17). There are also times where $T$ and $Q$ are positively correlated (Fig. 3.15). Conduit average magma density is the only parameter that could produce this in isolation. However, since the effect of average magma density on $Q$ is very minor, the positive correlations more likely indicate changes in some parameter combinations.

Variation in magma density in the Kīlauea shallow magma system primarily reflects changes in porosity, which is controlled by volatile contents, pressure, and temperature. In general, high porosity deeper in the conduit requires a large amount of total volatiles since both volatile solubility and gas density increase with increasing pressure [e.g., Gonnermann and Manga, 2007, Iacono-Marziano et al., 2012]. We show magma density as a function of volatile contents and pressure in Fig. 3.18 plot j. These densities are calculated using the average Kīlauea glass composition from Edmonds et al. [2013] and the $H_2O$-$CO_2$ solubility model of Iacono-Marziano et al. [2012]. At 1 MPa (∼50-100 m deep) the required

500 kg/m$^3$ change in density could arise from a two-fold increase in $H_2O$ or $CO_2$, while at 10 MPa (∼500-1000 m deep) this change would require a four-fold or more increase in $H_2O$ or $CO_2$. Estimates of primitive (or 'parent') magma volatile contents are variable from 0.5-1 wt% $CO_2$, 0.4-0.7 wt% $H_2O$, and up to 0.18 wt% sulfur [Edmonds et al., 2015]. However, different amounts of volatiles may be present at a given depth due to disequilibrium degassing (e.g., volatile accumulation or depletion due to gas fluxing and/or magma convection) since $CO_2$ begins exsolving well beneath the shallow reservoir and $H_2O$ and sulfur will generally begin exsolving around the shallow reservoir or conduit [e.g., Iacono-Marziano et al., 2012, Edmonds et al., 2015].

Variation in apparent magma viscosity (melt + bubbles) could be due to changing porosity (the effects of which depend upon the flow regime), dissolved $H_2O$ concentration, melt temperature, and crystal contents [e.g., Llewellin and Manga, 2005, Giordano et al., 2008, Mader et al., 2013]. We show how the apparent magma viscosity $\mu$ might vary in response to temperatures and porosity in Fig. 3.18 plot k. We calculate melt viscosity $\mu_l$ from the model of Giordano et al. [2008] using the average Kīlauea glass composition from Edmonds et al. [2013], then apply the low capillary-number model from Llewellin and Manga [2005] to account for porosity $\phi$ as

$$\mu = (1 - \phi)^{-1}\mu_l. \tag{3.4.11}$$

Porosity alone will generally only change viscosity by up to a factor of three, so the required order of magnitude changes likely also involve changes in temperature on the order of 100 C or significant changes in crystal contents [e.g., Mader et al., 2013].

Changes in convective regimes could cause changes in volatile contents, crystal contents, and melt temperature [e.g., Witham and Llewellin, 2006, Harris, 2008, Fowler and Robinson, 2018]. For example, a single convective cell extending from the lava lake surface through the conduit might result in lower average magma temperatures in the conduit than separate convective cells in the lava lake and conduit [Patrick et al., 2016b]. Injections of new volatiles and/or melt from depth, or changes in the background volatile/melt supply rate, could impact both temperature and volatile contents on various timescales. Stokes rise velocity of bubbles with radii of 1-100 mm are 0.01 mm/s-1 m/s, and simulations of bubble slugs show ascent velocities on the order of 1 m/s [Chouet et al., 2010]. Based on inferred magma upwelling rates in the lava lake of 0.15-0.3 m/s, circulation timescales in the lava lake would be on the order of hours [Patrick et al., 2016b]. So volatile rise timescales through the conduit/lava lake for large bubbles could be on the order of minutes, whereas smaller bubbles will mostly move by convecting with the surrounding melt. Shallowly-driven processes such as gas pistoning or foam buildup likely also contribute to changes in volatile contents on timescales of minutes to days [e.g., Nadeau et al., 2014, Patrick et al., 2016a, 2019b].

*Interpreting changes in lava lake sloshing*

The lava lake sloshing events at Halemaʻumaʻu have previously been interpreted from models for surface gravity wave resonance of inviscid and incompressible fluid in a cylindrical or wedge-shaped tank [Dawson and Chouet, 2014, Liang and Dunham, 2020]. The Halemaʻumaʻu crater geometry has remained roughly cylindrical over time [Patrick et al., 2019b], although variations in its planform shape at some times are significant enough to produce concurrent

sloshing signals with slightly different periods [Dawson and Chouet, 2014, Liang and Dunham, 2020]. The crater walls are also slightly inward dipping, but Liang and Dunham [2020] suggest that this dip will not produce appreciably different inviscid sloshing periods than vertical walls.

Studies of viscous incompressible fluid sloshing indicate that $T$ and $Q$ depend on fluid density, fluid viscosity, and tank geometry [e.g., Bauer, 1981, Ibrahim, 2005]. Due to the presence of bubbles, a solidified surface crust, and possible foam layers under the crust, magma in the Halemaʻumaʻu lava lake will generally be both compressible and stratified [e.g., Carbone et al., 2013, Patrick et al., 2016a, Poland and Carbone, 2016]. The surface crust will not always act as a fully rigid or elastic cap since videos of rockfall-triggered lava lake sloshing show that the crust sometimes disintegrates/overturns following event onsets [Orr

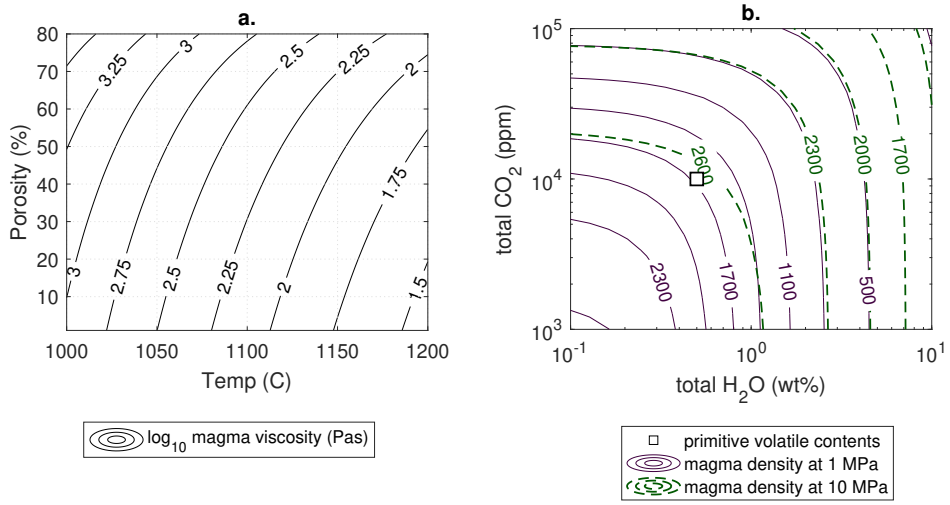


FIGURE 3.18. (a) Apparent magma viscosity as a function of temperature and porosity (section 3.4). (b) Magma density as a function of $H_2O$ and $CO_2$ contents at two pressures (1 and 10 MPa correspond to magmastatic depths of 40-100 m and 0.4-1 km respectively) and an assumed temperature of 1100 C (section 3.4). The density of pure melt is $\sim$2650 kg/m$^3$. Estimates of primitive (or 'parent') magma volatile contents are from Edmonds et al. [2015].

et al., 2013], but it may still impact the sloshing dynamics for some events. The isotropic component of deformation found in previous inversions by Liang and Dunham [2020] suggests that the lava lake sloshing drives magma in and out of the underlying conduit/reservoir, so viscous dissipation from the conduit may also be important. The degree of coupling between lateral fluid motion in the lava lake and vertical fluid motion in the conduit will depend on the offset of the top of the conduit along the lava lake sloshing axis, and thus on the direction of lava lake sloshing. Detailed analysis and inversions for $T$ and $Q$ for lava lake sloshing events would require modeling that can account for all these factors and is self-consistently coupled to the conduit-reservoir resonance. However, we can still gain some new insights from our timeline of lava lake sloshing events using existing models for viscous sloshing in an isolated tank.

We assume a cylindrical crater geometry, for which analytical solutions for viscous sloshing of an incompressible fluid are available [Case and Parkinson, 1957, Ibrahim, 2005]. The period for the fundamental sloshing eigenmode is given by

$$T = 2\pi \left( \frac{jg}{R_L} \tanh\left( \frac{jh_L}{R_L} \right) \right)^{-1/2}, \tag{3.4.12}$$

where $R_L$ is lava lake radius, $h_L$ is lava lake depth, $\rho_L$ is magma density in the lava lake, and $j$ is the root that satisfies $\partial J_1(jr)/\partial r|_{r=R_L} = 0$ where $J_1$ is a Bessel function of the first kind. $Q$ is primarily controlled by viscous damping from the lava lake sidewalls, with comparatively minimal contributions from the bottom and free-surface except when the lava lake is very shallow and/or narrow. Considering

only damping from the sidewalls gives

$$Q = 2\pi R_L \sqrt{\frac{2\rho_L}{\omega_L \mu_L}} \left( \frac{1 + (jR_L)^{-2}}{1 - (jR_L)^{-2}} - \frac{2jH_L}{\sinh(2jH_L)} \right)^{-1}, \tag{3.4.13}$$

where $\mu_L$ is magma viscosity in the lava lake. Figure 3.19 shows the effect of various parameters on $T$ and $Q$.

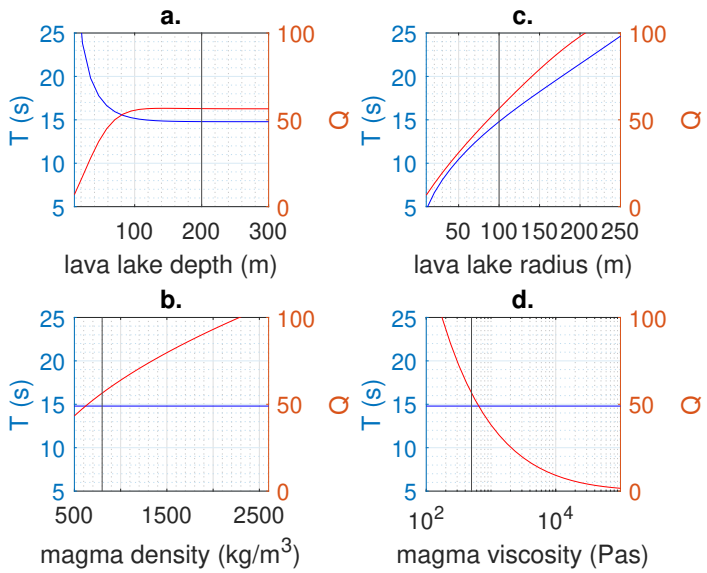


FIGURE 3.19. (a-d) Predicted variation in $T$ and $Q$ due to varying each model parameter in isolation in the viscous cylindrical tank model of [Case and Parkinson, 1957] (Eq. 3.4.12-3.4.13). Black lines indicate the default value used for each parameter.

The long-term increase in $T$ is roughly consistent with the observed increases in lava lake diameter according to Eq. 3.4.12 (Fig. 3.11, 3.19). On shorter timescales (months or less), the crater geometry should be relatively constant. The effective lava lake surface diameter could change slightly with changing lava lake height due to the irregular crater shape [Patrick et al., 2019b], which might explain the decrease in $T$ in late 2015. Lava lake sloshing $T$ does exhibit variability of up to ~3 s on timescales of months or less (Fig. 3.11), though part of this is

from sloshing along different axes of the lava lake which detailed seismic inversions and/or video of the lava lake could help resolve [Liang and Dunham, 2020].

Lava lake sloshing exhibits variation in average $Q$ by up to a factor of four on timescales of years (Fig. 3.11), and similar variability on timescales of days to weeks. Changes in lava lake depth should have a relatively minimal effect on $Q$ except when the lava lake is very shallow. Additionally, since many events with similar lava lake elevation have very different $Q$ (Fig. 3.11), we expect other factors are primary drivers of much of the variation in $Q$. For a density of 1000 kg/m$^3$, depth of 200 m, and radius of 100 m, producing the observed values of $Q$ requires viscosities ranging from ∼400-8000 Pas (Fig. 3.19). The higher end of this viscosity range could likely only be produced by magma cooler than ∼1000 C (Fig. 3.18), which is appreciably less than geochemically inferred temperatures of 1160-1300 C [Edmonds et al., 2013]. Low magma temperatures are expected near the lava lake surface, where the solid crust temperatures are often ∼300 C, but temperatures should increase with depth in a manner dependent upon the convective regime [Patrick et al., 2016b]. The model used here has no vertical stratification, so does not indicate the sensitivity of $Q$ to viscosity as a function of depth. However, it is likely that variation in magma properties with depth in the lava lake is required to explain the observed variation in $Q$.

For small amplitude perturbations with the same forcing mechanism (e.g., rockfall) and forcing location, if everything else is constant we would expect a linear relationship between lava lake sloshing and conduit-reservoir oscillation amplitudes. The observed scatter could be caused by variable forcing location or mechanism, changes in the shallow magma system geometry, or changes in magma properties in the lava lake or in the conduit-reservoir system. The lack of

observed correlation between $Q$ of conduit-reservoir oscillations and $Q$ of lava lake sloshing (Fig. 3.13), which is also apparent at short (months or less) timescales (Fig. 3.11), suggests that magma properties in the lava lake and conduit may be largely decoupled during sloshing events. Changes in porosity alone will generally not cause order of magnitude changes in magma viscosity (Fig. 3.18). Appreciably different magma temperatures in the conduit and lava lake at various times may thus be required to explain the large scatter in $Q$ between the two oscillations, which could suggest separate convective cells in the lava lake and conduit [Patrick et al., 2016b].

### *Timeline of Kīlauea VLP Seismicity*

Here we present a brief chronological overview of Kīlauea activity and summit VLP seismicity from 2008-2018, with particular focus on new observations not discussed in previous summaries of Kīlauea activity [Dawson and Chouet, 2014, Anderson et al., 2015, Poland and Carbone, 2016, Patrick et al., 2019b]. We break the timeline into one or two year long time-segments based on notable changes in VLP seismicity or eruptive activity.

#### January 2008-January 2010

The Overlook Crater first began forming inside the Halema‘uma‘u summit crater in March 2008, following months of elevated $SO_2$ emissions and seismicity [e.g., Patrick et al., 2011, Dawson and Chouet, 2014, Patrick et al., 2019b]. Two years of elevated seismicity, long-term ground deflation, and occasional explosive events led to the establishment of a persistent lava lake in early 2010 (Fig. 3.10). Much of the VLP seismicity during this time was periodic tremor (Fig. B.20,

B.22), although there were times where discrete events were apparent (Fig. B.19, B.21) [Dawson and Chouet, 2014]. Average $T$ increased and decreased significantly multiple times during this interval, from a maximum of around 25 s in July 2008 to minima of around 13 s in February and August of 2009. While measurements of lava lake level are limited during this time, the local minima in 2009 correspond with low reported lava lake levels and the local maxima around July 2008 corresponds with higher reported lava lake levels [Patrick et al., 2019b]. $Q$ was highly variable but mostly less than 25. The high variability in $T$ and $Q$ over timescales from hours to months during this timespan likely reflects changes in both magma system geometry and magma properties, indicating a highly dynamic shallow magma system.

January 2010-March 2011 Kamoamoa fissure eruption

In early 2010 the lava lake became persistent and filled from an elevation of 820 m to 950 m by early 2011, accompanied by corresponding long-term ground inflation (Fig. 3.10). Normal conduit-reservoir events with clear impulsive onsets and decays began occurring during this time, although VLP periodic tremor was also still present (Fig. 3.12) [Dawson and Chouet, 2014]. A more continuous band of conduit-reservoir VLP events began in November 2009 and continued until the March 2011 Kamoamoa fissure eruption. Lava lake sloshing events with $T$ around 11 s began to appear alongside some of the Normal conduit-reservoir oscillations (Fig. 3.10).

The long-term increase in conduit-reservoir $T$ from $\sim$20 s in early 2010 to $\sim$35 s by early 2011 is the largest change in $T$ observed during the 2008-2018 eruption. Changes in average magma density of more than $\sim$1600 kg/m$^3$

and/or changes in magma density contrast of more than ∼1000 kg/m$^3$ would be required to produce this increase in $T$ if the shallow magma system geometry were constant. While such a change in density contrast is feasible, it may also be likely that some evolution in geometry occurred over this time. Analysis of this is hindered by limited station availability (Fig. 3.2). There was a continuous decrease in the vertical/horizontal velocity ratio and Mogi source depth from early-mid 2010 (Fig. 3.16), though these may be partially due to the increasing contribution of tilt with increasing $T$ [e.g., Maeda et al., 2011]. Increases in conduit length of several hundred meters or decreases in conduit radius by around a factor of five could have produced the changes $T$ over this time-segment (Fig. 3.17). An increase in conduit length by several hundred meters over a 1-yr timescale due to the solidification of melt at the roof of an ellipsoidal reservoir is unfeasible [e.g., Karlstrom and Richards, 2011], but could be caused by a migration of the intersection between the conduit and reservoir (e.g., if the conduit connects further down along the sidewalls of an ellipsoidal reservoir or dipping dike). Changes in lava lake geometry and elevation during this time-segment likely also contribute, but are not considered in detail in existing models (section 3.4).

Our VLP catalog resolves two pronounced $T$ local maxima in March and June 2010 more clearly than the catalog of Dawson and Chouet [2014]; both are about 2 s above the background trend in $T$ and about a month long. The June maximum corresponded to a pronounced local maximum in ground inflation and lava lake elevation, but the March maximum is less clearly correlated with ground inflation or lava lake elevation. For the remainder of this time-segment, conduit-reservoir oscillation $T$ was well correlated with both ground inflation and lava lake elevation. There was a gradual increase in $Q$ starting around August 2010,

followed by a rapid drop around February 2011. $Q$ was correlated with $T$, ground inflation, and lava lake elevation in mid-2010, then became anti-correlated with all three datasets by late 2010. These changes in correlations in early and late 2010 indicate additional changes in the shallow magma system superimposed upon the long-term increase in $T$ over this time-segment.

March 2011 Kamoamoa fissure eruption-September 2011 Pu‘u ‘Ō‘ō eruption

After the March 2011 Kamoamoa fissure eruption, there was a gradual increase in lava lake elevation and ground inflation leading up to the August 2011 Pu‘u ‘Ō‘ō eruption, followed by another short stretch of ground inflation and lava lake refilling before the September 2011 Pu‘u ‘Ō‘ō eruption (Fig. 3.10). Similar to Dawson and Chouet [2014], we do not detect very many VLP events between the March 2011 Kamoamoa and August 2011 Pu‘u ‘Ō‘ō eruptions, though there were some that exhibited strong glides in period. Between the August and September 2011 Pu‘u ‘Ō‘ō eruptions there was a cluster of low $Q$ VLP activity with $T$ around 20 s, and some events that exhibited strong glides in period (Fig. B.25).

It is interesting that there were very few VLP events during most of this time-segment even at times when the lava lake elevation was relatively high, especially since the strongly fluctuating lava lake elevation might be expected to induce abundant rockfalls from the crater walls to trigger resonance. The changing lava lake elevation and good correlation between lava lake elevation and ground inflation during this time indicates that there was still an open hydraulic connection between the lava lake and the shallow magma reservoir. However, it is possible that the geometry of the conduit during this time changed in a manner

that inhibited magma flow on timescales of the conduit-reservoir oscillation (e.g., became more constricted or sinuous).

September 2011 Pu‘u ‘Ō‘ō eruption-October 2012 intrusion

Between the September 2011 Pu‘u ‘Ō‘ō eruption and May 2012 SSE, average lava lake level increased from ∼930 m to ∼960 m, although there was only a very slight corresponding ground inflation (Fig. 3.11). After the May 2012 SSE, which corresponded to a temporary 10-day drop in lava lake elevation, lava lake elevation and ground inflation both decreased until around August, then continually increased until the October 2012 intrusion. VLP seismicity during this time-segment consisted of Normal and Reverse events, VLP periodic tremor, sparse lava lake sloshing, and gliding-frequency events (Fig. 3.12, B.23, B.26). Until around the time of the May 2012 SSE conduit reservoir oscillations had very low $Q$, sometimes below our threshold for robust detections (section 3.2) which contributes to the apparent sparsity of events (Fig. 3.11). After the May 2012 SSE, average conduit-reservoir oscillation $Q$ continually increased until the October 2012 intrusion. Average conduit-reservoir oscillation $T$ decreased until around August, then continually increased until the October 2012 intrusion, remaining well correlated with lava lake elevation (Fig. 3.15). $T$ and $Q$ were positively correlated in late 2012 for the last time in the 2008-2018 timespan.

A steadily widening conduit, perhaps due to thermal erosion and/or increasing magmastatic pressure on the conduit walls, could explain the increase in conduit-reservoir $Q$ over 2012. A very narrow conduit at the start of this time-segment would also be consistent with the reduced conduit-reservoir VLP seismicity during the previous time-segment. Alternately, the increase in $Q$ could

be caused by a decrease in magma viscosity. This would likely not be from a decrease in porosity, since if everything else were constant the very gradual ground inflation rate that occurs over this time-segment relative to the lava lake filling rate would imply an increase in magma porosity. Viscosity decreases might instead reflect increases in magma temperature, perhaps indicating an influx of hotter magma from depth that may have been initiated by the 2012 SSE.

October 2012 intrusion-June 2014 Pu‘u ‘Ō‘ō eruption

Between the October 2012 intrusion and the June 2014 Pu‘u ‘Ō‘ō eruption there was a long-term ground inflation trend, while average lava lake level remained constant (Fig. 3.11). On shorter timescales, lava lake elevation and ground inflation were well correlated (Fig. 3.15). VLP seismicity during this time included both Normal and Reverse events, periodic tremor, and lava lake sloshing (Fig. 3.12, 3.13, B.24). Until around late 2013, the average conduit-reservoir $T$ varied from 38-41 s over timescales of months and was generally well correlated with lava lake elevation. After this, $T$ remained relatively constant despite continuing fluctuations in lava lake elevation, and became anti-correlated with lava lake height by April 2014. Average conduit-reservoir $Q$ decreases from $\sim$20 to $\sim$11 by May 2013, followed by a non-monotonic increase to $\sim$25 by the June 2014 Pu‘u ‘Ō‘ō eruption. Conduit-reservoir $Q$ was negatively correlated with $T$ over most of the time-segment but exhibited variable correlation with lava lake elevation and ground inflation. Local maxima in conduit-reservoir event density occurred during times of inflation in May 2013, August 2013, February 2014, and around the May 2014 intrusion (Fig. 3.13). Conduit-reservoir ground motions were constant over this time-segment, indicating a stable reservoir geometry (Fig. 3.16).

Average lava lake sloshing $Q$ was highly variable between 6-50 but increased on average over this time-segment (Fig. 3.11).

The lack of changes in conduit-reservoir ground motions patterns around either the October 2012 or May 2014 intrusions likely indicates that these intrusions did not have direct enough hydraulic connections to the main shallow reservoir to be involved in the oscillations. However, the changes in correlations between $T$, $Q$, and lava lake elevation around both intrusions do indicate some change in the shallow magma system. This could be related to a change in magma properties if some of the shallow magma and/or the supply of new melt/volatiles from depth was routed into the intrusions. It is also interesting that the highest post-2011 VLP event density occurs around the May 2014 intrusion, despite this intrusion having a relatively minor signature in the other datasets.

June 2014 Pu‘u ‘Ō‘ō eruption-May 2016 Pu‘u ‘Ō‘ō eruption

There was steady long-term ground inflation during most of this time-segment, with more rapid inflation in the months around the May 2015 intrusion (Fig. 3.11). Lava lake elevation varied between 950-1000 m, except for the months leading up to the May 2015 intrusion when it increased sharply to 130 m and overflowed out of the overlook crater, then sharply dropped following the intrusion. The months after the May 2015 intrusion exhibited the only anti-correlation between lava lake elevation and tilt after 2010 (Fig. 3.15). VLP seismicity during this time-segment included both Normal and Reverse conduit-reservoir events, periodic tremor, and lava lake sloshing (Fig. 3.13). Local maxima in conduit-reservoir event density occurred during the May 2015 intrusion, May 2016 Pu‘u ‘Ō‘ō eruption, and generally near the onset of long-term inflation periods (for

example October 2014, December 2014, and March 2015). After the June 2014 Pu‘u ‘Ō‘ō eruption there was an abrupt change in conduit-reservoir oscillation ground motions apparent as a decrease in vertical/horizontal ratios and in Mogi depths (Fig. 3.16). Ground motions then remained stable until around the October 2015 SSE when they became more variable. Conduit-reservoir $T$ was relatively constant around 39 s except for increasing to 41 s in the months leading up to the May 2015 intrusion. Interestingly, the subsequent decrease in $T$ occurred over months despite the rapid drop in lava lake elevation; $T$ remained correlated with lava lake elevation during this time but not with tilt (Fig. 3.15). There was a month-long $\sim$1 s local minima in $T$ corresponding to the October 2015 SSE. Conduit-reservoir $Q$ averaged around 25 until a few months before the May 2015 intrusion, when it dropped to around 18 and remained stable for the remainder of the time-segment. $Q$ was either anti-correlated or not correlated with $T$ during this time-segment and was not strongly correlated with lava lake elevation or ground inflation.

The change in conduit-reservoir event displacement patterns after the June 2014 Pu‘u ‘Ō‘ō eruption likely reflects a change in reservoir geometry, and the lack of any corresponding changes in $T$ or $Q$ indicates that the conduit geometry probably remained constant. Since this change is very abrupt it might reflect the opening/closing of a dike or sill, perhaps peripheral structures extending from the main reservoir region. However, it is not clear why this would have been related to the ERZ eruption since there were apparently no strong changes in summit reservoir pressure. Conduit-reservoir ground motions were highly variable around the May 2016 Pu‘u ‘Ō‘ō eruption, so it is difficult to conclude whether this eruption directly corresponded to a change in reservoir geometry as the 2014

one did. While there were minimal changes in conduit-reservoir $T$ and $Q$, lava lake elevation, and ground inflation around the May 2016 Pu‘u ‘Ō‘ō eruption, an abrupt change in $SO_2$ emissions indicates that this event did perturb the summit magma system.

The anticorrelation between tilt and lava lake elevation around the May 2015 intrusion is likely because the intruded magma contributed to ground inflation even while pressure dropped in the main shallow reservoir. As with the October 2012 and May 2014 intrusions, the lack of changes in conduit-reservoir ground motion patterns following this intrusion indicates that it did not have a direct enough hydraulic connection to the main shallow reservoir to be involved in the oscillations. Unlike those earlier intrusions the May 2015 intrusion does not correspond to clear changes in correlations between $T$, $Q$, and lava lake elevation.

Conduit-reservoir events after the October 2015 SSE exhibit increased variability in Mogi depths (Fig. 3.16), but no clear changes in the other metrics for ground displacement patterns. This could reflect a subtle change in the shallow magma system geometry or rock properties that made the Mogi inversions more sensitive to noise. Alternately, it could indicate that the hydraulic connection to some feature of the shallow magma system (e.g., a peripheral dike or sill) is variable over this time. Tectonic stress changes from the October 2015 SSE could have conceivably contributed to either scenario.

May 2016 Pu‘u ‘Ō‘ō eruption-May 2018 caldera collapse onset

Long-term averaged lava lake elevation increased gradually until late 2016 when small overflows occurred [Patrick et al., 2019b], then decreased gradually until mid-2017. Lava lake elevation began increasing again more steeply in March

2018 before eventually overflowing on April 26, then began draining rapidly on May 2 [e.g., Neal et al., 2019] (Fig. 3.11). There was long term ground inflation over most of this time-segment, and lava lake elevation and ground inflation were mostly correlated on shorter timescales except for a few months in mid-2017 (Fig. 3.15). VLP seismicity during this time included Normal and Reverse events, periodic tremor, and lava lake sloshing (Fig. 3.12, 3.13, B.14, B.15, B.16). Conduit-reservoir event density was relatively stable over this time-segment, while lava lake sloshing events were numerous until mid-2017 and then became much sparser. Conduit-reservoir oscillation $T$ was stable around 39 s until October 2017 when it dropped to 37 s; then increased again in the months leading up to the May 2018 collapse eruptions before sharply dropping from 40 s on May 5 to 32 s on May 7 when the last definitive conduit-reservoir event in our catalog occurred (Fig. 3.11). During this time-segment $T$ was alternately correlated and un-correlated or anti-correlated with lava lake elevation and ground inflation (Fig. 3.15). Conduit-reservoir oscillation $Q$ remained stable around 18 and was anti-correlated with $T$ until late 2017, when $Q$ began to vary and show a correlation with lava lake elevation and became uncorrelated with $T$. Conduit-reservoir ground motion patterns remained highly variable over this time-segment, but average Mogi depths decreased until early 2017, after which they remained consistent and with lower misfit (Fig. 3.16).

That different ground motion metrics show large variability at different times within this time-segment indicates that the evolution of reservoir geometry may have been complex, but it does seem that some gradual evolution was likely occurring at least until early 2017. The numerous changes in correlations around mid-2017 also indicate that some change occurred in the shallow magma system.

The continual increase in $T$ in the months leading up to the 2018 collapse eruption onset seems to be similar to the buildup to the October 2012 and May 2015 intrusions, which in all three cases seems to track increases in lava lake elevation and ground inflation indicating a buildup of magma/pressure in the shallow summit magma system. The month-timescale fluctuations in average $Q$ starting in late 2017 indicate some variability in magma properties, but that $Q$ remains relatively low (mostly $<$20) could indicate that there was not a significant increase in magma temperature. This would be consistent with the idea that the increase in pressure could be explained primarily by a blockage along the ERZ rather than by an increase in the flux of new hotter magma from depth [Patrick et al., 2020]. Detailed modeling of $T$, $Q$, and the other datasets available could yield more insight into what changes in the magmatic system were occurring during this time and what they could have indicated about the upcoming eruptions.

## Conclusions

We have presented a fully automated workflow using wavelet transforms to both detect and categorize VLP seismic signals that arise from magma resonance. These methods can detect multiple distinct spectral peaks and provide robust estimates of quality factors. They do not rely upon any training data and are readily transferable to other volcanoes as well as to long-period resonant signals in other geophysical time series such as infrasound data. We expect these methods will be useful for both analyzing historical seismic data and for near-real-time monitoring at various volcanoes.

We then used these methods to generate a catalog of VLP events that occurred between 2008-2018 during a prolonged open vent eruptive episode at

Kīlauea Volcano, Hawaii USA. This catalog expands upon earlier VLP catalogs by characterizing more types of signals and providing refined estimates of quality factors, revealing a rich time series of VLP seismicity. We focus particularly on two common classes of events: the 'conduit-reservoir' oscillation, which is prevalent over most of this timespan and represents the fundamental eigenmode of the shallow magma plumbing system, and a 'lava lake sloshing' resonance representing surface gravity wave propagation in the summit lava lake. We document changes in period, quality factor, and ground motion patterns over timescales ranging from hours to years for the conduit-reservoir oscillation. These include consistent patterns preceding and following intrusion and eruption events. We also characterize a trend of lava lake sloshing between 2010 and 2018 that exhibits a relatively consistent increase in period over time but wide variability in quality factors. Both classes of VLP events exhibit variable correlations with each other and with other geophysical data such as tilt, lava lake elevation, and $SO_2$ emissions.

VLP ground motions suggest that the shallow magma reservoir geometry was stable for years at a time, but did exhibit an abrupt change in 2014 and more gradual evolution over 2009-2010 and 2016-2018. Magma resonance models suggest that the variability in the period and quality factor of the conduit reservoir oscillation on timescales of months or less likely reflects changes in magma density of up to 500 kg/m$^3$ and changes in magma viscosity of up to an order of magnitude. Lava lake sloshing $T$ exhibits a long-term increase consistent with the increasing lava lake diameter. Lava lake sloshing $Q$ exhibits large variability on timescales of days to years that suggests orders of magnitude changes of magma viscosity in the lava lake, but which may not be representative of magma

viscosity in the conduit. This analysis places these resonant oscillations amongst a rich suite of existing data available to understand the evolution of the shallow magma system and the processes occurring within it. We anticipate that future co-inversions of these VLP oscillations and other geophysical data will lead to new insights into the physical processes responsible for a dynamic and long-lived eruptive episode at Kīlauea volcano.

## Bridge

This chapter has demonstrated the use of wavelet transforms for detecting and classifying volcano seismicity from magma resonance, and produced a catalog of VLP seismicity at Kīlauea Volcano. This chapter also discussed the limits of existing magma resonance models at explaining many observations from this catalog, which sets the stage for the next chapter. The next chapter will develop improved fluid dynamical models for magma resonance, and use these models to conduct inversions for magma properties over time at Kīlauea Volcano.

# CHAPTER IV

# KĪLAUEA VERY-LONG-PERIOD SEISMICITY INVERSION

This chapter represents material that was written with co-author Leif Karlstrom and that is in preparation for submission to Journal of Geophysical Research: Solid Earth. Joshua Crozier implemented modeling and data analysis with input from Leif Karlstrom. Joshua Crozier wrote the manuscript with input from Leif Karlstrom. Leif Karlstrom and Joshua Crozier conceived of the study. Leif Karlstrom obtained funding.

## Introduction

Magma rheology and volatile contents exert primary controls on whether eruptions occur, on the style of eruption that occurs, and on how eruptive dynamics progress over time [e.g., Gonnermann and Manga, 2007, Wallace et al., 2015, Siebert et al., 2015]. In shallow magma systems, these properties can change over a wide range of timescales due to processes such as recharge (influx of new melt and/or volatiles), convection, cooling/crystallization, and outgassing [e.g., Burgisser et al., 2015]. Being able to infer in-situ information about specific magma properties and how they are changing over time is thus vital for both volcano hazard monitoring and understanding the processes that drive volcanic activity. A wide variety of data, such as from seismicity, gravity, electromagnetism, ground deformation, gas flux, and erupted products, have been utilized for such inference [e.g., Pallister and McNutt, 2015]. However, limited progress has been made at resolving in-situ variation in magma properties over space and time, even at well instrumented and studied volcanoes such as Kīlauea (Hawaii, USA).

Very-long-period (VLP) seismic signals, which are prevalent at many volcanoes, have a disproportionate amount of energy at periods greater than ∼2 s [e.g., Chouet and Matoza, 2013]. These signals are often inferred to be caused by magma movement resulting from from magma flow through constrictions, bubble slug ascent, or resonant oscillations within various magma plumbing system components [e.g., Kumagai et al., 2003, Nakamichi et al., 2009, Jolly et al., 2017, Cesca et al., 2020]. They thus provide a direct probe of both magma properties and magma plumbing system geometry [e.g., Kumagai, 2006, Chouet et al., 2008, Dawson et al., 2011]. We consider VLP events from magma resonance, in which case the dominant periods, quality factors (decay rates), and associated ground motions encode the eigenmodes of the magmatic resonator and source-time function of excitation [Karlstrom and Dunham, 2016].

Kīlauea hosted thousands of resonant VLP events over its 2008-2018 summit eruptive episode [Dawson and Chouet, 2014, Crozier and Karlstrom, 2021]. The combined availability of a recent catalog of this VLP seismicity [Crozier and Karlstrom, 2021], an understanding of the resonance mechanism gained from previous modeling and inversions [Chouet and Dawson, 2013, Liang et al., 2020b,a], and a relative abundance of other data and observations make Kīlauea volcano an excellent study location to test what changes in the shallow magma system can be resolved from VLP seismicity. This eruption involved formation of a persistent lava lake in the Halemaʻumaʻu summit vent, multiple East Rift Zone (ERZ) eruptions (the Kamoamoa fissure eruption in Mar 2011 and Puʻu ʻŌʻō vent openings in Aug 2011, Sep 2011, Jun 2014, and May 2016), several inferred magma intrusions (in Oct 2012, May 2014, and May 2015), several regional slow-slip events (SSEs) which have been linked to magmatic activity (in Feb 2010, May 2012, and

Oct 2015), and culminated in the eruption of around 0.8 $km^3$ of magma from the ERZ and caldera collapse at the summit [e.g., Patrick et al., 2019b, Neal et al., 2019, Wang et al., 2019].

The geometry of the Kīlauea shallow summit magma system is approximately known from a multitude of previous seismic and geodetic studies [e.g., Baker and Amelung, 2012, Chouet and Dawson, 2013, Anderson et al., 2015, Crozier et al., 2018a, Anderson et al., 2019, Liang et al., 2020a]. It consists of the Overlook Crater which hosts the Halemaʻumaʻu lava lake, the Halemaʻumaʻu reservoir which is centered 1-2 km beneath the vent opening, and the deeper South Caldera reservoir. The Halemaʻumaʻu reservoir has a very open hydraulic connection to the lava lake at most times, but the details of connections to the South Caldera reservoir, ERZ, and deeper magma sources are not well known [Anderson et al., 2020]. VLP ground motion patterns indicate changes in Halemaʻumaʻu reservoir geometry might have occurred gradually over 2009-2010 and 2016, and abruptly in Jul 2014 [Crozier and Karlstrom, 2021]. Lava lake elevation and surface area data is available over most of the timespan [Patrick et al., 2019b]. Gravity data is available over some parts of the timespan and has provided estimates of the average magma density in the lava lake [Carbone et al., 2013, Poland and Carbone, 2016, 2018]. Rock sample analysis constrains variability in magma chemistry, temperatures, and volatile contents present in the shallow Halemaʻumaʻu magma, as well as in the assumed primitive or 'parent' magma that recharged the system from depth [e.g., Edmonds et al., 2013, 2015].

The combination of data on geodetic ground deformation, lava lake elevation, and VLP seismicity permits joint inversions of properties of the magma system over time with the development of an appropriate magma resonance model. The

dominant VLP resonant mode at Kīlauea is the "conduit-reservoir" oscillation, which consists of a vertical sloshing of the magma column in the conduit and lava lake in and out of the underlying magma reservoir [Liang et al., 2020b]. Gravity is the dominant restoring force and viscous drag is the dominant source of damping. We extend previous models for this resonance to include a more detailed treatment of the lava lake, variable conduit geometry, and stratified magma properties governed by joint $CO_2$-$H_2O$ volatile solubility models under disequilibrium degassing regimes. We explore the effects of various magma system properties on this model, which informs the sensitivity of the resonance to changes in these properties and the limits of what can be uniquely resolved. We conduct inversions with this model over the timeline of VLP seismic events, with additional constraints from the observed lava lake elevation and joint geodetic inversions for pressure changes in the two summit reservoirs. Focusing on timescales of years or less, over which the subsurface magma system geometry can be assumed to be relatively constant, allows unique inversion of relative changes in magma properties. This yields a timeline of magma evolution at various depths within the shallow magma system over timescales from hours to years. We interpret the timeline of magma properties in relation to other data and observations, and discuss the implications for volcano monitoring.

## Methods

*Conduit-reservoir magma oscillation model*

Model description

We consider a background state consisting of a static radially symmetric magma column with density and viscosity that are vertically stratified (but laterally uniform), underlain by a magma reservoir contained within an elastic half-space (Fig. 4.1). Our model domain extends from the bottom of the conduit (or top of the reservoir) to the surface of the lava lake (Fig. 4.1). We then use linearized governing equations for uni-directional magma flow induced by small-amplitude perturbations to this system. We neglect the compressibility of magma in the column and conduit wall elasticity in response to these perturbations, which is justified for this resonant mode [Liang et al., 2020b]. In this case magma density $\rho(z,t)$ will be given by

$$\rho = h\sin(\theta)\frac{d\bar{\rho}}{dz}, \tag{4.2.1}$$

where $\bar{\rho}(z)$ is background magma density and $h(z,r,t)$ is conduit-parallel fluid particle displacement, so the orientation of $h$ is a function of conduit dip angle $\theta(z)$. Linearized conservation of momentum for perturbations is then given by

$$\frac{\partial v}{\partial t}\bar{\rho} = h\sin(\theta)\frac{d\bar{\rho}}{dz}g - \sin(\theta)\frac{\partial p}{\partial z} + \bar{\mu}\frac{1}{r}\frac{\partial}{\partial r}\left(r\frac{\partial v}{\partial r}\right) \tag{4.2.2}$$

where $\bar{\mu}(z)$ is background magma viscosity, $g$ is gravitational acceleration, $p(z,t)$ is pressure perturbation, and $v(z,r,t)$ is fluid particle velocity in the conduit-parallel direction.

We assume a zero slip boundary condition along the magma column (conduit/lava lake) wall at radius $R$

$$v(z, R, t) = 0. \tag{4.2.3}$$

Cross-sectionally averaged viscous drag force can be determined from the shear stress at the magma column wall, so cross-sectionally averaging momentum (Eq. 4.2.2) gives

$$\frac{d\langle v \rangle}{dt}\bar{\rho} = \langle h \rangle \sin(\theta)\frac{d\bar{\rho}}{dz}g - \sin(\theta)\frac{\partial p}{\partial z} + \frac{2\bar{\mu}}{R}\frac{\partial v}{\partial r}\Big]_R \tag{4.2.4}$$

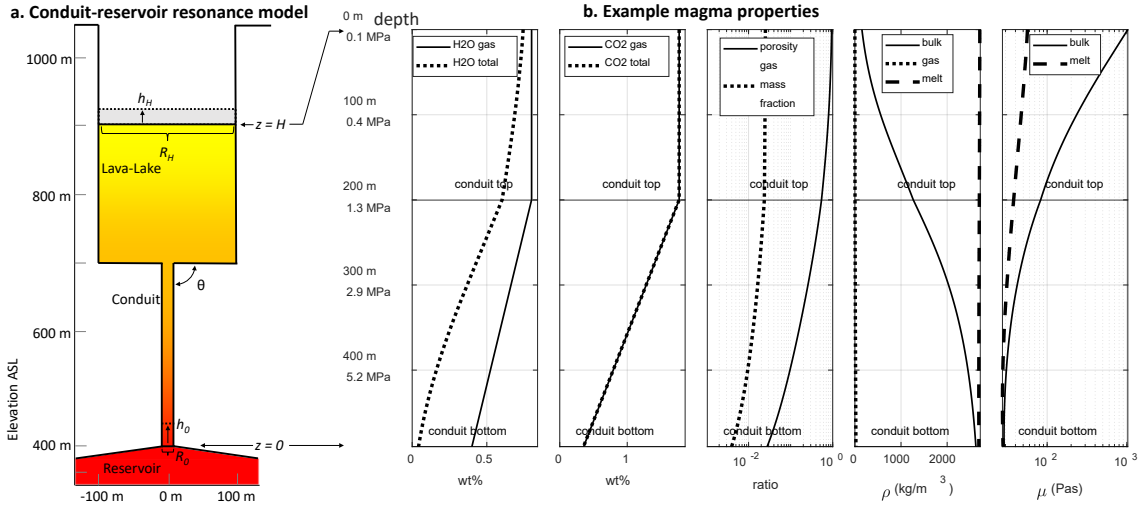


FIGURE 4.1. (a) Illustration of conduit-reservoir resonance model, approximately drawn to scale based on observed lava lake geometry and inferred conduit and reservoir geometries. The color gradient in the conduit and lava lake qualitatively indicates depth-varying magma properties. The black arrows at the top of the lava lake and bottom of the conduit illustrate vertical sloshing motion during the resonance (not to scale). (b) Example depth profiles of magma properties created from piecewise linear volatile profiles at a uniform temperature of 1200 C.

where $\langle\rangle$ indicates cross-sectional averaging, i.e., $\langle x\rangle = \frac{2}{R^2}\int_0^R rx(r)dr$ for some variable $x$. $\langle v\rangle$ is the time derivative of $\langle h\rangle$

$$\frac{d\langle h\rangle}{dt} = \langle v\rangle. \tag{4.2.5}$$

Incompressible linearized conservation of mass is

$$\langle h\rangle = \langle h\rangle_0 \frac{R_0^2}{R^2}. \tag{4.2.6}$$

where a zero subscript indicates evaluation at the bottom of the magma column (or top of the reservoir), e.g., $R_0 = R(z = 0)$, and subscript $H$ indicates evaluation at the top of the magma column (or top of the lava lake).

We apply pressure perturbation boundary conditions at the bottom and top of the magma column. Neglecting fluid inertia and viscous dissipation in the reservoir, which is a good approximation for this resonance [Liang et al., 2020b], linearized pressure perturbation at the base of the magma column $p_0$ is a function of displaced magma mass in the reservoir,

$$p_0 = -C_t^{-1}\pi R_0^2\langle h\rangle_0, \tag{4.2.7}$$

where $C_t$ is the total storativity (injected magma volume per unit pressure increase) of the reservoir,

$$C_t = (\beta_m + \beta_c)V, \tag{4.2.8}$$

where $V$ is reservoir volume, $\beta_m = \bar{\rho}^{-1}d\bar{\rho}/dp$ is effective magma compressibility in the reservoir, and $\beta_c = V^{-1}dV/dp$ is the elastic reservoir compressibility. For a

spherical reservoir

$$\beta_c = 3/(4G), \tag{4.2.9}$$

where $G$ is the elastic shear modulus; analytical solutions also exist for penny-shaped and rectangular cracks and ellipsoids [e.g., Fialko et al., 2001, Cervelli, 2013, McQuillan and Karlstrom, 2021]. Linearized pressure perturbation at the top of the magma column $p_H$ is a function of forcing pressure $p_{ex}$ and the displaced magma mass at the free surface,

$$p_H = p_{ex} + \langle h \rangle_H \bar{\rho}_H g = p_{ex} + \langle h \rangle_0 \frac{R_0^2}{R_H^2} \bar{\rho}_H g. \tag{4.2.10}$$

Integrating momentum (Eq. 4.2.4) in the $z$-direction over magma column height $H$ and substituting in conservation of mass (Eq. 4.2.6) and the boundary conditions (Eq. 4.2.7 and 4.2.10) gives

$$\begin{aligned} \frac{d^2\langle h \rangle_0}{dt^2} R_0^2 \int_0^H \frac{1}{\sin(\theta)} \frac{\bar{\rho}}{R^2} dz =& \langle h \rangle_0 R_0^2 \left( g \left( \int_0^H \frac{d\bar{\rho}}{dz} \frac{1}{R^2} dz - \bar{\rho}_H \frac{1}{R_H^2} \right) - C_t^{-1} \pi \right) \\ &+ \int_0^H \frac{1}{\sin(\theta)} \frac{2\bar{\mu}}{R} \frac{\partial v}{\partial r} \Big]_R dz - p_{ex}. \end{aligned} \tag{4.2.11}$$

Solutions

We assume a periodic pressure gradient with angular frequency $\omega$ and amplitude $f$,

$$\frac{\partial p}{\partial z} = f e^{i\omega t}. \tag{4.2.12}$$

Velocity can then be expressed analytically by [Womersley, 1955]

$$v = \frac{fe^{i\omega t}}{i\omega\bar{\rho}}\left(1 - \frac{J_0\left(r\alpha\right)}{J_0\left(R\alpha\right)}\right), \tag{4.2.13}$$

where $J_n$ is a Bessel function of the first kind and order $n$, and $\alpha$ is

$$\alpha = \sqrt{\frac{\omega\bar{\rho}}{\bar{\mu}}}i^{3/2}. \tag{4.2.14}$$

Shear strain at the conduit/lake wall is then

$$\frac{\partial v}{\partial r}\Big]_R = \frac{fe^{i\omega t}}{i\omega\bar{\rho}}\left(\frac{\alpha J_1\left(R\alpha\right)}{J_0\left(R\alpha\right)}\right), \tag{4.2.15}$$

and $\langle v\rangle$ is

$$\langle v\rangle = \frac{fe^{i\omega t}}{i\omega\bar{\rho}}\left(1 - \frac{2}{R\alpha}\frac{J_1\left(R\alpha\right)}{J_0\left(R\alpha\right)}\right). \tag{4.2.16}$$

Substituting Eq. 4.2.16 into Eq. 4.2.15 and simplifying with the Bessel function recurrence relation $J_{n+1}(x) = \frac{2n}{x}J_n(x) - J_{n-1}(x)$ yields

$$\frac{\partial v}{\partial r}\Big]_R = -\langle v\rangle\frac{\alpha J_1\left(R\alpha\right)}{J_2\left(R\alpha\right)}. \tag{4.2.17}$$

Substituting Eq. 4.2.17, 4.2.5, and 4.2.6 into Eq. 4.2.11 and taking the real part gives the simplified governing equation

$$\begin{aligned}\frac{d^2\langle h\rangle_0}{dt^2}R_0^2\int_0^H \frac{1}{\sin(\theta)}\frac{\bar{\rho}}{R^2}dz =& \langle h\rangle_0 R_0^2\left(g\left(\int_0^H \frac{d\bar{\rho}}{dz}\frac{1}{R^2}dz - \bar{\rho}_H\frac{1}{R_H^2}\right) - C_t^{-1}\pi\right)\\ &- \frac{d\langle h\rangle_0}{dt}2R_0^2\mathrm{Re}\left(\int_0^H \frac{1}{\sin(\theta)}\frac{\bar{\mu}}{R^3}\frac{\alpha J_1\left(R\alpha\right)}{J_2\left(R\alpha\right)}dz\right) - p_{ex}.\end{aligned} \tag{4.2.18}$$

Setting the top forcing pressure $p_{ex}$ in Eq. 4.2.18 to zero gives the governing equation for a homogeneous damped harmonic oscillator,

$$c_1 \frac{d^2\langle h\rangle_0}{dt^2} + c_2 \frac{d\langle h\rangle_0}{dt} + c_3\langle h\rangle_0 = 0. \tag{4.2.19}$$

In damped harmonic oscillator equation 4.2.19, $c_1$ is the inertial term

$$c_1 = R_0^2 \int_0^H \frac{1}{\sin(\theta)} \frac{\bar{\rho}}{R^2} dz, \tag{4.2.20}$$

$c_2$ is the viscous damping term,

$$c_2 = 2R_0^2 \mathrm{Re}\left( \int_0^H \frac{1}{\sin(\theta)} \frac{\bar{\mu}}{R^3} \frac{\alpha J_1(R\alpha)}{J_2(R\alpha)} dz \right), \tag{4.2.21}$$

and $c_3$ is the restoring force term (gravity and reservoir storativity),

$$c_3 = -R_0^2 \left( g \left( \int_0^H \frac{d\bar{\rho}}{dz} \frac{1}{R^2} dz - \frac{\bar{\rho}_H}{R_H^2} \right) - C_t^{-1}\pi \right) \tag{4.2.22}$$

Damped harmonic oscillator equation 4.2.19 has a general solution of the form

$$\langle h\rangle_0(t) = \langle h\rangle_0(t=0) e^{(\lambda + i\omega)t}, \tag{4.2.23}$$

with initial amplitude $\langle h\rangle_0(t=0)$, temporal exponential decay rate constant

$$\lambda = \frac{c_2}{2c_1} \tag{4.2.24}$$

and natural angular frequency

$$\omega = \sqrt{\frac{c_3}{c_1} - \left(\frac{c_2}{2c_1}\right)^2} = \sqrt{\omega_u^2 - \lambda^2} \tag{4.2.25}$$

where undamped (inviscid) natural angular frequency $\omega_u = \sqrt{c_3/c_1}$. Since $c_2$ and $\lambda$ are functions of $\omega$, Eq. 4.2.25 can be solved implicitly for $\omega$, which then may be used to calculate $\lambda$ from Eq. 4.2.24. Quality factor $Q$ gives the ratio of energy stored to energy lost per cycle,

$$Q = \frac{\omega}{2\lambda}. \tag{4.2.26}$$

Analytical solutions under simplified conditions

To gain more insight into these equations, we examine a simplified scenario that permits a concise analytical solution. We consider a vertical cylindrical magma column with uniform magma viscosity. We assume a linear magma density gradient between $\bar{\rho}_0$ and $\bar{\rho}_H$, alternately characterized by the density average and difference $\bar{\rho}_{avg}$ and $\Delta\bar{\rho}$. We assume fully developed (Poiseuille) flow, which will provide an upper bound on viscous damping. This simplified scenario is more similar to those considered in Chouet and Dawson [2013] and in the reduced conduit-reservoir eigenmode model of Liang et al. [2020b]. In this scenario, the inertial term reduces to

$$c_1 = H\bar{\rho}_{avg}, \tag{4.2.27}$$

the viscous damping term reduces to Poiseuille drag

$$c_2 = H\frac{8\bar{\mu}}{R^2}, \tag{4.2.28}$$

and the restoring force term reduces to

$$c_3 = g(\bar{\rho}_H - \Delta\bar{\rho}) + \pi R^2 C_t^{-1}. \tag{4.2.29}$$

This yields an exponential decay rate of

$$\lambda = \frac{4\bar{\mu}}{R^2\bar{\rho}_{avg}}, \tag{4.2.30}$$

a natural angular frequency of

$$\omega = \sqrt{\frac{g(\bar{\rho}_H - \Delta\bar{\rho}) + \pi R^2 C_t^{-1}}{H\bar{\rho}_{avg}} - \frac{16\bar{\mu}^2}{R^4\bar{\rho}_{avg}^2}}, \tag{4.2.31}$$

and a quality factor of

$$Q = \frac{R^2\bar{\rho}_{avg}}{8\bar{\mu}}\sqrt{\frac{g(\bar{\rho}_H - \Delta\bar{\rho}) + \pi R^2 C_t^{-1}}{H\bar{\rho}_{avg}} - \frac{16\bar{\mu}^2}{R^4\bar{\rho}_{avg}^2}}. \tag{4.2.32}$$

The natural frequency of flow that is not fully developed, as will be the case during Kīlauea VLP events [Liang et al., 2020b], will be between the natural frequency of fully developed flow and the undamped natural frequency

$$\omega_u = \sqrt{\frac{g(\bar{\rho}_H - \Delta\bar{\rho}) + \pi R^2 C_t^{-1}}{H\bar{\rho}_{avg}}}. \tag{4.2.33}$$

Stratified magma columns

We use two approaches for constructing background state stratified magma columns. In the density-based approach, we prescribe piecewise linear depth profiles of magma density and viscosity. In the volatile-based approach, we

prescribe piecewise linear depth profiles of magma temperature and volatile contents, from which density and viscosity are calculated (Fig. 4.1). In both approaches we assume magmastatic pressure gradients, although we note that exchange flow could result in lower pressures [e.g., Fowler and Robinson, 2018].

In either approach, by varying piecewise linear depth profiles we can examine a range of possible stratified magma columns that could result from both equilibrium and disequilibrium outgassing regimes. Considering disequilibrium outgassing regimes, where total (exsolved plus dissolved) volatile contents can be nonuniform because the flux of gas is decoupled from the melt phase, is especially important for lava lake volcanism where the magma is continuously convecting and outgassing. The piecewise linear approach allows us to evaluate a range of stratified magma depth profiles approximating those that might arise under various convective/outgassing regimes, while avoiding the need to explicitly simulate such dynamics in the spirit of simplicity (and sparse data constraints). For both approaches we parameterize the piecewise magma properties by their value at the bottom of the conduit, top of the conduit, and top of the lava lake.

For the volatile-based approach we consider both $CO_2$ and $H_2O$, but do not explicitly treat sulphur since its solubility is poorly constrained in reduced mafic melts. Sulphur has roughly similar solubility to $H_2O$ [e.g., Burgisser et al., 2015], and so will approximately trade-off with $H_2O$ contents in our models. Sulphur species are also inferred to be a smaller volatile component ($\sim$0.1 wt%) of the primitive/parent magma at Kīlauea than $H_2O$ and $CO_2$ ($\sim$0.5 wt% each) [e.g., Edmonds et al., 2013]. We assume a magmastatic (or hydrostatic) background pressure profile

$$\bar{P}(z) = \bar{P}_{atm} + \int_H^z \bar{\rho}(y) g dy, \tag{4.2.34}$$

where $y$ is a dummy integration variable for depth and where atmospheric pressure $\bar{P}_{atm} = 10^5$ Pa. Background bulk magma density is given by

$$\bar{\rho}(z) = \left( \frac{\bar{n}_g(z)}{\bar{\rho}_g(z)} + \frac{1 - \bar{n}_g(z)}{\bar{\rho}_m(z)} \right)^{-1}. \tag{4.2.35}$$

We calculate background melt density $\bar{\rho}_m(z)$ as a function of pressure, temperature, and composition using the model of Lange and Carmichael [1987] with average Halema‘uma‘u melt inclusion compositions from Table 7 in Edmonds et al. [2013]. We use the ideal gas law for background gas density:

$$\bar{\rho}_g(z) = \frac{\bar{P}(z)\big(\bar{n}_{H2O}(z)M_{H2O} + \bar{n}_{CO2}(z)M_{CO2}\big)}{R_g \bar{T}(z)} \tag{4.2.36}$$

where $\bar{n}(z)$ and $M$ are the background exsolved gas mass fraction and molar mass of each volatile species and $R_g$ is the ideal gas constant. To obtain exsolved gas mass fractions we interpolate from pre-computed grids of equilibrium $H_2O$ and $CO_2$ solubility as a function of pressure and $H_2O$ gas molar fraction obtained from the model of Iacono-Marziano et al. [2012], again using average Halema‘uma‘u melt inclusion compositions from [Edmonds et al., 2013]. The accuracy of the equilibrium solubility assumption will depend on the rate of magma ascent/descent relative to the rate of volatile diffusion in/out of bubbles. Estimated lava lake upwelling velocities of 0.15-0.3 m/s would yield circulation timescales on the order of hours [Patrick et al., 2016b]. $H_2O$ and $CO_2$ diffusivity are highly dependent on temperature $H_2O$ contents, but should be on the order of $10^{-9}$ to $10^{-11}$ $m^2/s$ in the shallow Kīlauea magma system [Zhang et al., 2007]. This could correspond to diffusion timescales from minutes to hours depending upon bubble spacing, which could range from $10^{-5}$ to $10^{-3}$ m [e.g., Mangan et al., 2014].

We calculate background melt viscosity $\bar{\mu}_l(z)$ as a function of temperature and dissolved $H_2O$ from the model of Giordano et al. [2008], again using the average Kīlauea glass composition from Table 7 in Edmonds et al. [2013]. Crystal contents [e.g., Mader et al., 2013] will increase viscosity, but we neglect this given the relatively low crystal contents of Halema‘uma‘u magma [e.g., Edmonds et al., 2013]. The effect bubbles have on bulk magma viscosity depends upon the flow regime [e.g., Pal, 2003, Llewellin and Manga, 2005]. For oscillatory flows this is governed by the dynamic capillary number, which is the ratio between the timescale over which bubbles relax to spherical shapes and the timescale over which changes in shear deformation occur,

$$C_d = \frac{\mu_l R_b}{\Gamma} \frac{\ddot{\epsilon}}{\dot{\epsilon}}. \tag{4.2.37}$$

For $C_d < 1$ bubbles will as obstacles to flow and increase bulk magma viscosity, whereas for $C_d > 1$ bubbles will act as weak regions that deform preferentially and reduce bulk magma viscosity.

Melt viscosity $\mu_l$ will be on the order of $10^1$ to $10^2$ Pa·s [Giordano et al., 2008]. Bubble radii $R_b$ in effusive Hawaiian eruptions are on the order of $10^{-4}$ to $10^{-3}$ m, though some much larger bubble slugs could be present due to coalescence [e.g., Mangan et al., 2014]. It is also likely that there would be some lateral variability in bubble size distribution depending upon the exchange flow regime [e.g., Fowler and Robinson, 2018], though for simplicity we have neglected lateral variation of all magma properties. Surface tension $\Gamma$ will be on the order of $10^{-1}$ N/m [Walker and Mullins, 1981]. The mean strain rate ratio $\ddot{\epsilon}/\dot{\epsilon}$ for a sinusoidal velocity will be approximately $2\pi/T$, so on the order of $10^{-1}$ $s^{-1}$ for these VLP events. $C_d$ will thus be on the order of $10^{-3}$ to $10^{-1}$. The presence

of larger bubbles would increase $C_d$, though when bubble slugs spanning an appreciable proportion of the conduit width are present other approximations in this model are likely no longer accurate. However, such large bubble slugs would ascend on the order of minutes and typically cause Strombolian-type bubble bursts on the lava lake surface, which are only observed intermittently [e.g., Chouet et al., 2010]. We thus assume that the conduit and lava lake are free of such large bubble slugs most of the time, and also note that if bursting bubble slugs trigger VLP resonance then said bubble slugs would be gone after the resonance onset. We thus assume that $C_d < 1$ and use the low capillary number model from Llewellin and Manga [2005] for background bulk magma viscosity,

$$\bar{\mu}(z) = \frac{\bar{\mu}_l(z)}{1 - \bar{\phi}(z)}, \tag{4.2.38}$$

where $\bar{\phi}(z)$ is background magma porosity. This relation becomes inaccurate as porosity approaches 1, such as in foam layers that might build up near the lava lake surface. Such layers will have low viscosity regardless of the parameterization used, and so will contribute negligibly to the overall viscous damping. Figure 3.18 shows the effects of temperature and volatile contents on magma properties.

Magma system geometry

In this study, we conduct all simulations using model parameters that are plausible for the Kīlauea magma system rather than focusing on more general parameter explorations. We thus present the model geometry in terms of depths and elevations that are relevant for Kīlauea. Digital elevation models of the Halemaʻumaʻu lava lake geometry are available from two times when the lava lake fully drained in 2011 and 2018 [Patrick et al., 2019b]. We approximate the

lake geometry as a vertical cylinder in all of our simulations. This is justified for the case of Kīlauea since at both times when the lava lake fully drained it's geometry was roughly cylindrical [Patrick et al., 2019b], and we also find that using a conical frustum approximation to the lava lake geometry does not produce appreciably different results in our models. There are no direct constraints on conduit geometry except for limited observations from the times when the lake drained fully, where it appears that the top of the conduit is appreciably smaller than the base of the lava lake [Carbone et al., 2013, Patrick et al., 2019b]. Previous VLP seismic modeling assuming a cylindrical conduit by [Liang et al., 2020a] indicates a most likely radius of 10-20 m. We consider conduit geometries consisting of either cylinders or conical frustums, and allow the conduit to dip at an angle $\theta$ from vertical (Fig. 4.1).

Anderson et al. [2019] inverted for reservoir geometry and rock properties by combining GPS, tilt, and InSAR data with constraints from lava lake elevation using the pitot tube relation. They found the most likely model to be a 4 $km^3$ vertically elongated ellipsoidal reservoir with centroid located 200 meters northeast of the lava lake at a depth of about 2 km and with a rock shear modulus of 3 GPa. While some previous VLP seismic inversions have inferred a source geometry of intersecting dikes [Chouet et al., 2010, Chouet and Dawson, 2011, 2013], an ellipsoidal reservoir is consistent with the collapse geometry observed in 2018 [e.g., Anderson et al., 2019], with previous geodetic inversions [e.g., Baker and Amelung, 2012, Poland et al., 2014], and previous work combining modeling with VLP seismic inversions [Crozier et al., 2018a, Liang et al., 2020a]. We thus adopt the ellipsoidal reservoir geometry and rock shear modulus found by Anderson et al. [2019] as the reference scenario for our simulations.

The simplified scenario considered in section 4.2 permits an easy examination of the relative importance of restoring forces from gravity and reservoir storativity for our assumed Kīlauea magma system geometry. The expression for elastic compressibility of an ellipsoidal reservoir is not shown here as it is somewhat messy [Cervelli, 2013], but given that the aspect ratio of the Halema‘uma‘u reservoir is close to one we approximate its compressibility as $\beta_c = 2.5 \times 10^{-10}$ Pa$^{-1}$ from the spherical reservoir expression in Eq. 4.2.9. Magma compressibility in the reservoir could range from $\sim 10^{-9}$ to $10^{-10}$ Pa$^{-1}$ [Liang et al., 2020a], from which Eq. 4.2.8 gives reservoir storativity of $\sim$1 to 5 m$^3$/Pa. For a conduit radius of 10 m the reservoir storativity restoring force term in Eq. 4.2.29 will range from $\sim$60 to 300 N/m$^3$. The density difference across the conduit will likely be at least $\sim$1000 kg/m$^3$ [Liang et al., 2020a]. The gravity restoring force term in Eq. 4.2.29 will thus be at least $\sim 10^4$ N/m$^3$, which is an order of magnitude larger than the reservoir storativity term. This is consistent with a similar analysis in Liang et al. [2020b]. Simulations with the non-simplified model for our assumed Kīlauea magma system geometry also verify that reservoir storativity has a negligible impact on $T$ and $Q$ in this system. We thus fix the compressibility of magma in the reservoir to $5 \times 10^{-10}$ Pa$^{-1}$ for all simulations.

Figures 4.2 and 4.3 show the effects of various magma system geometries and magma properties on $T$ or $Q$ in the density-based and volatile-based approaches. We note that for the density-based magma properties, lava lake elevation and magma properties in in the lava lake do not appreciably effect $T$ or $Q$ (Fig. 4.2). This occurs because the much larger surface area of the lava lake means that the viscous damping, inertial, and gravitational terms are minimal in the lava lake relative to the conduit. However, in the volatile-based scenario both

lava lake elevation and magma properties in the lake do effect $T$ and $Q$ (Fig. 4.3). This is because changing the total mass of magma in the lava lake changes the magmastatic pressure load on the conduit, and so can significantly effect the magma properties in the conduit by changing volatile solubility. This will inform interpretation of inverted changes in magma properties, and illustrates the importance of using a volcanologically informed background state model.

Prescribing magma system geometry for inversions

We will use the conduit-reservoir resonance model and solution method outlined in Eqs. 4.2.18-4.2.26 to conduct inversions for three properties associated with each VLP event: $T$, $Q$, and geodetically inverted reservoir pressure (discussed in section 4.2). VLP ground motions during each event are another potential fitting parameter. However, we do not include these for reasons discussed later in this section. We interpolate between measurements in Patrick et al. [2019b] to directly prescribe lava lake surface elevation and lava lake radius at the time of each event. With only three fitting parameters and one fixed parameter, there are too many poorly constrained parameters in the conduit-reservoir model to uniquely invert for all unknown parameter values. This can be readily inferred from the overlapping effects of various parameters in figures 4.2 and 4.3, and also seen in stochastic inversions for the simpler conduit-reservoir resonance model in Liang et al. [2020a]. The primary goal of this study is to resolve relative changes in magma properties over time, rather than attempting to solve for all possible configurations of the magma system that might be consistent with the data at a given time. We will thus seek to make assumptions and approximations that are reasonable over limited timescales to reduce the number of free parameters.

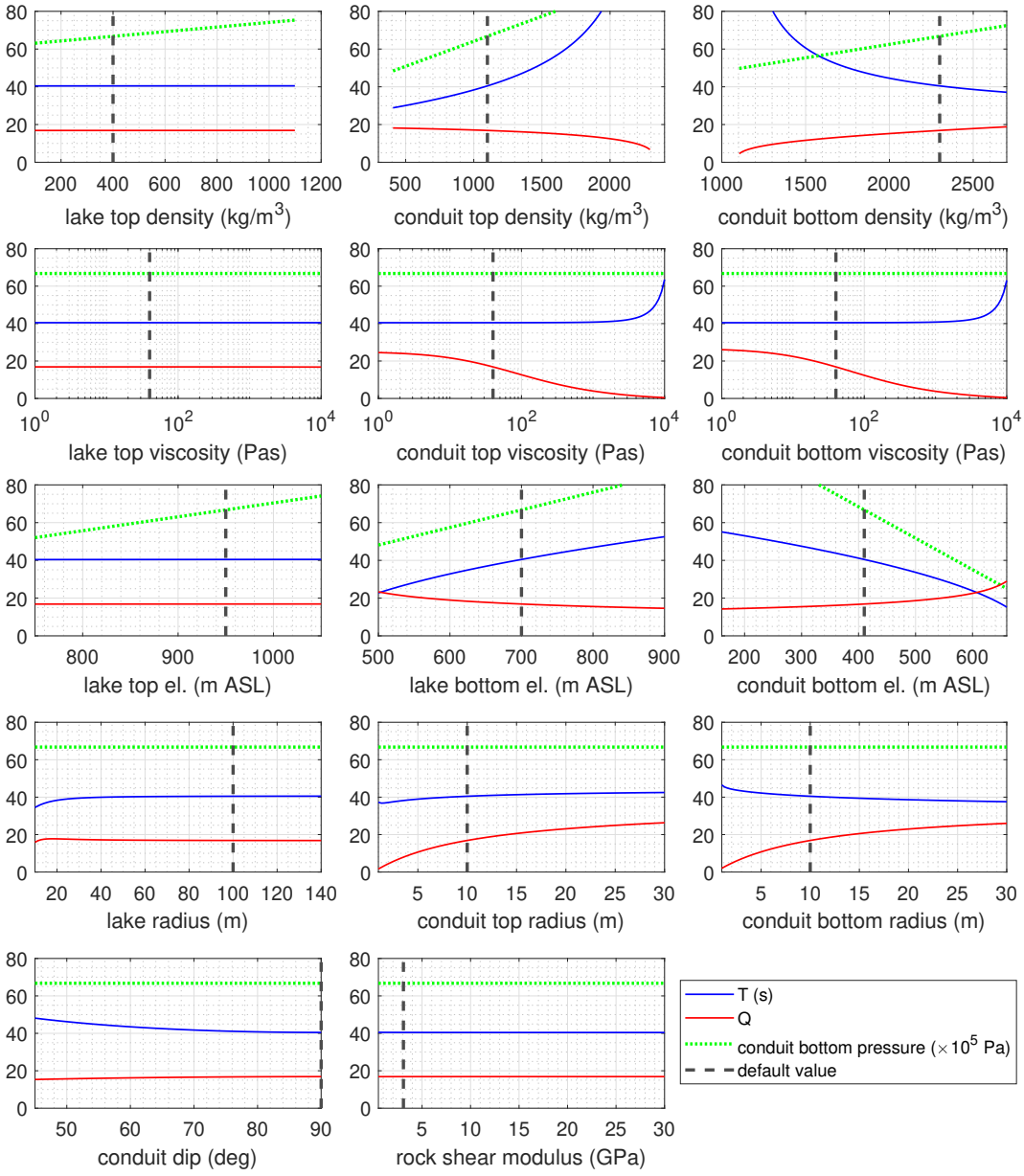


FIGURE 4.2. Predicted variation in $T$, $Q$, and pressure at the bottom of the conduit (or top of the reservoir) due to varying density-based model parameters in isolation. Here we assume an ellipsoidal reservoir geometry as in table 2 (with vertical semi-diameter adjusted for consistency with the varied conduit length) and fix compressibility of magma in the reservoir to $5 \times 10^{-10}$ Pa$^{-1}$. Dashed black lines indicate the default value of each parameter used to make the other plots.

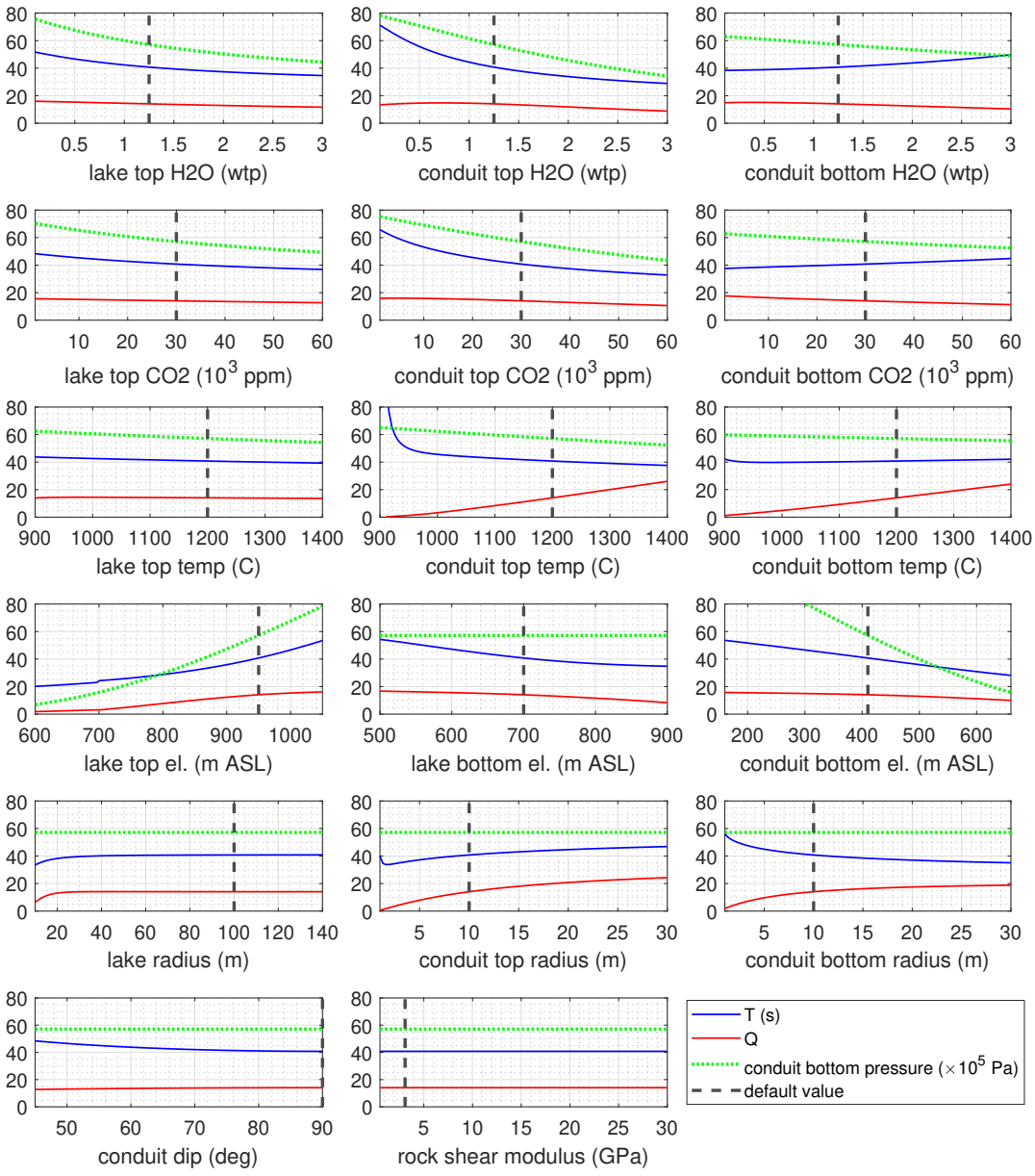


FIGURE 4.3. Predicted variation in $T$, $Q$, and pressure at the bottom of the conduit (or top of the reservoir) due to varying volatile-based model parameters in isolation. Here we assume an ellipsoidal reservoir geometry as in table 2 (with vertical semi-diameter adjusted for consistency with the varied conduit length) and fix compressibility of magma in the reservoir to $5 \times 10^{-10}$ Pa$^{-1}$. Dashed black lines indicate the default value of each parameter used to make the other plots.

One way to significantly reduce the number of free parameters is to assume that the geometry of the shallow subsurface magma system remains constant. The term subsurface here is used to exclude lava lake radius, which we can constrain from observations as mentioned above. We still include lava lake bottom elevation in the parameters being treated as constant, since there are only two measurements (in 2011 and 2018) which is not enough to reasonably interpolate between.

The assumption of constant magma system geometry is likely not accurate over the whole timespan, where analysis of ground motions indicates that there are some changes at least in reservoir geometry [Crozier and Karlstrom, 2021]. However, the exact nature and timing of these changes is difficult to resolve from either VLP seismic or geodetic data. There is significant noise in ground motions that would cause artificial variation in the inverted reservoir geometry over time [Anderson et al., 2015, Crozier and Karlstrom, 2021]. This would then cause artificial variation in other model parameters of interest. Temporal regularization that penalizes rapid and/or strong variation in some of the parameters, such as those governing subsurface magma system geometry, could be imposed. However, the choice of how to impose this regularization would be inherently arbitrary without a physics based model informing the evolution of magma system geometry, and would introduce additional complexity around presenting the uncertainty from this choice. Additionally, since the conduit-reservoir resonance at Kīlauea is insensitive to reservoir compressibility, the only changes in reservoir geometry that matter for this model will be those that raise or lower the reservoir roof elevation (thus changing conduit length). Changes in conduit shape also impact the resonance, but are even more difficult to directly constrain since the conduit

will generally be much less compliant than the underlying reservoir and so have a comparatively minimal contribution to VLP seismic and geodetic ground deformation [Liang et al., 2020b].

While we see self-consistent inversion involving changes in the plumbing system geometry as a promising future direction and a grand challenge in volcanology, it is outside the scope of this study. Prescribing a fixed subsurface magma system geometry thus better facilitates resolving relative changes in magma properties on timescales of years or less, although we note where where changes in the geometry might occur and interpret our results around these times accordingly. Table 2 shows the magma system geometry we prescribe.

We can consider various processes that might modify the subsurface magma system geometry to evaluate the timescales and conditions over which the assumption of constant geometry is likely to be accurate. Changes in conduit length (from changing reservoir-roof height) on the order of tens of meters or changes in conduit radius on the order of meters are required to appreciably impact VLP properties (Fig. 4.2, 4.3). Changes in geometry might occur gradually due to processes such as viscous deformation of the host rock, thermal erosion of the host rock, and crystallization/melting at the magma/rock interface. These processes can probably be neglected on timescales less than a year. Changes in the conduit shape could also occur either abruptly or gradually due to changes in the local stress field, which could be caused by inflation/deflation of the magma reservoirs, intrusions, slow-slip events, or the May 2018 M7 earthquake. All of these occur at known times, and so the possibility that they are influencing the conduit shape can be considered when interpreting our results. Lastly, changes in both conduit shape and reservoir roof height might occur due to mechanical failure

TABLE 2. Fixed parameters used in gradient descent inversions for magma properties

| **parameter** | **default value** | **units** |
|---|---|---|
| conduit and lava lake geometry | | |
| lava lake bottom elevation | 700 | m ASL |
| conduit bottom elevation | 410 | m ASL |
| conduit top radius | 10 | m |
| conduit bottom radius | 10 | m |
| conduit dip | 90 | degrees |
| conduit length | 290 | m |
| Halemaʻumaʻu reservoir | | |
| Halemaʻumaʻu reservoir centroid elevation | -840 | m ASL |
| Halemaʻumaʻu reservoir centroid latitude | 19.4090 | degrees |
| Halemaʻumaʻu reservoir centroid longitude | -155.2788 | degrees |
| Halemaʻumaʻu reservoir vertical semi-diameter | 1250 | m |
| Halemaʻumaʻu reservoir horizontal semi-diameter | 915 | m |
| Halemaʻumaʻu reservoir aspect ratio | 1.23 | |
| Halemaʻumaʻu reservoir volume | 3.94 | $km^3$ |
| Halemaʻumaʻu reservoir magma compressibility | $5 \times 10^{-10}$ | $Pa^-1$ |
| South Caldera reservoir | | |
| South Caldera reservoir centroid elevation | -4000 | m ASL |
| South Caldera reservoir centroid latitude | 19.3900 | degrees |
| South Caldera reservoir centroid longitude | -155.2710 | degrees |
| South Caldera reservoir radius | 1928 | m |
| South Caldera reservoir aspect ratio | 1 | |
| South Caldera reservoir volume | 30 | $km^3$ |
| other | | |
| rock shear modulus | 3.08 | GPa |
| density-based inversions | | |
| lava lake top density | 300 | $kg/m^3$ |
| baseline conduit bottom pressure | 2.6 | MPa |
| volatile-based inversions | | |
| $H_2O$:$CO_2$ mass ratio | 1 | |
| baseline conduit bottom pressure | 2.4 | MPa |
| melt composition | [a] | |

[a] average glass composition data from Table 7 in Edmonds et al. [2013]

along the magma-rock interface, as was observed along the overlook crater walls. Even with detailed geophysical analysis, it would likely be difficult to place robust constraints on when all of such events might have occurred or on the rate at which they might have caused changes in the subsurface magma system geometry.

*Geodetic inversions for reservoir pressure change*

An open hydraulic connection between the lava lake and underlying Halemaʻumaʻu reservoir implies that reservoir pressure depends upon the total mass of the overlying magma column, and that the lava lake acts as a pitot tube indicator of reservoir pressure [e.g., Patrick et al., 2015, Anderson et al., 2019]. Changes in the average density of the magma column over a given time window can thus be calculated if the corresponding changes in lava lake elevation and reservoir pressure are both known. This will provide an important constraint on possible density/volatile depth profiles at a given time. As discussed in section 4.2, we use the multi-data inversion results of Anderson et al. [2019] to prescribe Halemaʻumaʻu reservoir geometry and rock shear modulus (table 2), from which ground deformation data can then be used to invert for relative pressure changes.

Geodetic data and inversions suggest that other processes contribute to ground deformation around Kīlauea's summit in addition to the Halemaʻumaʻu reservoir. The central south flank of Kīlauea has been sliding southward for decades at a relatively steady background rate [e.g., Owen et al., 2000]. We correct for the steady background motion using the source model of [Owen et al., 2000] which consists of slip along low-angle normal faults as well as opening and strike-slip motion along segments of the east rift zone (Fig. 4.4).

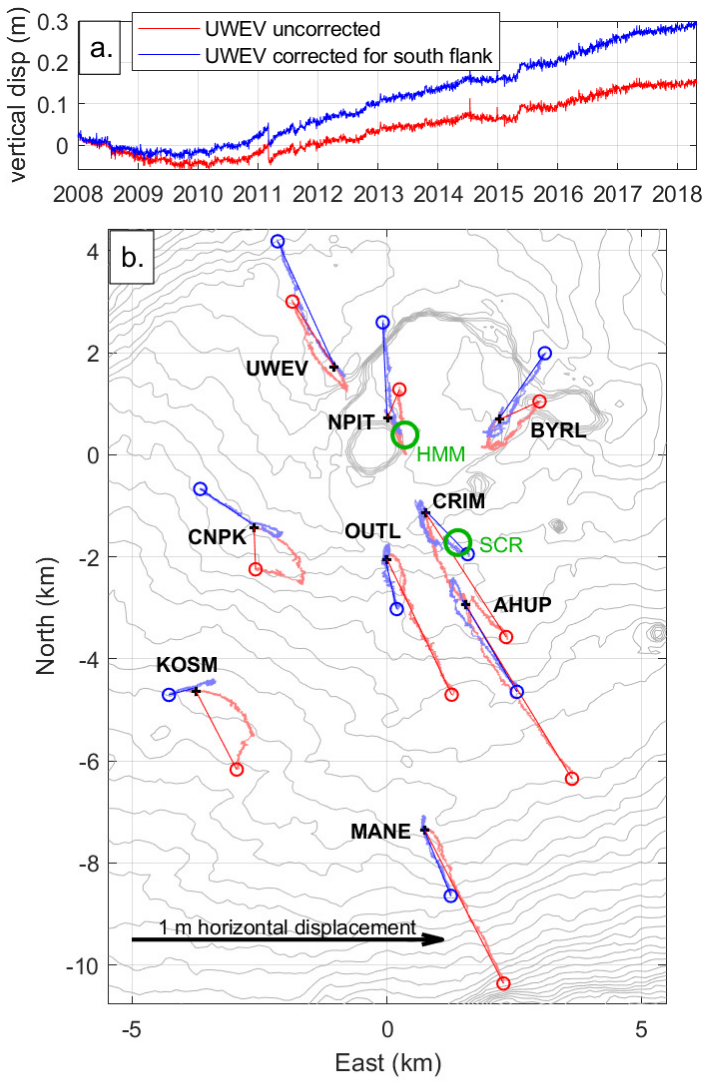


Figure 4.4 (a) Vertical ground displacement at GPS station UWEV. (b) Map of GPS stations and horizontal ground displacements from 2008-2018. Red lines are corrected for flank motion and blue are uncorrected. Lighter red and blue lines show the GPS displacement over time from Jan 1 2008 (black plus symbols) to May 1 2018 (red and blue circles). Straight red and blue lines show the net 2008 to 2018 displacement vectors. The inferred centroid locations of the Halemaʻumaʻu (HMM) and South Caldera (SCR) reservoirs are shown by green circles. UTM zone 5Q.

A deeper Kilauea magma storage zone termed the South Caldera reservoir also contributes significantly to ground deformation on timescales of years or more, and possibly also on timescales of days or less such as during deflation-inflation events [e.g., Baker and Amelung, 2012, Poland et al., 2014, Anderson et al., 2020]. The nature of the hydraulic connections between the South Caldera reservoir, Halemaʻumaʻu reservoir, and ERZ are not known and could have changed over time [e.g., Anderson et al., 2020]. The 2015 magma intrusion also caused significant ground deformation centered south of the Kīlauea summit vent, though shallower and farther west than the previous South Caldera reservoir deformation centroid [Johanson et al., 2016, Bemelmans et al., 2021]. Here we account for deformation from the South Caldera reservoir by jointly inverting for pressurization of the Halemaʻumaʻu and South Caldera reservoirs (Fig. 4.5).

We assume a horizontal centroid location of the South Caldera reservoir based on previous inversions in Poland et al. [2012] (Fig. 4.4, table 2). The depth and geometry of the South Caldera reservoir are less well constrained than its horizontal centroid location [e.g., Baker and Amelung, 2012, Poland et al., 2014]. For simplicity we assume an ellipsoidal reservoir geometry, which can be used to test a range of centroid depths, volumes, and aspect ratios (height/width) as detailed later in this section.

For both reservoirs we use the analytical source model for an ellipsoid in an elastic half space from Cervelli [2013]. We use daily average position solutions from Nevada Geodetic Laboratory [Blewitt et al., 2018] for GPS/GNSS stations within a few km of the Halemaʻumaʻu and South Caldera reservoirs: CRIM, OUTL, UWEV, AHUP, BYRL, CNPK, NPIT, KOSM, and MANE (Fig. 4.4). We do not use higher frequency GPS solutions due to significant noise, and do not

include tilt-meter data due to artificial drift that can be significant at timescales of months or longer. We find that Fourier domain first-order topography corrections [Williams and Wadge, 2000] change inverted pressures by less than 1%, so we do not include them for consistency with the south flank motion corrections which were derived without topography. For each time $t$ we use a linear least-squares inversion to jointly solve for pressure changes in the two reservoirs that best fit the observed displacement vector $\vec{U}$ (which includes all three components of all available stations) (Fig. 4.5),

$$\vec{U}(t) = \begin{bmatrix} & \\ \vec{G}_{HMM} & \vec{G}_{SCR} \\ & \end{bmatrix} \begin{bmatrix} P_{HMM}(t) \\ P_{SCR}(t) \end{bmatrix}, \tag{4.2.39}$$

where $\vec{G}_{HMM}$ and $\vec{G}_{SCR}$ are the Green's function vectors for the Halema‘uma‘u and South Caldera reservoirs, $P_{HMM}$ and $P_{SCR}$ are pressures in the two reservoirs, and brackets indicate concatenation.

South Caldera reservoir centroid depth and aspect ratio (height/width) both have relatively minimal effects on inverted pressure variations in the Halema‘uma‘u reservoir on short timescales (a year or less), where we will be focusing most of our analysis. However, increasing either parameter causes the inversions to assign more of the long-term deformation to the South Caldera reservoir, which decreases the magnitude of the longer term inflationary trend in Halema‘uma‘u reservoir pressure. We find that the South Caldera reservoir needs to be relatively deep and/or vertically elongated to produce time-series of pressure in the Halema‘uma‘u reservoir that are consistent with observed lava lake elevation. This is due to the pitot tube relation discussed above, which allows timelines of magmastatic pressure

changes to be calculated from lava lake elevation given an assumed average magma column density. For example, we show approximate bounds on such magmastatic pressure changes in figure 4.5 that were calculated assuming lower and upper bounds on average magma column densities of 1000 and 2700 kg/m$^3$.

Since previous studies have found either vertically shortened or spherical South Caldera reservoir geometries, we assume a spherical geometry. The volume of a spherical reservoir does not significantly effect ground deformation patterns [e.g., Segall, 2010] and thus does not impact inverted Halemaʻumaʻu reservoir pressure, so we just fix the South Caldera reservoir volume to 30 km$^3$. South Caldera reservoir centroid elevations of less than around -3 km ASL (depths of ∼4 km) can produce a feasible time-series of Halemaʻumaʻu reservoir pressure changes. We choose a reference South Caldera reservoir centroid elevation of -

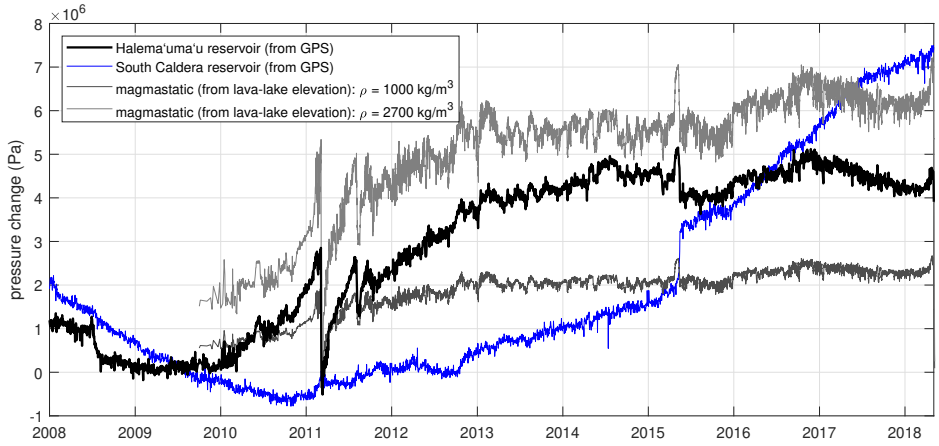


FIGURE 4.5. Joint GPS inversions for pressure change over 2008-2018 in the Halemaʻumaʻu and South Caldera reservoirs. Here we use the median Halemaʻumaʻu reservoir and host rock parameters from Anderson et al. [2019] and a South Caldera reservoir centroid elevation of -4 km ASL (depth of ∼5 km), aspect ratio of 1, and volume of 30 km$^3$. Magmastatic pressure changes calculated from lava lake elevation data with assumed average magma column densities of 1000 and 2700 kg/m$^3$ (approximate lower and upper bounds) are shown for comparison.

4 km ASL, which is at the lower end of the range found in previous studies [Baker and Amelung, 2012, Roman and Lundgren, 2021]. However, we also test the effects of other South Caldera reservoir depths on our results. Such tests will also help account for the uncertainty in the aspect ratio, since we find empirically that the two parameters have nearly identical impacts on inverted Halemaʻumaʻu reservoir pressure changes.

The joint inversions for pressure in the Halemaʻumaʻu and South Caldera reservoirs assign most of the deformation from the 2015 magma intrusion to the South Caldera reservoir, indicated by the step increase in our inverted south-caldera reservoir pressure at this time (Fig. 4.5). We find that including an additional source in the inversions for the 2015 intrusion following [Bemelmans et al., 2021] does not yield significantly different Halemaʻumaʻu reservoir pressure changes. We thus expect that the joint inversions provide a sufficient correction for this intrusion for obtaining Halemaʻumaʻu reservoir pressures. However, we exercise caution in interpreting our results at the time of the intrusion.

*Inversions for magma properties*

Grid searches over more than three free parameters

If we choose to parameterize the system such that there are four or more free parameters, a unique solution will generally not exist since there are only three parameters we fit for each event (period, quality factor, and pressure at the base of the conduit). Grid searches provide a simple and robust way to explore the range of possible mamga properties that can match the constraints for a given event. We define misfit $E$ for each free parameter combination with a weighted normalized L1

norm cost function:

$$E = W_T \frac{T - T^*}{T^*} + W_Q \frac{Q - Q^*}{Q^*} + W_P \frac{P_0 - P_0^*}{P_0^*} \tag{4.2.40}$$

where the asterisk $^*$ indicates observed/target values and $P_0$ is pressure at the bottom of the conduit. We set weights $W_T$ and $W_Q$ to one, and set weight $W_P$ to ten due to the smaller normalized variance in $P_0$ than in $T$ and $Q$. Given a misfit grid over the parameter space, we can readily evaluate the range of parameters that can match the data by examining the minimum misfit that can be produced for a given parameter value or combination of parameter values (Fig. 4.6, 4.7). We also show probability density functions (PDFs, Fig. 4.6, 4.7). For this we follow common practice of defining likelihood as the exponential of negative error. To calculate a PDF over a single parameter $\tilde{A}$ we sum over the likilihood of the set of remaining parameters $\{\tilde{B}, \tilde{C}, ..., \tilde{Z}\}$,

$$\text{PDF}\left(\tilde{A}_a\right) = \phi \sum_b \sum_c ... \sum_z e^{-E\left(\tilde{A}_a, \tilde{B}_b, \tilde{C}_c, ..., \tilde{Z}_z\right)}, \tag{4.2.41}$$

and similarly for PDFs over two parameters $\tilde{A}$ and $\tilde{B}$ we sum over remaining parameters $\{\tilde{C}, \tilde{D}, ..., \tilde{Z}\}$,

$$\text{PDF}\left(\tilde{A}_a, \tilde{B}_b\right) = \phi \sum_c \sum_d ... \sum_z e^{-E\left(\tilde{A}_a, \tilde{B}_b, \tilde{C}_c, \tilde{D}_d, ..., \tilde{Z}_z\right)}, \tag{4.2.42}$$

where $E$ is misfit and $a, b, c, d, ..., z$ indicate the values of each parameter. The normalizing scale factor $\phi$ would typically be chosen so that all values of the PDF integrate to one. However, since some of our parameters vary logarithmically we instead scale each PDF by the total number of parameter values in it. The PDFs

as presented will thus not integrate to 1, but interpreting how well constrained and/or unique a solution is only depends upon relative PDF values. This scaling also facilitates easier visual comparison of PDFs between parameters with different ranges.

For density-based magma properties, we reduce the free parameters by using a uniform viscosity, since the effects of viscosity at the top and bottom of the conduit are nearly identical and since the effect of viscosity in the lava lake is negligible (Fig. 4.2). We show an example grid search where we have reduced the model to four free parameters: (1) uniform magma viscosity, magma-density at the (2) bottom of the conduit, (3) top of the conduit, and (4) top of the lava lake (Fig. 4.6). In this example, we picked representative target values from the 2013-2016 time segment of $T^* = 40$ s, $Q^* = 20$ s, and $P_0^* = 5$ MPa. We chose a uniform conduit radius of 10 m, lava lake radius of 100 m, and lava lake top elevation of 950 m. In this case, even though there are more free parameters than fit parameters, all four free parameters exhibit a single global minimum in minimum misfit and a single global maximum in PDF. However, the global minimum in minimum misfit for all three density parameters are somewhat broad, so solutions can still be found over a range of these parameters.

For volatile-based magma properties, both $CO_2$ and $H_2O$ contents have strong effects on the simulations. However, as the effects of both volatiles are similar at a given depth (Fig. 4.3), allowing both to vary would result in strong trade-offs and non-uniqueness. We thus impose a fixed mass ratio of total $H_2O$ to total $CO_2$ and vary the total (dissolved plus exsolved) combined volatile contents. We chose a 1:1 mass ratio (where 1 wt% $H_2O$ corresponds to $1.4\times10^4$ ppm $CO_2$), which is within the range of inferred parent magma volatile ratios [e.g., Edmonds

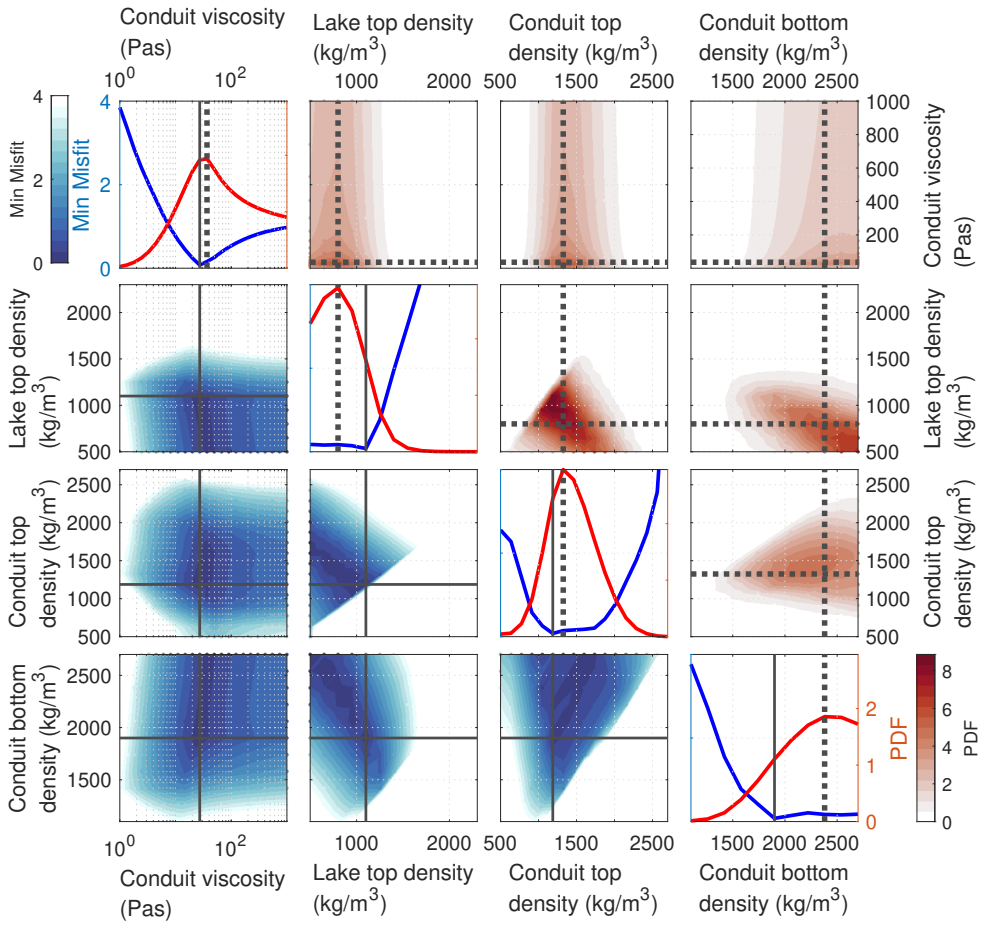


FIGURE 4.6. Grid search inversion for density-based magma properties with fixed geometry. Lava lake elevation was set to 950 m. The target values for period, quality factor, and pressure at the bottom of the conduit were set to 40 s, 20, and 5 MPa. Solid black lines indicate the parameter value where the minimum misfit is found, and dotted black lines indicate the parameter value where the maximum PDF is found.

et al., 2015] (see additional discussion of this ratio in section 4.2). We show an example grid search with four free parameters: (1) uniform magma temperature, total volatile contents at the (2) bottom of the conduit, (3) top of the conduit, and (4) top of the lava lake (Fig. 4.7). In this example, we picked representative target values from the 2013-2016 time segment of $T^* = 40$ s, $Q^* = 20$ s, and $P_0^* = 5$ MPa. We chose a uniform conduit radius of 10 m, lava lake radius of 100 m, and lava lake top elevation of 950 m. There is a single global minimum in minimum misfit and a single global maxima in PDF for magma temperature. However, none of the volatile parameters exhibit clear local minima in minimum misfit, so solutions can be found over a wide range of these parameters.

These grid searches help illustrate the limit to how well we can resolve magma properties without additional constraints, even with only four free parameters. In general, adding more free parameters (e.g., by including more piecewise depth segments in magma properties) results in more parameter trade-offs and non-uniqueness. Such non-uniqueness would make evaluating potential differences in parameters between events difficult, and thus hinder our primary goal of examining relative changes in the magma system over time.

Gradient descent inversions for three free parameters

Our primary goal of identifying relative changes in magma properties over time will be best facilitated by conducting inversions with a small enough number of free parameters that there is no non-uniqueness in the solutions for each event. This will allow changes between events to be readily analyzed. To conduct inversions over the whole event timeline, we thus consider only three free parameters, which matches the number of fitting parameters (period, quality

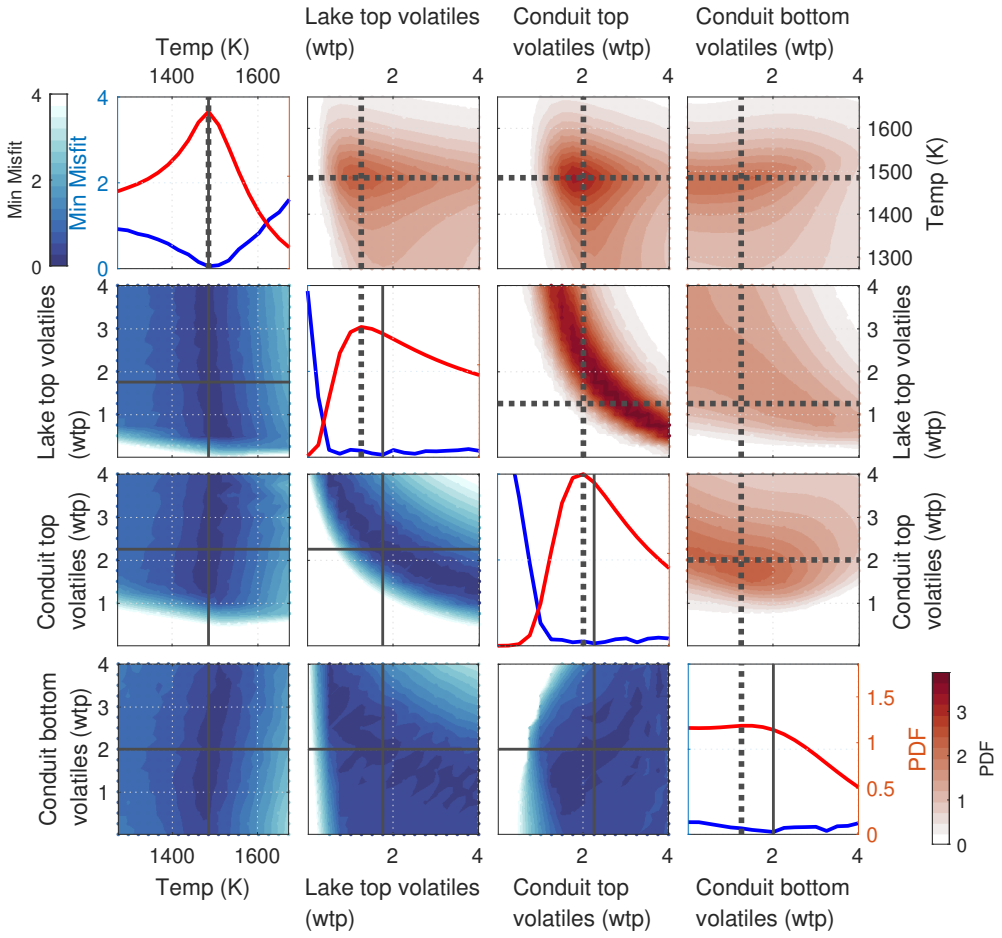


FIGURE 4.7. Grid search inversion for volatile-based magma properties with fixed geometry. Lava lake elevation was set to 950 m. The target values for period, quality factor, and pressure at the bottom of the conduit were set to 40 s, 20, and 5 MPa. Solid black lines indicate the parameter value where the minimum misfit is found,

factor, and pressure at the base of the conduit). The existence of unique solutions is still not necessarily guaranteed due to the nonlinearity of the system, but in practice we find that this is not an issue. We use an iterative gradient-descent solver (the trust-region-reflective algorithm in Matlab's lsqnonlin function) to find the combination of free parameter values that minimizes misfit with the fitting parameters according to Eq. 4.2.40.

In the density-based inversions, we reduce the number of free parameters to three by again assuming a uniform magma viscosity and by also prescribing a fixed magma density at the top of the lava lake, since magma density at the top of the lava lake does not appreciably impact predicted values of $T$ or $Q$ in the density-based simulations (Fig. 4.2). The three free parameters are thus: (1) magma density at the conduit top, (2) magma density at the conduit bottom, and (3) uniform magma viscosity. For easier interpretation and for consistency with Liang et al. [2020a], we present density in terms of the average value in the conduit and the difference between the top and bottom of the conduit.

In the volatile-based inversions, we impose a fixed mass ratio of total $H_2O$ to total $CO_2$ and vary the total (dissolved plus exsolved) combined volatile contents. As with the grid searches, this avoids the tradeoffs that would occur if $H_2O$ and $CO_2$ were allowed to vary independently since they have similar effects on $T$ and $Q$. However, by still including both volatile species we will obtain more feasible magma profiles than would be obtained from considering only one volatile species due to joint solubility effects. In reality, there is likely variation in the ratio between $H_2O$ and $CO_2$ (and also sulfur species), both due to variation in the parent magma volatile contents and variation in the magma outgassing regime. Because $CO_2$ will begin exsolving in significant quantities at depths beneath the

Halema‘uma‘u reservoir, it could exhibit strong variation at all depths in the shallow magma system due to changes in the overall "$CO_2$ fluxing" regime. While $H_2O$ will generally not exsolve in significant quantities until the upper part of the Halema‘uma‘u reservoir or the conduit (depending mainly upon magmastatic pressure and the amount of $CO_2$ present), it could still exhibit significant variation at depth due to convection.

We chose a one-to-one volatile mass ratio (or 1 wt% $H_2O$-to-$1.4\times10^4$ ppm $CO_2$), which is within the range of inferred parent magma volatile ratios [e.g., Edmonds et al., 2015]. Changing the ratio does have a small impact on the inverted volatiles for a given event, but a negligible impact on the qualitative patterns of variation in inverted volatiles over time. To reduce the number of free parameters further, we assume a uniform magma temperature as in the grid searches. We also assume uniform volatile contents in the lava lake, which we set equal to the volatile contents at the top of the conduit. We chose this assumption since volatiles at the top of the lava lake effect predictions of $T$ and $Q$ in a similar manner but to a lesser extent than volatiles at the top of the conduit (Fig. 4.3), and for consistency with the density-based inversions. The free parameters are thus: (1) uniform magma temperature, total volatile contents at the (2) conduit top, and (3) conduit bottom. For easier interpretation and consistency with the density-based inversions, we present total volatile contents in terms of the average value in the conduit and the difference between the top and bottom of the conduit (Fig. 4.8).

Table 2 lists all of the fixed parameters that are used for these time-series inversions (including those used in the joint inversions for reservoir pressure changes). To evaluate the robustness of the inverted relative changes in magma

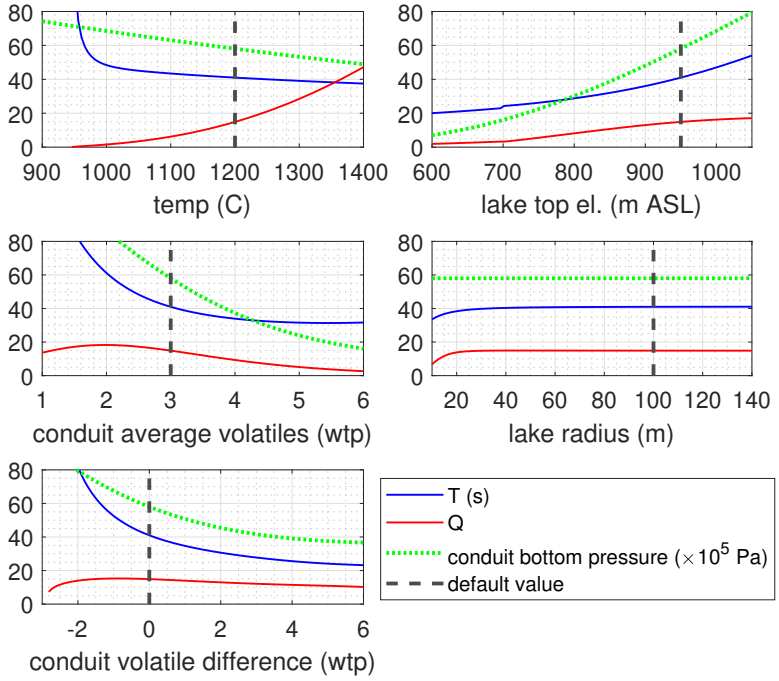


FIGURE 4.8. Effects of the parameters that we vary over time in the volatile-based inversions on $T$, $Q$, and pressure at the bottom of the conduit (or top of the reservoir). Dashed black lines indicate the default value of each parameter used to make the other plots.

properties, we conduct the time-series inversions with several different values of the fixed parameters that most strongly impact simulations. We note that such tests will not directly account for the potential temporal variation in fixed parameters, which could only be properly considered by treating them as free parameters in the inversions.

## Results

### *Density-based inversions*

We show the timeline of magma properties obtained from density-based inversions in figure 4.9. We emphasize that these inversions should be interpreted as showing relative changes in magma properties, since the whole timeline of parameter values would shift up/down depending on the assumed value of other poorly constrained parameters such as subsurface magma system geometry (table 2). The impact of varying any one such parameter can be roughly inferred from figure 4.2. Caution should additionally be taken in directly comparing magma properties separated by multiple years, as over longer timescales it is more likely that changes in the magma system geometry are also occurring or that there is artificial drift in the inverted reservoir pressure change.

There is over an order of magnitude of variation in inverted viscosity on timescales ranging from days to years. For the majority of the 2009-2018 timespan magma viscosity exhibits a clear inverse relationship with $Q$ (Fig. 4.9), consistent with the strong impact of viscosity on $Q$ (Fig. 4.2). Part of the large scatter in viscosity on shorter timescales is likely related to noise in the estimates of $Q$, which is inherently less well constrained than $T$ [Crozier and Karlstrom, 2021]. This is supported by the observation that inverted densities, which are less

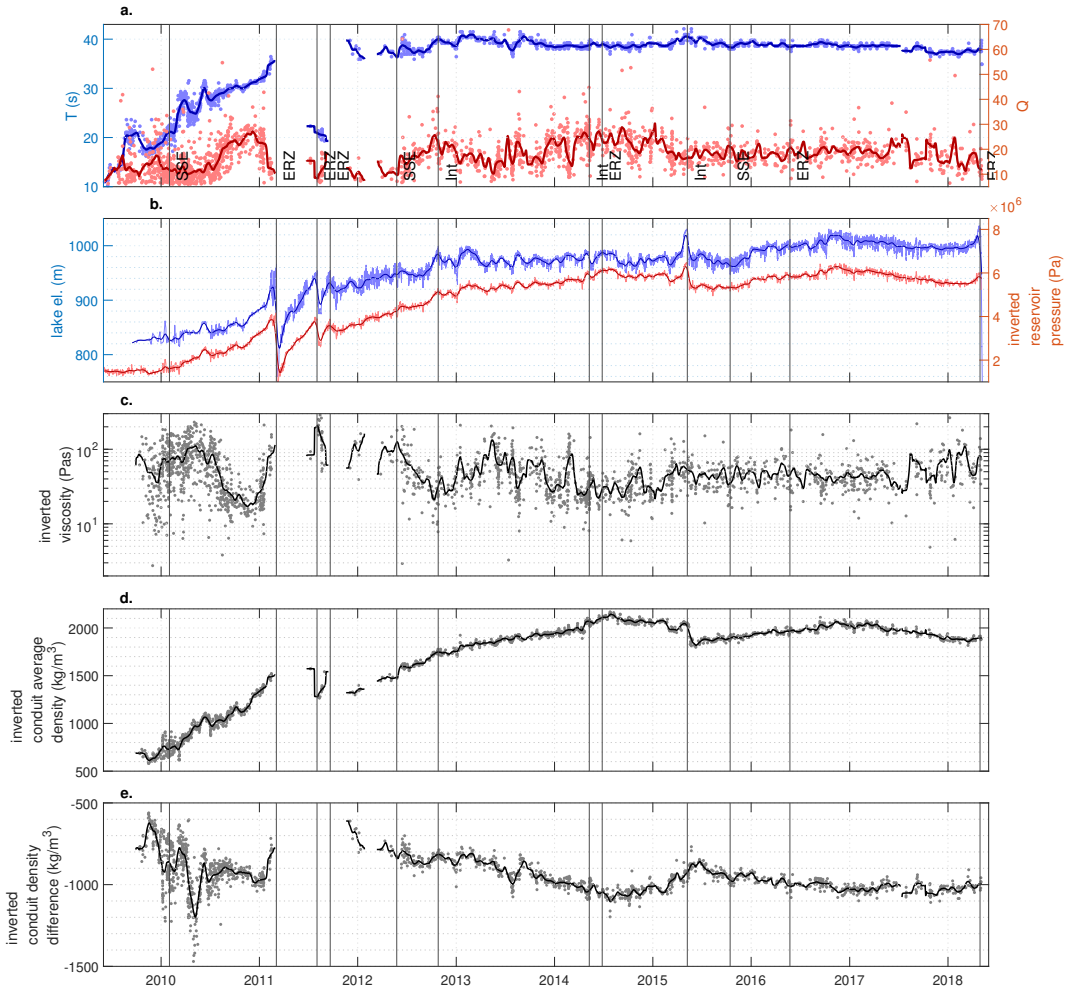


FIGURE 4.9. Inversion for density-based magma properties from 2009-2011, with fixed parameters from table 2. (a) Period (blue) and quality factor (red) of VLP events shown by colored dots; colored lines show 30-day moving averages. SSE indicates slow-slip-events and ERZ indicates East-Rift-Zone eruptions. (b) Lava lake elevation (blue) and the reservoir top pressure values we obtain from geodetic inversions for pressure change added to an assumed baseline pressure. (c) Inverted viscosity. (d) Inverted average magma density in the conduit. (e) Inverted conduit magma density difference (top minus bottom).

sensitive to $Q$, exhibit much less scatter. This contrasts with our expectation that the strongest variability on short timescales would occur in density, since bubbles can move and accumulate rapidly in the shallow magma system and have a stronger impact on density than viscosity. Temporally averaged values of viscosity are more likely to be robust, and still exhibit up to an order of magnitude of variation over timescales from weeks to years. Given the large scatter in viscosity, the event temporal density is generally not high enough to determine if there are robust changes in viscosity on timescales of days or less.

Throughout the timespan, average density roughly tracks lava lake elevation, inverted reservoir pressure, and $T$ (all of which are generally well correlated with each other [Crozier and Karlstrom, 2021]). With the shallow magma system geometry used, these simulations cannot produce the periods of less than $\sim$20 s in 2009 and early 2010 with feasible magma density values, regardless of the choice of baseline reservoir pressure. We thus do not expect the inverted densities at this time are accurate, which we elaborate on in the discussion section. A similar issue also exists for the isolated cluster of low period events in mid-2011. A positive relation between average magma density and lava lake elevation is expected since changing lava lake elevation is essentially shifting the whole stratified magma column up or down. This occurs because increasing lava lake elevation will increase the pressure at a given elevation in the conduit, which will generally increase density due to both compression of the gas phase and volatile resorption. This makes it difficult to infer potential changes in 'inherent' properties of the magma (such as volatile contents) from these average densities, and highlights an important advantage of the volatile-based inversions.

Conduit magma density difference roughly tracks lava lake elevation on timescales of days to months. This is also potentially consistent with a vertical shifting of the whole magma column if the density gradient is more gradual at greater depths. Such a density profile would generally be expected unless the volatile contents increase significantly with depth. Whether the variation in density difference can be fully explained by an upward/downward shifting of the magma column or also indicates other changes will be best addressed with the volatile-based inversions.

*Volatile-based inversions*

We show the timeline of magma properties obtained from the volatile-based inversions in figure 4.10. As with the density-based inversions, we emphasize that these should be interpreted as showing relative changes in magma properties over timescales of years or less, where the assumption of a fixed subsurface magma system geometry is more likely to be accurate. Figure 4.3 can be used to roughly infer how the timeline of parameter values might shift in response to different assumed values of the various poorly constrained fixed parameters (table 2). These are the inversions upon which we focus most of our analysis, as they provide more volcanologically relevant insight than the density-based inversions. We show moving 90-day correlation coefficients between the inverted magma properties and observations in figure 4.11). This provides a rough indication of how the various inverted parameters and data are related over time, although it will not resolve how these relations depend on timescales. We thus also show spectral coherence and phase lag between lava lake elevation and the inverted magma properties in figure 4.12 and 4.13. For calculating coherence and phase lag, the magma

properties were first resampled at uniform 4 hr intervals via linear interpolation, then analyzed with Morlet wavelets. Because at times VLP events are spaced several days or more apart, we note that coherence and phase lag on timescales of days will not always be well resolved.

Most of the inverted magma temperatures after 2011 fall within the ∼1150-1300 C range of geochemical estimates [e.g., Edmonds et al., 2013], although many of the pre-2011 temperatures and isolated outliers throughout the timespan are higher. That higher scatter is observed in inverted magma temperature than in inverted volatile contents indicates that noise in the estimates of $Q$ likely contributes to some of these outliers, as occurred with viscosity in the density-based inversions. The large variability in temperature could also reflect some combination of real variability that was not captured in the geochemical samples and changes in conduit radius (which would strongly impact inverted values of temperature). The temporally-averaged temperature variations are more likely to be robust, and still exhibit up to ∼100 C variation on timescales of weeks-years. For the majority of the 2009-2018 timespan, magma temperature exhibits a very strong positive relationship with $Q$ (Fig. 4.10, 4.11). This is consistent with the strong impact of temperature on $Q$ (Fig. 4.8), and with the inverse relationship between viscosity and $Q$ (Fig. 4.9). That the inverted temperatures so closely track $Q$ indicates that these inversions are mainly using temperature rather than porosity as the dominant control on viscosity variations (Fig. 3.18). This is likely because the viscosity variations are too large to be produced by porosity changes alone given the constraints on density changes from $T$ and reservoir pressure. Temperature exhibits inconsistent relationships with $T$, lava lake elevation, and inverted reservoir pressure (Fig. 4.12).

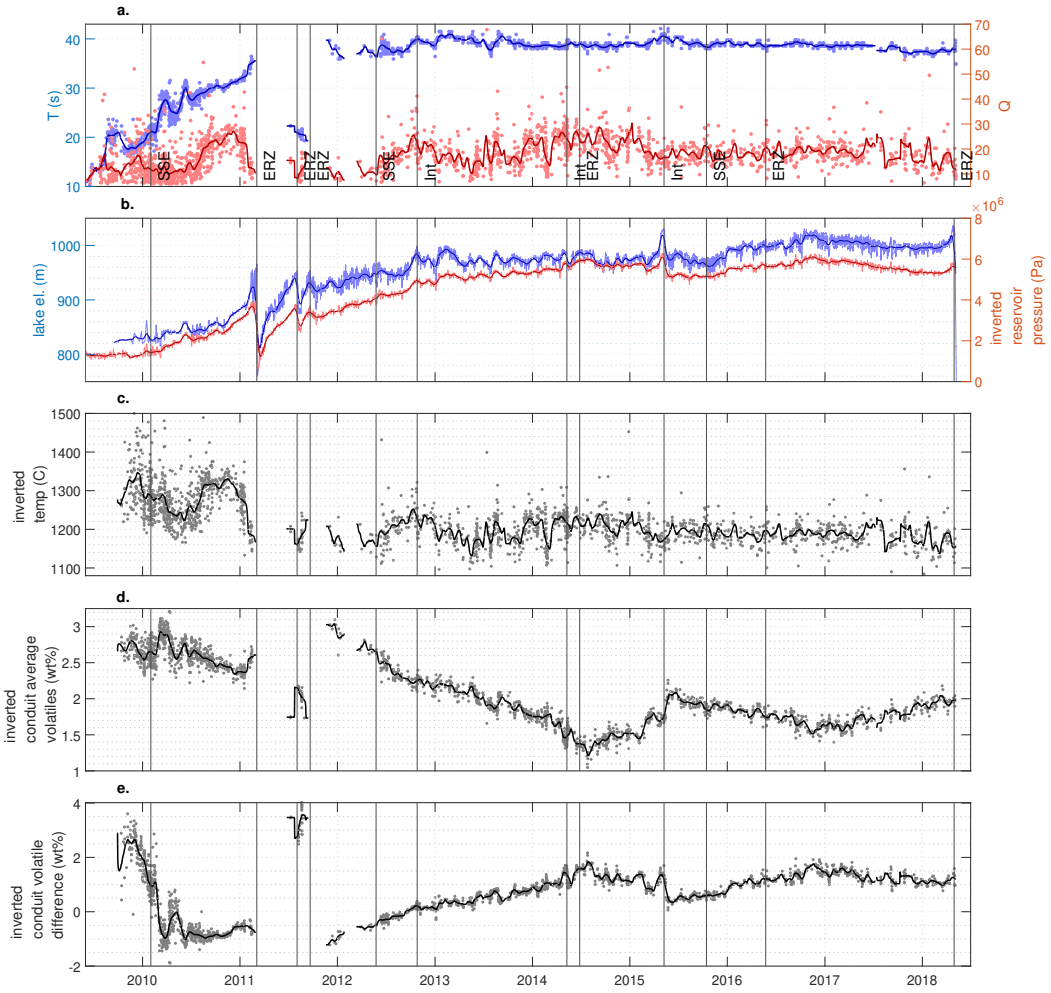


FIGURE 4.10. Inversion for volatile-based magma properties from 2009-2018, with fixed parameters from table 2. (a) Period (blue) and quality factor (red) of VLP events shown by colored dots; colored lines show 30-day moving averages. SSE indicates slow-slip-events and ERZ indicates East-Rift-Zone eruptions. (b) Lava lake elevation (blue) and the reservoir top pressure values we obtain from geodetic inversions for pressure change added to an assumed baseline pressure. (c) Inverted magma temperature. (d) Inverted conduit average total (dissolved plus exsolved) volatile contents. (e) Inverted conduit total (dissolved plus exsolved) volatile content difference (top minus bottom).

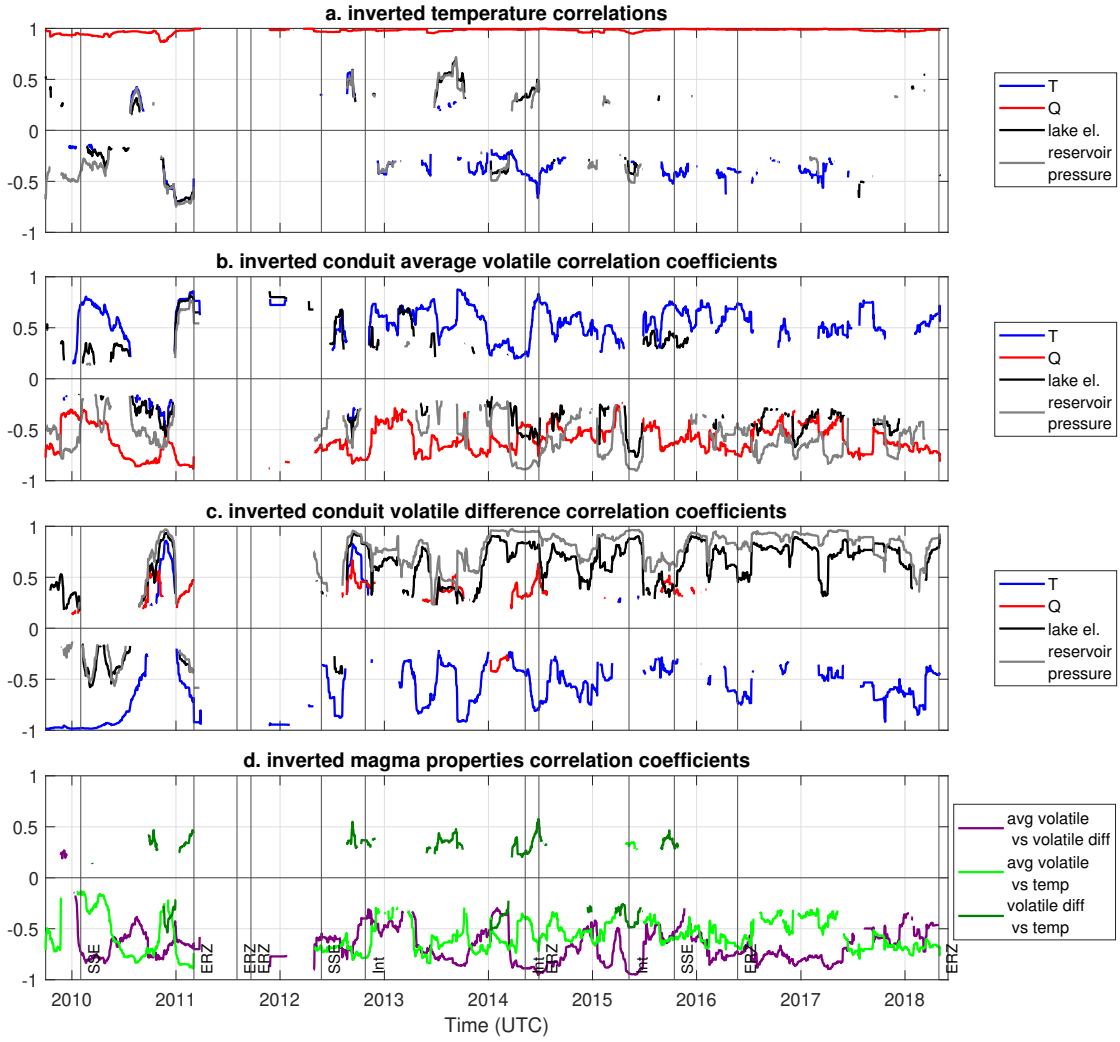


FIGURE 4.11. 90-day moving window Pearson's correlation coefficients between volatile-based magma properties. (a) Inverted magma temperature and data. (b) Inverted conduit average total (dissolved plus exsolved) volatile contents and data. (c) Inverted conduit total (dissolved plus exsolved) volatile content difference (top minus bottom) and data. (d) Inverted magma properties. SSE indicates slow-slip-events, Int indicates summit intrusions, and ERZ indicates East-Rift-Zone eruptions.

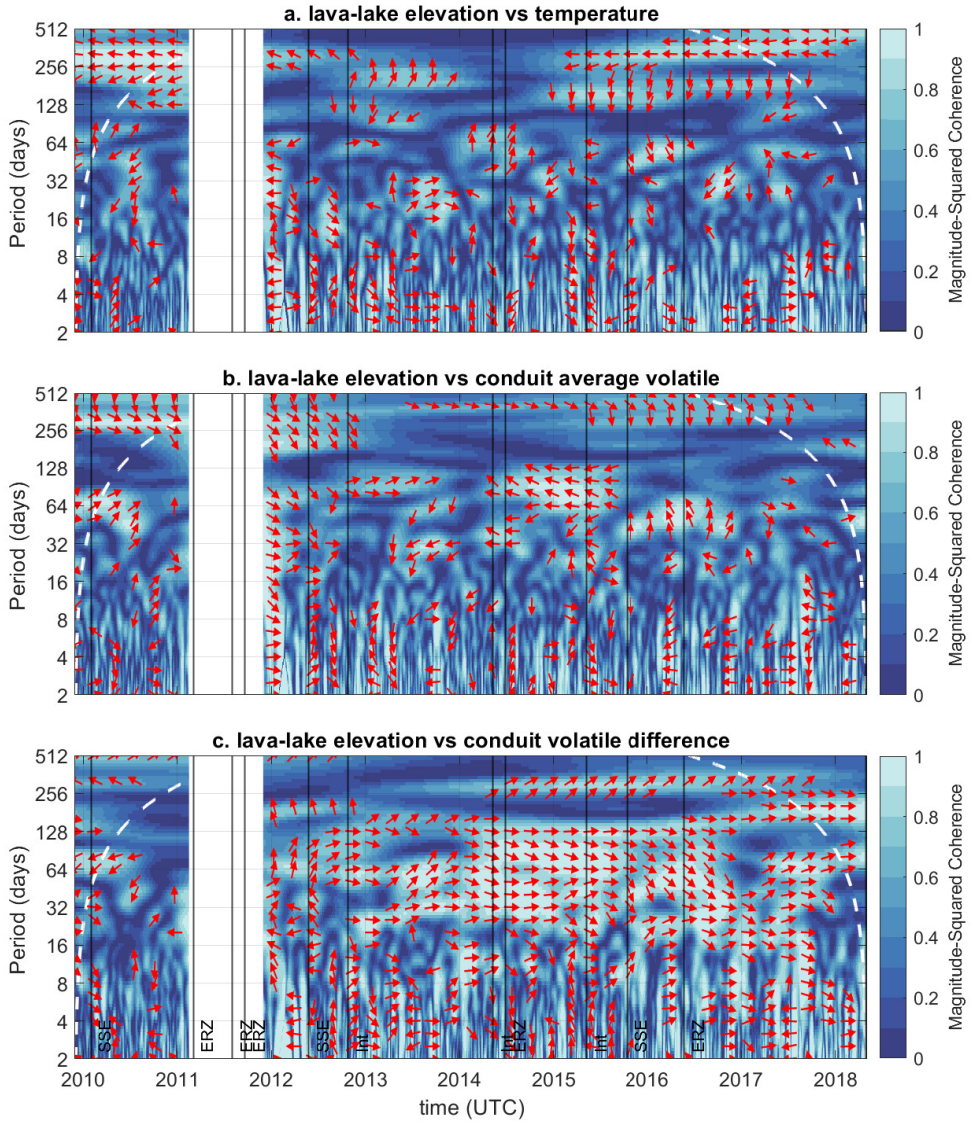


FIGURE 4.12. Spectral coherence and phase lags between lava lake elevation and volatile-based magma properties, calculated with Morlet wavelets on data resampled at 4 hr intervals via linear interpolation. (a) Lava lake elevation and temperature. Red arrows indicate the direction of phase lag where coherence is greater than 0.5; right indicates in-phase (so a positive correlation), left indicates 180 degrees out of phase (so a negative correlation), and up or down indicates 90 degrees out of phase. The white region in 2011 was excluded due to limited data. Dashed white lines indicate the region of edge influence. (b) Lava lake elevation and conduit average total volatile contents. (c) Lava lake elevation and conduit total volatile content difference (top minus bottom). SSE indicates slow-slip-events, Int indicates summit intrusions, and ERZ indicates East-Rift-Zone eruptions.

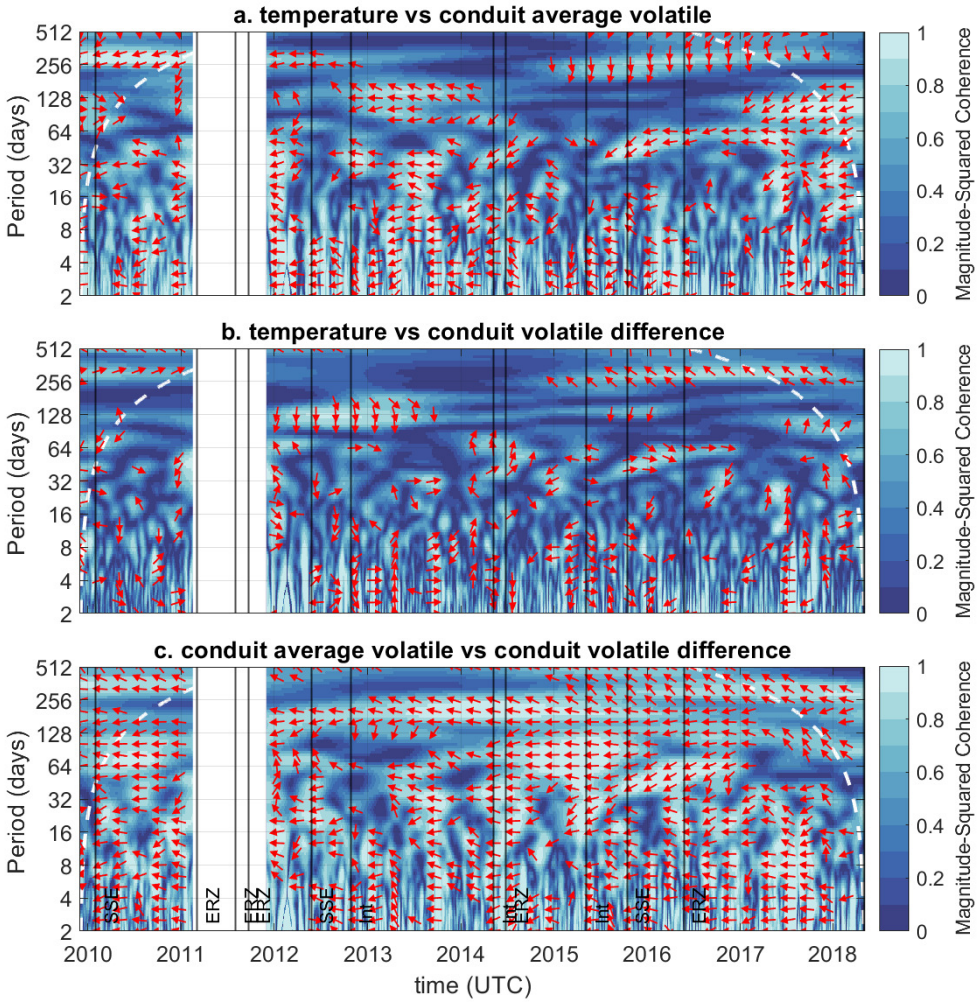


FIGURE 4.13. Spectral coherence and phase lags between volatile-based magma properties, calculated with Morlet wavelets on data resampled at 4 hr intervals via linear interpolation. (a) Temperature and conduit average total volatile contents. Red arrows indicate the direction of phase lag where coherence is greater than 0.5; right indicates in-phase (so a positive correlation), left indicates 180 degrees out of phase (so a negative correlation), and up or down indicates 90 degrees out of phase. The white region in 2011 was excluded due to limited data. Dashed white lines indicate the region of edge influence. (b) Temperature and conduit total volatile content difference (top minus bottom). (c) Conduit average total volatile contents and total volatile content difference. SSE indicates slow-slip-events, Int indicates summit intrusions, and ERZ indicates East-Rift-Zone eruptions.

Magma temperature exhibits a negative correlation with conduit average volatile contents over most of the timespan (Fig. 4.11). Because increasing temperature would generally decrease $T$ and decrease magma density (thus decreasing magmastatic pressure, Fig. 4.8), where $T$ and inverted reservoir pressure do not change decreasing volatile contents would be required to counteract increasing temperature. Particularly on shorter timescales, these correlations may thus be partly related to the noise in estimates of $Q$, an idea which is supported by the observation that temperature exhibits inconsistent coherence and phase lag with conduit average volatiles on timescales from weeks to years (Fig. 4.13). Temperature exhibits weak or no correlation with conduit volatile difference, though there are some time-spans and timescales over which the two properties are coherent and have a consistent phase shift. Interestingly, at periods $>\sim$60 days, over some time spans temperature appears to exhibit phase lags with both volatile parameters that are around $\pm$90 degrees. Such time lags should not be a model/inversion induced artifact, so where they are short lived this could be a coincidence but where they are persistent this likely represent some dynamics of the magma system.

The inverted volatile contents from 2009 and early 2010 would correspond to porosities of $\sim$95% at the top of the conduit, indicating that like the density based model this model has difficulty producing such low values of $T$ with feasible magma properties. On timescales of years, average conduit volatiles exhibit trends that show a rough inverse relation with reservoir pressure and lava lake elevation, while conduit volatile difference exhibits a positive relation with these data. The magnitudes of these long-term trends is very sensitive to poorly constrained South Caldera reservoir properties, although the sign of the trends is robust in response

to different fixed parameter values. However, we still caution that they may not be reliable due to potential changes in magma system geometry.

On timescales from days to months, conduit average volatiles vary by up to ∼0.5 wt%, and conduit volatile differences vary by up to ∼1 wt% (Fig. 4.10). The sign of these variations is robust, though the magnitude of variation in inverted average conduit volatile contents is sensitive to inverted Halema‘uma‘u reservoir pressure and could change by up to a factor of two for plausible values of rock shear modulus or Halema‘uma‘u reservoir volume. The variability in volatile contents is similar to the parent magma's inferred total volatile contents of around 1 wt%, and thus likely indicates appreciable variation in the outgassing regime [e.g., Edmonds et al., 2015]. Even if the multi-year trends in conduit volatile difference were removed (i.e., if the timeline were highpass filtered or detrended), the volatile differences present during many events would be around ±0.5 wt%. This indicates significant departures from equilibrium outgassing (where volatile contents would be uniform).

Conduit volatile differences are negatively correlated with conduit average volatiles over most of the timespan (Fig. 4.11), and also exhibit high spectral coherence over most timescales (Fig. 4.13). Conduit average volatile contents are positively correlated with $T$ over most of the timespan, except for late 2010 and in the months leading up to the Sep 2012 intrusion. They display mostly weak and inconsistent correlations with lava lake elevation, and slightly more consistent negative correlations with reservoir pressure (except in the months leading up to the May 2011 ERZ eruption). Lastly, they are negatively correlated with $Q$ over most of the timespan, though we expect this partly represents the inversions compensating for the density variations caused by artificial temperature

variations needed to fit noise in estimates of $Q$. As might be expected from the strong negative relation between conduit volatile differences and conduit average volatiles, volatile differences exhibit opposite correlations with $T$ and reservoir pressure. However, conduit volatile differences exhibit much stronger correlations with lava lake elevation, particularly on timescales of weeks to months (Fig. 4.12).

There are significant differences, and even sign changes, in these correlations over time. This indicates that conduit average volatiles and volatile differences are both varying in complex ways in relation to the other datasets, which likely reflects a variety of magmatic processes. Since reservoir pressure and lava lake elevation constrain the average density of the magma column, it is not unexpected that they might exhibit some correlations with conduit volatile contents. However, it is interesting that volatile difference generally exhibits stronger correlations than average volatiles with these datasets. This indicates that the inversions are primarily invoking changes in volatiles at the top of the conduit, and thus also in the lava lake (given how we have parameterized these models), to produce changes in magma column density. That the strongest variation occurs in the shallowest parts of the magma system is perhaps not surprising since the lava lake is where most gas is lost from the magma, and is also consistent with observations of significant changes in lava lake density accompanying activity such as gas-pistoning [e.g., Poland and Carbone, 2018, Patrick et al., 2019b].

## Discussion

### *Timeline of magmatic processes*

Here we discuss the implications of our inversions on the evolution of the Kīlauea magma system from 2009-2018, loosely following the timeline segments outlined in Crozier and Karlstrom [2021].

#### Sep 2009 persistent lava lake-Mar 2011 Kamoamoa fissure eruption

One notable aspect of our inverted magma properties during this timespan is that very high volatile contents (and low densities) are required to fit the low periods of events in the earlier part of this time segment (Fig. 4.9, 4.10). The difficulty of producing such low periods is indicated by figures 4.2, and 4.3, which show that magma volatile contents (or density) and conduit length are the primary controls on period. Producing periods less than ∼20 s requires either high enough volatile contents that the upper part of the conduit is essentially just a foam (in which case some aspects of our model are likely no longer accurate), or shortening the conduit to lengths of less than around 100 m (so conduit base elevations >∼600 m ASL). While it is likely that the magma system geometry changed over time, particularly near the start of the eruption, a situation where only 100 m of rock separates the top of the reservoir from the bottom of the lava lake may be mechanically unstable. Additionally, if such a configuration did exist in 2009, it is unlikely that several hundred meters of crystallization would have occurred at the top of the magma reservoir to produce the geometry inferred in 2018 [Anderson et al., 2019].

One possibility is that the reservoir geometry was completely different during this time segment. For example, [Liang et al., 2020a] find that a much smaller ellipsoidal reservoir or crack-shaped reservoir are both plausible and could shift the simulations into the regime where reservoir compressibility also impacts the resonance, although they infer that these configurations are less likely. Additionally, it is unlikely that such a reservoir geometry could have transitioned over 10 years into the much larger ellipsoid that is inferred to exist by 2018 [Anderson et al., 2019].

Another possibility is that the resonating structure involved in the earlier events was a shallow fracture (dike or sill) above the main ellipsoidal reservoir, and that at some point the hydraulic connections shifted so that the main ellipsoidal reservoir became the source. However, a change in the resonating source structure would need to be reconciled with the relatively continuous trend in VLP properties over time [Crozier and Karlstrom, 2021]. A related possibility is that such a secondary fracture remained involved in the VLP resonance over the whole timespan, but the fracture geometry and/or magma compressibility in the fracture evolved over time. Kinematic inversions for the 2018 collapse events in Crozier et al. [2018a] find that the combination of a spherical reservoir and fracture can fit ground motions better than just a spherical reservoir, but that the potential fracture geometry is very poorly constrained. McQuillan and Karlstrom [2021] indicate that whether connecting additional fractures to a water-filled conduit impacts the fundamental coupled conduit-reservoir oscillation depends upon the geometry of the fractures. Higher frequency eigenmodes could be diagnostic of such a configuration.

A final possibility, which is not mutually exclusive, is that the conduit geometry changed significantly over time. In particular, a conduit radius that increased strongly with depth would produce shorter periods (Fig. 4.2, 4.3). Such changes in conduit geometry would generally also effect $Q$. While there is a significant increase in $Q$ over the latter part of 2010, this is followed by a subsequent decrease and so would not be readily explained by a step change in conduit geometry.

The strong increase in $Q$ in late 2010 also gives rise to another interesting inversion result from this time segment: an increase in temporally-averaged magma temperature by over 100 C, followed by a sharp drop in magma temperature of 150 C in the months leading up to the Mar 2011 ERZ eruption. These final months are also accompanied by a $\sim$0.5 wt% increase in conduit average volatile contents. The initial increase in temperature could represent an influx of hotter melt from depth, which would be consistent with the reservoir inflation and lava lake filling occurring during this time, but might be difficult to reconcile with the lack of a corresponding increase in volatile contents. One possibility is that the volatiles that might have been associated with such and injection could have fluxed up through the shallow magma system earlier while the melt took longer to convect up into the conduit. This would be consistent with the high volatile contents our inversions found in the earlier part of this time segment. Explaining the sharp drop in magma temperature in the months leading up to the Mar 2011 ERZ eruption likely requires down-welling of cool magma that had been stagnating in the lava lake. Such a change in the convective regime could also be consistent with the significant increase in the variability of lava lake elevation around this time (Fig. 4.10). It is possible that the increase in conduit average volatiles could

represent a buildup due to less efficient outgassing of magma in the conduit under this different convective regime.

Mar 2011 Kamoamoa fissure eruption-Sep 2011 Pu‘u ‘Ō‘ō eruption

The very limited number of robust VLP events during this highly dynamic time inhibits analysis with these inversions. The one cluster of events present can be fit with reasonable values of temperature and/or viscosity, but requires unfeasibly large volatile or density differences in the conduit (Fig. 4.9, 4.10). As with the previous time segment, we suspect this is evidence that the geometry of the shallow magma system is different than in later years. Crozier and Karlstrom [2021] suggested one possible reason for the limited VLP seismicity during most of this time-segment is that the geometry of the conduit during this time changed in a manner that inhibited magma flow on the timescales of the conduit-reservoir oscillation. If the top of the conduit became very narrow but the bottom remained wide (as was proposed in the previous time segment), this could explain the low values of $T$ and $Q$ when VLP events do occur during this time segment. Such a constriction could have developed following the Mar 2011 lava lake draining, possibly due to collapse of the newly unsupported upper conduit/lower crater walls. It is tempting to invoke the development of such a constriction earlier, to explain the sharp decrease in $Q$ in the months before Mar 2011, but this would be inconsistent with the increase in $T$.

Sep 2011 Pu‘u ‘Ō‘ō eruption-Oct 2012 intrusion

Over this time segment there is a fairly steady increase in inverted magma temperature (and a decrease in viscosity) corresponding to the increase in $Q$ (Fig.

4.9, 4.10). This could represent an influx of hotter magma from depth, which is presumably occurring to some extent due to the filling of the lava lake. However, this may be difficult to reconcile with the steady decrease in average volatiles over this time. The decrease in volatiles could be caused by more efficient convective outgassing facilitated by the growing lava lake, and possibly also by the less viscous magma allowing more rapid bubble rise and/or magma flow. A change in the convective regime would be consistent with the sign change in inverted volatile difference during this time segment.

As Crozier and Karlstrom [2021] suggested, the increase in $Q$ might also partly represent a widening of the conduit from its potentially constricted configuration during the previous time segment. Since such a constriction would likely have been near the top of the conduit, widening the top of conduit would also increase $T$ (Fig. 4.2, 4.3). Counteracting this could be achieved with reasonable increases over time in average volatiles and/or volatile difference compared to what our inversions show.

Oct 2012 intrusion-Jun 2014 Pu‘u ‘Ō‘ō eruption

We do see slight changes in the average and difference in conduit volatiles in the week around the Oct 2012 intrusion, but both are subtle and do not stand out from the background variation around this time. Magma temperature does exhibit a clear change from increasing to decreasing following the Oct 2012 intrusion. This could be explained by a decrease in the supply of hot magma from depth to the conduit, which would be consistent with the slowing reservoir pressurization. If the hypothesis about the top of the conduit widening in the previous time segment is accurate, then the cessation of said widening could help facilitate the decrease

in $Q$. However, this would still need to be accompanied by a decrease in magma temperature unless we invoked a subsequent decrease in conduit radius, which we suspect is less likely over these timescales in the absence of any additional evidence pointing toward such changes in conduit geometry.

From mid-2013 through the remainder of this time-segment, temporally averaged magma temperature varies by up to 100 degrees over timescales from weeks to months. We expect this also most likely represents real changes in magma temperature rather than conduit geometry. These changes in temperature are fairly coherent with the average conduit volatiles on timescales of months or less, but with a negative relation (or 180 degree phase lag). While the variation could be related to injections of hot new melt, we would generally expect this to increase both temperature and volatiles. It is possible that there is a delay from the volatiles reaching the shallow magma system before the hot melt, though perhaps unlikely that this delay corresponds to the intrusion interval well enough to appear as a consistent 180 degree phase lag. We thus expect that changes in the convective regime, and potentially interactions of said convection with magma injections, are the likely cause of many of these temperature and volatile variations.

The May 2014 intrusion is preceded roughly a week in advance by a pronounced decrease in conduit average volatiles and an increase in volatile difference, and is immediately followed by opposite changes in both. However, some caution should be used in interpreting these values since the intrusion could influence our inverted reservoir pressure changes. The temperature drop following the intrusion should be more robust, and could indicate that some of the hotter

magma from depth is being fed into the intrusion rather than circulating up to the conduit.

Jun 2014 Pu‘u ‘Ō‘ō eruption-May 2016 Pu‘u ‘Ō‘ō eruption

The Jun 2014 Pu‘u ‘Ō‘ō eruption does not correspond to any obvious changes in magma properties, $T$, or $Q$, despite being followed by a distinct change in ground motion patterns [Crozier and Karlstrom, 2021]. This indicates that any change in source reservoir geometry likely did not involve changes in conduit length or geometry. However, within a month after the eruption onset there is a significant change in the trends in both the average and difference in conduit volatiles that persists until the May 2015 intrusion. Due to the delay in these changes from the ERZ eruption onset, it is difficult to definitively determine if they are linked. One possibility is that the magma pathway changed such that more volatiles escaped to the summit from the magma that eventually flowed along the ERZ, which could also explain the change in VLP ground motion patterns. Another possibility is that a change in magma system geometry changed the effective Halema‘uma‘u reservoir elastic compressibility and caused an artificial step change in our reservoir pressure inversions, which would impact inverted volatile contents.

As discussed in the methods section, our inverted reservoir pressures following the May 2015 intrusion may be influenced by the intrusion, which we expect contributes to the change in trends in volatiles at this time. However, the changes in magma properties preceding the intrusion should be robust. These include a decrease in magma temperature which began several months in advance, and a decrease in conduit average volatiles and an increase in conduit volatile

difference that began about a month in advance. These precursory changes in average volatiles are similar to those that preceded the May 2014 intrusion. The combination of a decrease in average volatiles and magma temperature, despite the significant buildup of magma in the summit evidenced by increasing Halemaʻumaʻu reservoir pressure and lava lake elevation, indicates that if hotter and/or volatile-rich magma from depth was contributing to this buildup it remained beneath the conduit and lava lake. It is possible that either the increased lava lake elevation and/or whatever blockage caused the magma buildup disturbed the convective regime such that the shallowest magma continued to outgas without being replenished from depth.

The October 2015 SSE corresponded to a noticeable minimum in conduit average volatiles and a more subtle maximum in temperature. The May 2016 Puʻu ʻŌʻō eruption does not appear to correspond to obvious changes in magma properties. This is not necessarily unexpected, as ERZ vent openings could occur due to processes such as rock failure along the ERZ without directly involving the summit magma system.

May 2016 Puʻu ʻŌʻō eruption-May 2018 caldera collapse onset

The shallow magma system appears to be relatively stable over most of this timespan. As in other time segments, we expect the long-term trends in volatiles, which roughly track lava lake elevation, may be exaggerated due to inaccuracy of the inverted Halemaʻumaʻu reservoir pressure. The volatiles even remain relatively stable during Apr 2018 when the lava lake level begins increasing significantly. The biggest variability is seen in magma temperature, which exhibits month-scale variability of 50-100 degrees. Magma temperature decreases by about 50

degrees over Apr 2018. The lack of an increase in volatiles or magma temperature indicates that the magma buildup in the summit did not result in hotter or more volatile rich magma reaching the conduit and lava lake. In this case, it is thus not clear that the VLP seismicity could have provided any earlier indications about the potential upcoming eruption than could have been inferred from the increasing ground deformation and lava lake elevation. However, the lack of change in magma properties helps support the idea that the activity was driven primarily by the blockage and opening of magma pathways along the ERZ rather than by magmatic processes at or beneath the summit [Patrick et al., 2020].

*Applications for monitoring and analyzing other volcanoes*

While the conduit-reservoir resonance model was developed based off of the shallow magma system at Kīlauea Volcano during its 2008-2018 summit eruption, this type of resonance could occur wherever open-vent volcanic systems containing lava lakes are perturbed [Liang et al., 2020b]. We expect these models could be applicable to other open-vent volcanoes where the approximations used remain valid, but note that more general analysis of possible resonant modes in open-vent conduits/reservoirs [e.g., Karlstrom and Dunham, 2016, Liang et al., 2020b] could be useful in determining possible source mechanisms for a given signal. Volcanoes with lava lakes that have exhibited seismicity with dominant periods greater than around 10 s and clear decaying oscillations indicative of resonance include Vanuatu and Erebus [e.g., Knox et al., 2018, Shreve et al., 2019]. Minimal analysis has been published for the events of interest at Vanuatu, but a source mechanism similar to the conduit-reservoir oscillation has been proposed for Erebus [Aster, 2003].

The gradient-descent inversions for changes in magma properties used in this study are very computationally efficient (around 1 s per event on a laptop). They could thus be conducted in an automated manner in near-real time once a VLP event has been cataloged and the other data being used to constrain the inversions is available. Only one nearby seismic station is often sufficient to produce estimates of $T$ and $Q$, which would allow limited inversions for changes in magma properties to be conducted. Additional constraints from continuous data will allow more free parameters to be used in the inversions, and thus yield more accurate and/or detailed results. Continuous gravity data would provide a constraint on magma density that could complement or replace the inversions for reservoir pressure from ground deformation that we used. Continuous gas flux data, gas composition data, and thermal imagery could also be used to constrain volatile contents and magma temperatures at/near the lava lake surface, although consideration would need to be given as to how these relate to magma beneath the very near-surface region of the lava lake. Lastly, incorporating models for exchange flow in the conduit and/or lava lake could yield additional constraints on feasible values of magma properties and how they covary. The results of these inversions could also be used to inform such models.

## Conclusions

We developed an expanded model for the dominant magma resonance at Kīlauea Volcano, the conduit-reservoir oscillation which consists of a vertical sloshing of the shallow magma column. This model incorporates variable conduit and lava lake geometry, viscous boundary layer flow, and magma properties as a function of temperature and volatile contents using joint $H_2O$-

$CO_2$ solubility, including depth stratification that could arise from disequilibrium outgassing/convective regimes. The resonance is sensitive to changes in conduit length and shape, changes in lava lake elevation, and has depth-dependent sensitivity to magma properties.

We use this model to conduct inversions for magma properties over time from a recent catalog of VLP signals over the 2008-2018 eruption of Kīlauea Volcano. We constrain these inversions using lava lake elevation data and joint geodetic inversions for pressure changes in Kīlauea's summit magma reservoirs. These inversions demonstrate the limits of what can be uniquely resolved given available constraints, but still yield an unprecedented resolution of relative changes in magma properties over various timescales.

We find that a different magma system geometry is needed to produce the low values of $T$ observed before 2011 than the higher values in the rest of the timespan. Variability in temperature of 100 C or more occurs over timescales from days to months, likely often reflecting down-welling of cooler magma from the lava lake. We cannot robustly resolve changes in volatile contents over multiple years without more accurate constraints on reservoir pressure and/or continuous gravity data, but up to around 1 wt% variability in both average volatile contents and in the depth stratification of volatile contents occurs over timescales from days to months. This is significant compared to the inferred parent magma volatile contents, and thus indicates a highly disequilibrium and unsteady outgassing regime. There are similar patterns in magma properties preceding some intrusions or rift zone eruptions, indicating that this type of analysis could have predictive value. For other volcanic events we do not see any precursory changes in magma properties, though this lack of change still informs the processes that could have

been involved. For example, magma properties prior to climactic 2018 caldera collapse onset appear relatively stable, supporting the idea that this event was primarily driven by activity along the ERZ.

These inversions could be readily automated to make a useful near-real-time monitoring tool, and the limits of what they can resolve could be improved with the appropriate inclusion of continuous gas emission and gravity data. We expect that this VLP magma resonance model could also apply to some signals at other lava lake hosting volcanoes.

# CHAPTER V

# CONCLUSION

This dissertation combined fluid dynamics modeling with a variety of spectral analysis techniques and multiple types of data to address questions in glaciology and volcanology. In aggregate, this dissertation represents multiple new contributions to the earth sciences related to both methods and scientific ideas.

The first chapter demonstrated that ∼1-10 km scale ice surface topography and meltwater routing on the Greenland Ice Sheet ablation zone can be well-explained by transfer of the underlying bedrock topography. It predicted that changes in basal sliding or ice thickness will have significant influences on the spatial distribution of supraglacial catchments, which could affect subglacial hydrology and overall ice sheet evolution.

The second chapter presented a fully automated signal processing workflow using wavelet transforms to detect and classify resonant signals. This was used to generate a catalog of VLP seismicity over the 2008-2018 summit eruption of Kīlauea Volcano. VLP ground motion patterns showed both abrupt and gradual changes in shallow magma reservoir geometry. Variation in resonant periods and decay rates occurred on timescales from hours to years. A decoupling between magma in the conduit and lava lake was inferred. The relations between resonance characteristics and other datasets change over time, including around magma intrusions and rift zone eruptions.

The third chapter used the VLP catalog and observations from the second chapter to inform an extended model for Kīlauea Volcano magma resonance that accounts for empirically constrained melt and volatile physics. This model

was used to conduct joint inversions for the VLP seismicity catalog and other geodetic data which yielded an unprecedented resolution of evolving magma volatile contents and temperature over timescales from days to years. Variation of magma properties at different depths, including consistent precursors to known intrusions and rift zone eruptions, suggested changes in the convective/outgassing regime due to both magma recharge and lava lake overturn.

I expect the work in this dissertation will inform future scientific work and have important practical implications for modeling ice sheet evolution and volcano monitoring.

# APPENDIX A

## SUPPLEMENTAL INFORMATION FOR: CHAPTER II

### Transfer Function Dependence on 2D Bed Topography

The two-dimensionality of the transfer functions is important, as mentioned in section 2.3.2 of the main text. This can be demonstrated by examining a scenario with different single-wavenumber components of bed topography (plane-waves) that have the same apparent wavenumbers in a transect interpolated across bed topography along an ice flowline (a bed elevation profile along the ice flow direction). The same apparent wavenumber in the ice flow direction $k_U$ could arise from any single wavenumber component of bed topography with absolute wavenumber $k = k_U \cos(\theta)$ aligned at angle $\theta$ from the ice flow direction, where the plane-wave ridge alignment is perpendicular to the direction of ice flow when $\theta = 0$. If we evaluate the predicted transfer functions for a given $k_U$ and set $k = k_U \cos(\theta)$ for a range of $\theta$, transfer amplitude and phase will both depend upon $\theta$ even though the apparent flowline bed topography is the same for all $\theta \neq \frac{n\pi}{2}$. We

use the bed topography transfer functions from Gudmundsson [2003] to calculate

$$\hat{A}_B(\theta) = \Bigg( k_U^{*(2)} \cos(\theta) \Bigg( \cosh(k_U^* \cos(\theta)) \left( C^{0*(2)} k_U^{*(2)} \cos^2(\theta) + 2U^* \right) + ... \\ C^{0*} k_U^* U^* \cos(\theta) \sinh(k_U^* \cos(\theta)) \Bigg) \Bigg) / ... \\ \Bigg( k_U^{*(4)} U^{*(2)} \cos^2(\theta) \Bigg( \frac{1}{2} C^{0*} k_U^* \cos(\theta) \sinh(2k_U^* \cos(\theta)) + ... \\ k_U^{*(2)} U^* \cos^2(\theta) + \cosh^2(k_U^* \cos(\theta)) + 1 \Bigg)^2 + ... \\ \cot^2(\alpha) \left( k_U^* \cos(\theta) \left( C^{0*} \sinh^2(k_U^* \cos(\theta)) - 1 \right) + \frac{1}{2} \sinh(2k_U^* \cos(\theta)) \right)^2 \Bigg)^{1/2}. \tag{A.1.1}$$

It can similarly be shown that bed topography transfer phase also depends upon $\theta$ as

$$\hat{\phi}_B(\theta) = -\operatorname{arccot} \Bigg( \Bigg( k_U^{*(2)} v \tan(\alpha) \cos(\theta) \Big( C^{0*} k_U^* \cos(\theta) \sinh(2k_U^* \cos(\theta)) + ... \\ 2k_U^{*(2)} v \cos^2(\theta) + \cosh(2k_U^* \cos(\theta)) + 3 \Big) \Bigg) / ... \\ \Big( 2k_U^* \cos(\theta) \left( C^{0*} \sinh^2(k_U^* \cos(\theta)) - 1 \right) + \sinh(2k_U^* \cos(\theta)) \Big) \Bigg). \tag{A.1.2}$$

These equations give the potential variation in bed topography transfer amplitude and phase that could result from examining bed topography only along ice flowline transects, and thus demonstrate the importance of predicting the ice surface over 2D bed topography, since the configuration of bed topography off of a flowline can influence the ice surface over said flowline. With ice flow parameters representative of the western Greenland Ice Sheet ablation zone, the predicted transfer amplitude

of IDC-scale (∼1-10 km) bed features could vary by up to a factor of 10 depending upon the 2D alignment of those features (Fig. A.1).

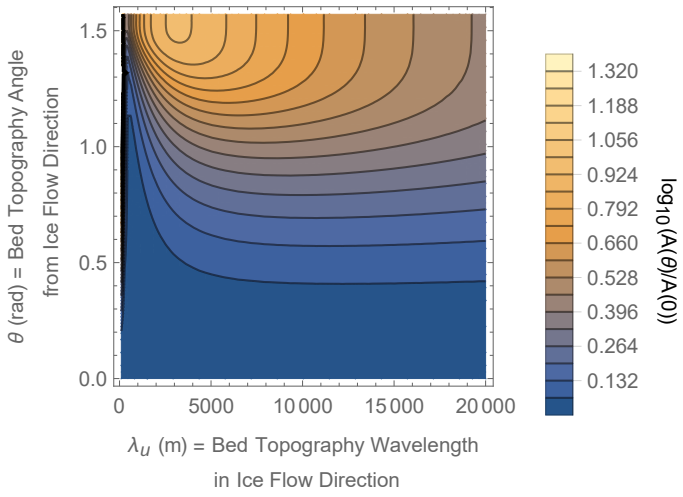


Appendix Figure A.1 Effect of 2D bed topography on ice flowline bed topography transfer amplitude, defined in Appendix A.1. $A(\theta)$ is predicted transfer amplitude for ice-flowline-equivalent bed topography aligned at angle $\theta$ from the ice flow direction, and $A(0)$ is the predicted flowline-only (equivalent to $\theta = 0$) transfer amplitude. Ice flow parameters used are from region R1 (Fig. 1.A and Table 1 of the main text) with $\eta = 10^{14}$ Pa s and $C^{0*} = 10$.

### Conformity Metrics

We use two conformity metrics, $\%d$ and $\Lambda$, to examine how well stream network geometry is explained by surface topography lowpass filtered at various wavelengths as described in section 2.4.3 of the main text. We project stream networks onto filtered surfaces and then for each stream we calculate conformity factor as:

$$\Lambda = \frac{1}{L} \int_{l=1}^{L} \left| \frac{\vec{D}(l) \bullet \left( \vec{\nabla} Z(l) \right)}{\|\vec{D}(l)\| \|\vec{\nabla} Z(l)\|} \right| dl \tag{A.2.3}$$

where $\|\|$ indicates vector magnitude, $\vec{D}(l) = (D_x(l), D_y(l))$ is the stream channel horizontal direction vector (the east-north direction of water flow, calculated with a 2nd order centered difference approximation of the stream channel tangent in map-view) at location $l$ along a stream of length $L$, and $\vec{\nabla} Z(l)$ is the corresponding ice surface gradient $\left( \frac{\partial Z}{\partial x}|_l, \frac{\partial Z}{\partial y}|_l \right)$ (calculated with a 2nd order centered difference approximation). We calculate percent downhill (here using discrete notation) as:

$$\%d = \frac{100}{N-1} \sum_{n=1}^{N-1} \begin{cases} 0 & \text{if } Z(n) \leq Z(n+1) \\ 1 & \text{if } Z(n) > Z(n+1) \end{cases} \tag{A.2.4}$$

where $n$ indexes discrete location along a stream ($n$ increases in the downstream direction), $Z(n)$ is the corresponding ice surface elevation, and $N$ is the number of discrete locations along the stream, where each location corresponds to a DEM pixel. To calculate $\%d$ and $\Lambda$ for a whole stream network we calculate $\%d$ and $\Lambda$ for each stream segment in the network, then take a weighted average of each

metric over all stream segments, where data from each stream segment is weighted by the number of data points in that segment ($N$).

## Supplemental Figures

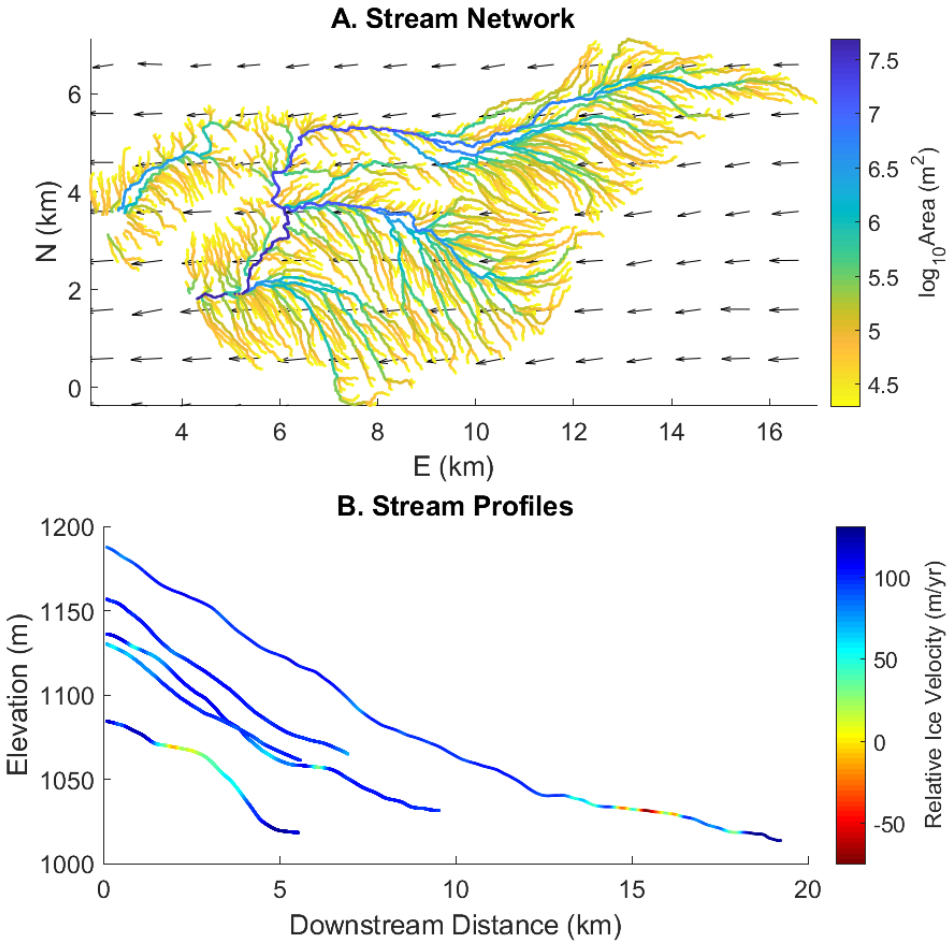


FIGURE A.2. (A) Stream network obtained by flow routing from study region R1 (Fig. 1.A and Table 1 of the main text) colored by accumulated upstream drainage area; black arrows indicate ice surface velocity field. (B) Smoothed longitudinal stream elevation profiles from the longest streams in this network, colored by the component of ice surface velocity in the direction of stream flow (indicating stream meanders, negative values are where the stream is flowing against the ice flow direction). Fluvial incision-dominated profiles with a fixed terminal elevation should generally approach concave-up longitudinal profiles [Karlstrom and Dunham, 2016]. There are many visible convexities in supraglacial stream profiles, many of which do not simply correspond with stream meanders.

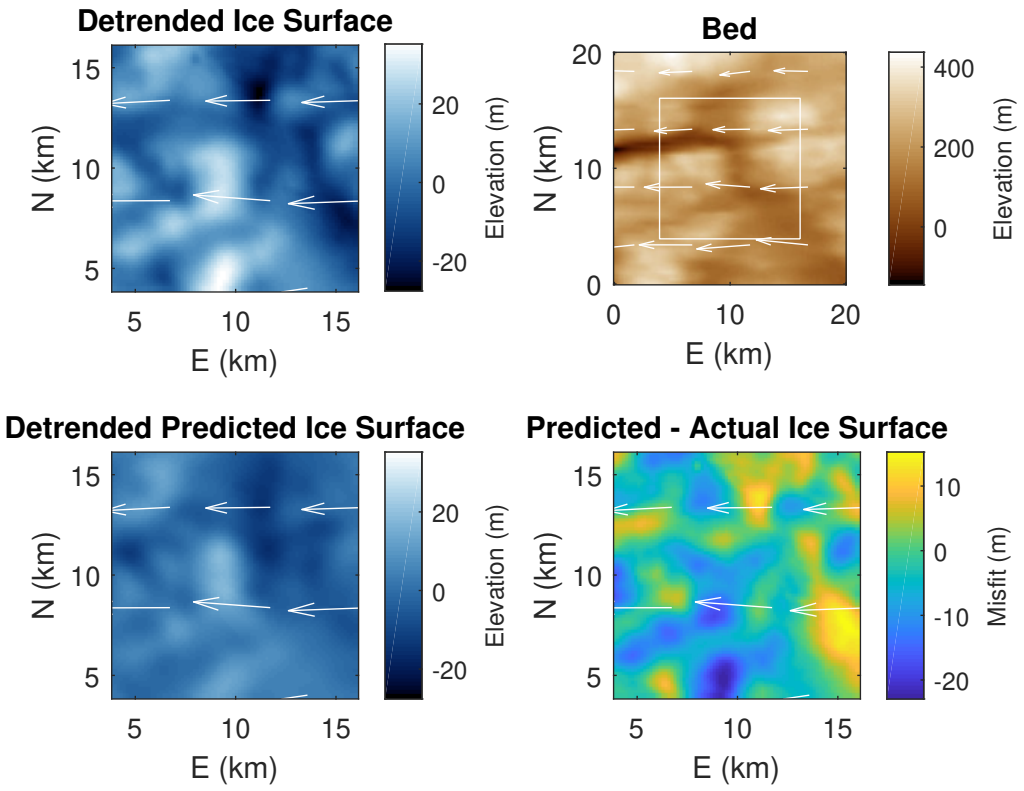


FIGURE A.3. (top left) Detrended ice surface DEM from study region R2 (Fig. 1.A and Table 1 in main text). (bottom left) Detrended bed topography transfer predicted ice surface, with $\eta = 10^{14}$ Pa s and $C^{0*} = 10$. (top right) Underlying BedMachine bed DEM, white box indicates the area over which the ice surface is predicted. (bottom right) Prediction misfit (subtraction between the actual and predicted ice surfaces). White arrows in all plots indicate ice surface velocity field.

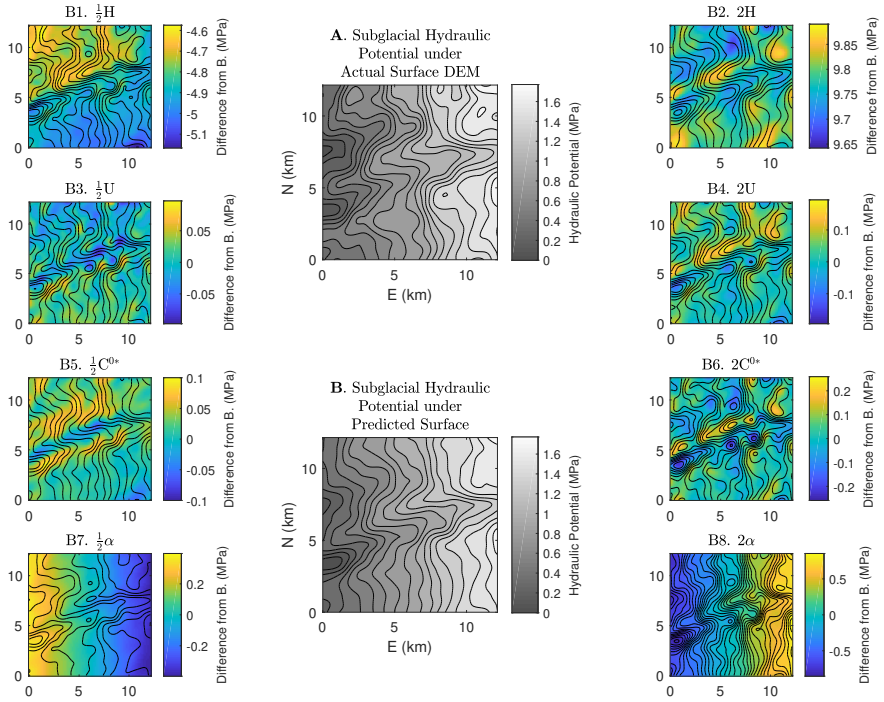


FIGURE A.4. (A) Subglacial hydraulic potential calculated under the actual ice surface DEM from BedMachine/GIMP, [Howat et al., 2014, Morlighem et al., 2017b]. Black contours in all plots are 0.1 MPa hydraulic potential contours. (B, B1-B8) Subglacial hydraulic potential calculated under the bed topography transfer predicted ice surface with various ice flow parameters. Plots B1-B8 are colored by difference from the baseline hydraulic potential in plot B. From study region R1 (Fig. 1.A and Table 1 in the main text) with $\eta = 10^{14}$ Pa s and baseline $C^{0*} = 10$. Changes to all ice flow parameters result in at least subtle changes in the hydraulic potential gradient (which drives water flow).

APPENDIX B

SUPPLEMENTAL INFORMATION FOR: CHAPTER III

## Synthetic Waveform Tests

We construct synthetic seismograms to test the resonant signal detection and classification methods described in the methods section. Displacements are calculated from an isotropic point source in an elastic half-space model Aki and Richards [1993], with the source located 1 km beneath the Halemaʻumaʻu vent. The synthetic source-time functions consist of combinations of step displacements and exponentially decaying sinusoids with impulsive onsets. We apply a sinusoidal taper to the signal onsets to prevent sharp discontinuities and create signals with continuous first derivatives (Fig. B.1). The sinusoid used as a taper has the same period as the signal, an amplitude equal to the initial signal amplitude divided by $\sqrt{2}$, and is joined at the location where the derivative and position of the taper match those of the signal. Where step displacements are also added, we taper the step displacement over the same wavelength used to taper the oscillation onsets (Fig. B.2). We then add white noise from a standard normal distribution, scaled to various fractions of the signal amplitude as listed in each test figure. We then calculate displacements and tilts at each station location using the point source Green's functions, and convolve these with the instrument responses Maeda et al. [2011], Liang et al. [2020a].

## Supplemental Figures

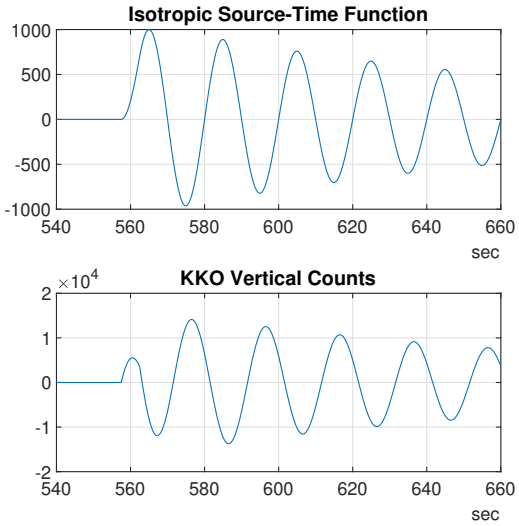


FIGURE B.1. Example synthetic source-time function and corresponding synthetic seismogram (which has been convolved with the elastic Green's functions and instrument response), zoomed in around the signal onset to show the tapers used (see appendix). This source-time function is for an impulsive onset oscillation with $T = 20$ s and $Q = 20$.

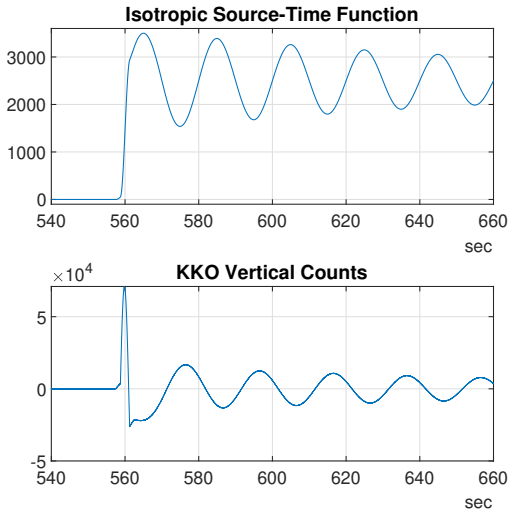


FIGURE B.2. Example synthetic source-time function and corresponding synthetic seismogram (which has been convolved with the elastic Green's functions and instrument response), zoomed in around the signal onset to show the tapers used (see appendix). This source-time function is for an impulsive onset oscillation with $T = 20$ s and $Q = 20$.

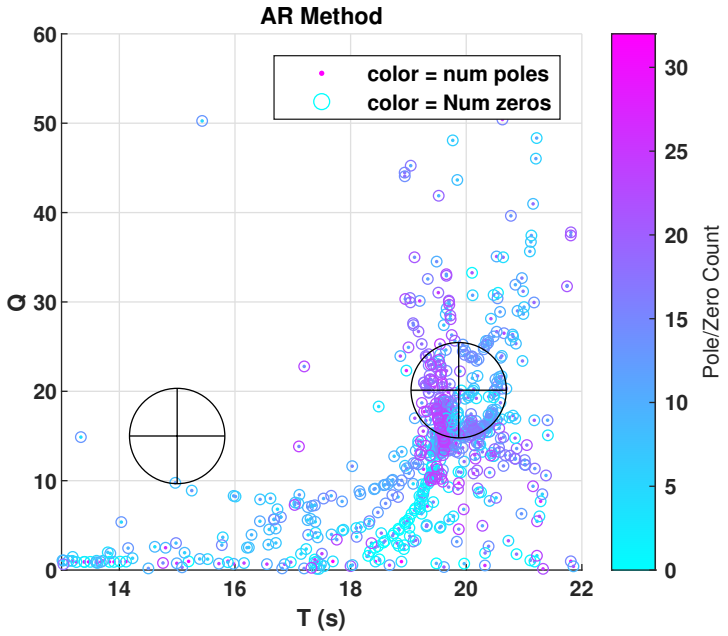


FIGURE B.3. Example 'Sompi' AR method for estimating $T$ and $Q$ applied to a synthetic seismogram. Code used from Lesage 2009. In this case the method was applied to a data window from 10-200 s following the onset of a 20 s oscillation with $Q = 20$ and a smaller (by a factor of 4) 15 s oscillation with $Q = 15$ (indicated by black crosses/circles) and with white noise scaled by 1 percent of the signal amplitude. Results from filters with 4-32 poles and 0-32 zeros are shown to test a wide parameter space; for practical use narrower ranges would likely be used. A cluster near the actual $T$ and $Q$ of the 20 s oscillation does occur, though mean $T$ and $Q$ values within this cluster are offset from the correct value and exhibit significant scatter. No cluster occurs near the smaller 15 s oscillation, so it would be missed entirely by this AR method.

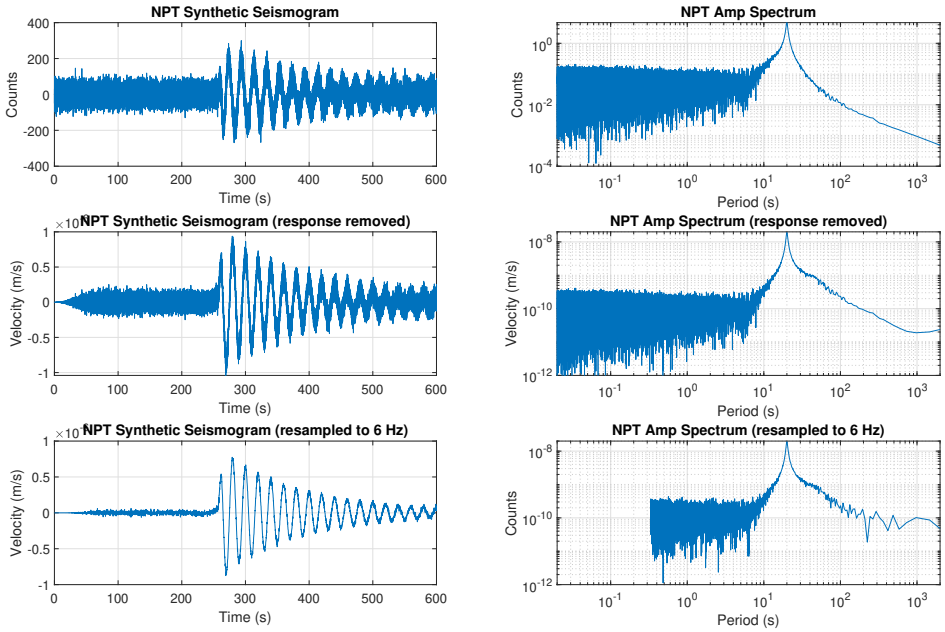


FIGURE B.4. Example instrument response removal and smoothing/resampling of a synthetic seismogram consisting of an impulsive onset oscillation with $T = 20$ s, $Q = 20$, and added white noise.

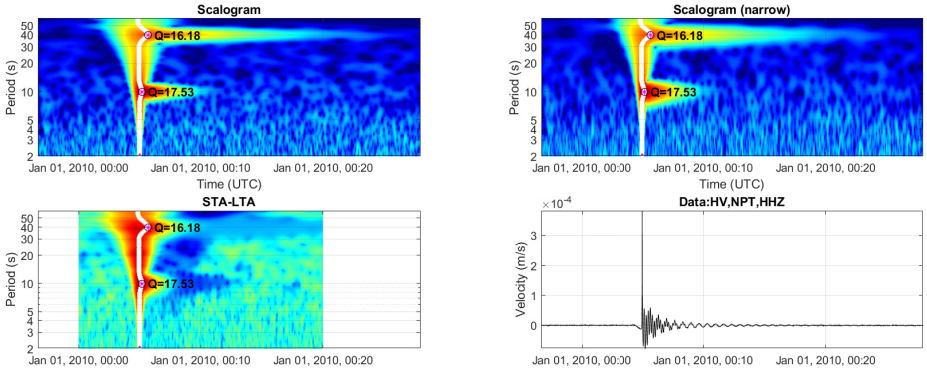


FIGURE B.5. Example scalograms and detected resonant signals from a synthetic seismogram consisting of a large step displacement (velocity spike) at time 00:05 plus two resonant signals with [start time, $T$, $Q$] = [00:05, 40, 20] and [00:05, 10, 20] plus white noise from a standard normal distribution scaled by 0.1% of the signal amplitude. The presence of the step function decreases the estimated quality factors by 12-19% due to the increased energy at the start of the signals, but otherwise does not appreciably impact the results.

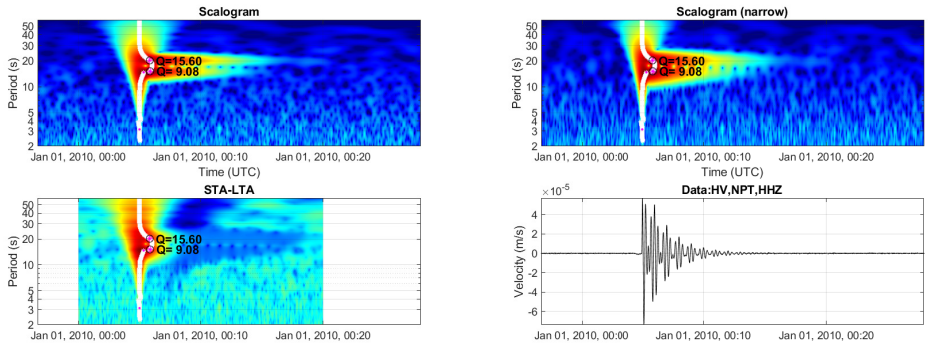


FIGURE B.6. Example scalograms and detected resonant signals from a synthetic seismogram consisting of two resonant signals with [start time, $T$, $Q$] = [00:05, 20, 20], [00:05, 15, 20], plus white noise from a standard normal distribution scaled by 0.1% of the signal amplitude. In this case the spectral proximity of the two signals means that wavelets at the period of one signal are influenced by the other signal, which causes both quality factors to be under-estimated (by 22-54%).

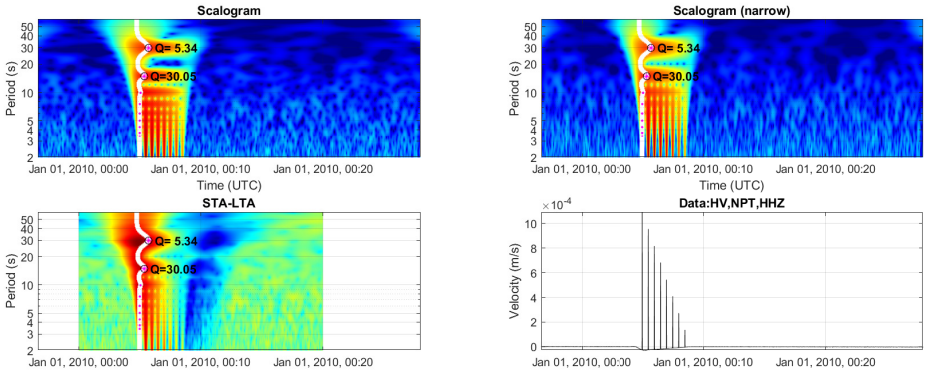


FIGURE B.7. Example scalograms and detected resonant signals from a synthetic seismogram consisting of eight step displacements (velocity spikes) spaced 30 s apart, plus white noise from a standard normal distribution scaled by 1.0% of the signal amplitude. The closely spaced spikes create a Dirac comb effect, where the spectrum would indicate apparent resonances at 15 s, 7.5 s, 3.25 s, and etc. The temporal resolution of our narrow ($\beta$=20) wavelet, which is used for calculating $Q$, is high enough that apparent resonances with $T$ less than 15 s are not picked.

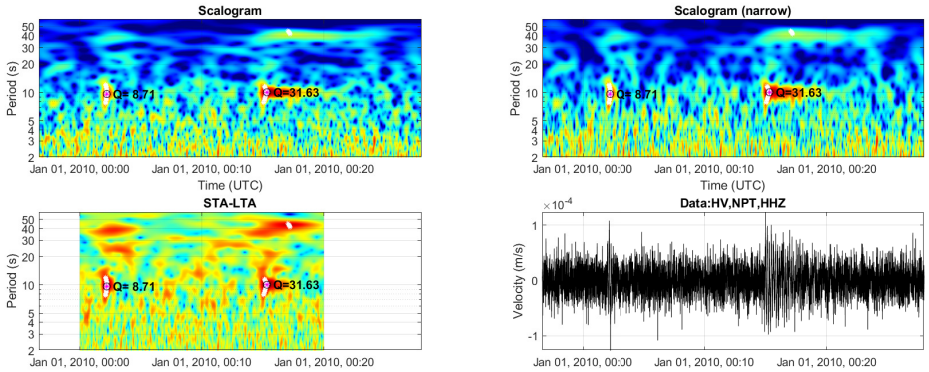


FIGURE B.8. Example scalograms and detected resonant signals from a synthetic seismogram consisting of four resonant signals with [start time, $T$, $Q$] = [00:05, 40, 6], [00:05, 10, 6], [00:15, 40, 40], [00:15, 40, 40], plus white noise from a standard normal distribution scaled by 5.0% of the signal amplitude. At this noise level only two of the signals are found at the detection thresholds used, and the quality factor estimates are less accurate (off by ∼25%).

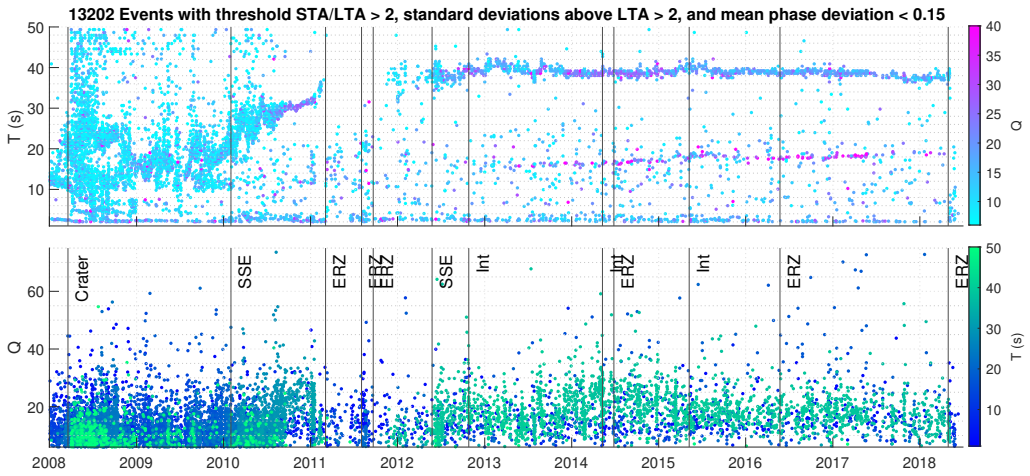


FIGURE B.9. Resonant signal catalog from 2008-2018 with less strict event detection thresholds than presented in the main text yielding ∼13,000 events. The thresholds used in this version are: STA/LTA $> 2$, standard deviations above the LTA $> 2$, $Q > 4$, and mean phase deviation $< 0.15$ radians. 'Crater' indicates where the Halema'uma'u crater first formed, 'SSE' indicates slow slip events, 'Int' indicates documented summit intrusions, and 'ERZ' indicates eruptions along the East-Rift-Zone.

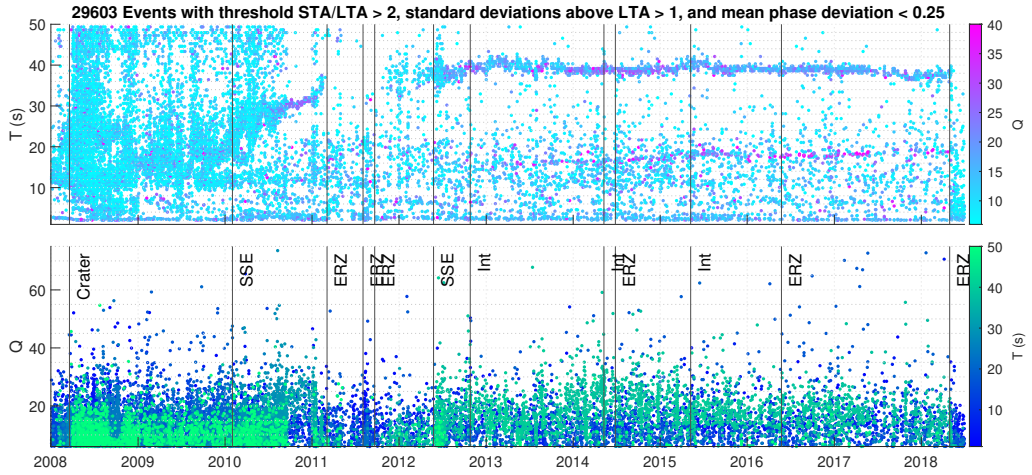


FIGURE B.10. Resonant signal catalog from 2008-2018 with less strict event detection thresholds than presented in the main text yielding ∼30,000 events. The thresholds used in this version are: STA/LTA $> 2$, standard deviations above the LTA $> 1$, $Q > 4$, and mean phase deviation $< 0.25$ radians. 'Crater' indicates where the Halema'uma'u crater first formed, 'SSE' indicates slow slip events, 'Int' indicates documented summit intrusions, and 'ERZ' indicates eruptions along the East-Rift-Zone.

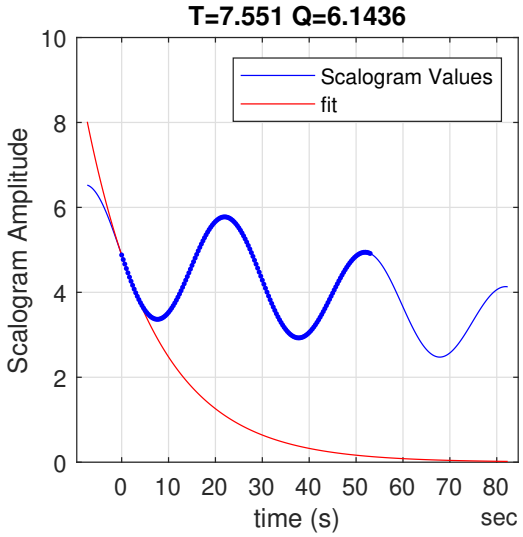


FIGURE B.11. Example estimation of $Q$ by scalogram exponential fit. Applied to synthetic seismograms consisting of a series of tapered step displacements (velocity spikes) spaced 30 s apart, plus white noise from a standard normal distribution scaled by 0.1% of the signal amplitude. The closely spaced spikes create a Dirac comb effect, where the frequency spectrum would indicate apparent resonances at 15 s, 7.5 s, 3.25 s, and etc. The time resolution of the $\beta$=20 wavelet we use for calculating $Q$ is sufficient to distinguish gaps in this apparent 7.5 s resonance, so our fit avoids overestimating $Q$ as a standard least-squares exponential regression would.

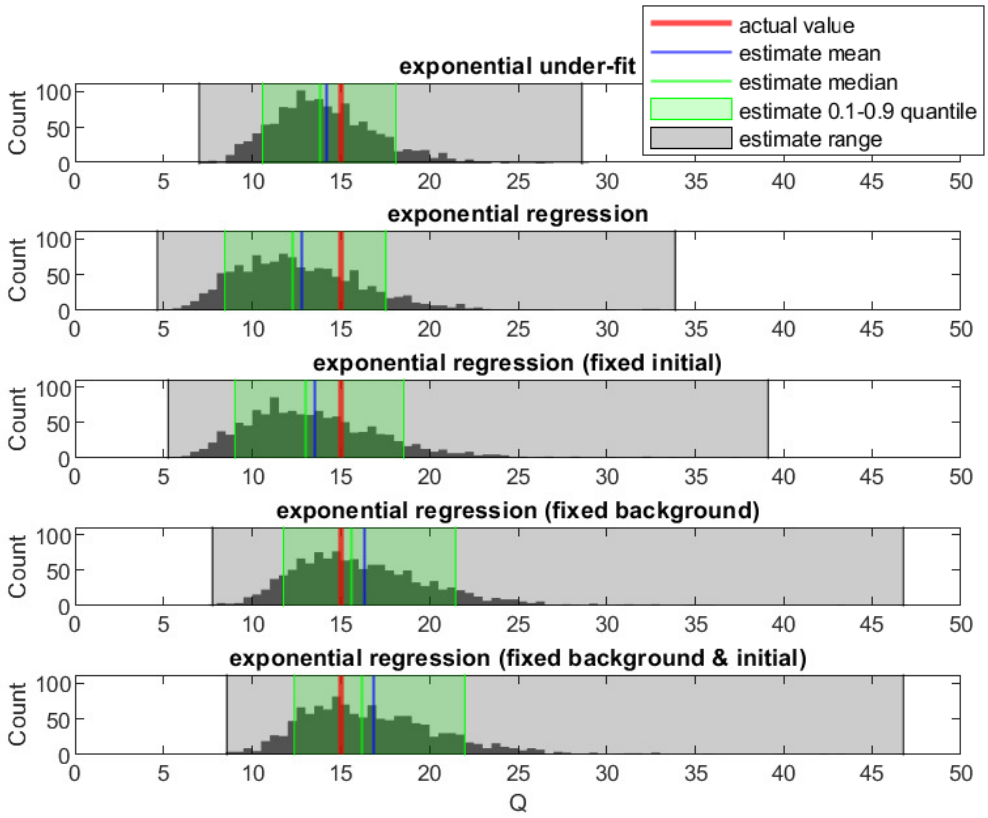


FIGURE B.12. Comparison of exponential fit methods for estimating $Q$ from 1255 synthetic seismograms with different random noise. These seismograms consist of a VLP signal with $[T, Q] = [20\text{ s}, 15]$, plus white noise from a standard normal distribution scaled by 200% of the signal amplitude. All of the methods work well at low noise levels; at the high noise levels used here the Sompi AR method generally does not detect resonance and so is not shown for comparison. 'Under-fit' is the fit we use (Eq. 2, Fig. 6), the other fits are least-squares exponential regressions with various parameters fixed. 'Initial' means amplitude at the first time being fit ($t_1$) is fixed to the CWT amplitude at that time. 'Background' means the asymptotic value approached as time goes to infinity is fixed to the minimum noise value in the full 4 hr time window. While the 'under-fit' has a bias towards smaller $Q$, this bias is small (less than 2 in these simulations) and the spread is smaller than any of the other fitting approaches.

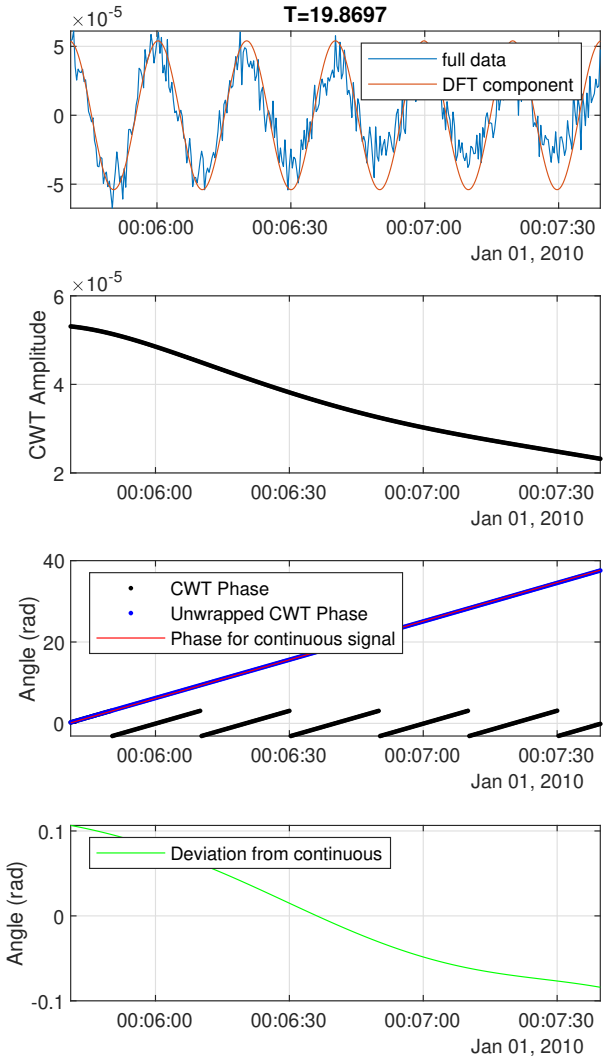


FIGURE B.13. Example phase continuity from a synthetic seismogram consisting of a resonant signal with $T$=20 s and $Q$=20, plus white noise from a standard normal distribution scaled by 0.1% of the signal amplitude. In this case the phase deviation is small (mean of around 0.05 radians), correctly indicating that this is likely a continuous oscillation.

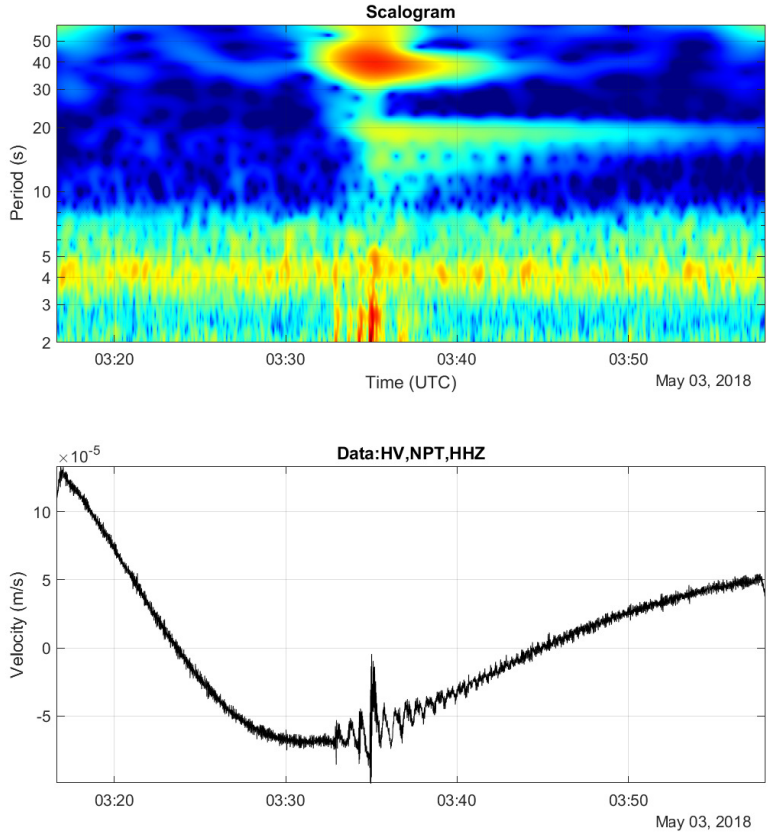


FIGURE B.14. VLP event with two clear lava-lake-sloshing modes from May 2018, a day after the lava-lake began draining. The dominant 40 s mode for this event started with impulsive inflationary motions, though with only a very faint high frequency trigger, but then grew for several minutes until a second impulse occurred and exponential decay began. The lava-lake-sloshing modes appeared alongside this second impulse.

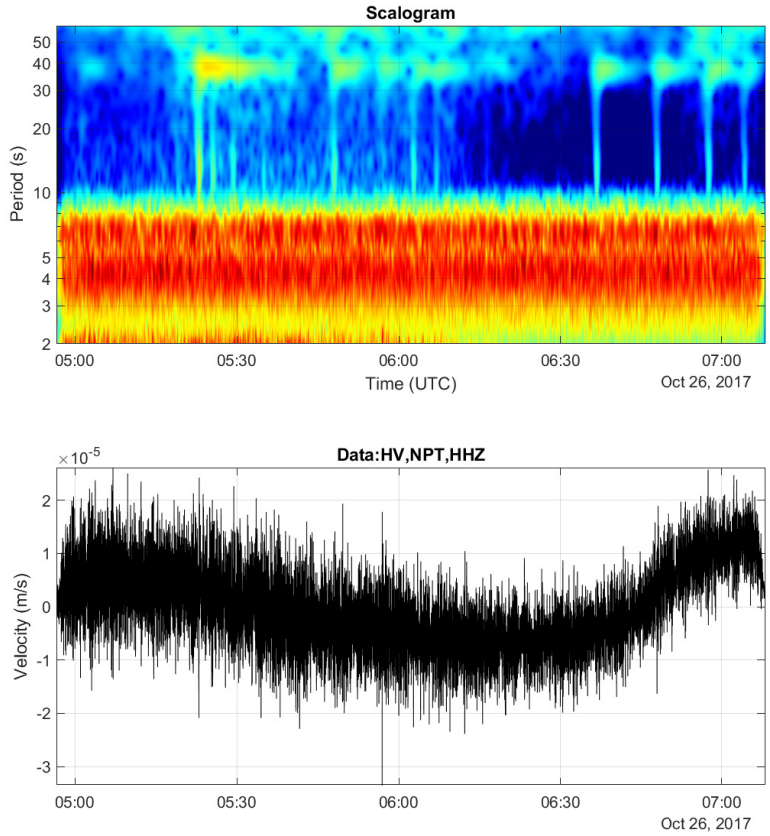


FIGURE B.15. Closely spaced Normal conduit-reservoir events from October 2017.

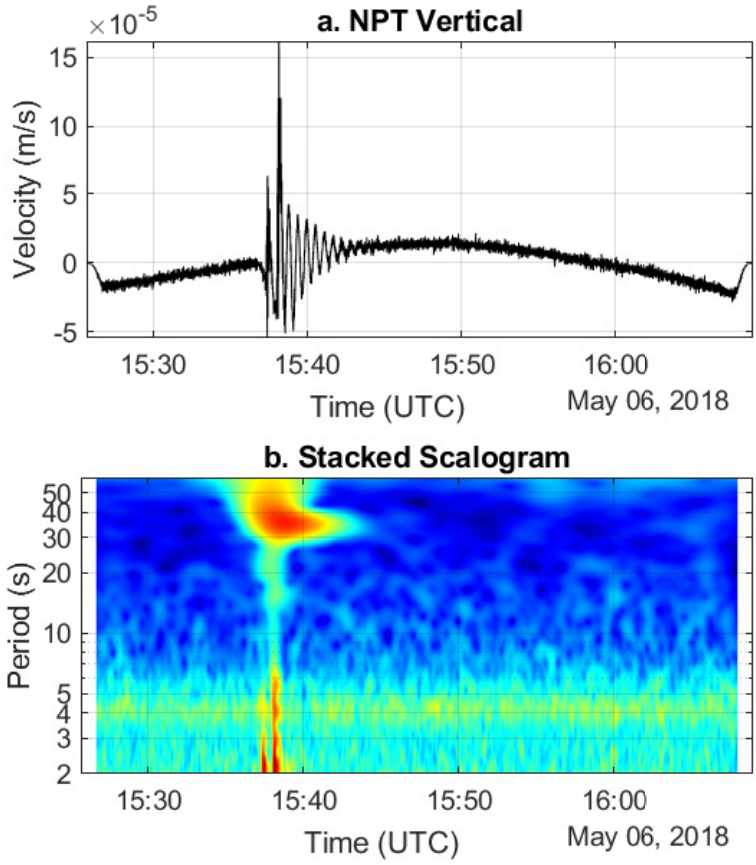


FIGURE B.16. Normal VLP event from May 2018, 4 days after the lava-lake began draining. This event exhibited a distinctly lower $T$ than preceding events (35 s as compared to 37-40 s), and is the last event conduit-reservoir event recorded in our catalog. This event started with an impulsive inflation, though with minimal broadband energy. Another larger broadband impulse occurred a minute later that corresponded to increased oscillation amplitude, after which the oscillation decayed exponentially.

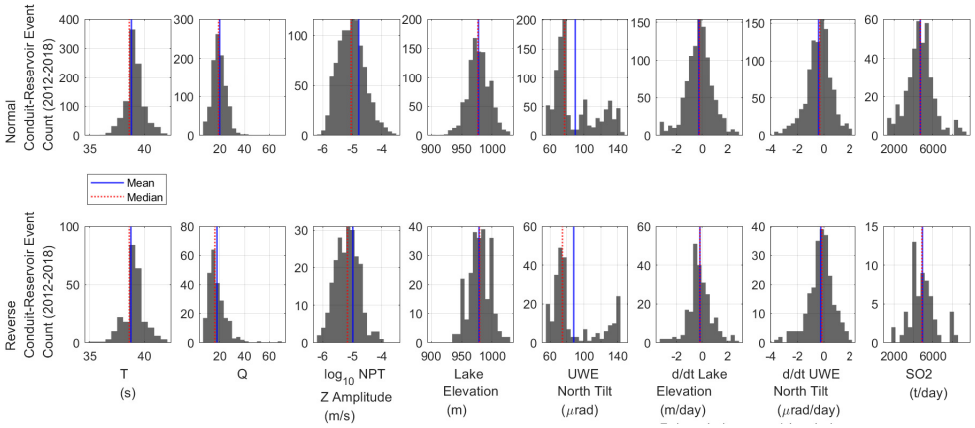


FIGURE B.17. Histograms of Normal and Reverse conduit-reservoir mode event parameters from 2012-2018.

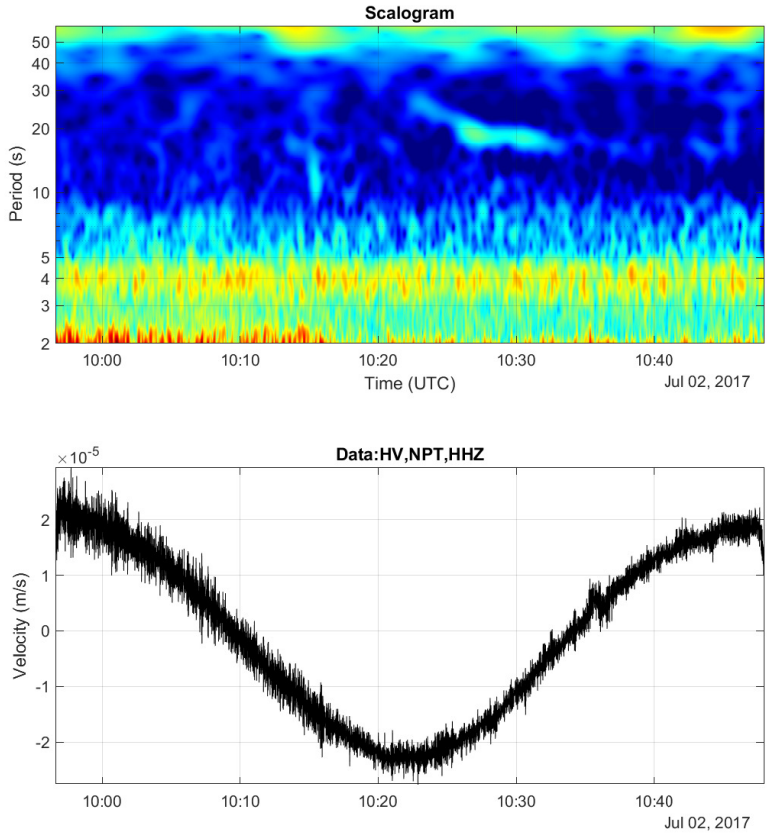


FIGURE B.18. Isolated lake sloshing mode with possible gliding-frequency onset from July 2017.

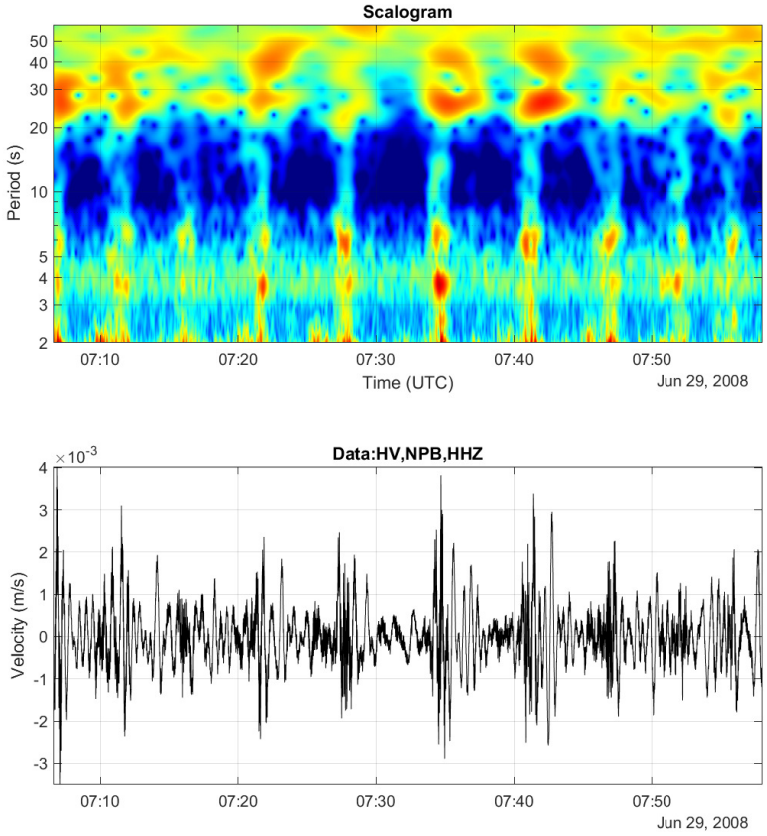


FIGURE B.19. VLP events with regular recurrence interval from June 2008, a few months after the Overlook Crater began forming. These events occurred roughly every 5 minutes and contained broadband energy with spectral peaks at around 3.5 s, 6 s, 25 s, and possibly 40 s. These events exhibited less clear onsets and exponential decays than typical rockfall-triggered events.

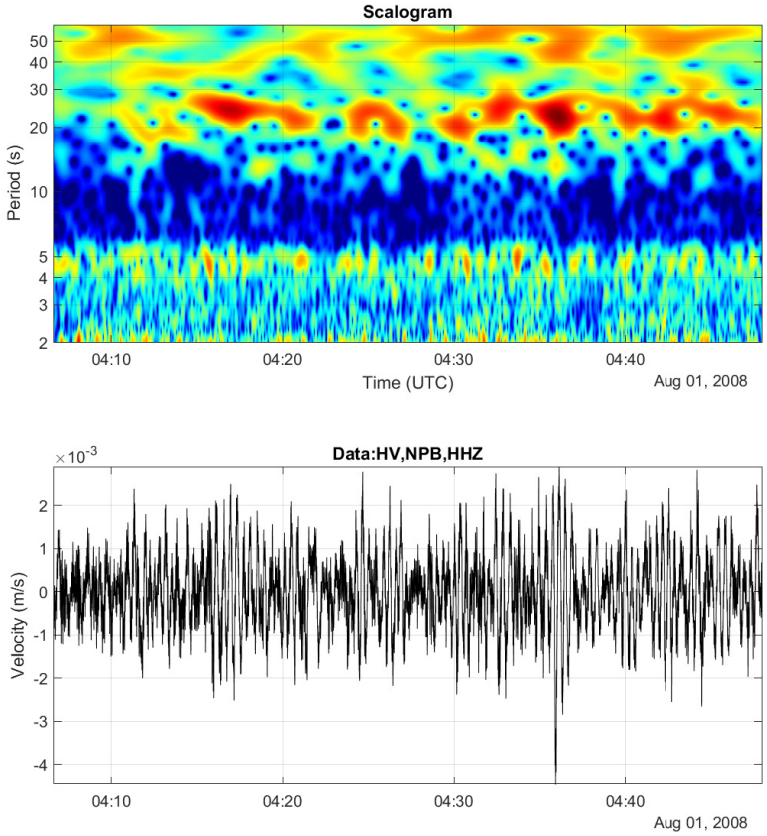


FIGURE B.20. VLP tremor from August 2008, in the first focused cluster of VLP signals. There was elevated energy at periods from 15-30 s and 4-5 s, though the dominant periods were not clearly focused and were variable over time. The signal cannot readily be separated into distinct events, and exhibited no clear high frequency triggers.

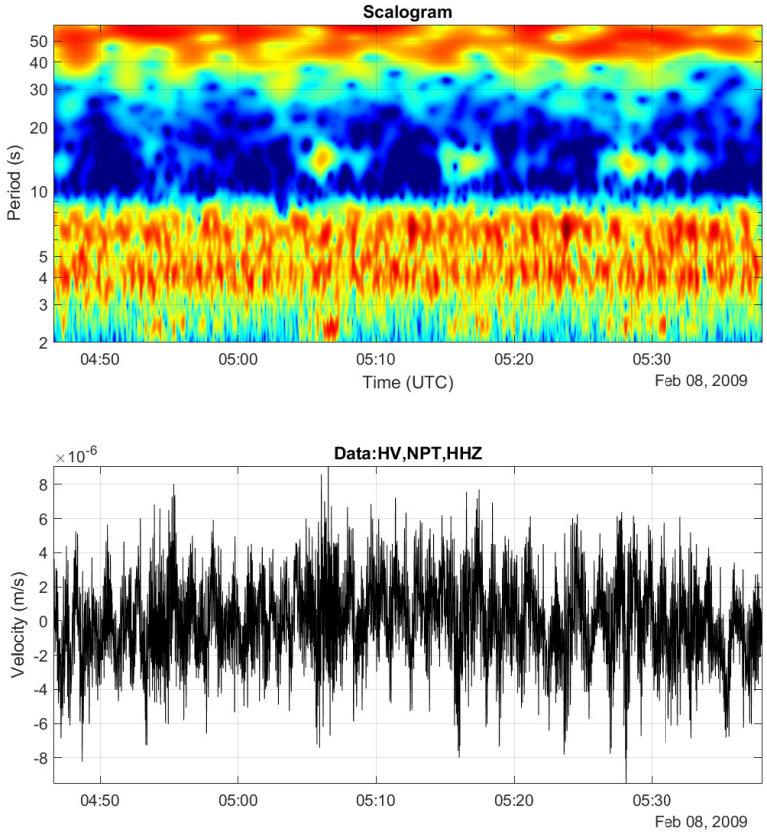


FIGURE B.21. VLP events from February 2009, around the time where dominant VLP period is at a minimum. These appear to be distinct VLP events, thought onsets of some were gradual and first motions were not well defined. Elevated energy at periods $< 2$ s occurred alongside these signals, but did not appear to represent the more broadband impulsive trigger mechanisms that occur at the onset of typical rockfall events.

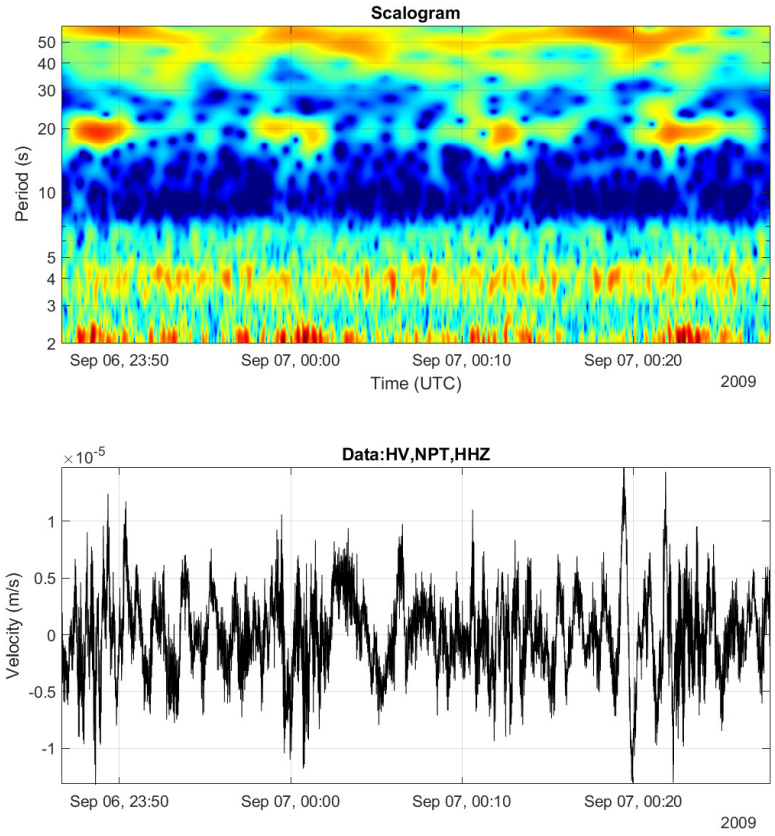


FIGURE B.22. VLP tremor from September 2009, in a signal cluster that seems to represent a local maxima in VLP period (around 20 s).

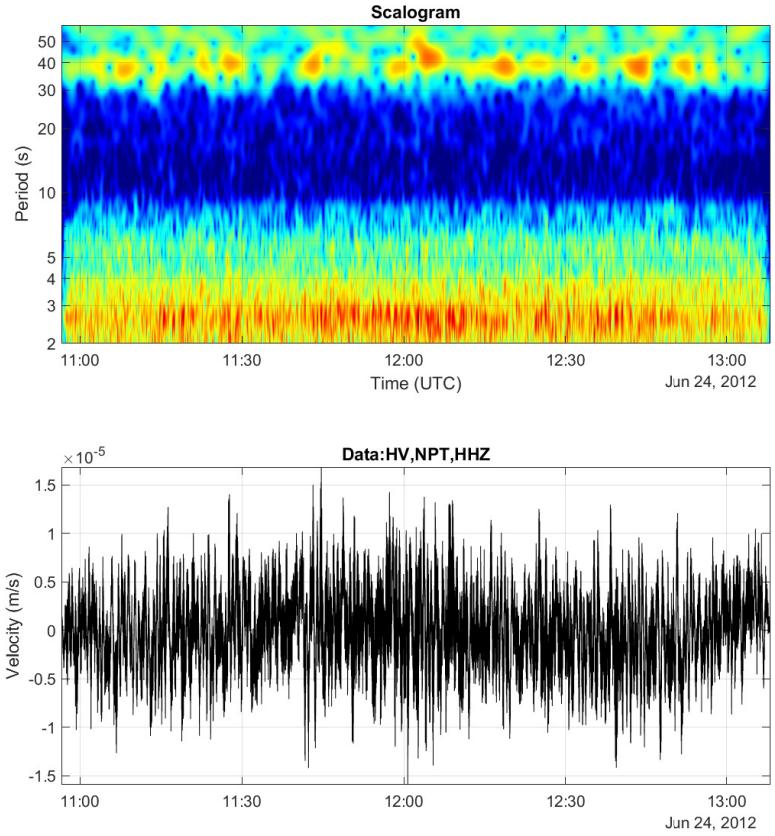


FIGURE B.23. VLP tremor from June 2012, shortly after the May SSE and around when higher $Q$ VLP events start occurring again after a year with minimal VLP seismicity.

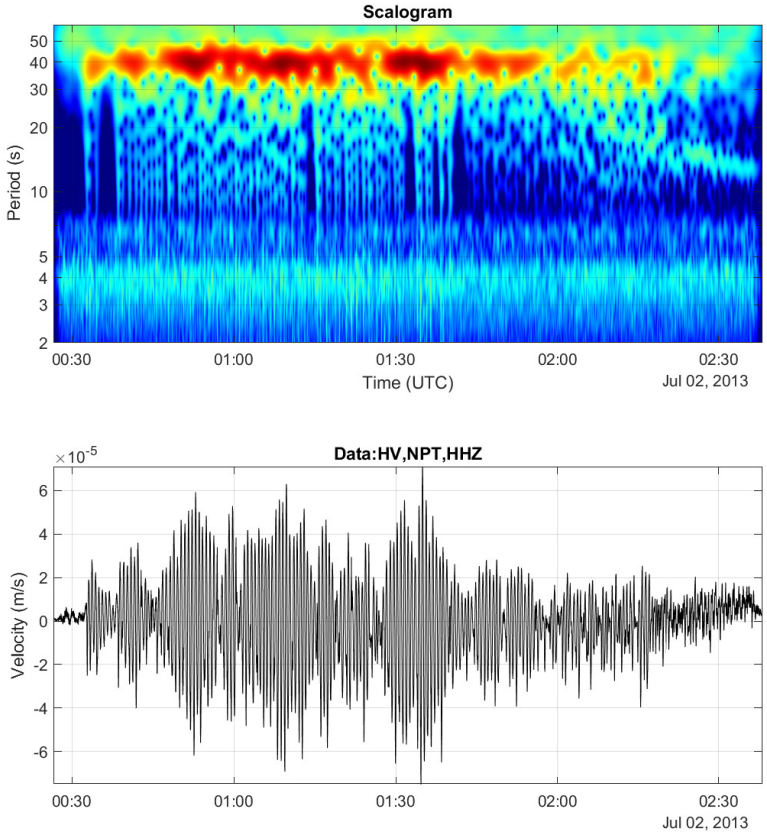


FIGURE B.24. VLP event/tremor from July 2013. This signal consisted of sustained 40 s oscillations at varying amplitudes and irregular bursts of higher frequency energy. These bursts were much weaker relative to the main VLP oscillation than typical rockfall trigger signals. The main VLP signal had an impulsive onset with deflationary first motions.

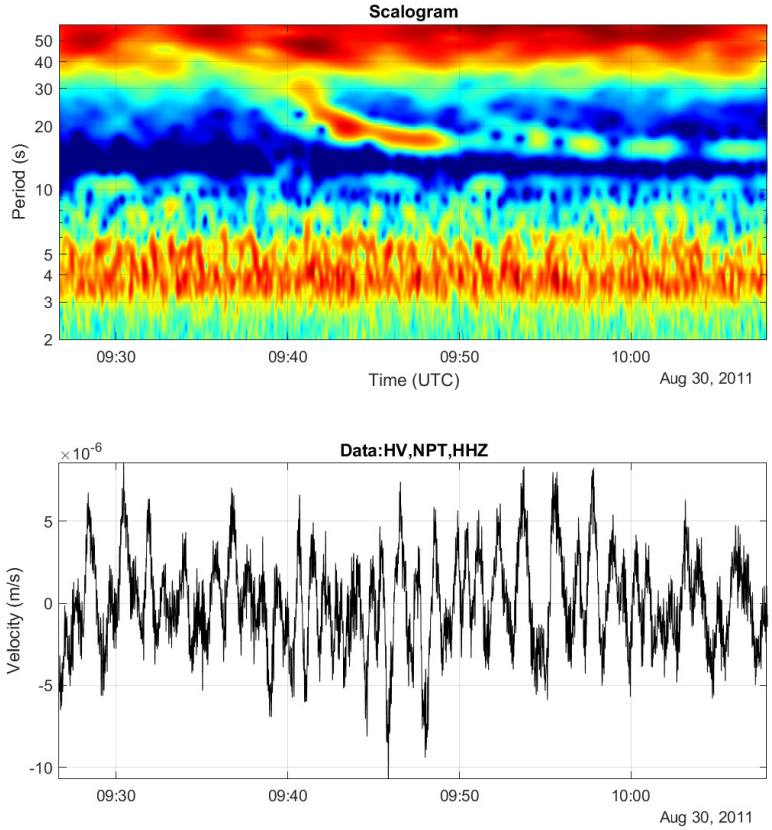


FIGURE B.25. Gliding-frequency VLP signal from August 2011, part of a small cluster of VLP seismicity following the August 2011 Puʻu ʻŌʻō eruption. This event had no apparent high frequency trigger. VLP energy remained elevated for 10s of minutes after the event, though this energy did not appear to represent continuous decay of the initial resonance but rather continued intermittent forcing, perhaps partly by what may be a second smaller gliding-frequency signal around 10 minutes after the first. There was also background VLP tremor present with a period of around 11 s that does not appear to have been effected by the gliding-frequency event.

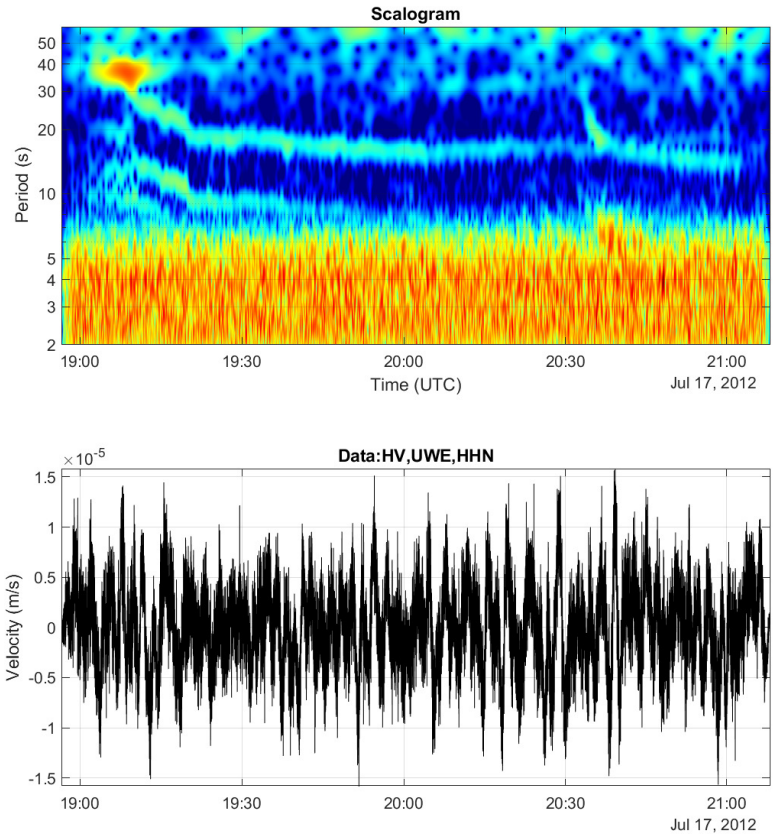


FIGURE B.26. Gliding-frequency VLP signals from July 2012. There was a set of three resonant modes starting around 19:10, and a single resonant mode that started about 90 minutes later. No high frequency triggers were apparent. The first 3 modes all exhibited a similar glide to lower periods over about 10 minutes, then maintained more stable periods. The later mode had a more rapid initial glide to lower periods (over about 5 minutes) but then continued more slowly gliding for another 20 minutes.

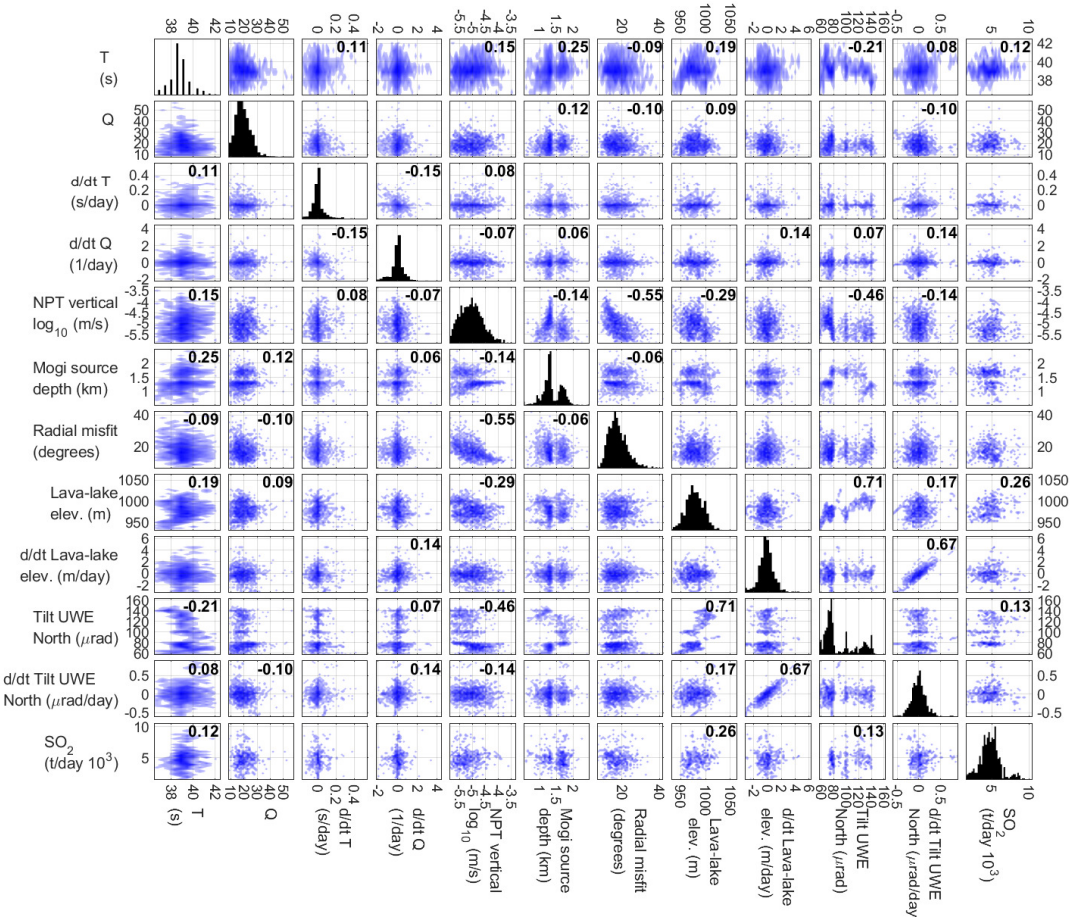


FIGURE B.27. Conduit-reservoir mode correlation matrices from 2012-2018. Off-diagonal plots are shaded by the logarithm of the number of points in a given parameter bin, and histograms on diagonal plots show the distribution of each parameter. Numbers are Pearson's correlation coefficients, only shown for correlations with P-values less than 0.05. All time derivatives were calculated with a 7-day cutoff-period differentiator filter.

# REFERENCES CITED


A. P. Ahlstrøm, D. Petersen, P. L. Langen, M. Citterio, and J. E. Box. Abrupt shift in the observed runoff from the southwestern Greenland ice sheet. *Science Advances*, 3(12), 2017. doi: 10.1126/sciadv.1701169.

K. Aki and P. G. Richards. *Quantitative Seismology*. University Science Books, 2 edition, 1993. ISBN 978-1-891389-63-4.

B. K. Alsberg, A. M. Woodward, and D. B. Kell. An introduction to wavelet transforms for chemometricians: A time- frequency approach. *Chemometrics and Intelligent Laboratory Systems*, 37(2):215–239, 6 1997. ISSN 01697439. doi: 10.1016/S0169-7439(97)00029-4.

M. Andersen, L. Stenseng, H. Skourup, W. Colgan, S. Khan, S. Kristensen, S. Andersen, J. Box, A. Ahlstrøm, X. Fettweis, and R. Forsbergb. Basin-scale partitioning of Greenland ice sheet mass balance components (2007–2011). *Earth and Planetary Science Letters*, 409:89–95, 2015. doi: 10.1016/j.epsl.2014.10.015.

A. Anderson, J. Foster, and N. Frazer. Implications of deflation-inflation event models on Kilauea Volcano, Hawai'i. *Journal of Volcanology and Geothermal Research*, 397:106832, 5 2020. ISSN 03770273. doi: 10.1016/j.jvolgeores.2020.106832.

K. Anderson and M. Poland. Bayesian estimation of magma supply, storage, and eruption rates using a multiphysical volcano model: Kilauea Volcano, 2000–2012. *Earth and Planetary Science Letters*, 447:161–171, 8 2016. ISSN 0012821X. doi: 10.1016/j.epsl.2016.04.029.

K. Anderson, M. Poland, J. Johnson, and A. Miklius. Episodic Deflation–Inflation Events at Kilauea Volcano and Implications for the Shallow Magma System. In *Hawaiian Volcanoes*, chapter 11, pages 229–250. American Geophysical Union (AGU), 2015. ISBN 9781118872079. doi: 10.1002/9781118872079.ch11.

K. Anderson, I. Johanson, M. Patrick, M. Gu, P. Segall, M. Poland, E. Montgomery-Brown, and A. Miklius. Magma reservoir failure and the onset of caldera collapse at Kilauea Volcano in 2018. *Science*, 366(6470): eaaz1822, 12 2019. ISSN 10959203. doi: 10.1126/science.aaz1822.

L. C. Andrews, G. A. Catania, M. J. Hoffman, J. D. Gulley, M. P. Lüthi, C. Ryser, R. L. Hawley, and T. A. Neumann. Direct observations of evolving subglacial drainage beneath the Greenland Ice Sheet. *Nature*, 514:80–83, 2014. doi: https://doi.org/10.1038/nature13796.

A. Arciniega-Ceballos, B. Chouet, P. Dawson, and G. Asch. Broadband seismic measurements of degassing activity associated with lava effusion at Popocatépetl Volcano, Mexico. *Journal of Volcanology and Geothermal Research*, 170(1-2):12–23, 2 2008. ISSN 03770273. doi: 10.1016/j.jvolgeores.2007.09.007.

ArcticDEM. DEMs provided by the Polar Geospatial Center under NSF OPP awards 1043681, 1559691 and 1542736. 2017.

R. Aster. Very long period oscillations of Mount Erebus Volcano. *Journal of Geophysical Research*, 108(B11), 11 2003. ISSN 0148-0227. doi: 10.1029/2002jb002101.

R. Aster, D. Zandomeneghi, S. Mah, S. McNamara, D. Henderson, H. Knox, and K. Jones. Moment tensor inversion of very long period seismic signals from Strombolian eruptions of Erebus Volcano. *Journal of Volcanology and Geothermal Research*, 177(3):635–647, 11 2008. ISSN 03770273. doi: 10.1016/j.jvolgeores.2008.08.013.

S. Baker and F. Amelung. Top-down inflation and deflation at the summit of Klauea Volcano, Hawaii observed with InSAR. *Journal of Geophysical Research B: Solid Earth*, 117(12), 12 2012. ISSN 21699356. doi: 10.1029/2011JB009123.

A. Banwell, I. Hewitt, I. Willis, and N. Arnold. Moulin density controls drainage development beneath the Greenland ice sheet. *Journal of Geophysical Research: Earth Surface*, 121(12):2248–2269, 2016. doi: 10.1002/2015JF003801.

A. F. Banwell, N. S. Arnold, I. C. Willis, M. Tedesco, and A. P. Ahlstrøm. Modeling supraglacial water routing and lake filling on the Greenland Ice Sheet. *Journal of Geophysical Research: Earth Surface*, 117(F4), 2012. doi: 10.1029/2012JF002393.

I. D. Bartholomew, P. Nienow, A. Sole, D. Mair, T. Cowton, M. A. King, and S. Palmer. Seasonal variations in Greenland Ice Sheet motion: Inland extent and behaviour at higher elevations. *Earth and Planetary Science Letters*, 307: 271–278, 2011.

J. Battaglia. Location of long-period events below Kilauea Volcano using seismic amplitudes and accurate relative relocation. *Journal of Geophysical Research*, 108(B12), 12 2003. ISSN 0148-0227. doi: 10.1029/2003jb002517.

H. F. Bauer. Liquid oscillations with a free surface in wedge-shaped tanks. *Acta Mechanica*, 38(1-2):31–54, 1981. ISSN 1619-6937. doi: 10.1007/BF01351461.

J. Bell. *Machine Learning*. John Wiley & Sons, Inc, Indianapolis, IN, USA, 11 2014. ISBN 9781119183464. doi: 10.1002/9781119183464.

M. J. Bemelmans, E. de Zeeuw-van Dalfsen, M. P. Poland, and I. A. Johanson. Insight into the May 2015 summit inflation event at Kilauea Volcano, Hawaii. *Journal of Volcanology and Geothermal Research*, 415:107250, 7 2021. ISSN 03770273. doi: 10.1016/j.jvolgeores.2021.107250.

K. J. Bergen and G. C. Beroza. Earthquake Fingerprints: Extracting Waveform Features for Similarity-Based Earthquake Detection. *Pure and Applied Geophysics*, 176(3):1037–1059, 3 2019. ISSN 14209136. doi: 10.1007/s00024-018-1995-6.

J. Berger, P. Davis, and G. Ekström. Ambient Earth noise: A survey of the Global Seismographic Network. *Journal of Geophysical Research: Solid Earth*, 109 (11):1–10, 11 2004. ISSN 21699356. doi: 10.1029/2004JB003408.

B. A. Black, T. J. Perron, D. Hemingway, E. Bailey, F. Nimmo, and H. Zebker. Global drainage patterns and the origins of topographic relief on Earth, Mars, and Titan. *Science*, 356:727–731, 2017. doi: 10.1126/science.aag0171.

G. Blewitt, W. Hammond, and C. Kreemer. Harnessing the GPS Data Explosion for Interdisciplinary Science. *Eos*, 99, 9 2018. ISSN 0096-3941. doi: 10.1029/2018eo104623.

L. N. Boisvert, J. N. Lee, J. T. M. Lenaerts, B. Noël, M. R. van˜den˜Broeke, and A. W. Nolin. Using remotely sensed data from AIRS to estimate the vapor flux on the Greenland ice sheet: Comparisons with observations and a regional climate model. *Journal of Geophysical Research:Atmosphere*, 122: 202–229, 2017. doi: 10.1002/2016JD025674.

W. F. Budd. Ice Flow Over Bedrock Perturbations. *Journal of Glaciology*, 9(55): 29–48, 1970. doi: 10.3189/S0022143000026770.

A. Burgisser, M. Alletti, and B. Scaillet. Simulating the behavior of volatiles belonging to the C–O–H–S system in silicate melts under magmatic conditions with the software D-Compress. *Computers & Geosciences*, 79: 1–14, 2015. ISSN 0098-3004. doi: https://doi.org/10.1016/j.cageo.2015.03.002.

D. Carbone, M. Poland, M. Patrick, and T. Orr. Continuous gravity measurements reveal a low-density lava lake at Kilauea Volcano, Hawai'i. *Earth and Planetary Science Letters*, 376:178–185, 2013. ISSN 0012-821X. doi: https://doi.org/10.1016/j.epsl.2013.06.024.

K. M. Case and W. C. Parkinson. Damping of surface waves in an incompressible liquid. *Journal of Fluid Mechanics*, 2(2):172–184, 1957. ISSN 14697645. doi: 10.1017/S0022112057000051.

G. A. Catania, T. A. Neumann, and S. F. Price. Characterizing englacial drainage in the ablation zone of the Greenland ice sheet. *Journal of Glaciology*, 54 (187):567–578, 2008. doi: 10.3189/002214308786570854.

P. Cervelli. Analytical Expressions for Deformation from an Arbitrarily Oriented Spheroid in a Half-Space. USGS, 2013. URL `volcanoes.usgs.gov/software/spheroid`.

S. Cesca, J. Letort, H. Razafindrakoto, S. Heimann, E. Rivalta, M. Isken, M. Nikkhoo, L. Passarelli, G. Petersen, F. Cotton, and T. Dahm. Drainage of a deep magma reservoir near Mayotte inferred from seismicity and deformation. *Nature Geoscience*, 13(1):87–93, 1 2020. ISSN 17520908. doi: 10.1038/s41561-019-0505-5.

D. M. Chandler, J. L. Wadham, G. P. Lis, T. Cowton, A. Sole, I. Bartholomew, J. Telling, P. Nienow, E. B. Bagshaw, D. Mair, S. Vinen, and A. Hubbard. Evolution of the subglacial drainage system beneath the Greenland Ice Sheet revealed by tracers. *Nature Geoscience*, 6:195–198, 2013. doi: 10.1038/ngeo1737.

M. O. Chevrel, A. J. Harris, M. R. James, L. Calabrò, L. Gurioli, and H. Pinkerton. The viscosity of pahoehoe lava: In situ syn-eruptive measurements from Kilauea, Hawaii. *Earth and Planetary Science Letters*, 493:161–171, 7 2018. ISSN 0012821X. doi: 10.1016/j.epsl.2018.04.028.

B. Chouet and P. Dawson. Shallow conduit system at Kilauea Volcano, Hawaii, revealed by seismic signals associated with degassing bursts. *JGR*, 116(12): B12317, 12 2011. ISSN 21699356. doi: 10.1029/2011JB008677.

B. Chouet and P. Dawson. Very long period conduit oscillations induced by rockfalls at Kilauea Volcano, Hawaii. *JGR Solid Earth*, 118(10):5352–5371, 10 2013. ISSN 21699356. doi: 10.1002/jgrb.50376.

B. Chouet and P. Dawson. Origin of the pulse-like signature of shallow long-period volcano seismicity. *Journal of Geophysical Research: Solid Earth*, 121(8): 5931–5941, 8 2016. ISSN 21699356. doi: 10.1002/2016JB013152.

B. Chouet and R. Matoza. A multi-decadal view of seismic methods for detecting precursors of magma movement and eruption. *Journal of Volcanology and Geothermal Research*, 252:108–175, 2013. doi: 10.1016/j.jvolgeores.2012.11.013.

B. Chouet, P. Dawson, and M. Martini. Shallow-conduit dynamics at Stromboli Volcano, Italy, imaged from waveform inversions. *Geological Society Special Publication*, 307(1):57–84, 1 2008. ISSN 03058719. doi: 10.1144/SP307.5.

B. Chouet, P. Dawson, M. James, and S. Lane. Seismic source mechanism of degassing bursts at Kilauea Volcano, Hawaii: Results from waveform inversion in the 10–50 s band. *JGR*, 115, 2010. doi: 10.1029/2009JB006661.

V. W. Chu. Greenland ice sheet hydrology: A review. *Progress in Physical Geography: Earth and Environment*, 38(1):19–54, 2014. doi: 10.1177/0309133313507075.

M. G. Cooper, L. C. Smith, A. K. Rennermalm, C. Miège, L. H. Pitcher, J. C. Ryan, K. Yang, and S. W. Cooley. Meltwater storage in low-density near-surface bare ice in the Greenland ice sheet ablation zone. *The Cryosphere*, 12(3):955–970, 2018. doi: 10.5194/tc-12-955-2018.

CReSIS. CReSIS Radar Depth Sounder Data. *Lawrence, Kansas, USA. Digital Media*, 2016. doi: http://data.cresis.ku.edu/.

J. Crozier and L. Karlstrom. Wavelet-based characterization of very-long-period seismicity reveals temporal evolution of shallow magma system over the 2008-2018 eruption of Kilauea Volcano. *Journal of Geophysical Research: Solid Earth*, 126(6):e2020JB020837, jun 2021. ISSN 2169-9313. doi: 10.1029/2020jb020837.

J. Crozier, L. Karlstrom, J. Dufek, K. Anderson, W. Thelen, M. Benage, and C. Liang. Hindcasting May 2018 Kilauea Summit Explosions with Remote Sensing, Geophysical Monitoring, and Eruption Simulations. Part 1: Seismic Source Inversions and Self-consistent Initial Conditions for Plume Models. *AGUFM*, 2018:V43J–0274, 2018a. URL `https://ui.adsabs.harvard.edu/abs/2018AGUFM.V43J0274C/abstract`.

J. Crozier, L. Karlstrom, and K. Yang. Basal control of supraglacial meltwater catchments on the Greenland Ice Sheet. *Cryosphere*, 12(10):3383–3407, 2018b. ISSN 19940424. doi: 10.5194/tc-12-3383-2018.

K. M. Cuffey and W. S. B. Paterson. *The Physics of Glaciers*. Academic Press, 4 edition, 2010. ISBN 9780123694614.

S. B. Das, I. Joughin, M. D. Behn, I. M. Howat, M. A. King, D. Lizarralde, and M. P. Bhatia. Fracture Propagation to the Base of the Greenland Ice Sheet During Supraglacial Lake Drainage. *Science*, 320:778–781, 2008. doi: 10.1126/science.1153360.

P. Dawson and B. Chouet. Characterization of very-long-period seismicity accompanying summit activity at Kilauea Volcano, Hawai'i: 2007–2013. *Journal of Volcanology and Geothermal Research*, 278-279:59–85, 5 2014. ISSN 03770273. doi: 10.1016/j.jvolgeores.2014.04.010.

P. Dawson, B. Chouet, P. Okubo, A. Villaseñor, and H. Benz. Three-dimensional velocity structure of the Kilauea Caldera, Hawaii. *GRL*, 26(18):2805–2808, 9 1999. ISSN 00948276. doi: 10.1029/1999GL005379.

P. Dawson, M. Benítez, B. Chouet, D. Wilson, and P. Okubo. Monitoring very-long-period seismicity at Kilauea Volcano, Hawaii. *Geophysical Research Letters*, 37(18):n/a–n/a, 9 2010. ISSN 00948276. doi: 10.1029/2010GL044418.

P. Dawson, B. Chouet, and J. Power. Determining the seismic source mechanism and location for an explosive eruption with limited observational data: Augustine Volcano, Alaska. *Geophysical Research Letters*, 38(3):n/a–n/a, 2 2011. ISSN 00948276. doi: 10.1029/2010GL045977.

J. De Rydt, G. H. Gudmundsson, H. F. J. Corr, and P. Christoffersen. Surface undulations of Antarctic ice streams tightly controlled by bedrock topography. *The Cryosphere*, 7(2):407–417, 2013. doi: 10.5194/tc-7-407-2013.

K. Echelmeyer, T. S. Clarke, and W. D. Harrison. Surficial glaciology of Jakobshavns Isbræ, West Greenland: Part I. Surface morphology. *Journal of Glaciology*, 37(127):368–382, 1991. doi: 10.3189/S0022143000005803.

M. Edmonds, I. Sides, D. Swanson, C. Werner, R. Martin, T. Mather, R. Herd, R. Jones, M. Mead, G. Sawyer, T. Roberts, A. Sutton, and T. Elias. Magma storage, transport and degassing during the 2008-10 summit eruption at Kilauea Volcano, Hawai'i. *Geochimica et Cosmochimica Acta*, 123:284–301, 12 2013. ISSN 00167037. doi: 10.1016/j.gca.2013.05.038.

M. Edmonds, I. Sides, and J. Maclennan. Insights Into Mixing, Fractionation, and Degassing of Primitive Melts at Kilauea Volcano, Hawai'i. In *Hawaiian Volcanoes*, chapter 15, pages 323–349. American Geophysical Union (AGU), 2015. ISBN 9781118872079. doi: 10.1002/9781118872079.ch15.

T. Elias and A. J. Sutton. Sulfur dioxide emission rates from Kilauea Volcano, Hawai'i, 2007–2010. *U.S. Geological Survey Open-File Report 2012-1107*, page 25 p, 2012. URL `https://pubs.usgs.gov/of/2012/1107/`.

T. Elias, C. Kern, K. A. Horton, A. J. Sutton, and H. Garbeil. Measuring SO2 Emission Rates at Kilauea Volcano, Hawaii, Using an Array of Upward-Looking UV Spectrometers, 2014–2017. *Frontiers in Earth Science*, 6:214, 12 2018. ISSN 2296-6463. doi: 10.3389/feart.2018.00214.

E. M. Enderlin, I. M. Howat, S. Jeong, M.-J. Noh, J. H. van˜Angelen, and M. R. van˜den˜Broeke. An improved mass budget for the Greenland ice sheet. *Geophysical Research Letters*, 41(3):866–872, 2014. ISSN 1944-8007. doi: 10.1002/2013GL059010. URL http://dx.doi.org/10.1002/2013GL059010.

D. Fee and R. S. Matoza. An overview of volcano infrasound: From hawaiian to plinian, local to global. *Journal of Volcanology and Geothermal Research*, 249:123–139, 1 2013. ISSN 03770273. doi: 10.1016/j.jvolgeores.2012.09.002.

X. Fettweis, B. Franco, M. Tedesco, J. H. van˜Angelen, J. T. M. Lenaerts, M. R. van˜den˜Broeke, and H. Gallée. Estimating the Greenland ice sheet surface mass balance contribution to future sea level rise using the regional atmospheric climate model MAR. *The Cryosphere*, 7(2):469–489, 2013. doi: 10.5194/tc-7-469-2013. URL https://www.the-cryosphere.net/7/469/2013/.

Y. Fialko, Y. Khazan, and M. Simons. Deformation due to a pressurized horizontal circular crack in an elastic half-space, with applications to volcano geodesy. *Geophysical Journal International*, 146(1):181–190, 7 2001. ISSN 0956540X. doi: 10.1046/j.1365-246X.2001.00452.x.

A. G. Fountain and J. S. Walder. Water flow through temperate glaciers. *Reviews of Geophysics*, 36(3):299–328, 1998. ISSN 1944-9208. doi: 10.1029/97RG03579. URL http://dx.doi.org/10.1029/97RG03579.

A. C. Fowler. Restricted access A sliding law for glaciers of constant viscosity in the presence of subglacial cavitation. *Procedings of the Royal Society*, 407: 147–170, 1986. doi: 10.1098/rspa.1986.0090.

A. C. Fowler and M. Robinson. Counter-current convection in a volcanic conduit. *Journal of Volcanology and Geothermal Research*, 356:141–162, 5 2018. ISSN 03770273. doi: 10.1016/j.jvolgeores.2018.03.004.

O. Gagliardini, T. Zwinger, F. Gillet-Chaulet, G. Durand, L. Favier, B. de Fleurian, R. Greve, M. Malinen, C. Mart\'\in, P. Råback, J. Ruokolainen, M. Sacchettini, M. Schäfer, H. Seddik, and J. Thies. Capabilities and performance of Elmer/Ice, a new-generation ice sheet model. *Geoscientific Model Development*, 6(4):1299–1318, 2013. doi: 10.5194/gmd-6-1299-2013. URL https://www.geosci-model-dev.net/6/1299/2013/.

M. Garcés, D. Fee, and R. Matoza. Volcano acoustics. In *Modeling Volcanic Processes: The Physics and Mathematics of Volcanism*, volume 9780521895, pages 359–383. Cambridge University Press, 1 2009. ISBN 9781139021562. doi: 10.1017/CBO9781139021562.016.

G. K. Gilbert. Geology of the Henry Mountains. *U.S Geographical and Geological Survey of the Rocky Mountain Region*, 1877.

F. Gillet-Chaulet, O. Gagliardini, H. Seddik, M. Nodet, G. Durand, C. Ritz, T. Zwinger, R. Greve, and D. G. Vaughan. Greenland ice sheet contribution to sea-level rise from a new-generation ice-sheet model. *The Cryosphere*, 6(6): 1561–1576, 2012. doi: 10.5194/tc-6-1561-2012.

D. Giordano, J. K. Russell, and D. B. Dingwell. Viscosity of magmatic liquids: A model. *Earth and Planetary Science Letters*, 271(1-4):123–134, 7 2008. ISSN 0012821X. doi: 10.1016/j.epsl.2008.03.038.

H. M. Gonnermann and M. Manga. The Fluid Mechanics Inside a Volcano. *Annual Review of Fluid Mechanics*, 39(1):321–356, 2007. doi: 10.1146/annurev.fluid.39.050905.110207.

I. Goodfellow, Y. B. Bengio, and A. Courville. *Deep Learning*. MIT Press, 2016. URL `http://www.deeplearningbook.org`.

F. S. Graham, M. Morlighem, R. C. Warner, and A. Treverrow. Implementing an empirical scalar tertiary anisotropic rheology (ESTAR) into large-scale ice sheet models. *The Cryosphere Discuss*, 2017. doi: 10.5194/tc-2017-54.

G. H. Gudmundsson. Transmission of basal variability to a glacier surface. *Journal of Geophysical Research*, 108, 2003. doi: 10.1029/2002JB002107.

J. T. Hack. Studies of longitudinal stream profiles in Virginia and Maryland. *USGS Professional Papers*, 294-B, 1957.

M. Haney, B. Chouet, P. Dawson, and J. Power. Source characterization for an explosion during the 2009 eruption of Redoubt Volcano from very-long-period seismic waves. *Journal of Volcanology and Geothermal Research*, 259:77–88, 6 2013. ISSN 03770273. doi: 10.1016/j.jvolgeores.2012.04.018.

A. J. Harris. Modeling lava lake heat loss, rheology, and convection. *Geophysical Research Letters*, 35(7):n/a–n/a, 4 2008. ISSN 00948276. doi: 10.1029/2008GL033190.

J. K. Hart. Subglacial erosion, deposition and deformation associated with deformable beds. *Progress in Physical Geography: Earth and Environment*, 19(2):173–191, 1995. doi: 10.1177/030913339501900202.

M. Hellweg. Physical models for the source of Lascar's harmonic tremor. *Journal of Volcanology and Geothermal Research*, 101(1-2):183–198, 8 2000. ISSN 03770273. doi: 10.1016/S0377-0273(00)00163-3.

V. Helm, A. Humbert, and H. Miller. Elevation and elevation change of Greenland and Antarctica derived from CryoSat-2. *The Cryosphere*, 8:1539–1559, 2014. doi: 10.5194/tc-8-1539-2014.

I. J. Hewitt. Modelling distributed and channelized subglacial drainage: the spacing of channels. *Journal of Glaciology*, 57(202):302–314, 2011. doi: 10.3189/002214311796405951.

I. J. Hewitt and A. C. Fowler. Seasonal waves on glaciers. *Hydrological Processes*, 22(19):3919–3930, 2008. doi: 10.1002/hyp.7029.

M. J. Hoffman, G. A. Catania, T. A. Neumann, L. C. Andrews, and J. A. Rumrill. Links between acceleration, melting, and supraglacial lake drainage of the western Greenland Ice Sheet. *Journal of Geophysical Research: Earth Surface*, 116, 2011. doi: 10.1029/2010JF001934.

M. J. Hoffman, L. C. Andrews, S. F. Price, G. A. Catania, T. A. Neumann, M. P. Lüthi, J. Gulley, C. Ryser, R. L. Hawley, and B. Morriss. Greenland subglacial drainage evolution regulated by weakly connected regions of the bed. *Nature Communications*, 7, 2016. doi: https://doi.org/10.1038/ncomms13903.

M. J. Hoffman, M. Perego, L. C. Andrews, S. F. Price, T. A. Neumann, J. V. Johnson, G. Catania, and M. P. Lüthi. Widespread Moulin Formation During Supraglacial Lake Drainages in Greenland. *Geophysical Research Letters*, 45(2):778–788, 2018. doi: 10.1002/2017GL075659.

A. D. Howard and G. Kerby. Channel changes in badlands. *Geological Society of America Bulletin*, 94:739–752, 1983.

I. M. Howat, A. Negrete, and B. E. Smith. The Greenland Ice Mapping Project (GIMP) land classification and surface elevation data sets. *The Cryosphere*, 8 (4):1509–1518, 2014. doi: 10.5194/tc-8-1509-2014.

K. Hutter, F. Legerer, and U. Spring. First-Order Stresses and Deformations in Glaciers and Ice Sheets. *Journal of Glaciology*, 27(96):227–270, 1981. doi: 10.3189/S0022143000015379.

P. Huybrechts. Basal temperature conditions of the Greenland ice sheet during the glacial cycles. *Annals of Glaciology*, 23:226–236, 1996. doi: 10.3189/S0260305500013483.

G. Iacono-Marziano, Y. Morizet, E. Le Trong, and F. Gaillard. New experimental data and semi-empirical parameterization of H 2O-CO 2 solubility in mafic melts. *Geochimica et Cosmochimica Acta*, 97:1–23, 11 2012. ISSN 00167037. doi: 10.1016/j.gca.2012.08.035.

R. A. Ibrahim. *Liquid sloshing dynamics*, volume 9780521838. Cambridge University Press, 1 2005. ISBN 9780511536656. doi: 10.1017/CBO9780511536656.

A. Igneczi, A. J. Sole, S. J. Livingstone, A. A. Leeson, X. Fettweis, N. Selmes, N. Gourmelen, and K. Briggs. Northeast sector of the Greenland Ice Sheet to undergo the greatest inland expansion of supraglacial lakes during the 21st century. *Geophysical Research Letters*, 43:9729–9738, 2016. doi: 10.1002/2016GL070338.

A. Igneczi, A. J. Sole, S. J. Livingstone, F. S. L. Ng, and K. Yang. Greenland Ice Sheet Surface Topography and Drainage Structure Controlled by the Transfer of Basal Variability. *Frontiers in Earth Science*, 6:101, 2018. doi: 10.3389/feart.2018.00101.

M. R. James, S. J. Lane, and S. B. Corder. Modelling the rapid near-surface expansion of gas slugs in low-viscosity magmas. *Geological Society Special Publication*, 307(1):147–167, 1 2008. ISSN 03058719. doi: 10.1144/SP307.9.

S. Jennings, D. Hasterok, and J. Payne. A new compositionally based thermal conductivity model for plutonic rocks. *Geophysical Journal International*, 219 (2):1377–1394, 2019. ISSN 1365246X. doi: 10.1093/gji/ggz376.

I. Johanson. Planned USGS Data Release: doi.org/10.5066/P9LBDSDM, 2020.

I. Johanson, A. Miklius, and M. Poland. Principle component analysis to separate deformation signals from multiple sources during a 2015 intrusive sequence at Kilauea Volcano. *AGUFM*, 2016:G14A–02, 2016. URL `https://ui.adsabs.harvard.edu/abs/2016AGUFM.G14A..02J/abstract`.

A. D. Jolly, I. Lokmer, J. Thun, J. Salichon, B. Fry, and L. Chardot. Insights into fluid transport mechanisms at White Island from analysis of coupled very long-period (VLP), long-period (LP) and high-frequency (HF) earthquakes. *Journal of Volcanology and Geothermal Research*, 343:75–94, 9 2017. ISSN 03770273. doi: 10.1016/j.jvolgeores.2017.06.006.

I. Joughin, B. Smith, I. Howat, and T. Scambos. MEaSUREs Greenland Ice Velocity Map from InSAR Data. *National Snow and Ice Data Center*, 2010a. doi: 10.5067/MEASURES/CRYOSPHERE/nsidc-0478.001.

I. Joughin, B. Smith, I. M. Howat, T. Scambos, and T. Moon. Greenland Flow Variability from Ice-Sheet-Wide Velocity Mapping. *Journal of Glaciology*, 56: 415–430, 2010b. doi: 10.3189/002214310792447734.

I. Joughin, S. B. Das, G. E. Flowers, M. D. Behn, R. B. Alley, M. A. King, B. E. Smith, J. L. Bamber, M. R. van den Broeke, and J. H. van Angelen. Influence of ice-sheet geometry and supraglacial lakes on seasonal ice-flow variability. *The Cryosphere*, 7(4):1185–1192, 2013. doi: 10.5194/tc-7-1185-2013.

B. R. Julian. Volcanic tremor: nonlinear excitation by fluid flow. *Journal of Geophysical Research*, 99(B6), 1994. ISSN 01480227. doi: 10.1029/93jb03129.

L. Karlstrom and E. M. Dunham. Excitation and resonance of acoustic-gravity waves in a column of stratified, bubbly magma. *Journal of Fluid Mechanics*, 797:431–470, 6 2016. ISSN 14697645. doi: 10.1017/jfm.2016.257.

L. Karlstrom and M. Richards. On the evolution of large ultramafic magma chambers and timescales for flood basalt eruptions. *Journal of Geophysical Research: Solid Earth*, 116(8):B08216, 8 2011. ISSN 21699356. doi: 10.1029/2010JB008159.

L. Karlstrom, S. Hurwitz, R. Sohn, J. Vandemeulebrouck, F. Murphy, M. L. Rudolph, M. J. S. Johnston, M. Manga, and R. B. McCleskey. Eruptions at Lone Star Geyser, Yellowstone National Park, USA: 1. Energetics and eruption dynamics. *Journal of Geophysical Research: Solid Earth*, 118(8): 4048–4062, 2013. doi: 10.1002/jgrb.50251.

L. Karlstrom, A. Zok, and M. Manga. Near-surface permeability in a supraglacial drainage basin on the Llewellyn glacier, Juneau Ice Field, British Columbia,. *The Cryosphere*, 8:537–546, 2014. doi: 10.5194/tc-8-537-2014.

J. L. Kavanaugh and G. K. C. Clarke. Evidence for extreme pressure pulses in the subglacial water system. *Journal of Glaciology*, 46(153):206–212, 2000. doi: 10.3189/172756500781832963.

S. A. Khan, A. Aschwanden, A. A. Bjørk, J. Wahr, K. K. Kjeldsen, and K. H. Kjær. Greenland ice sheet mass balance: a review. *IOP Reports on Progress in Physics*, 2015. doi: https://doi.org/10.1088/0034-4885/78/4/046801.

H. A. Knox, J. A. Chaput, R. C. Aster, and P. R. Kyle. Multiyear Shallow Conduit Changes Observed With Lava Lake Eruption Seismograms at Erebus Volcano, Antarctica. *Journal of Geophysical Research: Solid Earth*, 123(4): 3178–3196, 2018. ISSN 21699356. doi: 10.1002/2017JB015045.

S. S. Köcher, T. Heydenreich, and S. J. Glaser. Visualization and analysis of modulated pulses in magnetic resonance by joint time-frequency representations. *Journal of Magnetic Resonance*, 249:63–71, 12 2014. ISSN 10960856. doi: 10.1016/j.jmr.2014.10.004.

L. S. Koenig, A. Ivanoff, P. M. Alexander, J. A. MacGregor, X. Fettweis, B. Panzer, J. D. Paden, R. R. Forster, I. Das, J. R. McConnell, M. Tedesco, C. Leuschen, and P. Gogineni. Annual Greenland accumulation rates (2009–2012)\hack{\newline} from airborne snow radar. *The Cryosphere*, 10 (4):1739–1752, 2016. doi: 10.5194/tc-10-1739-2016.

A. Kohler, M. Ohrnberger, and F. Scherbaum. Unsupervised pattern recognition in continuous seismic wavefield records using Self-Organizing Maps. *Geophysical Journal International*, 182(3):1619–1630, 9 2010. ISSN 0956540X. doi: 10.1111/j.1365-246X.2010.04709.x.

H. Kumagai. Temporal evolution of a magmatic dike system inferred from the complex frequencies of very long period seismic signals. *Journal of Geophysical Research: Solid Earth*, 111(6):n/a–n/a, 6 2006. ISSN 21699356. doi: 10.1029/2005JB003881.

H. Kumagai and B. Chouet. Acoustic properties of a crack containing magmatic or hydrothermal fluids. *Journal of Geophysical Research: Solid Earth*, 105(B11): 25493–25512, 11 2000. ISSN 21699356. doi: 10.1029/2000jb900273.

H. Kumagai, K. Miyakawa, H. Negishi, H. Inoue, K. Obara, and D. Suetsugu. Magmatic dike resonances inferred from very-long-period seismic signals. *Science*, 299(5615):2058–2061, 3 2003. ISSN 00368075. doi: 10.1126/science.1081195.

H. Kumagai, M. Nakano, T. Maeda, H. Yepes, P. Palacios, M. Ruiz, S. Arrais, M. Vaca, I. Molina, and T. Yamashima. Broadband seismic monitoring of active volcanoes using deterministic and stochastic approaches. *Journal of Geophysical Research: Solid Earth*, 115(8), 8 2010. ISSN 21699356. doi: 10.1029/2009JB006889.

M. Kumazawa, Y. Imanishi, Y. Fukao, M. Furumoto, and A. Yamamoto. A theory of spectral analysis based on the characteristic property of a linear dynamic system. *Geophysical Journal International*, 101(3):613–630, 6 1990. ISSN 1365246X. doi: 10.1111/j.1365-246X.1990.tb05574.x.

D. J. Lampkin. Supraglacial lake spatial structure in western Greenland during the 2007 ablation season. *Journal of Geophysical Research: Earth Surface*, 116 (F4):n/a–n/a, 2011. ISSN 2156-2202. doi: 10.1029/2010JF001725. URL `http://dx.doi.org/10.1029/2010JF001725`.

D. J. Lampkin and J. van˜der˜Berg. A preliminary investigation of the influence of basal and surface topography on supraglacial lake distribution near Jakobshavn Isbrae, western Greenland. *Hydrological Processes*, 25(21): 3347–3355, 2011. doi: 10.1002/hyp.8170.

R. A. Lange and I. S. E. Carmichael. Densities of Na2O-K2O-CaO-MgO-FeO-Fe2O3-Al2O3-TiO2-SiO2 liquids: New measurements and derived partial molar properties. *Geochimica et Cosmochimica Acta*, 51(11):2931–2946, 1987. ISSN 0016-7037. doi: https://doi.org/10.1016/0016-7037(87)90368-1.

S. Lapins, D. C. Roman, J. Rougier, S. De Angelis, K. V. Cashman, and J. M. Kendall. An examination of the continuous wavelet transform for volcano-seismic spectral analysis. *Journal of Volcanology and Geothermal Research*, 389:106728, 1 2020. ISSN 03770273. doi: 10.1016/j.jvolgeores.2019.106728.

E. Larour, H. Seroussi, M. Morlighem, and E. Rignot. Continental scale, high order, high spatial resolution, ice sheet modeling using the Ice Sheet System Model (ISSM). *Journal of Geophysical Research: Earth Surface*, 117(F1), 2012. doi: 10.1029/2011JF002140.

A. A. Leeson, A. Shepherd, K. Briggs, I. Howat, X. Fettweis, M. Morlighem, and E. Rignot. Supraglacial lakes on the Greenland ice sheet advance inland under warming climate. *Nature Climate Change*, 5:51–55, 2015. doi: 10.1038/nclimate2463.

D. Legrand, S. Kaneshima, and H. Kawakatsu. Moment tensor analysis of near-field broadband waveforms observed at Aso volcano, Japan. *Journal of Volcanology and Geothermal Research*, 101(1-2):155–169, 8 2000. ISSN 03770273. doi: 10.1016/S0377-0273(00)00167-0.

P. Lesage. Interactive Matlab software for the analysis of seismic volcanic signals. *Computers and Geosciences*, 35(10):2137–2144, 10 2009. ISSN 00983004. doi: 10.1016/j.cageo.2009.01.010.

P. Lesage, F. Glangeaud, and J. Mars. Applications of autoregressive models and time-frequency analysis to the study of volcanic tremor and long-period events. *Journal of Volcanology and Geothermal Research*, 114(3-4):391–417, 5 2002. ISSN 03770273. doi: 10.1016/S0377-0273(01)00298-0.

C. Liang and E. Dunham. Lava lake sloshing modes during the 2018 Kilauea Volcano eruption probe magma reservoir storativity. *Earth and Planetary Science Letters*, 535:116110, 4 2020. ISSN 0012821X. doi: 10.1016/j.epsl.2020.116110.

C. Liang, J. Crozier, L. Karlstrom, and E. Dunham. Magma Oscillations in a Conduit-Reservoir System, Application to Very Long Period (VLP) Seismicity at Basaltic Volcanoes: 2. Data Inversion and Interpretation at Kilauea Volcano. *Journal of Geophysical Research: Solid Earth*, 125(1), 1 2020a. ISSN 21699356. doi: 10.1029/2019JB017456.

C. Liang, L. Karlstrom, and E. Dunham. Magma Oscillations in a Conduit-Reservoir System, Application to Very Long Period (VLP) Seismicity at Basaltic Volcanoes: 1. Theory. *Journal of Geophysical Research: Solid Earth*, 125(1), 1 2020b. ISSN 21699356. doi: 10.1029/2019JB017437.

Y. Liao, S. A. Soule, and M. Jones. On the Mechanical Effects of Poroelastic Crystal Mush in Classical Magma Chamber Models. *Journal of Geophysical Research: Solid Earth*, 123(11):9376–9406, 2018. doi: 10.1029/2018JB015985.

J. M. Lilly and S. C. Olhede. Higher-order properties of analytic wavelets. *IEEE Transactions on Signal Processing*, 57(1):146–160, 2009. ISSN 1053587X. doi: 10.1109/TSP.2008.2007607.

G. Lin, P. Shearer, R. Matoza, P. Okubo, and F. Amelung. Three-dimensional seismic velocity structure of Mauna Loa and Kilauea volcanoes in Hawaii from local seismic tomography. *Journal of Geophysical Research: Solid Earth*, 119(5):4377–4392, 2014. ISSN 21699356. doi: 10.1002/2013JB010820.

W. H. Lipscomb, J. G. Fyke, M. Vizcaíno, W. J. Sacks, J. Wolfe, M. Vertenstein, A. Craig, E. Kluzek, and D. M. Lawrence. Implementation and Initial Evaluation of the Glimmer Community Ice Sheet Model in the Community Earth System Model. *Journal of Climate*, 26(19):7352–7371, 2013. doi: 10.1175/JCLI-D-12-00557.1.

E. W. Llewellin and M. Manga. Bubble suspension rheology and implications for conduit flow. *Journal of Volcanology and Geothermal Research*, 143(1-3): 205–217, 5 2005. ISSN 03770273. doi: 10.1016/j.jvolgeores.2004.09.018.

I. Lokmer, G. Saccorotti, B. Di Lieto, and C. J. Bean. Temporal evolution of long-period seismicity at Etna Volcano, Italy, and its relationships with the 2004-2005 eruption. *Earth and Planetary Science Letters*, 266(1-2):205–220, 2 2008. ISSN 0012821X. doi: 10.1016/j.epsl.2007.11.017.

J. J. Lyons and G. P. Waite. Dynamics of explosive volcanism at Fuego volcano imaged with very long period seismicity. *Journal of Geophysical Research: Solid Earth*, 116(9), 9 2011. ISSN 21699356. doi: 10.1029/2011JB008521.

J. A. MacGregor, M. A. Fahnestock, G. A. Catania, A. Aschwanden, G. D. Clow, W. T. Colgan, S. P. Gogineni, M. Morlighem, S. M. J. Nowicki, J. D. Paden, S. F. Price, and H. Seroussi. A synthesis of the basal thermal state of the Greenland Ice Sheet. *Journal of Geophysical Research: Earth Surface*, 121(7): 1328–1350, 2016. doi: 10.1002/2015JF003803.

B. H. Mackey and J. J. Roering. Sediment yield, spatial characteristics, and the long-term evolution of active earthflows determined from airborne LiDAR and historical aerial photographs, Eel River, California. *GSA Bulletin*, 123: 1560–1576, 2011. doi: 10.1130/B30306.1.

H. Mader, E. Llewellin, and S. Mueller. The rheology of two-phase magmas: A review and analysis. *Journal of Volcanology and Geothermal Research*, 257: 135–158, 5 2013. ISSN 03770273. doi: 10.1016/j.jvolgeores.2013.02.014.

Y. Maeda and M. Takeo. Very-long-period pulses at Asama volcano, central Japan, inferred from dense seismic observations. *Geophysical Journal International*, 185(1):265–282, 4 2011. ISSN 0956540X. doi: 10.1111/j.1365-246X.2011.04938.x.

Y. Maeda, M. Takeo, and T. Ohminato. A waveform inversion including tilt: Method and simple tests. *Geophysical Journal International*, 184(2):907–918, 2 2011. ISSN 0956540X. doi: 10.1111/j.1365-246X.2010.04892.x.

M. Mangan, K. Cashman, and D. Swanson. The dynamics of Hawaiian-style eruptions: A century of study. *USGS Professional Paper*, pages 323–354, 2014. ISSN 2330-7102. doi: 10.3133/PP18018.

R. Matoza, D. Fee, and M. Garcs. Infrasonic tremor wavefield of the Pu'u 'O'o crater complex and lava tube system, Hawaii, in April 2007. *Journal of Geophysical Research: Solid Earth*, 115(12):B12312, 12 2010. ISSN 21699356. doi: 10.1029/2009JB007192.

R. Matoza, D. Fee, D. Green, and P. Mialle. Volcano infrasound and the international monitoring system. In *Infrasound Monitoring for Atmospheric Studies: Challenges in Middle Atmosphere Dynamics and Societal Benefits: Second Edition*, pages 1023–1077. Springer International Publishing, 10 2018. ISBN 9783319751405. doi: 10.1007/978-3-319-75140-5_33.

S. McNutt and D. Roman. Volcanic Seismicity. In *The Encyclopedia of Volcanoes*, pages 1011–1034. Elsevier, 1 2015. doi: 10.1016/b978-0-12-385938-9.00059-6.

M. McQuillan and L. Karlstrom. Fluid resonance in elastic-walled englacial transport networks. *Journal of Glaciology*, 2021. doi: (Accepted).

T. Meierbachtol, J. Harper, and N. Humphrey. Basal Drainage System Response to Increasing Surface Melt on the Greenland Ice Sheet. *Science*, 341:777–779, 2013. doi: 10.1126/science.1235905.

C. R. Meyer and I. J. Hewitt. A continuum model for meltwater flow through compacting snow. *The Cryosphere*, 11(6):2799–2813, 2017. doi: 10.5194/tc-11-2799-2017. URL `https://www.the-cryosphere.net/11/2799/2017/`.

A. Miklius. Hawaii GPS Network, 2008. URL https://www.unavco.org/data/doi/doi-app/dois.php?doi=T5RR1WGN.

K. Mogi. Relation between the eruptions of various volcanoes and deformations of the ground surfaces around them. *Bulletin of the Earthquake Research Institute*, 36:99–134, 1958.

D. Montgomery. Slope Distributions, Threshold Hillslopes, and Steady-state Topography. *American Journal of Science*, 301:432–454, 2001. doi: 10.2475/ajs.301.4-5.432.

E. Montgomery-brown, M. Poland, and A. Miklius. Delicate balance of magmatic-tectonic interaction at Kilauea Volcano, Hawai'i, revealed from slow slip events. In *Geophysical Monograph Series: Hawaiian Volcanoes: From Source to Surface*, volume 208, pages 269–288. Blackwell Publishing Ltd, 2 2015. doi: 10.1002/9781118872079.ch13.

M. Morlighem, E. Rignot, H. Seroussi, E. Larour, H. Ben Dhia, and D. Aubry. A mass conservation approach for mapping glacier ice thickness. *Geophysical Research Letters*, 38(19), 2011. doi: 10.1029/2011GL048659.

M. Morlighem, H. Seroussi, E. Larour, and E. Rignot. Inversion of basal friction in Antarctica using exact and incomplete adjoints of a higher-order model. *Journal of Geophysical Research: Earth Surface*, 118(3):1746–1753, 2013. doi: 10.1002/jgrf.20125.

M. Morlighem, E. Rignot, J. Mouginot, H. Seroussi, and E. Larour. Deeply incised submarine glacial valleys beneath the Greenland Ice Sheet. *Nature Geoscience*, 7:418–422, 2014. doi: 10.1038/ngeo2167.

M. Morlighem, E. Rignot, J. Mouginot, H. Seroussi, and E. Larour. IceBridge BedMachine Greenland, Version 2. *NASA DAAC at the National Snow and Ice Data Center*, 2015. doi: 10.5067/AD7B0HQNSJ29.

M. Morlighem, C. N. Williams, E. Rignot, L. An, J. E. Arndt, J. L. Bamber, G. Catania, N. Chauché, J. A. Dowdeswell, B. Dorschel, I. Fenty, K. Hogan, I. Howat, A. Hubbard, M. Jakobsson, T. M. Jordan, K. K. Kjeldsen, R. Millan, L. Mayer, J. Mouginot, B. P. Y. Noël, C. O'Cofaigh, S. Palmer, S. Rysgaard, H. Seroussi, M. J. Siegert, P. Slabon, F. Straneo, M. R. van den Broeke, W. Weinrebe, M. Wood, and K. B. Zinglersen. IceBridge BedMachine Greenland, Version 3. *Boulder, Colorado USA. NASA National Snow and Ice Data Center Distributed Active Archive Center*, 2017a. doi: https://doi.org/10.5067/2CIX82HUV88Y.

M. Morlighem, C. N. Williams, E. Rignot, L. An, J. E. Arndt, J. L. Bamber, G. Catania, N. Chauché, J. A. Dowdeswell, B. Dorschel, I. Fenty, K. Hogan, I. Howat, A. Hubbard, M. Jakobsson, T. M. Jordan, K. K. Kjeldsen, R. Millan, L. Mayer, J. Mouginot, B. P. Y. Noël, C. O'Cofaigh, S. Palmer, S. Rysgaard, H. Seroussi, M. J. Siegert, P. Slabon, F. Straneo, M. R. van˜den˜Broeke, W. Weinrebe, M. Wood, and K. B. Zinglersen. BedMachine v3: Complete Bed Topography and Ocean Bathymetry Mapping of Greenland From Multibeam Echo Sounding Combined With Mass Conservation. *Geophysical Research Letters*, 44(21):11–51, 2017b. doi: 10.1002/2017GL074954.

S. M. Mousavi, W. Zhu, W. Ellsworth, and G. Beroza. Unsupervised Clustering of Seismic Signals Using Deep Convolutional Autoencoders. *IEEE Geoscience and Remote Sensing Letters*, 16(11):1693–1697, 11 2019. ISSN 15580571. doi: 10.1109/LGRS.2019.2909218.

P. Nadeau, C. Werner, G. Waite, S. Carn, I. Brewer, T. Elias, A. Sutton, and C. Kern. Using SO2 camera imagery and seismicity to examine degassing and gas accumulation at Kilauea Volcano, May 2010. *Journal of Volcanology and Geothermal Research*, 300:70–80, 5 2014. ISSN 03770273. doi: 10.1016/j.jvolgeores.2014.12.005.

T. Nagler, H. Rott, M. Hetzenecker, J. Wuite, and P. Potin. The Sentinel-1 Mission: New Opportunities for Ice Sheet Observations. *Remote Sensing*, 7: 9371–9389, 2015. doi: 10.3390/rs70709371.

H. Nakamichi, H. Kumagai, M. Nakano, M. Okubo, F. Kimata, Y. Ito, and K. Obara. Source mechanism of a very-long-period event at Mt Ontake, central Japan: Response of a hydrothermal system to magma intrusion beneath the summit. *Journal of Volcanology and Geothermal Research*, 187 (3-4):167–177, 11 2009. ISSN 03770273. doi: 10.1016/j.jvolgeores.2009.09.006.

M. Nakano, H. Kumagai, M. Kumazawa, K. Yamaoka, and B. Chouet. The excitation and characteristic frequency of the long-period volcanic event: An approach based on an inhomogeneous autoregressive model of a linear dynamic system. *Journal of Geophysical Research: Solid Earth*, 103(B5): 10031–10046, 5 1998. ISSN 2169-9356. doi: 10.1029/98jb00387.

C. Neal, S. Brantley, L. Antolik, J. Babb, M. Burgess, K. Calles, M. Cappos, J. Chang, S. Conway, L. Desmither, P. Dotray, T. Elias, P. Fukunaga, S. Fuke, I. Johanson, K. Kamibayashi, J. Kauahikaua, R. Lee, S. Pekalib, A. Miklius, W. Million, C. Moniz, P. Nadeau, P. Okubo, C. Parcheta, M. Patrick, B. Shiro, D. Swanson, W. Tollett, F. Trusdell, E. Younger, M. Zoeller, E. Montgomery-Brown, K. Anderson, M. Poland, J. Ball, J. Bard, M. Coombs, H. Dietterich, C. Kern, W. Thelen, P. Cervelli, T. Orr, B. Houghton, C. Gansecki, R. Hazlett, P. Lundgren, A. Diefenbach, A. Lerner, G. Waite, P. Kelly, L. Clor, C. Werner, K. Mulliken, G. Fisher, and D. Damby. Volcanology: The 2018 rift eruption and summit collapse of Kilauea Volcano. *Science*, 363(6425):367–374, 1 2019. ISSN 10959203. doi: 10.1126/science.aav7046.

F. S. L. Ng, A. Igneczi, A. J. Sole, and S. J. Livingstone. Response of surface topography to basal variability along glacial flowlines. *Journal of Geophysical Research: Earth Surface*, 0(ja), 2018. doi: 10.1029/2017JF004555.

B. Noel, W. J. van˜de˜Berg, E. van˜Meijgaard, P. K. Munneke, R. S. W. van˜de˜Wal, and M. R. van˜den˜Broeke. Evaluation of the updated regional climate model RACMO2.3: summer snowfall impact on the Greenland Ice Sheet. *The Cryosphere*, 9:1831–1844, 2015. doi: doi:10.5194/tc-9-1831-2015.

M.-J. Noh and I. M. Howat. Automated stereo-photogrammetric DEM generation at high latitudes: Surface Extraction with TIN-based Search-space Minimization (SETSM) validation and demonstration over glaciated regions. *GIScience and Remote Sensing*, 52:198–217, 2015. doi: 10.1080/15481603.2015.1008621.

J. F. Nye. The response of glaciers and ice-sheets to seasonal and climatic changes. *Proc. Royal Society*, 256:559–584, 1960. doi: 10.1098/rspa.1960.0127.

D. O'Hara, L. Karlstrom, and J. Roering. Distributed landscape response to localized uplift and the fragility of steady states. *Earth and Planetary Science Letters*, 506:243–254, 2019. doi: 10.1016/j.epsl.2018.11.006.

T. Orr, W. Thelen, M. Patrick, D. Swanson, and D. Wilson. Explosive eruptions triggered by rockfalls at Kilauea volcano, Hawai'i. *Geology*, 41(2):207–210, 2013. ISSN 00917613. doi: 10.1130/G33564.1.

T. Orr, M. Poland, M. Patrick, W. Thelen, A. Sutton, T. Elias, C. Thornber, C. Parcheta, and K. Wooten. Kilauea's 5–9 march 2011 Kamoamoa fissure eruption and its relation to 30+ years of activity from Pu‘u ‘O‘o. In *Geophysical Monograph Series*, volume 208, pages 393–420. Blackwell Publishing Ltd, 2 2015. doi: 10.1002/9781118872079.ch18.

S. Owen, P. Segall, M. Lisowski, A. Miklius, R. Denlinger, and M. Sako. Rapid deformation of Kilauea Volcano: Global Positioning System measurements between 1990 and 1996. *Journal of Geophysical Research: Solid Earth*, 105 (B8):18983–18998, 8 2000. ISSN 21699356. doi: 10.1029/2000jb900109.

R. Pal. Rheological behavior of bubble-bearing magmas. *Earth and Planetary Science Letters*, 207(1-4):165–179, 2 2003. ISSN 0012821X. doi: 10.1016/S0012-821X(02)01104-4.

J. Pallister and S. R. McNutt. Synthesis of Volcano Monitoring. In *The Encyclopedia of Volcanoes*, pages 1151–1171. Elsevier, 1 2015. doi: 10.1016/b978-0-12-385938-9.00066-3.

I. Park, A. Jolly, I. Lokmer, and B. Kennedy. Classification of long-term very long period (VLP) volcanic earthquakes at Whakaari/White Island volcano, New Zealand. *Earth, Planets and Space*, 72(1):92, 12 2020. ISSN 18805981. doi: 10.1186/s40623-020-01224-z.

G. Parker. Meandering of supraglacial melt streams. *Water Resources Research*, 11:551–552, 1975.

M. Patrick, D. Wilson, D. Fee, T. Orr, and D. Swanson. Shallow degassing events as a trigger for very-long-period seismicity at Kilauea Volcano, Hawai'i. *Bulletin of Volcanology*, 73(9):1179–1186, 2011. ISSN 02588900. doi: 10.1007/s00445-011-0475-y.

M. Patrick, K. Anderson, M. Poland, T. Orr, and D. Swanson. Lava lake level as a gauge of magma reservoir pressure and eruptive hazard. *Geology*, 43(9): 831–834, 9 2015. ISSN 19432682. doi: 10.1130/G36896.1.

M. Patrick, T. Orr, A. Sutton, E. Lev, W. Thelen, and D. Fee. Shallowly driven fluctuations in lava lake outgassing (gas pistoning), Kilauea Volcano. *Earth and Planetary Science Letters*, 433:326–338, 1 2016a. ISSN 0012821X. doi: 10.1016/j.epsl.2015.10.052.

M. Patrick, T. Orr, D. Swanson, and E. Lev. Shallow and deep controls on lava lake surface motion at Kilauea Volcano. *Journal of Volcanology and Geothermal Research*, 328:247–261, 12 2016b. ISSN 03770273. doi: 10.1016/j.jvolgeores.2016.11.010.

M. Patrick, T. Orr, K. Anderson, and D. Swanson. Eruptions in sync: Improved constraints on Kilauea Volcano's hydraulic connection. *Earth and Planetary Science Letters*, 507:50–61, 2019a. ISSN 0012-821X. doi: https://doi.org/10.1016/j.epsl.2018.11.030.

M. Patrick, D. Swanson, and T. Orr. A review of controls on lava lake level: insights from Halemaʻumaʻu Crater, Kilauea Volcano. *Bulletin of Volcanology*, 81(3):1–26, 3 2019b. ISSN 14320819. doi: 10.1007/s00445-019-1268-y.

M. Patrick, B. Houghton, K. Anderson, M. Poland, E. Montgomery-Brown, I. Johanson, W. Thelen, and T. Elias. The cascading origin of the 2018 Kīlauea eruption and implications for future forecasting. *Nature Communications*, 11(1):5646, 2020. ISSN 2041-1723. doi: 10.1038/s41467-020-19190-1.

T. Perol, M. Gharbi, and M. Denolle. Convolutional neural network for earthquake detection and location. *Science Advances*, 4(2):e1700578, 2 2018. ISSN 23752548. doi: 10.1126/sciadv.1700578.

J. T. Perron, J. W. Kirchner, and W. E. Dietrich. Spectral signatures of characteristic spatial scales and nonfractal structure in landscapes. *Journal of Geophysical Research*, 113, 2008. doi: 10.1029/2007JF000866.

M. Poland and D. Carbone. Insights into shallow magmatic processes at Kilauea Volcano, Hawaii, from a multiyear continuous gravity time series. *Journal of Geophysical Research: Solid Earth*, 121(7):5477–5492, 2016. doi: 10.1002/2016JB013057.

M. Poland and D. Carbone. Continuous Gravity and Tilt Reveal Anomalous Pressure and Density Changes Associated With Gas Pistoning Within the Summit Lava Lake of Kilauea Volcano, Hawaiʻi. *Geophysical Research Letters*, 45(5):2319–2327, 2018. ISSN 19448007. doi: 10.1002/2017GL076936.

M. Poland, A. Miklius, A. Jeff Sutton, and C. Thornber. A mantle-driven surge in magma supply to Kilauea Volcano during 2003-2007. *Nature Geoscience*, 5 (4):295–300, 4 2012. ISSN 17520894. doi: 10.1038/ngeo1426.

M. Poland, T. Orr, J. Kauahikaua, S. Brantley, J. Babb, M. Patrick, C. Neal, K. Anderson, L. Antolik, M. Burgess, T. Elias, S. Fuke, P. Fukunaga, I. Johanson, M. Kagimoto, K. Kamibayashi, L. Lee, A. Miklius, W. Million, C. Moniz, P. Okubo, A. Sutton, T. Takahashi, W. Thelen, W. Tollett, and F. Trusdell. The 2014-2015 Pahoa lava flow crisis at Kilauea Volcano, Hawai'i: Disaster avoided and lessons learned. *GSA Today*, 26(2):4–10, 2 2016. ISSN 10525173. doi: 10.1130/GSATG262A.1.

M. P. Poland, A. Miklius, and E. K. Montgomery-Brown. Magma supply, storage, and transport at shield-stage Hawaiian volcanoes: Chapter 5 in Characteristics of Hawaiian volcanoes. In M. P. Poland, T. J. Takahashi, and C. M. Landowski, editors, *Characteristics of Hawaiian volcanoes*, volume 1801, pages 179–234. U.S. Geological Survey Professional Paper, 2014. ISBN 18015. doi: 10.3133/pp18015.

W. H. Press, S. A. Teukolsky, W. T. Vetterling, and B. P. Flannery. Numerical Recipes The Art of Scientific Computing 3rd Edition. *Cambridge University Press*, 2007. doi: ISBN-13: 9780521880688.

J. G. Proakis and D. G. Monolakis. *Digital Signal Processing: principles, devices and applications*. Peter Peregrinus Ltd, 1990. ISBN 0-13-394338-9. doi: 10.1049/pbce042e.

P. Quinn, K. Beven, P. Chevallier, and O. Planchon. The prediction of hillslope flow paths for distributed hydrological modelling using digital terrain models. *Hydrological Processes*, 5(1):59–79, 1991. doi: 10.1002/hyp.3360050106.

J. G. L. Rae, G. AÃ°algeirsdóttir, T. L. Edwards, X. Fettweis, J. M. Gregory, H. T. Hewitt, J. A. Lowe, P. Lucas-Picher, R. H. Mottram, A. J. Payne, J. K. Ridley, S. R. Shannon, W. J. van˜de˜Berg, R. S. W. van˜de˜Wal, and M. R. van˜den˜Broeke. Greenland ice sheet surface mass balance: evaluating simulations and making projections with regional climate models. *The Cryosphere*, 6(6):1275–1294, 2012. doi: 10.5194/tc-6-1275-2012. URL `https://www.the-cryosphere.net/6/1275/2012/`.

M. J. Raymond and G. H. Gudmundsson. Estimating basal properties of ice streams from surface measurements: a non-linear Bayesian inverse approach applied to synthetic data. *The Cryosphere*, 3:265–278, 2009. doi: 10.5194/tc-3-265-2009.

M. J. Raymond and G. H. Gudmundsson. On the relationship between surface and basal properties on glaciers, ice sheets, and ice streams. *Journal of Geophysical Research: Solid Earth*, 110(B8), 2011. doi: 10.1029/2005JB003681.

A. W. Rempel. Effective stress profiles and seepage flows beneath glaciers and ice sheets. *Journal of Glaciology*, 55(191):431–443, 2009. doi: 10.3189/002214309788816713.

M. Ripepe, D. D. Donne, R. Genco, G. Maggio, M. Pistolesi, E. Marchetti, G. Lacanna, G. Ulivieri, and P. Poggi. Volcano seismicity and ground deformation unveil the gravity-driven magma discharge dynamics of a volcanic eruption. *Nature Communications*, 6(1):1–6, 5 2015. ISSN 20411723. doi: 10.1038/ncomms7998.

A. Roman and P. Lundgren. Dynamics of large effusive eruptions driven by caldera collapse. *Nature*, 592(7854):392–396, 4 2021. ISSN 0028-0836. doi: 10.1038/s41586-021-03414-5. URL http://www.nature.com/articles/s41586-021-03414-5.

L. Royden and J. T. Perron. Solutions of the stream power equation and application to the evolution of river longitudinal profiles. *Journal of Geophysical Research Earth Surface*, 118:497–518, 2013. doi: 10.1002/jgrf.20031.

C. Ryser, M. P. Lüthi, L. C. Andrews, G. A. Catania, M. Funk, R. Hawley, M. Hoffman, and T. A. Neumann. Caterpillar-like ice motion in the ablation zone of the Greenland ice sheet. *Journal of Geophysical Research: Earth Surface*, 119(10):2258–2271, 2014a. doi: 10.1002/2013JF003067.

C. Ryser, M. P. Lüthi, L. C. Andrews, M. J. Hoffman, G. A. Catania, R. L. Hawley, T. A. Neumann, and S. S. Kristensen. Sustained high basal motion of the Greenland ice sheet revealed by borehole deformation. *Journal of Glaciology*, 60(222):647–660, 2014b. doi: 10.3189/2014JoG13J196.

D. P. Schaff. Semiempirical statistics of correlation-detector performance. *Bulletin of the Seismological Society of America*, 98(3):1495–1507, 6 2008. ISSN 00371106. doi: 10.1785/0120060263.

C. Schoof. Ice-sheet acceleration driven by melt supply variability. *Nature*, 468: 803–806, 2010. doi: 10.1038/nature09618.

N. Schorghofer and D. H. Rothman. Acausal relations between topographic slope and drainage area. *Geophysical Research Letters*, 29(13):11–14, 2002. ISSN 1944-8007. doi: 10.1029/2002GL015144. URL http://dx.doi.org/10.1029/2002GL015144.

S. D. Schwanghart W. TopoToolbox 2 – MATLAB-based software for topographic analysis and modeling in Earth surface sciences. *Earth Surface Dynamics*, 2: 1–7, 2014. doi: 10.5194/esurf-2-1-2014.

P. Segall. *Earthquake and volcano deformation*. Princeton University Press, 2010. ISBN 9780691133027. doi: 10.5860/choice.48-0287.

M. A. Seidl and W. E. Dietrich. The problem of channel erosion into bedrock. *Catena Supplement*, 23:101–124, 1992.

I. W. Selesnick, R. G. Baraniuk, and N. G. Kingsbury. The dual-tree complex wavelet transform. *IEEE Signal Processing Magazine*, 22(6):123–151, 2005. ISSN 10535888. doi: 10.1109/MSP.2005.1550194.

N. Selmes, T. Murray, and T. D. James. Fast draining lakes on the Greenland Ice Sheet. *Geophysical Research Letters*, 38(15):n/a–n/a, 2011. ISSN 1944-8007. doi: 10.1029/2011GL047872. URL http://dx.doi.org/10.1029/2011GL047872.

O. V. Sergienko. Glaciological twins: basally controlled subglacial and supraglacial lakes. *Journal of Glaciology*, 59(213):3–8, 2013. doi: 10.3189/2013JoG12J040.

S. R. Shannon, A. J. Payne, I. D. Bartholomew, M. R. van˜den˜Broeke, T. L. Edwards, X. Fettwei, O. Gagliardini, F. Gillet-Chaulet, H. Goelzer, M. J. Hoffman, P. Huybrechts, D. W. F. Mair, P. W. Nienow, M. Perego, S. F. Price, C. J. P. P. Smeets, A. J. Sole, R. S. W. van˜de˜Wal, and T. Zwinger. Enhanced basal lubrication and the contribution of the Greenland ice sheet to future sea-level rise. *Proceedings of the National Academy of Sciences*, 110: 14156–14161, 2013. doi: 10.1073/pnas.1212647110.

T. Shreve, R. Grandin, M. Boichu, E. Garaebiti, Y. Moussallam, V. Ballu, F. Delgado, F. Leclerc, M. Vallée, N. Henriot, S. Cevuard, D. Tari, P. Lebellegard, and B. Pelletier. From prodigious volcanic degassing to caldera subsidence and quiescence at Ambrym (Vanuatu): the influence of regional tectonics. *Scientific Reports*, 9(1):1–13, 12 2019. ISSN 20452322. doi: 10.1038/s41598-019-55141-7.

L. Siebert, E. Cottrell, E. Venzke, and B. Andrews. Earth's Volcanoes and Their Eruptions: An Overview. In *The Encyclopedia of Volcanoes*, pages 239–255. Elsevier, 1 2015. doi: 10.1016/b978-0-12-385938-9.00012-2.

L. Smith, K. Yang, L. Pitcher, B. Overstreet, V. Chu, A. Rennermalm, J. Ryan, M. Cooper, C. Gleason, M. Tedesco, J. Jeyeratnam, D. As, M. Broeke, W. Berg, B. Noel, P. Langen, R. Cullather, B. Zhao, M. Willis, A. Hubbard, J. Box, B. Jenner, and A. Behar. Direct measurements of meltwater runoff on the Greenland ice sheet surface. *Proceedings of the National Academy of Sciences*, 2017. doi: 10.1073/pnas.1707743114.

L. C. Smith, V. W. Chu, K. Yang, C. J. Gleason, L. H. Pitcher, A. K. Rennermalm, C. J. Legleiter, A. E. Behar, B. T. Overstreet, S. E. Moustafa, M. Tedesco, R. R. Forster, A. L. LeWinter, D. C. Finnegan, Y. Sheng, and J. Balog. Efficient meltwater drainage through supraglacial streams and rivers on the southwest Greenland ice sheet. *Proceedings of the National Academy of Sciences*, 112:1001–1006, 2015. doi: 10.1073/pnas.1413024112.

A. J. Sole, D. W. F. Mair, P. W. Nienow, I. D. Bartholomew, M. A. King, M. J. Burke, and I. Joughin. Seasonal speedup of a Greenland marine-terminating outlet glacier forced by surface melt–induced changes in subglacial hydrology. *Journal of Geophysical Research: Earth Surface*, 116(F3), 2011. ISSN 2156-2202. doi: 10.1029/2010JF001948. URL `http://dx.doi.org/10.1029/2010JF001948`.

S. Stein and M. Wysession. An Introduction to Seismology, Earthquakes, and Earth Structure. *Blackwell Publishing*, 2005.

L. A. Stevens, M. D. Behn, J. J. McGuire, S. B. Das, I. Joughin, T. Herring, D. E. Shean, and M. A. King. Greenland supraglacial lake drainages triggered by hydrologically induced basal slip. *Nature*, 522:73–76, 2015. doi: 10.1038/nature14480.

D. E. Sugden. Glacial Erosion by the Laurentide Ice Sheet. *Journal of Glaciology*, 20(83):367–391, 1978. doi: 10.3189/S0022143000013915.

A. J. Tedstone, P. W. Nienow, N. Gourmelen, and A. J. Sole. Greenland ice sheet annual motion insensitive to spatial variations in subglacial hydraulic structure. *Geophysical Research Letters*, 41(24):8910–8917, 2014. doi: 10.1002/2014GL062386.

S. Tulaczyk, W. B. Kamb, and H. F. Engelhardt. Basal mechanics of Ice Stream B, west Antarctica: 2 Undrained plastic bed model. *Journal of Geophysical Research: Solid Earth*, 105(B1):483–494, 2000. ISSN 2156-2202. doi: 10.1029/1999JB900328.

K. Unglert and A. M. Jellinek. Volcanic tremor and frequency gliding during dike intrusions at Kilauea-A tale of three eruptions. *Journal of Geophysical Research: Solid Earth*, 120(2):1142–1158, 2 2015. ISSN 21699356. doi: 10.1002/2014JB011596.

M. van˜den˜Broeke, J. Bamber, J. Ettema, E. Rignot, E. Schrama, W. J. van˜de˜Berg, E. van˜Meijgaard, I. Velicogna, and B. Wouters. Partitioning Recent Greenland Mass Loss. *Science*, 326:984–986, 2009. doi: 10.1126/science.1178176.

M. R. van˜den˜Broeke, C. J. P. P. Smeets, and R. S. W. Van˜de˜Wal. The seasonal cycle and interannual variability of surface energy balance and melt in the ablation zone of the west Greenland ice sheet. *The Cryosphere*, 5(2): 377–390, 2011. doi: 10.5194/tc-5-377-2011.

R. S. W. van˜de˜Wal and J. Oerlemans. Response of valley glaciers to climate change and kinematic waves: A study with a numerical ice-flow model. *Journal of Glaciology*, 41:142–152, 1995.

D. Walker and O. Mullins. Surface tension of natural silicate melts from 1,200°-1,500° C and implications for melt structure. *Contributions to Mineralogy and Petrology*, 76(4):455–462, 7 1981. ISSN 00107999. doi: 10.1007/BF00371487.

P. Wallace, T. Plank, M. Edmonds, and E. Hauri. Volatiles in Magmas. In *The Encyclopedia of Volcanoes*, pages 163–183. Elsevier, 2015. ISBN 9780123859389.

K. Wang, H. MacArthur, I. Johanson, E. Montgomery-Brown, M. Poland, E. Cannon, M. D'Alessio, and R. Bürgmann. Interseismic Quiescence and Triggered Slip of Active Normal Faults of Kilauea Volcano's South Flank During 2001–2018. *Journal of Geophysical Research: Solid Earth*, 124(9): 9780–9794, 9 2019. ISSN 21699356. doi: 10.1029/2019JB017419.

S. D. Warren, M. G. Hohmann, K. Auerswald, and H. Mitasova. An evaluation of methods to determine slope using digital elevation data. *CATENA*, 58: 215–233, 2004. doi: 10.1016/j.catena.2004.05.001.

A. Wech, W. Thelen, and A. Thomas. Deep long-period earthquakes generated by second boiling beneath Mauna Kea volcano. *Science (New York, N.Y.)*, 368 (6492):775–779, 5 2020. ISSN 10959203. doi: 10.1126/science.aba4798.

J. Weertman. Traveling waves on glaciers. *Physics of the Movement of Ice*, 1958.

K. W. Wegmann, B. D. Zurek, C. A. Regalla, D. Bilardello, J. L. Wollenberg, S. E. Kopczynski, J. M. Ziemann, S. L. Haight, J. D. Apgar, C. Zhao, and F. J. Pazzaglia. Position of the Snake River watershed divide as an indicator of geodynamic processes in the greater Yellowstone region, western North America. *Geosphere*, 3:271–281, 2007. doi: 10.1130/GES00083.1.

M. A. Werder, I. J. Hewitt, C. G. Schoof, and G. E. Flowers. Modeling channelized and distributed subglacial drainage in two dimensions. *Journal of Geophysical Research: Earth Surface*, 118(4):2140–2158, 2013. ISSN 2169-9011. doi: 10.1002/jgrf.20146.

K. X. Whipple and G. E. Tucker. Dynamics of the stream-power river incision model: Implications for height limits of mountain ranges, landscape response timescales, and research needs. *Journal of Geophysical Research: Solid Earth*, 104(B8):17661–17674, 1999. ISSN 2156-2202. doi: 10.1029/1999JB900120.

R. C. Whitty, E. Ilyinskaya, E. Mason, P. E. Wieser, E. J. Liu, A. Schmidt, T. Roberts, M. A. Pfeffer, B. Brooks, T. A. Mather, M. Edmonds, T. Elias, D. J. Schneider, C. Oppenheimer, A. Dybwad, P. A. Nadeau, and C. Kern. Spatial and Temporal Variations in SO2 and PM2.5 Levels Around Kilauea Volcano, Hawai'i During 2007–2018. *Frontiers in Earth Science*, 8:36, 2 2020. ISSN 22966463. doi: 10.3389/feart.2020.00036.

C. A. Williams and G. Wadge. An accurate and efficient method for including the effects of topography in three-dimensional elastic models of ground deformation with applications to radar interferometry. *Journal of Geophysical Research: Solid Earth*, 105(B4):8103–8120, 2000. doi: 10.1029/1999JB900307.

F. Witham and E. W. Llewellin. Stability of lava lakes. *Journal of Volcanology and Geothermal Research*, 158(3-4):321–332, 11 2006. ISSN 03770273. doi: 10.1016/j.jvolgeores.2006.07.004.

J. R. Womersley. Method for the calculation of velocity, rate of flow and viscous drag in arteries when the pressure gradient is known. *The Journal of Physiology*, 127(3):553–563, 3 1955. ISSN 14697793. doi: 10.1113/jphysiol.1955.sp005276.

P. Wright, J. Harper, N. Humphrey, and T. Meierbachtol. Measured basal water pressure variability of the western Greenland Ice Sheet: Implications for hydraulic potential. *Journal of Geophysical Research: Earth Surface*, 121(6): 1134–1147, 2016. doi: 10.1002/2016JF003819.

T. L. Wright and F. W. Klein. Two hundred years of magma transport and storage at Kilauea Volcano, Hawai'i, 1790–2008. *U.S. Geological Survey Professional Paper 1806*, page 240 p., 2014. ISSN 2330-7102. doi: doi:10.3133/pp1806.

K. Yang and L. C. Smith. Internally drained catchments dominate supraglacial hydrology of the southwest Greenland Ice Sheet. *Journal of Geophysical Research: Earth Surface*, 121, 2016. doi: 10.1002/2016JF003927.

K. Yang, L. C. Smith, V. W. Chu, C. J. Gleason, and M. Li. A Caution on the Use of Surface Digital Elevation Models to Simulate Supraglacial Hydrology of the Greenland Ice Sheet. *IEEE Journal of Selected Topics in Applied Earth Observations and Remote Sensing*, 8(11):5212–5224, 11 2015. ISSN 1939-1404. doi: 10.1109/JSTARS.2015.2483483.

C. E. Yoon, O. O'Reilly, K. J. Bergen, and G. C. Beroza. Earthquake detection through computationally efficient similarity search. *Science Advances*, 1(11): e1501057, 12 2015. ISSN 23752548. doi: 10.1126/sciadv.1501057.

T. J. Young, D. M. Schroeder, P. Christoffersen, L. B. Lok, K. W. Nicholls, P. V. Brennan, S. H. Doyle, B. Hubbard, and A. Hubbard. Resolving the internal and basal geometry of ice masses using imaging phase-sensitive radar. *Journal of Glaciology*, 64(246):649–660, 2018. doi: 10.1017/jog.2018.54.

B. J. Zadler, J. H. Le Rousseau, J. A. Scales, and M. L. Smith. Resonant ultrasound spectroscopy: Theory and application. *Geophysical Journal International*, 156(1):154–169, 1 2004. ISSN 0956540X. doi: 10.1111/j.1365-246X.2004.02093.x.

Y. Zhang, Z. Xu, M. Zhu, and H. Wang. Silicate melt properties and volcanic eruptions. *Reviews of Geophysics*, 45(4), 2007. doi: 10.1029/2006RG000216.

L. Zuccarello, M. Burton, G. Saccorotti, C. Bean, and D. Patanè. The coupling between very long period seismic events, volcanic tremor, and degassing rates at Mount Etna volcano. *Journal of Geophysical Research: Solid Earth*, 118 (9):4910–4921, 9 2013. ISSN 21699356. doi: 10.1002/jgrb.50363.

H. J. Zwally, W. Abdalati, T. Herring, K. Larson, J. Saba, and K. Steffen. Surface Melt-Induced Acceleration of Greenland Ice-Sheet Flow. *Science*, 297: 218–222, 2002. doi: 10.1126/science.1072708.